Sustainable Civil Infrastructures

Laureano R. Hoyos
John McCartney *Editors*

Advances in Characterization and Analysis of Expansive Soils and Rocks

Proceedings of the 1st GeoMEast International Congress and Exhibition, Egypt 2017 on Sustainable Civil Infrastructures

SSIGE

Springer

Sustainable Civil Infrastructures

About this Series

Sustainable Infrastructure impacts our well-being and day-to-day lives. The infrastructures we are building today will shape our lives tomorrow. The complex and diverse nature of the impacts due to weather extremes on transportation and civil infrastructures can be seen in our roadways, bridges, and buildings. Extreme summer temperatures, droughts, flash floods, and rising numbers of freeze-thaw cycles pose challenges for civil infrastructure and can endanger public safety. We constantly hear how civil infrastructures need constant attention, preservation, and upgrading. Such improvements and developments would obviously benefit from our desired book series that provide sustainable engineering materials and designs. The economic impact is huge and much research has been conducted worldwide. The future holds many opportunities, not only for researchers in a given country, but also for the worldwide field engineers who apply and implement these technologies. We believe that no approach can succeed if it does not unite the efforts of various engineering disciplines from all over the world under one umbrella to offer a beacon of modern solutions to the global infrastructure. Experts from the various engineering disciplines around the globe will participate in this series, including: Geotechnical, Geological, Geoscience, Petroleum, Structural, Transportation, Bridge, Infrastructure, Energy, Architectural, Chemical and Materials, and other related Engineering disciplines.

More information about this series at http://www.springer.com/series/15140

Laureano R. Hoyos · John McCartney
Editors

Advances in Characterization and Analysis of Expansive Soils and Rocks

Proceedings of the 1st GeoMEast International Congress and Exhibition, Egypt 2017 on Sustainable Civil Infrastructures

Editors
Laureano R. Hoyos
Department of Civil Engineering
University of Texas at Arlington
Arlington, TX
USA

John McCartney
University of California, San Diego
La Jolla, CA
USA

ISSN 2366-3405 ISSN 2366-3413 (electronic)
Sustainable Civil Infrastructures
ISBN 978-3-319-61930-9 ISBN 978-3-319-61931-6 (eBook)
DOI 10.1007/978-3-319-61931-6

Library of Congress Control Number: 2017946441

Printed on acid-free paper

This Springer imprint is published by Springer Nature
The registered company is Springer International Publishing AG
The registered company address is: Gewerbestrasse 11, 6330 Cham, Switzerland

Preface

Toward building sustainable and longer civil infrastructures, the engineering community around the globe continues undertaking research and development to improve existing design, modeling, and analytical capability. Such initiatives are also the core mission of the Soil-Structure Interaction Group in Egypt (SSIGE) to contribute to the ongoing research toward sustainable infrastructure. This conference series "GeoMEast International Congress and Exhibition" is one of these initiatives.

Ancient peoples built their structures to withstand the test of time. If we think in the same way, our current projects will be a heritage for future generations. In this context, an urgent need has quickly motivated the SSIGE and its friends around the globe to start a new congress series that can bring together researchers and practitioners to pursue "Sustainable Civil Infrastructures." The GeoMEast 2017 is a unique forum in the Middle East and Africa that transfers from the innovation in research into the practical wisdom to serve directly the practitioners of the industry.

More than eight hundred abstracts were received for the first edition of this conference series "GeoMEast 2017" in response to the Call for Papers. The abstracts were reviewed by the Organizing and Scientific Committees. All papers were reviewed following the same procedure and at the same technical standards of practice of the TRB, ASCE, ICE, ISSMGE, IGS, IAEG, DFI, ISAP, ISCP, ITA, ISHMII, PDCA, IUGS, ICC, and other professional organizations who have supported the technical program of the GeoMEast 2017. All papers received a minimum of two full reviews coordinated by various track chairs and supervised by the volumes editors through the Editorial Manager of the SUCI "Sustainable Civil Infrastructure" book series. As a result, 15 volumes have been formed of the final +320 accepted papers. The authors of the accepted papers have addressed all the comments of the reviewers to the satisfaction of the track chairs, the volumes editors, and the proceedings editor. It is hoped that readers of this proceedings of the GeoMEast 2017 will be stimulated and inspired by the wide range of papers written by a distinguished group of national and international authors.

This volume of technical papers includes research on two important topics in geotechnical engineering: the behavior and treatment of expansive soils, and the characterization of rock properties. The four studies on rock properties cover a range of topics, including the thermo-hydro-mechanical behavior of gypsum rock, the role of rock strength in blastability, indirect methods to estimate rock strength, and variations in isotope distributions in Permian rocks. The twelve studies on expansive soils include investigations into novel stabilization techniques for expansive soils using different admixtures or mechanical consolidation techniques, as well as new experimental approaches to evaluate the behavior of expansive soils. They also include an evaluation of wetting boundary conditions on the volume change of expansive soils, as well as the role of hydrologic boundary conditions in arid climates. The two themes in this collection are representative of local challenges facing geotechnical engineers in the Middle East, but their contributions can also be extended to other regions of the world. The efforts of all authors and their peer reviewers, many of them from the Unsaturated Soils committee of the Geo-Institute of the American Society of Civil Engineers (ASCE), are gratefully acknowledged.

Publication of this quality of technical papers would not have been possible without the dedication and professionalism of the anonymous papers reviewers. We are thankful to Dr. Hany Farouk Shehata, Dr. Nabil Khelifi, Dr. Khalid M. ElZahaby, Dr. Mohamed F. Shehata, and to all the distinguished volumes editors of the proceedings of the GeoMEast 2017. Appreciation is extended to the authors and track chairs for their significant contributions. Thanks are also extended to Springer for their coordination and enthusiastic support to this conference. The editors acknowledge the assistance of Ms. Janet Sterritt-Brunner and Mr. Arulmurugan Venkatasalam in the final production of the 15 edited volumes "Proceedings of GeoMEast 2017".

Contents

Influence of Chemical Additives and Flyash on the Swelling and Bearing Resistance of Expansive Subgrade Soil

G. Radhakrishnan[1(✉)], M. Anjan Kumar[2], and G.V.R. Prasada Raju[3]

[1] JNTUK, Kakinada 533 004, India
radhakrishnan.gunupudi@gmail.com
[2] BVC College of Engineering, Palacharla 533 104, India
anjan_mantri@yahoo.com
[3] UCE, JNTUK, Kakinada 533 004, India
gvrp_raju@yahoo.com

Abstract. The geotechnical properties of expansive soil with inherent montmorillonite clay mineral are highly amenable to changes in the moisture content. These changes lead to distortions to the structures built on them. Flyash had been used extensively as a stabilizer to inhibit heave of expansive soil subgrade. Contemporary researchers have been trying to control the heave with the help of many additives viz. construction waste, industrial by products, chemicals compounds. Our current study is aimed to evaluate the combined effect of flyash and aluminum chloride as an accelerator to enhance geotechnical properties of the expansive soil. Twenty soil samples were prepared with a mix of flyash (0% to 15%) and aluminum chloride (0% to 2%) and the resulting soil matrixes were subjected to laboratory testing. Experimental results enhanced the CBR which is critical to the design of pavement thickness and there has been a simultaneous reduction in the swelling nature of soil.

Keywords: Expansive soil · Stabilization · Flyash and aluminum chloride

Notations

$AlCl_3$	Aluminum Chloride
DFS	Differential Free Swell
CBR	California Bearing Ratio
MDD	Maximum Dry Density
OMC	Optimum Moisture Content

1 Introduction

Expansive soils, most common in the deltaic regions along the sea cost of Andhra Pradesh in India, undergo swelling and shrinking due to seasonal moisture variations. This movement leads to the damage of lightly loaded structures like flexible pavements, pipe lines, slopes and canal linings. The expected retrofitting cost often exceeds loss due to natural hazards (Jones and Holtz 1973). Flexible pavements constructed on

L.R. Hoyos and J. McCartney (eds.), *Advances in Characterization and Analysis of Expansive Soils and Rocks*, Sustainable Civil Infrastructures,
DOI 10.1007/978-3-319-61931-6_1

these soils show signs of continuous damage during their service life, rendering it a challenge to the practicing engineers. Researchers, practicing engineers and highway research organizations have been making attempts to treat these soils with different compounds (Lime, Chloride Compounds, Fluorides, Hydroxides, Acids, Phosphates, Sulphates etc.), construction waste (Waste plastic strips, waste tire pieces, ceramic waste etc.) and industrial sludge, slag and ashes (Flyash, Rice husk ash, Blast furnace slag, Wood ash, Bagasse ash).

Soil stabilization with the combination of above materials serves the dual purpose of disposal of waste material and recycling of the industrial waste thus striking the economy.

Many researchers have contributed to the gainful utilization of flyash in improving the properties of expansive soil. Ferguson (1993) stated that the flyash exhibits self cementing characteristics making it useful in soil stabilization. There is an appreciable increase in CBR and Resilient modulus values of expansive soil with the addition of flyash (Edil et al. 2006). The interaction between expansive soil and flyash was studied by Srivastava et al. (1997) and found that maximum dry density (MDD) increases and optimum moisture content (OMC) decreases with the addition of flyash. Investigation made by Buhler and Cerato (2007), found that with increasing percentages of both lime and flyash, linear shrinkage gets reduced. Lime and flyash could be used effectively for stabilizing the black cotton soil having montmorillonite mineral content (Pankaj et al. 2012) and with the addition of flyash and lime, the CBR value increased to a great extent which resulted in the reduced pavement thickness. For strengthening the expansive subgrade soil, Rice Husk Ash (RHA) and flyash were recommended by Robert (2009). Similarly other researchers have been making attempts to modify the engineering properties of the soil using other additives. Petry and Armstrong (1989) have researched with calcium chloride ($CaCl_2$) which has the advantage of total solubility in water and resulting higher cation exchange capacity. Gangadhara Reddy et al. (2015) have attempted to investigate the influence of cation valence and mean particle diameter on the swelling properties of expansive soil and concluded that the cation valance has profound influence in modifying the engineering properties of expansive soil. The effect of magnesium chloride solution on the engineering properties of clay soils was evaluated by Murat Turkoz et al. (2014). Treatment of expansive soil using trivalent cations like Fe^{+3} and Al^{+3} was studied by Matsuo and Kamon (1981). Efficiency of $CaCl_2$ on the plasticity and swell characteristics of an expansive clay bed was evaluated by Ramana Murthy and Hari Karishna (2006). Tamadher et al. (2007) evaluated the engineering properties of silty clay using sodium chloride (NaCl), magnesium chloride ($MgCl_2$) and calcium chloride ($CaCl_2$). These results point out the potential for utilization of flyash along with chloride compounds in improving the geotechnical properties of expansive soil.

The present work is an attempt to examine the effect of mixture of flyash and aluminum chloride on swelling, CBR characteristics of an expansive soil.

2 Materials Used and Experimental Methods

2.1 Natural Soil

Highly expansive soil sample collected for analysis is obtained from a construction site near Amalapuram area of Andhra Pradesh, India at a depth of 1.5 m from ground level. The basic geotechnical properties of expansive soil are presented in Table 1.

Table 1. Geotechnical Properties of the natural soil

Property	Value	Property	Value
Liquid limit (%)	85	Swell potential (kPa)	20
Plastic limit (%)	33	DFS (%)	145
Plasticity index (%)	52	Max dry density (g/cc)	1.55
Shrinkage limit (%)	12	Optimum moisture content (%)	24.70
Specific gravity	2.61	Soaked CBR (%)	
Swell pressure (kPa)	295		

2.2 Flyash

Flyash used in this study is procured from Vijayawada Thermal Power Station of Andhra Pradesh, India, is class C type and available in abundance at free cost. Laboratory testing of flyash have shown the following geotechnical and geochemical properties: Specific gravity - 1.95, Liquid limit - 25%, MDD and OMC of the soil - 1.35 g/cc and 24% respectively, the CBR - 6%. The chemical composition of flyash is SiO_2 - 61.29%, Al_2O_3 - 21.60%, Fe_2O_3 - 3.09%, CaO - 1.02%, MgO - 0.5% and loss on ignition - 0.2%.

2.3 Aluminum Chloride

Aluminum chloride ($AlCl_3$) used in the current study is easily soluble in water, rendering its application for adding to the soil is convenient in the form of chemical solution.

2.4 Sample Preparation and Curing

Prior to the testing, expansive soil was air dried and pulverized. Representative soil sample passing 4.75 mm IS sieve and air dried flyash were collected and stored in air tight containers. Twenty soil samples of each weighing 40 kg were prepared with different percentages of flyash and chemical contents. Flyash and aluminum chloride contents were added in different proportions of 0%, 5%, 10%, 15% and 0%, 0.5%, 1.0%, 1.5%, 2.0% of dry weight of soil respectively. Expansive soil and flyash were mixed in dry state. Aluminum chloride was added to this mixture in solution form to achieve uniform mixing. Soil samples thus prepared were kept aside in wet gunny bags

for maturing in the laboratory at room temperature and are maintained wet by sprinkling water regularly. The soil samples were labeled for easy reference.

2.5 Methods of Testing

The laboratory experimentation was carried out as per the procedures laid down in the Indian Standard Code: 2720 series, shown in Table 2. During the CBR test, the rate of penetration of the plunger was kept at 1.25 mm/min and proving ring capacity is 10 KN. Soaked CBR values at 2.5 mm and 5 mm penetration were calculated for all the samples. All the specimens prepared from different soil matrices for CBR and swell pressure testing are corresponding to the predetermined maximum dry density and optimum moisture content as tabulated in Table 3.

Table 2. List of IS codes used in the laboratory testing

Tests	Standards
Consistency limits	IS 2720 (Part 5)-1985 & (Part VI)-1972
OMC and MDD	IS 2720 (Part8)-1983
Differential free swell	IS 2720 (Part XL)-1977
Swell pressure	IS 2720 (PartXLI)-1977
California bearing ratio	IS 2720 (Part 16)-1987
Unconfined compressive strength	IS 2720 (Part10)-1991

Table 3. MDD and OMC values of different soil, flyash and Aluminum chloride mixtures

Flyash	Aluminum chloride									
	0%		0.5%		1.0%		1.5%		2.0%	
	OMC (%)	MDD (g/cc)	OMC (%)	MDD (g/cc)	OMC (%)	MDD (g/cc)	OMC (%)	MDD (g/cc)	OMC (%)	MDD (g/cc)
0%	24.70	1.551	24.26	1.615	23.54	1.628	23.04	1.637	22.82	1.640
5%	23.56	1.738	23.55	1.741	22.49	1.752	22.09	1.759	22.00	1.759
10%	23.25	1.745	23.15	1.759	22.40	1.765	22.00	1.772	22.00	1.775
15%	23.00	1.710	22.75	1.721	22.25	1.736	21.92	1.742	21.90	1.745

3 Results and Discussion

3.1 Effect of Additives on Consistency Limits

The variation of consistency limits with the addition of flyash and aluminum chloride is shown in Fig. 1. With the addition of 10% flyash content, the liquid limit and plasticity indices are reduced from 85% to 79% and from 56% to 48% respectively. In order to further reduce the consistency limits, aluminum chloride was used. Considering an optimum value of 1% aluminum chloride, the above values were reduced to 53% and 22% respectively. Considering an optimum value of 10% flyash and 1% aluminum chloride, the percentage reduction in liquid limit and plasticity index are about 38% and

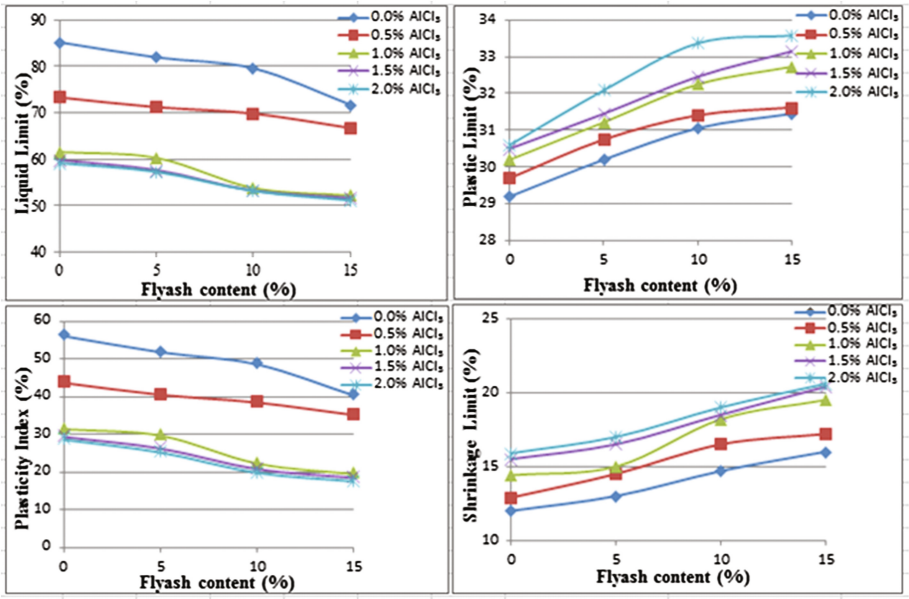

Fig. 1. Variation of index limits with flyash and Aluminum chloride

61% respectively. This proves that the combined effect of flyash and aluminum chloride is more vital in reducing the plasticity characteristics.

3.2 Effect of Additives on Swell Properties

The swelling potential of the expansive soil was established by differential free swell (DFS) tests. The swelling value of untreated soil is 145%. The variation of the DFS and swell pressure with different additives are presented in Fig. 2. The addition of flyash has a little improvement in reducing the DFS value of the soil. Addition of flyash content by 5%, 10% and 15% caused the percentage reduction in DFS in the order of 17%, 31% and 38% respectively. Whereas, the addition of 1% aluminium chloride ($AlCl_3$) the DFS is reduced from 145% to 60%. Similarly, the swelling pressure decreased with the increase in flyash and aluminum chloride content. Reduction is more significant in the case of aluminum chloride content than the addition of flyash. Untreated soil has a swell pressure value of 295 kPa and it is decreased to 110 kPa with the addition of 1% aluminum chloride. In our study, the addition of flyash by 5%, 10% and 15% reduced the swell pressure to 225, 176 and 144 kPa respectively. Thus the combined use of flyash and aluminum chloride proved to be more critical. Based on the results obtained, blending of 10% flyash + 1% aluminum chloride to the expansive soil caused 80% of reduction in the swell pressure.

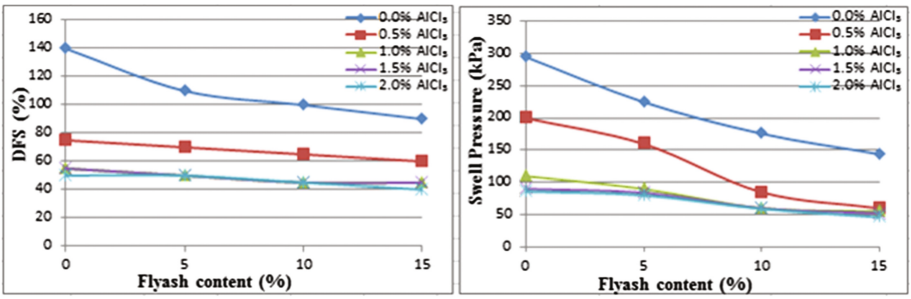

Fig. 2. Variation of DFS and Swell Pressure with Flyash and Aluminum chloride

3.3 California Bearing Ratio

The CBR value of untreated soil in soaked condition was found to be 2.12%. But when flyash is added to the expansive soil, CBR value increased to 6.14%. With a view to further increasing the CBR, aluminum chloride is added to the expansive soil plus flyash mix. Upon addition of flyash (10%) and aluminum chloride (1%) content, the CBR value increased to 9.58% which is nearly five times that of the untreated value. The combined influence of additives on California Bearing Ratio (CBR) is shown in Fig. 3.

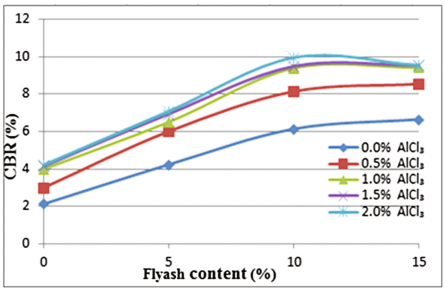

Fig. 3. Variation of CBR with flyash & Aluminum chloride

4 Conclusion

An Experimental study was conducted to evaluate the effect of flyash and aluminum chloride on the swelling and bearing resistance of the expansive soil. Based on the results, the following conclusions have been made.

1. Combination of flyash and aluminum chloride is effective in reducing the plasticity characteristics of the expansive soil. Addition of these components has shown to reduce the liquid limit, slight increase in the plastic limit. With the combination of flyash (10%) and aluminum chloride (1%), the percentage reduction in plasticity index was found to be about 61%.

2. The potential expansiveness of the soil measured by differential free swell got reduced by 67% and the swelling pressure by 80%. Flyash and aluminum chloride are effective in reducing the swelling nature of soil, out of which aluminum chloride is more effective compared to flyash.
3. CBR test results indicated that the aluminum chloride has no considerable effect on CBR. The CBR increased by three times when flyash was only added. But the combined effect was found to be more crucial and the bearing capacity resistance rose by five times of the original value.

Finally, the study attempted to show an insight on the combined effect of addition of flyash and aluminum chloride on the swelling and bearing resistance of the expansive soil subgrade. The results disclosed that an optimum quantity of 10% flyash and 1% aluminum chloride is effective in minimizing the soil swelling and improving the bearing resistance of the expansive soil.

References

Buhler, R.L., Cerato, A.B.: Stabilizaton of Oklahoma expansive soils using lime and class C flyash. In: Problematic Soils and Rocks and Insitu Characterization, ASCE, GSP 162, pp. 1–10 (2007)

Edil, T., et.al.: Stabilizing soft fine-grained soils with fly ash. In: Stabilization of Geomedia Using Cementitious Materials, ASCE, vol. 18, no. 2, pp. 283–294 (2006)

Ferguson, G.: Use of self commenting flyash as a soil stabilizing agent. In: Geotechnical Special Publication, ASCE, no. 36, pp. 1–15 (1993)

Jones, D.E., Holtz, W.G.: Expansive soils-the hidden disaster. In: Civil Engineering, vol. 43, no. 8 (1973)

Matsuo, S., Kamon, M.: Soil stabilisation by multivalent cations. In: Proceedings of 10th ICSMFE, Stockholm, vol. 3, pp. 735–738 (1981)

Turkoz, M., et al.: The effect of magnesium chloride solution on the engineering properties of clay soil with expansive and dispersive characteristics. Appl. Clay Sci. **101**, 1–9 (2014)

Gangadhara Reddy, N., et al.: Evaluating the influence of additives on swelling characteristics of expansive soils. Int. J. Geosynth. Ground Eng. **1**(1), 1–13 (2015)

Pankaj, R.M., et al.: Stabilization of black cotton soil using admixtures. Int. J. Eng. Innov. Technol. **1**(5), 1–3 (2012)

Petry, T.M., Armstrong, J.C.: Stabilisation of expansive clay soils, RR-1219, pp. 103–112. Transportation Research Board (1989)

Ramana Murthy, V., HariKarishna, P.: Stabilization of expansive clay bed using $CaCl_2$ solution. In: Ground Improvement, vol. 10, no. 1 (2006)

Robert, M.B.: Soil stabilization with flyash and rice husk ash. Int. J. Res. Rev. Appl. Sci. **1**(3), 209–217 (2009)

Srivastava, R.K., et.al.: SEM analysis and geotechnical characterization of industrial waste–expansive soil interaction behavior. In: Proceedings of Indian Geotechnical Conference (1997)

Tamadher, T.A., et al.: Stabilization of silty clay soil using chloride compounds. J. Eng. Sci. Technol. **2**(1), 102–109 (2007)

Characterization of Unsaturated Shrink-Swell Soils Properties in Egypt

Fayek Hassona[1(✉)], Remon I. Abdelmalak[1], and Beshoy M. Hakeem[2]

[1] Civil Engineering Department, Faculty of Engineering, El-Minia University, El-Minia, Egypt
Fhassona@excite.com, remonisaac@gmail.com
[2] Civil Engineering Department, Higher Institute of Engineering and Technology, El-Minia, Egypt
civileng_beshoy@yahoo.com

Abstract. Expansive soils show high volumetric changes with changes in water content. When they imbibe water during wet season, they expand and upon evaporation thereof through dry season, they shrink. Because of this alternate swelling and shrinkage, structures founded on them are severally damaged. Potentially problematic shrink-swell soils can be found almost anywhere in the world especially in arid and semi-arid regions of the tropical and temperate climate. Due to the lack of experience pertinent to characterization and dealing with problematic shrink-swell soils in Egypt, many defects appear in some structures established in development projects. Density and severity of problems associated with the presence of shrink-swell soils differ from region to another. Many factors contribute to the problem such as: soil type, soil engineering properties, foundation type, nature of development project, and the extension of development zone…etc. In this research, extensive experimental work has been performed on sixty two (62) soil samples obtained from various sites all over Egypt. The investigation targeted to assess volumetric change and moisture diffusion characteristics as well as index properties of unsaturated clayey soils. Test results confirm that volumetric change and moisture diffusion characteristics for unsaturated soils can be reasonably related to conventional soil index properties. Based on the obtained comprehensive database of results, ten (10) equations expressing relationships among different engineering properties of unsaturated shrink-swell soils in Egypt are proposed and discussed.

Keywords: Expansive soil · Shrink-swell soil · Soil water characteristic curve · Swell potential · Bentonite · Montmorillonite · Volumetric change · Moisture diffusion · Unsaturated soils

1 Introduction

Expansive soils in many areas of the world impose a substantial threat to foundations especially for light buildings. Jahangir et al. (2011) reported that shrinkage-swelling of clayey soils is a natural hazard, which may significantly affect buildings by differential settlements. Dafalla et al. (2010) concluded that the distortion is normally observed in the light structures due to relative flexibility of the frames and substructure foundations.

L.R. Hoyos and J. McCartney (eds.), *Advances in Characterization and Analysis of Expansive Soils and Rocks*, Sustainable Civil Infrastructures,
DOI 10.1007/978-3-319-61931-6_2

This is not tolerated by the brick walls normally used to fill up the panels in concrete frame structures. Severe cracks can be shown when twist or movement takes place. Therefore the use of rigid design methodology approach is expected to give less flexible support and reduce the chances of cracks and damage.

Expansive soils attribute their characteristics to the presence of swelling clay minerals. As they get wet, the clay minerals absorb water molecules and expand. Conversely as they dry, they shrink and leave large voids or cracks in the soil. Soils with active clay minerals, such as montmorillonite, exhibit the most dangerous swelling and shrinking properties. According to Lajurkar et al. (2013), expansive soil exhibits very complex and undesirable characteristics when used as engineering material.

Briaud et al. (2003) proposed a new method to estimate the vertical movement of the ground surface for soil that swells and shrinks due to variations in water content. They estimated the change in water content and the depth of seasonal moisture changes from local databases or from existing techniques. The method was evaluated by comparing the predicted movement and the measured movement of four full-scale spread footings over a period of 2 years.

According to Sood (2005), footings of a structure founded on an unsaturated soil are subjected to stresses developed due to swelling or shrinking of the soil. This is due to the change in suction (negative pore water pressure) of the soil due to the variation in the water content. These movements can be predicted by using the diffusion equation which defines the movement of moisture through unsaturated soils. The equation for moisture diffusion in unsaturated soils is similar to the consolidation equation for saturated soils when suction is expressed in logarithmic scale unit (pF).

Suction is mainly measured in units of water pressure such as kPa. Typical suction range is from 1 kPa, for a very wet soil close to 100% degree of saturation, to a 10^6 kPa, for an oven dried soil sample. As the value of suction can be very high, it is usually expressed on a logarithmic scale. The commonly used pF scale, [U (pF) = $\log_{10} |u_w|$] provides another alternative unit to measure of suction where u_w is the total suction expressed in units of cm of water head.

Expansion of soils can directly be measured in the laboratory, by immersing a remolded soil sample and measuring its volume change through 24-hour free swell test, (Hammam and Abdel-Salam 2013). Israr et al. (2014) found that there exist unique relationships between the index properties and the swelling characteristics of swelling soils. The results showed that, the increasing Atterberg's limits such as plasticity index (P.I.) from 18% to 150% impart significant increases in the values of swell potential (SP) and swell pressure (P_{sw}) from 2.62% to 13.36% and 94.2 kPa to 928.6 kPa, respectively. Erzin and Erol (2007) Concluded that an increase in the bentonite content in the clay mixtures yielded an increase in the specific surface area (SSA) value, the cation exchange capacity (CEC) value, the liquid limit (L.L.) and the plasticity index (P.I.) values. Meanwhile, plastic limit (P.L.) value was nearly unaffected by increases in the bentonite content. These results indicate that the SSA, the CEC, the L.L. and the P.I. values of the clay mixtures are more sensitive to changes in clay mineralogy than the P.L. is. It was also observed that the L.L. values were controlled by the SSA and CEC values.

Zapata et al. (2000) defined the soil water characteristic curve (SWCC) as the relationship between soil suction and some measure of the water content, which can be

measured or predicted based on soil index properties such as the grain size distribution (GSD) function. Estimation based on index properties is highly desirable due to its simplicity and low cost and would be the path of choice to the SWCC, provided the accuracy of the estimate were adequate. According to AL-Shihabi (2010), suction compressibility indices (γ_h) can be obtained by determination of the slope of Soil Water Characteristic Curve (SWCC).

The main objective of this paper is to assess soil engineering properties (mainly volumetric change and moisture diffusion characteristics) for expansive soils samples obtained from various sites in Egypt. The soil water characteristic curve (SWCC) was determined to investigate the water retention capacity of the soil. Geotechnical index properties were determined for preliminary soil assessment as well as find reliable correlations with key unsaturated soil parameters. Finally, a new proposed set of relationships were developed that may be treated as are liable tool to estimate the swelling and shrinking characteristics with carefully evaluated index properties in hand.

2 Laboratory Investigations

In this study, a comprehensive experimental scheme has been undertaken at Geotechnical Engineering Laboratory, Faculty of Engineering, and EL-Minia University, to investigate various factors controlling the swelling and shrinking characteristics of expansive soils. Extensive experimental work was carried out on sixty two (62) soil samples. The shrink-swell behavior of the soil was studied by obtaining the volumetric increase and decrease of soil samples during swelling and shrinking. The analysis of test results and observations made during the experiments have been reported herein. The interpretations facilitated the development of a set of simple empirical correlations between soil index properties and key swelling and shrinking parameters of expansive soils.

2.1 Natural Soil Samples

Natural soil samples were obtained from 12 sites located at different regions in Egypt such as: Fayoum (two sites), BeniSuif (three sites), El-max Elkebly (El-Wadi El-Gedid), Abo-Tartor (El-Kharga, El-Wadi EL-Gedid), El-Mokatam area, Zahra El-Maadi area, the 6th of October, and Qena (two sites), as illustrated in Fig. 1.

Only two samples were undisturbed (obtained from EL-Mokatam and Zahra EL-Maadi areas). The rest of the soil samples (taken from 10 sites) were dry and cracked and had to be remolded. Hence, four remolded samples from each site were prepared in oedometer cells using remolding pressures of 400, 800, 1200, and 1600 kPa. This ended up with forty two natural soil samples (40 remolded samples and two undisturbed). Figure 1 shows the scattering of the selected 12 sites for the collected soil samples.

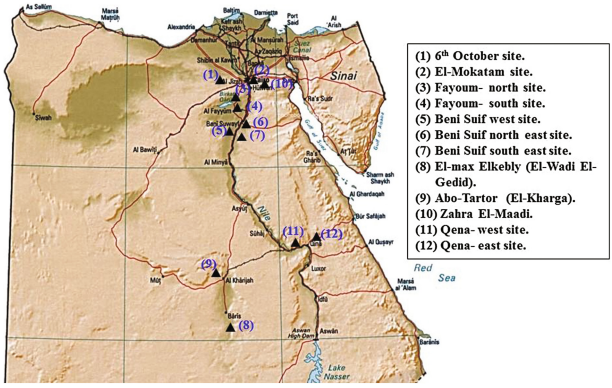

Fig. 1. Map of Egypt with locations of the samples sites.

2.2 Bentonite-Silty Clay Soil Mixtures

To widen the range of shrink-swell potentials of the tested samples, additional five bentonite-silty clay soil mixtures were used in the experimental program. In the same way, Lajurkar et al. (2013) considered five soil mixes with different Bentonite contents to develop characterizing parameters for soils with different shrink-swell capacity characteristics. Generally, increasing the number of tested samples enriches the obtained database of results and improve the reliability of the developed correlation equations expressing relationships among different shrink-swell parameters.

Bentonite is a family of clay minerals, produced by the weathering of volcanic ash, and is highly hygroscopic in nature. (OCMA DFCP.4) is a commercial bentonite, produced by Egyptian Gulf Chemical Company "EGCC", located at Sadat city – Industrial Zone 6 – Cairo, which has been used in the current research work. The laboratory investigation classified it as high plastic clay (CH), exhibiting liquid limit of 149.77%, plastic limit of 40.49%, and plasticity index of 109.28%. The bentonite was mixed with different proportions of non-swelling natural silty clay soil obtained from a site located at Damaris, EL-Minya city. The obtained five bentonite-silty clay soil mixtures will be denoted according to their bentonite contents for easy reference (i.e. 100 Bent., 80 Bent., 60 Bent., 40 Bent. and 20 Bent.). The five bentonite-silty clay soil mixtures were reconstituted using four different remolding pressures, similar to the remolded natural soil samples, resulting in a total of twenty soil mixture samples.

3 Testing Program

3.1 Soil Index Properties

Identification tests were performed in order to have a background data base for the soil properties. The conducted tests were:

- Atterberge limits: Liquid Limit (L.L.), Plastic Limit (P.L.), and Plasticity Index P.I., according to (ECP 202-2001).

- Dry unit weight (γ_{dry}), and specific gravity of soil solids (G_s), according to (ECP 202-2001).
- Free swell (F.S. %), and swelling potential (SP %), according to (ECP 201-2001).
- Swell limit (I_{sw}), shrink limit (I_{sh}), and shrink-swell index (I_{ss}) following Abdelmalak (2007) procedure.

3.2 Moisture Diffusion and Volume Change Properties

For the sixty two soil samples, coefficients of soil unsaturated diffusivity in shrink and swell cases as well as the suction compressibility indices were determined.

Coefficients of soil unsaturated diffusivity in shrink condition (α_{sh}) were determined using α-shrink test procedure developed by Abdelmalak (2007). However, coefficients of soil unsaturated diffusivity in swell condition (α_{sw}) were determined using 1-D time factors similar to commonly used in consolidation test, Das (2008). This is referred to the similarity between 1-D unsaturated diffusion equation when suction expressed in logarithmic units and 1-D consolidation equation, Abdelmalak (2007). In α-shrink test, a cylindrical soil specimen shrinks in both the vertical and horizontal directions (i.e. 2-D axisymmetric problem), which obliged Abdelmalak (2007) to develop time factors for 2-D axisymmetric diffusion problem. Meanwhile, in α-swell test, a cylindrical soil specimen is allowed to swell in the vertical direction only as the swelling in the horizontal direction is constrained by the oedometer ring (i.e. 1-D problem).

The Soil Water Characteristic curves (SWCC), expressed as gravimetric water content versus suction in pF unit, were determined following Sood (2005) and Bulut (2001). Slope of the straight line in the desaturation zone were determined, which equals to the suction compressibility index (γ_h).

Vapor equilibrium technique was implemented to determine SWCC by controlling the relative humidity in an air space above saturated salt solutions in a closed system. The tests were carried out in closed-lid desiccator for inducing suctions of 2.5, 3.5, 4.5 and 5.5 pF using saturated salt solutions of Na CL.

4 Results and Discussion

The liquid limit, plasticity index, as well as free swell of the soil samples increased with the increase of bentonite percentage for the bentonite-soil mixtures as indicated in Fig. 2.

Ten different regression equations were established among swelling characteristics and soil index properties, as illustrated in Table 1. For example, to develop reliable predictive equation for the soil suction compressibility index (γ_h), relationships between (γ_h) and many parameters and combinations of parameters (such as: α_{sh}, α_{sw}, SP, P.I./γ_{dry}, P.I., L.L./γ_{dry}, P.L./γ_{dry}) have been investigated. Various mathematical

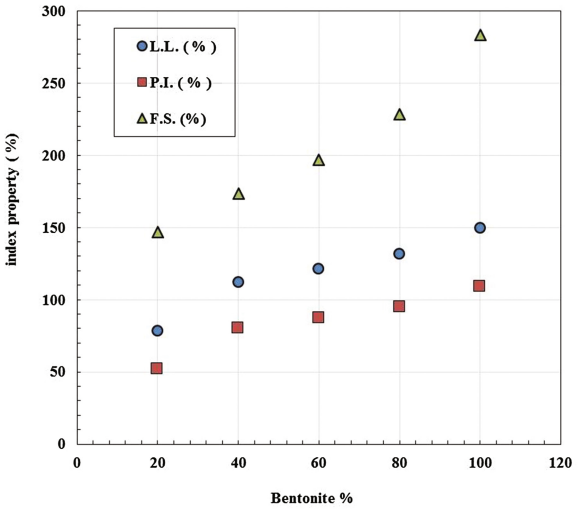

Fig. 2. Effect of Bentonite content in Bentonite-soil mixtures

Table 1. Swelling characteristics correlation equations based on soil index properties.

Equation no.	Equation	Regression statistics (R^2)
(1)	$\mathbf{I_{ss} = PI/(1.07 + 0.0011 \times PI)}$	0.96
(2)	$\mathbf{I_{ss} = 0.30 \times (F.S.) + 8.60}$	0.93
(3)	$\mathbf{I_{sw} = 3.13 \times (PI)^{0.7415}}$	0.93
(4)	$\mathbf{I_{sw} = 0.0004 \times (F.S.)^2 + 0.1909 \times (F.S.) + 27.30}$	0.93
(5)	$\mathbf{\gamma_h = 55.83\ Ln\ (PI/\gamma_{dry}) - 158.63}$	0.83
(6)	$\mathbf{\alpha_{sh} = 0.026 \times (\gamma_h)^{-0.4973}}$	0.74
(7)	$\mathbf{\alpha_{sh} = 0.0023\ Ln\ (\gamma_h/\gamma_{dry}) + 0.012}$	0.73
(8)	$\mathbf{\alpha_{sw} = 1.20 \times \alpha_{sh}}$	0.98
(9)	$\mathbf{SP = 32.40\ Ln\ (PI) - 97.47}$	0.77
(10)	$\mathbf{SP = 36.91\ Ln\ (I_{ss}) - 110.54}$	0.87

Table 2. R^2 values for different correlations between suction compressibility index and several combinations of soil – index parameters.

Curve fitting	α_{sh}	α_{sw}	SP	P.I./γ_{dry}	P.I.	L.L./γ_{dry}	P.L./γ_{dry}
Hyperbolic	0.57	0.51	0.04	0.51	0.50	0.53	0.51
Linear	0.65	0.65	0.49	0.79	0.79	0.80	0.74
2^{nd} degree polynomial	0.71	0.68	0.51	0.80	0.80	0.81	0.76
Logarithmic	0.72	0.70	0.35	**0.83**	0.79	0.78	0.75
Exponential	0.73	0.69	0.27	0.72	0.72	0.72	0.67

functions were employed to find the best curve fitting for each relationship such as: exponential, linear, 2nd degree polynomial, hyperbolic, and logarithmic. Table 2 presents resulting (R^2) values from curve fittings. Logarithmic curve fitting equation between (γ_h) and (P.I./γ_{dry}) was found to have the highest value (R^2 = 0.83), and hence chosen as the predictive model equation. In the same manner, the rest of equations, illustrated in Table 1, were developed.

The established relationships that estimate swelling characteristics based on carefully determined index properties will be presented and discussed in the following section.

4.1 Soil Shrink-Swell Index

Relationship between soil shrink-swell index and corresponding plasticity index for the 62 samples is presented in Fig. 3. The regression analysis revealed that hyperbolic curve fitting for the measurements has high coefficient of determination (R^2 = 0.96, refer to Eq. 1 in Table 1), which confirms the existence of strong correlation between shrink-swell index and plasticity index of soil.

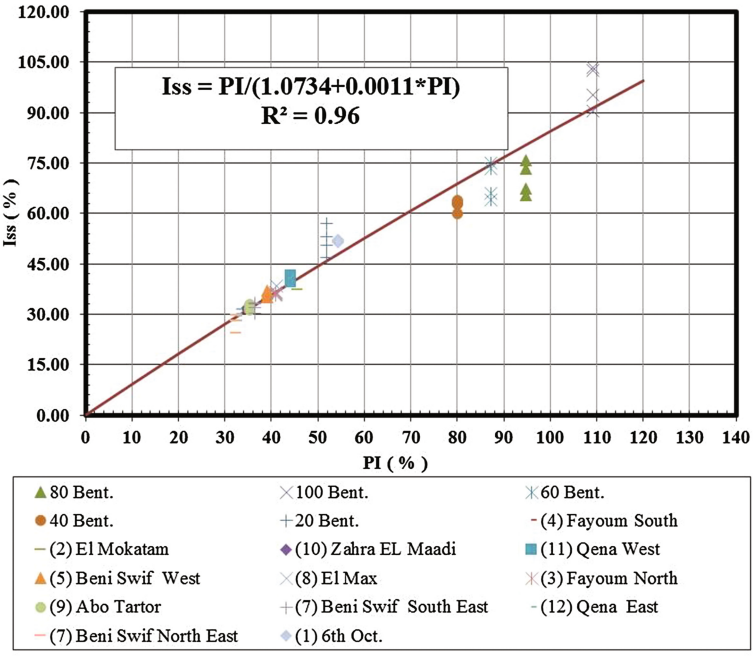

Fig. 3. Relationship between soil shrink-swell index and plasticity index.

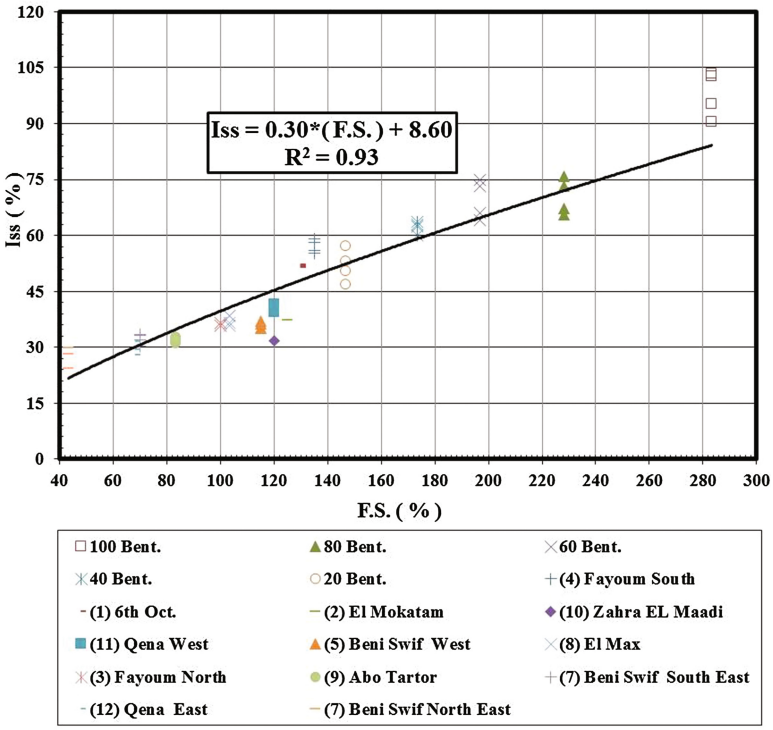

Fig. 4. Relationship between soil shrink-swell index and free swell.

Similarly, soil shrink-swell indices were plotted against free swell values, as shown in Fig. 4. The data indicate the existence of a linear relationship between soil shrink-swell index and free swell. The determined coefficient of determination value (R^2 = 0.93, refer to Eq. 2 in Table 1) was high indicating the strong correlation.

4.2 Soil Swell Limit

Exponential regression equation (Eq. 3 in Table 1) was found to be perfectly representing the relationship between soil swell limit and plasticity index. This regression analysis resulted in a high coefficient of determination (R^2 = 0.93, as shown in Fig. 5), which suggests the high degree of correlation between swell limit and plasticity index of soil.

The same level of correlation was found between the soil swell limit and free swell value, as illustrated in Fig. 6. A 2nd degree polynomial well represented the relationship

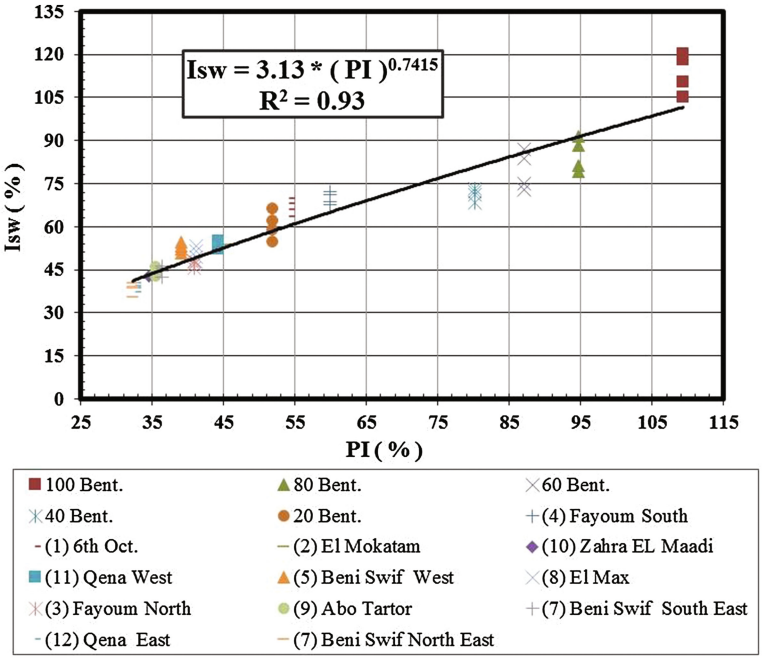

Fig. 5. Relationship between swell limit and plasticity index.

between soil swell limit and free swell with a high coefficient of determination (R^2 = 0.93, Eq. 4 in Table 1).

4.3 Suction Compressibility Index

Figure 7 demonstrates the relationship between measured soil suction compressibility indices and their corresponding determined ratios between plasticity index and dry unit weight. Logarithmic regression (Eq. 5 in Table 1) reflected the good correlation between suction compressibility of soil and the ratio of plasticity index to dry unit weight (R^2 = 0.83).

4.4 Soil Coefficients of Unsaturated Diffusivity

The soil coefficients of unsaturated diffusivity in shrink condition (α_{sh}) were plotted against suction compressibility index (γ_h), as shown in Fig. 8, and against the ratio of suction compressibility index to dry unit weight (γ_h/γ_{dry}), as shown in Fig. 9. The data indicated the existence of an exponential relationship between soil coefficients of unsaturated diffusivity (α_{sh}) and suction compressibility index (γ_h). The regression analysis revealed reasonable correlation (R^2 = 0.74, Eq. 6 in Table 1). Almost the same level of correlation (R^2 = 0.73, Eq. 7 in Table 1) was found between coefficients

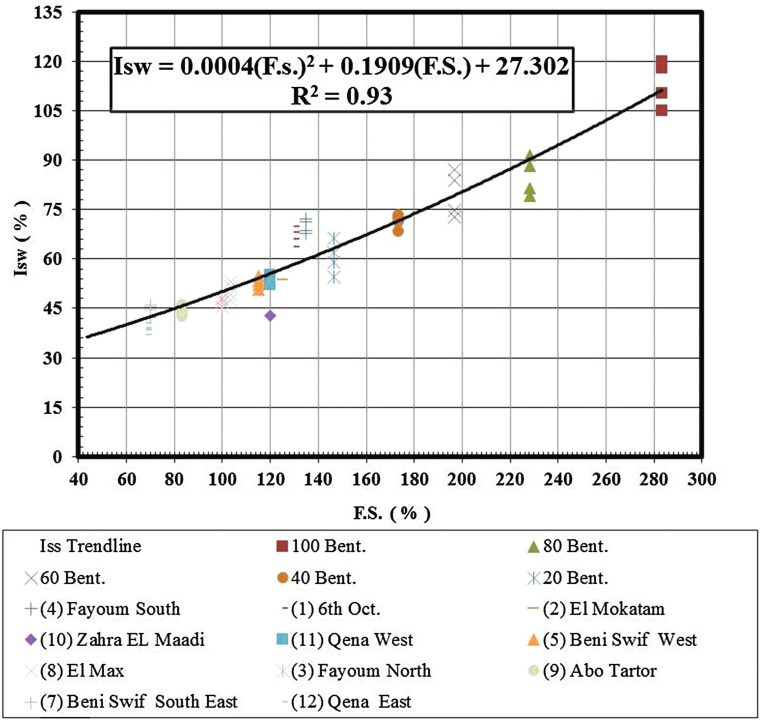

Fig. 6. Relationship between swell limit and free swell.

of unsaturated diffusivity in shrink condition (α_{sh}) and the ratio of suction compressibility index to dry unit weight (γ_h/γ_{dry}).

To investigate the correlation between soil coefficients of unsaturated diffusivities in shrink condition (α_{sh}) and in swell conditions (α_{sw}), Fig. 10. was presented. The linear regression analysis revealed very high degree of correlation between them with coefficient of determination of $R^2 = 0.98$, Eq. 8 in Table 1.

4.5 Soil Swell Potential

It is commonly recognized that soil swell potential correlates well with plasticity index for soils. However, better correlation was found to be soil swell potential and shrink-swell index, as shown in Figs. 11 and 12. The regression analysis indicated that $R^2 = 0.77$ (Eq. 9 in Table 1) for relationship between swell potential and plasticity index. Meanwhile, $R^2 = 0.87$ (Eq. 10 in Table 1) for relationship between swell potential and shrink-swell index.

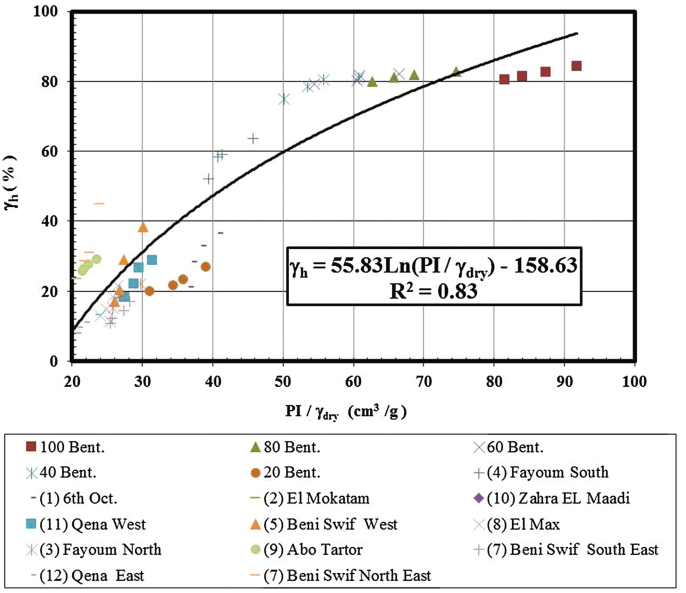

Fig. 7. Relationship between suction compressibility index and the ratio between plasticity index and dry unit weight.

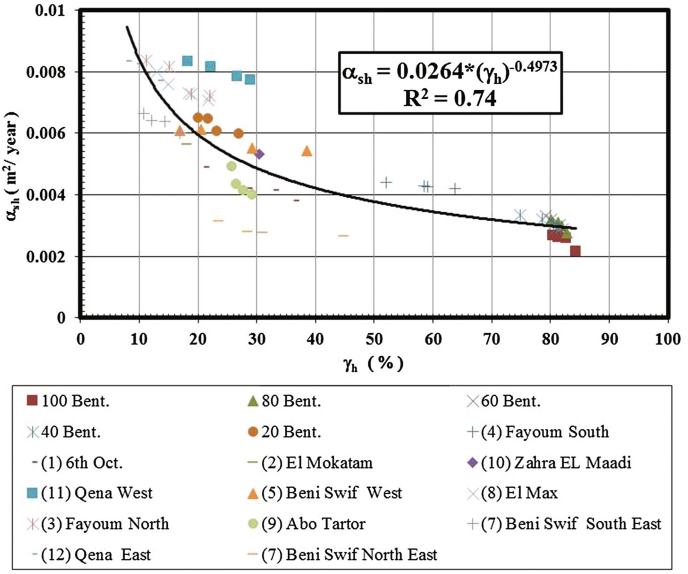

Fig. 8. Relationship between soil coefficient of unsaturated diffusivity in shrink condition and suction compressibility index.

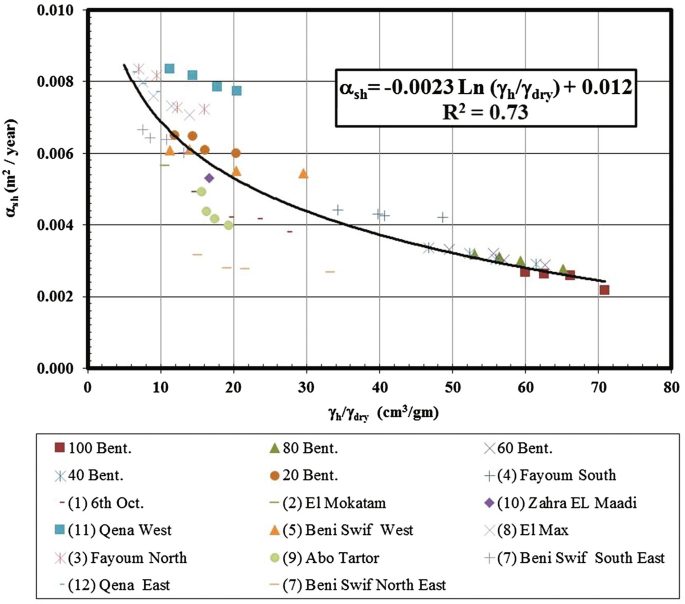

Fig. 9. Relationship between soil coefficient of unsaturated diffusivity in shrink condition and ratio of suction compressibility index to dry unit weight.

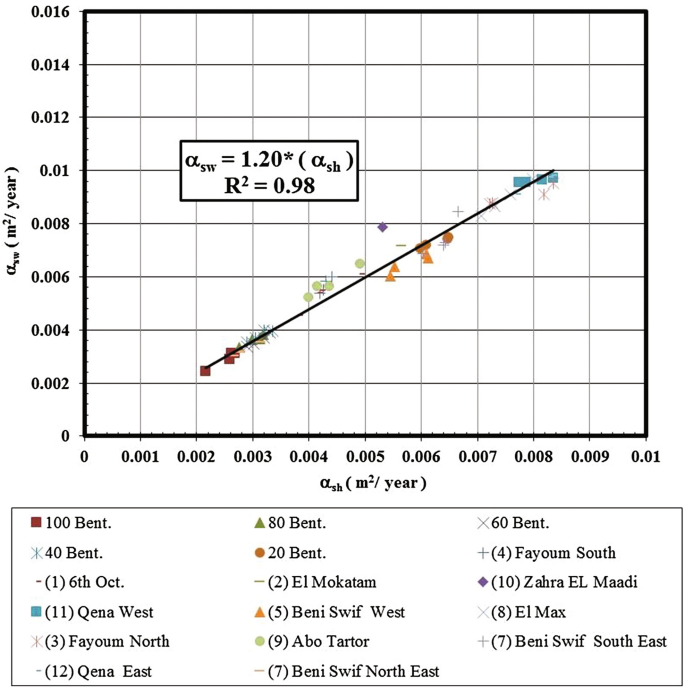

Fig. 10. Relationship between soil coefficients of unsaturated diffusivities in shrink and swell conditions.

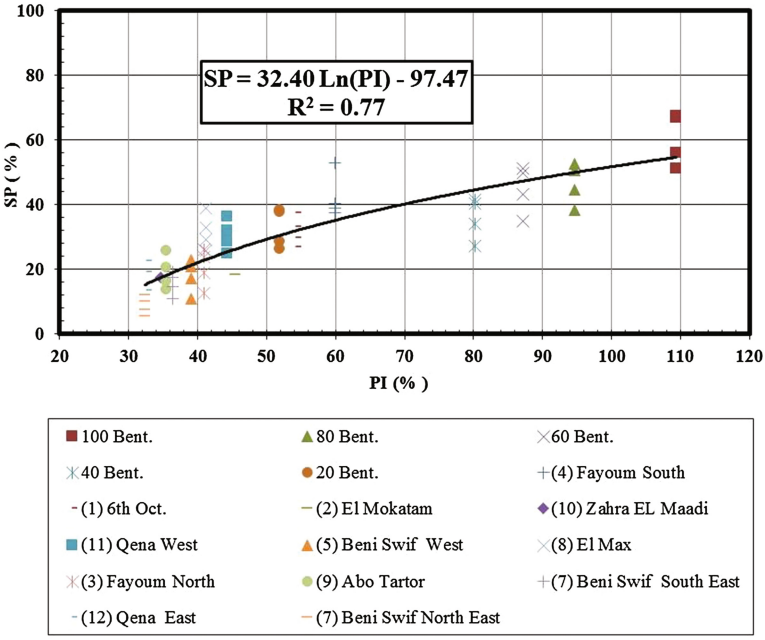

Fig. 11. Relationship between soil swell potential and plasticity index.

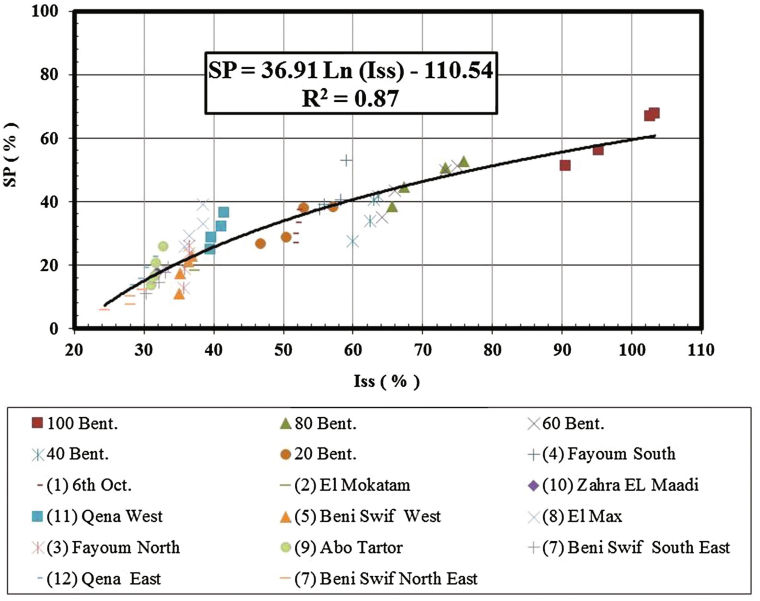

Fig. 12. Relationship between soil swell potential and shrink-swell index.

5 Model Verification

The Assuit Transformers electric substation is located about 370 km south of Cairo on the eastern plateau, within premises on New Assuit city. The electric substation is founded on a dry clay formation with high shrink-swell characteristics. Three undisturbed soil samples were obtained from executed boreholes located around the main building (a two-story reinforced concrete structure), which suffered from severe cracks. Values of main shrink-swell characteristics (I_{sw}, I_{ss}, α_{sh}, α_{sw}, γ_h, and SP) as well as values of soil index properties (LL, PL, PI, γ_{dry}) were determined via laboratory testing program as explained above. Table 3 presents soil samples index properties.

Table 3. Soil samples index properties for Assuit Transformers Station.

Soil sample	L.L. (%)	P.L. (%)	P.I. (%)	γ_{dry} (KN/m^3)
(1)	61.53	20.66	40.87	15
(2)	71.54	22.84	48.7	14.15
(3)	61.64	22.84	38.8	14.5

Table 4. Comparison of experimental scheme and predicted equations for Assuit Transformers Electric Substation Samples.

Soil sample	Soil properties	Measured values	Predicted values	Difference	% Difference
Sample (1)	**I_{sw} (%)**	52.18	49.02	3.16	6.05
	I_{ss} (%)	38.94	36.66	2.28	5.85
	αsh (cm^2/min)	0.000074	0.0001037	−0.000030	40.54
	αsw (cm^2/min)	0.0000589	0.0000888	−0.000003	5.09
	γ_h (%)	23.13	25.88	−2.75	11.88
	SP (%)	37.91	24.63	13.28	35.03
Sample (2)	**I_{sw} (%)**	60.21	55.83	4.38	7.27
	I_{ss} (%)	45.67	43.34	2.33	5.10
	αsh (cm^2/min)	0.000083	0.0001032	−0.000020	24.09
	αsw (cm^2/min)	0.0001103	0.0000996	0.000011	9.97
	γ_h (%)	23.26	38.93	−15.57	66.93
	SP (%)	46.96	30.51	16.45	32.93
Sample (3)	**I_{sw}(%)**	48.08	47.17	0.91	1.89
	I_{ss} (%)	35.28	34.87	0.41	1.16
	αsh (cm^2/min)	0.00008	0.0001163	−0.00036	45
	αsw (cm^2/min)	0.0001112	0.000096	0.000015	1.34
	γ_h (%)	18.39	24.88	−6.49	35.29
	SP (%)	35.11	20.98	14.13	40.24

Furthermore, the same main shrink-swell parameters were estimated using the developed correlation equations based on measured index properties of the obtained soil samples. Hence, comparisons between measured and corresponding estimated parameter were carried out, as shown in Table 4, to check the validity of the developed predictive model. Comparisons show the presence of reasonably good agreement between predictions and measurements.

6 Conclusions

Extensive experimental work has been conducted on sixty two (62) soil samples obtained from twelve (12) sites scattered all over Egypt as well as carefully prepared bentonite-silty clay soil mixtures. Most of the soil samples were remolded using different remolding pressures, yet few natural soil samples were undisturbed. The experimental laboratory testing program revealed the following main findings:

The liquid limit, plasticity index, as well as free swell of the soil samples increased with the increase of bentonite percentage for the bentonite-soil mixtures. There exist unique relationships between the index properties and the swelling characteristics of the tested swelling soils.

A new set of correlation equations was proposed to estimate the swelling characteristics with carefully evaluated index properties in hand. Despite the obvious scattering and variability of the collected and prepared swelling soil samples, high degrees of correlations were proven in the developed equations, which may entitle them to be treated as a reliable tool. The developed equations were rationally verified using available laboratory measurements from another site located south east of Cairo.

The main intend for developing these relationships is to provide geotechnical practitioners with first order estimations of main shrink-swell parameters using available conventional soil index properties.

Notations

L.L. = Liquid Limit.
P.I. = Plasticity Index.
P.L. = Plastic Limit.
SWCC = Soil Water Characteristic Curve.
γ_h = Suction Compressibility.
U = Total Suction expressed as logarithmic unit (pF).
u_w = Total Suction expressed in units of cm of water head.
γ_{dry} = Dry Unit Weight.
G_s = Specific Gravity of Soil Solids.
I_{sw} = Swell Limit.
I_{sh} = Shrink Limit.
I_{ss} = Shrink-Swell Index.
F.S. = Free Swell.

SP = Swelling Potential.
α_{sh} = Coefficient of Unsaturated Diffusivity in shrink condition.
α_{sw} = Coefficient of Unsaturated Diffusivity in swell condition.

References

Abdelmalak, R.I.: Soil Structure Interaction for Shrink-Swell Soils: A New Design Procedure for Foundation Slabs on Shrink-Swell Soils. Ph.D. Dissertation, Texas A&M University (2007)

AL-Shihabi, O.: Estimation of soil suction using salt solutions method and filter paper. Damascus J. Agric. Sci. (DJAS) **26**(2), 59–76 (2010)

Briaud, J.-L., Zhang, X., Moon, S.: Shrink test–water content method for shrink and swell predictions. J. Geotech. Geoenvironmental Eng. ASCE **129**(7), 590–600 (2003). doi:10.1061/(ASCE)1090-0241(2003)129:7(590)

Bulut, R.: Total and matric suction measurements with the filter paper method. Ph.D. thesis, Texas A&M University (2001)

Dafalla, M.A., Shamrani, M.A., Puppala, A.J., Ali, H.E.: Use of rigid foundation system on expansive soils. In: Geo-Florida 2010: Advances in Analysis, Modeling & Design (GSP 199) 2010, ASCE, BRCES, Civil Engineering Department, King Saud University, Riyadh, Saudi (2010)

Das, B.M.: Advanced Soil Mechanics, 3rd edn., pp. 288–289 (2008). ISBN: 0-203-93584-5 Master e-book ISBN. http://www.taylorandfrancis.com

Erzin, Y., Erol, O.: Swell pressure prediction by suction methods. Eng. Geol. **92**, 133–145 (2007). doi:10.1016/j.enggeo.2007.04.002. Received 4 August 2005, ENGEO-02678

Hammam, A.H., Abdel-Salam, A.E.: Comparisons between behaviors of undisturbed and remolded swelling soil. In: Pan-Am CGS Geotechnical Conference, Montreal, Canada (2013)

Israr, J., Farooq, K., Mujtaba, H.: Modelling of swelling parameters and associated characteristics based on index properties of expansive soils. Pak. J. Eng. Appl. Sci. **15**, 1–9 (2014)

Jahangir, E., Deck,O., Masrouri, F.: Influence of foundation embedding on clays shrinkage-swelling hazard consequences. In: Vogt, N., Schuppener, B., Straub, D., Bräu, G. (eds.) ISGSR 2011. Bundesanstalt für Wasserbau (2011). ISBN: 978-3-939230-01-4

Lajurkar, S.P., Khandeshwar, S.R., Dhoble, R.S., Bade, R.G.: Experimental study on shrink-swell behavior of expansive soil. Int. J. Innovative Res. Sci. Eng. Technol. **2**(6), 2085–2090 (2013). ISSN: 2319-8753

Sood, E.: Determination of the diffusion coefficient for unsaturated soils. M.Sc. thesis, Texas A&M University (2005)

Zapata, C.E., Houston, W.N., Houston, S.L., Walsh, K.D.: Soil – water characteristic curve variability. Adv. Unsaturated Geotechnics **287**, 84–124 (2000). doi:10.1061/40510(287)7

Strength Property of Expansive Soils Treated with Bagasse Ash and Lime

Hayder Hasan(✉), Hadi Khabbaz, and Behzad Fatahi

School of Civil and Environmental Engineering,
University of Technology Sydney (UTS), Sydney, Australia
Hayder.A.Hasan@student.uts.edu.au

Abstract. Minimising the cost of stabilisation and improving the load bearing capacity of expansive soils are major concerns to geotechnical engineers dealing with road construction over problematic subgrades. Bagasse ash, an agricultural waste by-product, may be used to improve the bearing capacity of expansive soil, treated with lime as well as to solve the disposal problem caused by bagasse ash which is an environmental challenge. The primary goal of this experimental research is to examine the feasibility of using bagasse ash with lime as a soil stabilisation technique. Various contents of hydrated lime, i.e. 2.5%, 4.5%, and 6.25% with different percentages of bagasse ash depending on the combination ratio of lime to bagasse ash, were used in this study. The mixing ratio between lime (L) and bagasse ash (BA) was sandwiched between 1:1 and 1:5 to obtain the optimum mix for stabilising expansive soil. The effects of stabilisers were evaluated through an array of experimental tests including unconfined compressive strength (UCS) tests at different curing times (3, 7, 28, and 90 days). The durability properties were also investigated through studying the influence of water immersion (7 days) on UCS and wetting-drying cycles on UCS after the samples were cured for 28 days. The experimental results showed that the UCS of samples with the mixing ratio of 1:3 when the lime content was 6.25% resulted in a better improvement than 6.25% lime-soil without adding bagasse ash. The findings of this study revealed that bagasse ash in combination with hydrated lime could be used as a pozzolanic material in soil stabilisation to reach the target strength.

1 Introduction

The construction of roads on reactive soils is generally suffered from the phenomena of shrinkage and swelling, associated with the change in soil moisture content. To enhance the strength and durability of subgrade soil, while minimising the thickness of the pavement, is a key challenge for construction cost optimisation. The common solutions used to overcome the shrink-swell potential of expansive soil in road construction include excavating and replacing the problematic soil with suitable materials, adding chemical agents to soil or increasing the thickness of the base layer. Among these methods, the chemical stabilisation can be more cost effective than other solutions, especially when a pozzolanic waste material is utilised. Disposal of different waste materials produced from various industries is a critical problem. Innovative methods are

L.R. Hoyos and J. McCartney (eds.), *Advances in Characterization and Analysis of Expansive Soils and Rocks*, Sustainable Civil Infrastructures,
DOI 10.1007/978-3-319-61931-6_3

required to minimise the adverse effects of agricultural and industrial wastes. The abundance of waste bagasse ash poses an environmental problem to the surrounding disposal area, since bagasse ash is not biodegradable. Bagasse ash may be classified as a potential pozzolanic material and holds some characteristic, which are useful in stabilising soil. The utilization of agricultural wastes in road construction has been of great interest in many countries during recent years.

For several decades, extensive attempts have been made to use lime either in the form of quicklime (CaO_2) or as hydrated lime ($Ca(OH)_2$) to reduce the volume change of expansive clays and increase the soil strength. The important processes involved in application of this material are: cation exchange, flocculation - agglomeration, cementitious hydration and pozzolanic reaction (Prusinski and Bhattacharja 1999). The cation exchange and flocculation - agglomeration reaction takes place rapidly and brings immediate change in soil properties, whereas pozzolanic reaction is time dependent. The pozzolanic reaction includes interactions between silica and/or alumina from the soil and lime to form different types of cementation products thus improving the strength.

During the last few decades, an extensive amount of research has been carried out to investigate the utilization of lime combined with other additives such as fly ash, rice husk ash, coconut shell ash, as stabilising materials in soil improvement. The main motivation to add ash is to enhance the effectiveness of lime treatment of soil through pozzolanic reaction. The high percentage of siliceous material indicates that ash can be an appropriate material for stabilisation, as previous research on fly ash and rice husk ash showed that the stabilised strength depends on the percentage of silicon and aluminium oxides available (Jha and Gill 2006; Jha et al. 2009; Kampala et al. 2013). The stabilisation of expansive soil through addition of bagasse ash, a locally available waste material, to improve soil engineering properties was investigated in previous studies, since appropriate materials for constructing roads on expansive are not economically available in many region around the globe (Dang et al. 2016; Hasan et al. 2016a).

Strength and durability are two features among several key engineering properties of cemented soil which play key roles in selecting paving materials (Shihata and Baghdadi 2001). Dempsey and Thompson (1967) expressed that the durability clearly reveals the ability of a material to retain stability and integrity over the years of exposure to the destructive forces of weathering. Ali et al. (1992) used the wetting-drying (W-D) cycles tests following the procedure proposed by Hoover et al. (1958) to evaluate the durability of the soil-lime-fly ash mixtures based on unconfined compressive strength tests. Ali et al. (1992) examined the durability of soil samples stabilised with 9% lime plus two different rice husk ash (RHA) contents (12% and 18%). They conducted UCS tests after the samples experienced up to 12 wetting-drying cycles. The results revealed that addition of RHA produced samples which are not only stronger but also more durable and less sensitive to the detrimental saturation effects when compared to those samples treated with lime only. Similar results found by Jha and Gill (2006) while the study was focused on the impact of using different percentages of RHA as a pozzolane to enhance the soil treated with different lime contents. Muntohar et al. (2012) presented the unconfined compressive strength (UCS) of the stabilised and reinforced specimens with various wetting-drying cycles. The results indicated that 9% lime-stabilised soil samples collapsed due to the wetting/drying effect after three cycles. However, the 9% RHA mixed with 9% lime - soil mixture was more

durable and not collapsed even after applying 12 wetting-drying cycles. Anggraini et al. (2016) investigated the reinforcing effect of Nanomodified coir fibres on wetting-drying cycles to assess the durability of marine clay. A series of tests were conducted by Basha et al. (2005) on specimens soaked underwater for seven days to simulate the effect of heavy rain on the unconfined compressive strength of soil samples. The experiments exhibited that the strength of stabilised residual soil after addition 5%, 20% and 25% RHA combined with 4% cement to residual granite soil was greater than samples stabilised with 4% cement only. Silitonga et al. (2009) evaluated the suitability of dredged sediments treated with pozzolanic binders. The samples were subjected to 10 wetting-drying cycles consisting of 24 h curing at 60 °C followed by 24 h of immersion in water containers stored in the curing room. The loss of mass for the soil stabilised with 30% fly ash - 2% lime was 30% after 10 cycles, whereas the soil stabilised with 6% cement exhibited 37% loss of mass after 2 cycles and the soil stabilised with 6% lime suffered from 32% loss of mass after 3 cycles.

Kampala et al. (2013) studied the durability of calcium carbide residue (CCR) and fly ash (FA) stabilised silty clay against wetting and drying (W-D) cycles according to ASTM D559 for determining mass loss (%). The results showed that the UCS values, after different W-D cycles and the resistance to water absorption, have significantly been improved with addition of 20% fly ash.

Durability characteristics have been investigated using different techniques by Khalife et al. (2012) to evaluate the effect of cementitiously stabilised subgrade soils. It should be noted that UCS could not be determined beyond the first W-D cycle sines the samples were severely cracked and damaged. The failure of specimens might have been due to the tensile stress exceeding the tensile strength of the stabilised material, leading to unbound material with reduced strength and stiffness. Additionally, the crack can facilitate the penetration of water generating considerable pressure and degrading the surrounding material (Prusinski and Bhattacharja 1999). Jha et al. (2009) evaluated the effects of class F fly ash as pozzolana a performance of lime treatment soils particularly when mixture possess large fraction of ash. Durability characteristics based on mass loss and UCS criteria of stabilised soil with fly ash as pozzolana and lime were evaluated after 12 cycles of wetting and drying. They suggested replacing (mass loss) method with the compressive strength since UCS values were more consistent and suitable to gauge the deterioration of the mix. In addition, a number of researchers (Baghdadi and Shihata 1999; Shihata and Baghdadi 2001) recommended to use the residual compressive strength without brushing the specimens to determine the durability since the results of UCS were more consistent.

The shrinkage cracking and deformation characteristics of untreated soil or stabilised soil have been studied extensively by many researchers (e.g. Little et al. 2003; and Sebesta 2005). They have reported that shrinkage cracking is the main concern imposing significant limits the use of chemical stabilisation. Because of shrinkage cracking of treated soil, causing the infiltration of water into the soil as well as leading to reduce the strength of treated soil, structures may be influenced significantly. Therefore, the reduction of shrinkage cracking could significantly expand the use of local materials, recycled materials, or waste/by-products for ground improvement. The Shrinkage of soils may be classified into four types: (a) autogenous shrinkage due to hydration, (b) drying shrinkage due to loss of moisture, (c) thermal shrinkage due to

low-temperature contraction and (d) carbonation shrinkage, occurring during curing and under the subsequent exposure to the atmosphere. Carbonation shrinkage can be a long-term reaction, especially when the cementitiously stabilised materials (CSM) have low relative humidity values, and CSM are covered by an upper layer (ACI 2008). Chakrabarti et al. (2002) reported that drying shrinkage is the major cause of shrinkage cracking, which is associated with the use of CSM in pavement construction. The loss of moisture from stabilised soil pavement layers can affect the drying shrinkage. The capillary tension, solid surface tension and the withdrawal of hindered adsorbed water and interlayer water movement from the cement gel may be considered as the main factors causing the drying shrinkage (Bažant 2001). Moreover, the development of shrinkage cracking depends on the tensile stress. When the tensile stress exceeds the tensile strength of the stabilised materials, shrinkage cracking occurs (George 1990).

According to the study conducted by Chakrabarti et al. (2002), the matric suction, osmotic suction and thermal cooling due to losing moisture can cause shrinkage. George (1990) suggested several approaches to minimise the shrinkage cracks, reducing water content used in the mix, increasing the compaction effort, avoiding montmorillonite clay, and limiting the degree of saturation up to 70% can be utilised. George (2002) found that shrinkage cracks for kaolinite-cement mixtures occurred quicker than montmorillonite-cement samples. Because the size of kaolin particles is larger than montmorillonite, the inter-particle moisture can easily evaporate. Sebesta (2005) recommended that if the UCS after 7 days was in the range between 300–400 psi, the surface cracking could be minimised. Scullion et al. (2005) recommended the following specifications to reduce shrinkage: the maximum linear shrinkage of raw soil passing #40 sieve being less than 2.5%; the maximum plasticity index less than 4%, the maximum percentage of fines passing #200 sieve less than 7.0%, and the linear shrinkage of cement-treated base material should not exceed 250 microstrain after 21 days.

This paper describes a series of unconfined compression strength tests (UCS) results based on an experimental study, particularly investigating different proportion of soil, bagasse ash and lime in the mixes. Test specimens were subjected with different curing times including 3, 7, 28, and 90 days. Moreover, UCS values haves been determined under different wetting-drying (W-D) cycles to evaluate the durability of the specimens after 28 days of curing.

2 Materials and Experimental Work

2.1 Materials

The adopted expansive soil in this study a mixture of 20% Bentonite and 80% Kaolinite according to an initial study conducted by Hasan et al. (2016b). The physical properties of the exploited expansive soil are summarised in Table 1. Bagasse ash (BA) was collected from the ISIS Central Sugar Mill Company Limited in Queensland, Australia. The remaining ash on sieve 425 μm was rejected to remove unburned bagasse particles. The loss on ignition (LOI) for BA passing sieve 425 μm was 2.9%, which was considered acceptable according to ASTM C618 C. Bagasse ash was

Table 1. Properties of expansive soil

Property	Quantity
Liquid limit (%)	95
Plastic limit (%)	30
Plasticity index (%)	65
Linear shrinkage (%)	17
Maximum dry weight (g/cm^3)	1.31
Optimum water content (%)	30
UCS (kPa)	244

classified as asymptotic to the fine sand. The lime, used in this investigation, is a commercial hydrated lime, manufactured by Adelaide Brighton Cement Limited.

2.2 Mixture Preparation

The general expression for the total dry weight (W) of a soil-lime-bagasse ash mixture is:

$$W = W_s + W_b + W_l \tag{1}$$

where W_s, W_b, W_l, are the dry weights of soil, bagasse ash, and lime, respectively in the mix. The soil was thoroughly mixed with 30% moisture content and allowed to reach the equilibrium for 24 h prior to preparation of the compacted samples. The testing program for the investigation is shown in Table 2. It can be noted that these tests are part of a comprehensive experimental program to assess the effectiveness of bagasse ash to improve the properties of lime treated expansive soils.

Table 2. Summary of mixture material content

Soil (%)	Bagasse ash (%)	Lime (%)
100	0	0
100	2.5, 5, 7.5	2.5
100	4.5, 9, 13.5	4.5
100	6.25, 12.5, 18.75	6.25

2.3 The Unconfined Compressive Strength (UCS) Tests

The UCS is the maximum axial compressive stress that a right-cylindrical sample of material can withstand under unconfined conditions. It is also known as the uniaxial compressive strength. Each specimen used in unconfined compressive tests were statically compacted in a cylindrical mould, 50 mm in diameter and a high of 100 mm, with 30% moisture content. The specific dry densities were determined from the standard compaction tests.

The tests were conducted according to Australian Standards (AS) 1289.5. It should be noted that the dry weight of the mixture (W) was calculated from Eq. (1).

The UCS tests were performed for various combinations of soil-bagasse ash-lime mixtures as detailed in Table 3. The unconfined compressive strength was determined at a loading rate of 1.0 mm/min. Each sample was placed in a plastic bag to prevent the moisture loss. Samples were cured for 3, 7, 28 and 90 days in a moist room with a constant relative humidity and a temperature around 22 °C. The prepared specimens were put in the loading machine at a loading rate of 1.0 mm/min.

Table 3. Unconfined compressive strength test with different lime-bagasse ash at different curing time

Lime (%)	Bagasse ash (%)	Curing period (Days)
0	0	0
2.5	2.5, 5, 7.5	3, 7, 28
4.5	4.5, 9, 13.5	3, 7, 28
6.25	6.25, 12.5, 18.75, 25, 31.25	3, 7, 28, 90

2.4 Effect of Wetting-Drying Cycles on UCS

Three different techniques were applied to investigate the durability of stabilised soils. For each method, ten samples were prepared. In the first technique (Method A), the samples were put in potable water for one week after the samples were cured for 28 days in a plastic bag at room temperature to simulate the effect of heavy rain on the strength, following Basha et al. (2005) method. Basha et al. (2005) carried out a series of tests by soaking samples in water for seven days. Then two samples from each group were tested to determine the UCS values. Afterward, the eight remaining samples were laid in the room temperature to dry.

In the second technique (Method B), ten samples with different composition were exposed to air to dry at room temperature. Subsequently, the samples were soaked in potable water. Many researchers, as mentioned earlier in the literature review, have used this technique.

In the third attempt (Method C), the samples were fully immersed for one day in water, containing dissolved lime, according to ASTM C 31 (2 compared at various curings lime per liter), to prevent leaching the cementitious materials such as CaO from soil samples. This approach resulted in a weak cementation process. In addition, the samples were fully covered with two filter papers to allow moisture exchange without surface erosion. Then, the samples were subjected to 1-day air drying at room temperature. This process is referred to a one wetting-drying cycle. These two steps were carried out after curing the samples for a period of 28 days in plastic bags at 22 °C ambient temperature.

3 Results and Discussion

3.1 Effect of Bagasse Ash Curing Time on UCS

The UCS values of samples with different bagasse ash and lime contents are compared at various curing periods. Figures 1, 2 and 3 show the effect of BA on the strength of the soil, treated with various lime contents. As expected, the addition of lime increases the axial soil strength. Furthermore, extending the curing time is reflected in the UCS.

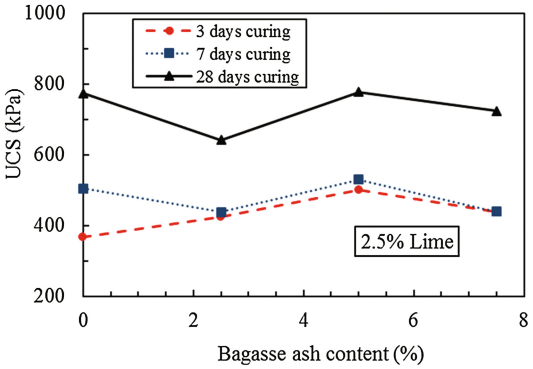

Fig. 1. Effect of BA on soil-2.5% Lime with different curing time

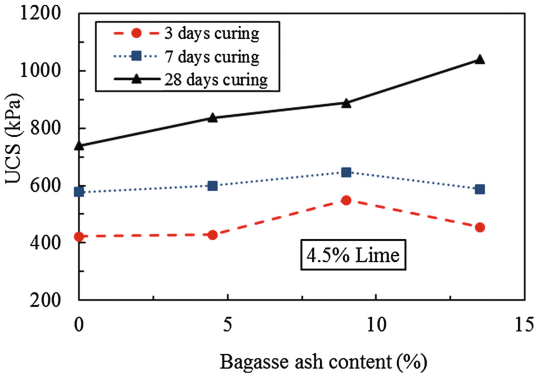

Fig. 2. Effect of BA on soil-4.5% Lime with different curing time

Figure 1 demonstrates the influence of curing time (3, 7 and 28 days) and gradual increase of BA content on strength of soil samples, treated with 2.5% of lime. The used doses of BA were 2.5, 5 and 7.5% by weight of dry soil, while adding the same amount of lime. When no BA is used, lime has an actual substantial effect on strength. The effect of BA was produced a much more advanced strength with increasing the curing time. This may associate with the pozzolanic reaction between the lime and silica and

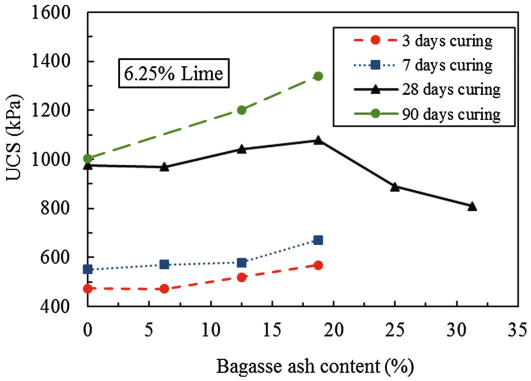

Fig. 3. Effect of BA on soil-6.25% Lime with different curing time

alumina in soil. When employing BA, the observed increase in the strength for curing period with 5% of BA suggests that the presence of 5% BA accelerates the cementitious reaction of lime and soil.

The effect of BA content on unconfined compressive strength of soil treated with 4.5% lime after 3, 7, and 28 days of curing is shown in Fig. 2. It was observed that duration of curing did not result in notable increase in strength up to 9% of BA. However, there was a notable strength enhancement, when 13.5% BA was used particularly from 7 to 28 days.

The influence of adding BA on the UCS of soil treated with 6.25% lime at 3, 7, 28 and 90 days are presented in Fig. 3. As a general pattern, at 28 days of curing, the strength increased with the increasing BA until the ratio of BA to lime was reached to an optimum (i.e. when the weight of BA was three times of lime); beyond that ratio, the strength began to reduce. Besides, the maximum strength considerably enhanced as curing was extended to 90 days. It can be seen that addition of BA provides not only greater strength but also a higher initial rate of strength gain. For example, 12.5% BA content produces an average increase in strength of 15% as the curing time increased from 28 to 90 days at the room temperature, while 18.75% BA content provides an increase of 24% for the same increase in the curing time. At 28 days of curing, when the percentage of addition of BA to each soil-6.25% L mixes increased, the UCS values also increased. For example, the UCS increased to 11%, when 18.75% BA was added to soil-6.25% L. Increase in strength of the soil treated with 6.25%L may be due to an increase in the pozzolanic reaction between calcium presented in lime and alumina and silica presented in bagasse ash to form various types of cementation products, thus enhancing the strength.

3.2 Effect of Bagasse Ash on Durability

The cycles of humidity and drought are considered a serious environmental factor due to expansion and contraction of some types of clayey soils. On the other hand, these cycles may result in erosion and cracking even in treated soil. Therefore, the durability

test is probably one of the most appropriate tests to determine the potential of soil-lime to withstand the moisture content changes.

In the first set of testing program, ten soil samples were prepared, containing 6.25% L, 6.25% L-12.5% BA, and 6.25% L-18.75% BA. After 28 days of curing, the soil samples were soaked in potable water for one week to simulate the effect of heavy rain on the soil. The results showed that the strength of soil-6.25% L mixed with 12.5% BA and 18.75% BA were better than soil mixed with 6.25% L. For example, the value of UCS for soil-6.25% L mixed with 12.5% and 18.75% BA were 728 and 746 kPa, respectively. In addition, the UCS value of soil-6.25% L was 507 kPa. Then, eight soil samples from each group were put in water after one-week of drying in air. Subsequently, all of the soil samples were started to collapse.

In the second series of wet-dry tests, the method suggested by a number of researchers (Ali et al. 1992; Hoover et al. 1958; Jha et al. 2009) was followed. The samples were air-dried for 24 h at the room temperature before the samples being fully immersed in potable water. Once again all soil samples were gradually slacked and damaged.

Table 4. The value of UCS after different wetting-drying cycles

Number of cycles	UCS (kPa)	
	Soil-6.25% L	Soil-6.25% L-18.75% BA
0	976	1079
1	927	993
2	869	982
4	712	939
7	634	745
10	410	680

The results of durability test after diverse wetting-drying cycles are presented in Table 5. The variation of compressive strength after the wetting/drying cycles can be expressed as the residual strength index (R) which is the ratio between the compressive strength after the wetting/drying cycles (Kampala et al. 2013; Muntohar et al. 2012).

$$R = \frac{\mathrm{UCS}_{cycled-soaked}}{\mathrm{UCS}_{unsoaked}} \tag{2}$$

It can be seen that the residual strength index has reduced with increasing the wetting/drying cycles as illustrated in Fig. 4. The result indicated that the BA/mixed lime/soil mixture shows slightly more resistance to wetting-drying than the lime/soil specimen. The amount of 6.25% lime for this soil was enough to prevent swelling phenomena with 28 days curing (the results are not provided in this paper), but the absorbed water during wetting period produced a softer mixture reflecting a reduction in the UCS when the samples were submerged 7 days in potable water.

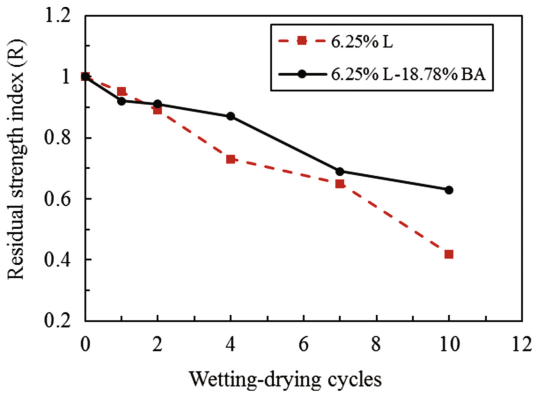

Fig. 4. Effect of wetting-drying cycles on residual strength index (R) of the expansive soil stabilised with different binder content

Losing water from soil pores leads to generation of surface tension (suction) causing shrinkage cracks (Kampala et al. 2013). Moreover, according to Holtz and Gibbs (1956), the shrinkage limit for low expansive soil is approximately above 15%; the moisture content of the soil sample was 30% (close to the plastic limit PL = 30%). As expected, when the moisture content is above the shrinkage limit, the volume of water is also more than the minimum volume of voids. Thus, when the soil sample loses moisture content, the micro shrinkage cracks can be abundant.

4 Conclusions

The addition of bagasse ash (BA) to lime stabilised expansive soil contributes significantly to its strength development. The UCS of lime stabilised soil with addition of bagasse ash is greater than that of soil treated with lime alone.

A series of durability tests were conducted to study the effect of bagasse ash on the strength of stabilised soil with 6.25% lime after wetting-drying cycles. The addition of BA enhances the durability due to accelerated enhanced pozzolanic reactions. In comparison with soil samples stabilised with lime only, the samples treated with both lime and bagasse ash showed higher UCS values when subjected to wetting and drying cycles.

Based on the results of this study, when montmorillonite clay was presented in the soil, even if, the soil was treated with 6.25% lime combined with 18.75% bagasse ash, the cementation bond could be broken due to shrinkage cracks. Hence it is suggested to practicing engineer to isolate the treated soil with geomembranc, emulsified asphalt or cushion to prevent water loss.

References

ACI. Guide for Modeling and Calculating Shrinkage and Creep in Hardened Concrete (2008)
Ali, F.H., Adnan, A., Choy, C.K.: Geotechnical properties of a chemically stabilized soil from Malaysia with rice husk ash as an additive. Geotech. Geol. Eng. **10**(2), 117–134 (1992)
Anggraini, V., Asadi, A., Farzadnia, N., Jahangirian, H., Huat, B.B.: Reinforcement benefits of nanomodified coir fiber in lime-treated marine clay. J. Mater. Civil Eng. **28**(6), 06016005 (2016)
Baghdadi, Z., Shihata, S.: On the durability and strength of soil-cement. Proc. Inst. Civil Eng. Ground Improv. **3**(1), 1–6 (1999)
Basha, E., Hashim, R., Mahmud, H., Muntohar, A.: Stabilization of residual soil with rice husk ash and cement. Constr. Build. Mater. **19**(6), 448–453 (2005)
Bažant, Z.P.: Prediction of concrete creep and shrinkage: past, present and future. Nuclear Eng. Des. **203**(1), 27–38 (2001)
Chakrabarti, S., Kodikara, J.K., Pardo, L.: Survey results on stabilisation methods and performance of local government roads in Australia. Road Transp. Res. **11**(3), 3 (2002)
Dang, L.C., Hasan, H., Fatahi, B., Jones, R., Khabbaz, H.: Enhancing the engineering properties of expansive soil using bagasse ash and hydrated lime. Int. J. **11**(25), 2447–2454 (2016)
Dempsey, B.J., Thompson, M.R.: Durability properties of lime-soil mixtures (1967)
George, K.: Characterization and structural design of cement-treated base. Transp. Res. Rec. **1288**, 78–87 (1990)
George, K.: Minimizing cracking in cement-treated materials for improved performance (2002)
Hasan, H., Dang, L., Khabbaz, H., Fatahi, B., Terzaghi, S.: Remediation of expansive soils using agricultural waste bagasse ash. Procedia Eng. **143**, 1368–1375 (2016)
Hasan, H., Khabbaz, H., Fatahi, B.: Impact of quicklime and fly ash on the geotechnical properties of expansive clay. In: Paper Presented at the Geo-China 2016, GSP 258 (2016b)
Holtz, W.G., Gibbs, H.J.: Engineering properties of expansive clays. Trans. Am. Soc. Civil Eng. **121**(1), 641–663 (1956)
Hoover, J., Handy, R., Davidson, D.: Durability of Soil-Lime-Flyash mixes compacted above standard proctor density. Highway Res. Board Bull. **193**, 1–11 (1958)
Jha, J., Gill, K.: Effect of rice husk ash on lime stabilization of soil. J. Inst. Eng. (India) Part CV Civil Eng. Div. **87**, 33–39 (2006)
Jha, J., Gill, K., Choudhary, A.: Effect of high fraction class F flyash on lime stabilization of soil. Int. J. Geotech. Environ. **1**(2), 105–128 (2009)
Kampala, A., Horpibulsuk, S., Prongmanee, N., Chinkulkijniwat, A.: Influence of wet-dry cycles on compressive strength of calcium carbide residue–fly ash stabilized clay. J. Mater. Civil Eng. **26**(4), 633–643 (2013)
Khalife, R., Solanki, P., Zaman, M.M.: Evaluation of durability of stabilized clay specimens using different laboratory procedures. J. Test. Eval. **40**(3), 363–375 (2012)
Little, D., Godiwalla, A., Oshiro, P., Tang, P.: Characterization of design properties (compressive strength and resiliente modulus) of lime, cement, fly ash stabilized recycled concrete base as function of curing time. In: Paper Presented at the Maintenance and Rehabilitation of Pavements and Technological Control (2003)
Muntohar, A.S., Widianti, A., Hartono, E., Diana, W.: Engineering properties of silty soil stabilized with lime and rice husk ash and reinforced with waste plastic fiber. J. Mater. Civil Eng. **25**(9), 1260–1270 (2012)
Prusinski, J., Bhattacharja, S.: Effectiveness of portland cement and lime in stabilizing clay soils. Transp. Res. Rec. J Transp. Res. Board **1652**, 215–227 (1999)

Scullion, T., Sebesta, S., Harris, J., Syed, I.: Evaluating the performance of soil–cement modified soil for pavements: a laboratory investigation: Publication RD120. Portland Cement Association, Skokie, Ill (2005)

Sebesta, S.: Use of microcracking to reduce shrinkage cracking in cement treated bases [M/CD]. In: TRB 2005 Annual Meeting (CD-ROM). Transportation Research Board, Washington, DC (2005)

Shihata, S.A., Baghdadi, Z.A.: Long-term strength and durability of soil cement. J. Mater. Civil Eng. **13**(3), 161–165 (2001)

Silitonga, E., Levacher, D., Mezazigh, S.: Effects of the use of fly ash as a binder on the mechanical behaviour of treated dredged sediments. Environ. Technol. **30**(8), 799–807 (2009)

Stabilization of an Expansive Soil Using Alkali Activated Fly Ash Based Geopolymer

Partha Sarathi Parhi[1(✉)], Lasyamayee Garanayak[2], Mahasakti Mahamaya[2], and Sarat Kumar Das[2]

[1] Department of Civil Engineering, Indian Institute of Technology Hydrabad, Hyderabad, Telangana 502285, India
partha.nitrkl@gmail.com
[2] Department of Civil Engineering, NIT, Rourkela 769008, India
lizaoec@gmail.com, mahamaya.2008@gmail.com, saratdas@rediffmail.com

Abstract. Expansive soil is one of the most devastation types of soil damaging roads, building, and pipe line each year. Various efforts are being done to stabilize the soil and mitigate the damage due to it. Utilization of industrial waste as low CO_2 cement is one of the sustainable method for industrial growth. In the present study alkali activated fly ash used as an alternating cementitious material to stabilize an Indian expansive soil. Different combination of sodium hydroxide and sodium silicate were used in terms of Na_2/SiO_2 ratio. The activator to ash ratios (liquid to solid mass ratio) was also varied with different percentage of class F fly ash percentage. The fly ash is activated with 10, 12.5 and 15 molal of sodium hydroxide concentrations of along with 1 molar sodium silicate solution. The various percentages fly ash (20, 30 and 40%) relatively to the total solids of the expansive soil are used. The activator to ash ratios (liquid to solid mass ratio) was kept between 1 and 2.5. The effectiveness of this binder is discussed in terms of unconfined compressive strength (UCS) of the stabilized soil after 3, 7 and 28 days of curing. The effect of alkali activation is discussed in terms of stabilization of expansive soil with only fly ash. The mineralogical development of the stabilized expansive soil is discussed through x-ray diffraction analysis. The effect of activator to ash ratio is also discussed. Suitability of alkaline activated fly ash mixture as a grouting material is also ascertained by studying the rheological properties of the grout such as, setting time, density and viscosity and is compared with that of common cement grouts.

Keywords: Expansive soil · Alkali activated fly ash · Unconfined compressive strength · Rheological properties

1 Introduction

Expansive soil and bedrock underlie more than one third of world‘s land surface. Each year, damage to buildings, roads, pipelines, and other structures by expansive soils is much higher than damage that are caused by floods, hurricanes, tornadoes, and earthquakes combined. The estimated annual cost of damage due to expansive soils is

L.R. Hoyos and J. McCartney (eds.), *Advances in Characterization and Analysis of Expansive Soils and Rocks*, Sustainable Civil Infrastructures,
DOI 10.1007/978-3-319-61931-6_4

$1000 million in the USA, £150 million in the UK, and many billions of pounds worldwide. However, as the hazards due to expansive soils develop gradually and seldom present a threat to life, this has not drawn emergency attention, despite their severe effects on the economy.

Several innovative techniques, such as special foundations that include belled piers, drilled piers, friction piers and moisture barriers have been developed to mitigate the problems posed by expansive soils (Chen 1975). Stabilization of expansive soils with various admixtures such as cement, lime, fly ash, lime, calcium chloride are found to be effective (Desai and Oza 1997; Cokca 2001; Phani Kumar et al. 2001; Saylak et al. 2008). Mutaz et al. (2011) discussed about various chemical stabilization of expansive soil. The cement is the most commonly used and effective stabilizer particularly for high expansive soil. However, the cement industry is becoming unsustainable as the greenhouse gas emission produced worldwide by this industry, is estimated to be approximately 7 percent of the total greenhouse gas emissions to the earth's atmosphere (Carido et al. 2007). Hence, to reduce greenhouse gas emissions, efforts are being made to develop environmentally friendly construction materials. The alkali activation of waste materials has become an important area of research in many laboratories because it is possible to use these materials to synthesize inexpensive and ecologically sound cement like construction materials Palomo et al. (1999). Duxson et al. (2005), Pacheco-Torgal et al. (2012) Villa et al. (2010), Xu and Van Deventer (2000, 2003) concluded that alkaline activated materials are more durable and stable and are generally better performing materials than available conventional cements. Discussed about alkali activated red mud and fly ash mixture as an effective cementitious material. Recently, Cristelo et al. (2013) investigated the effect of sodium based alkaline activated fly ash and Portland cement on the strength of soft soils.

With above in view, the present paper discusses about the strength properties of alkali activated fly ash stabilized expansive soil, which is part of the research on development of methodology towards development of alkali activated cementitious material from industrial waste. The main objective of the present study is to stabilize the expansive soil using alkali activated Class F fly ash. Sodium hydroxide (NaOH) and sodium silicate (Na_2SiO_3) of different molal concentration are used as the alkali activator and the unconfined compressive strength (UCS) of the expansive soils after 3, 7 and 28 days curing was determined.

2 Materials and Methods

2.1 Material Characterization

The expansive soil used in this study was collected from a natural deposit near, Nagpur, Maharashtra India and locally known as 'Black cotton' soil. The soil was collected by method of disturbed sampling after removing the top soil at 500 mm depth and transported in sacks to the laboratory. Little amount of the sample was sealed in polythene bag for determining its natural moisture content. The soil was air dried, pulverized and sieved with 4.75 mm sieve. The materials passing through 4.75 mm sieve was used for laboratory tests. The geotechnical characterization of the sample as

per relevant ASTM standard is shown in Table 1. Table 1 shows geotechnical characterization of expansive soil having specific gravity (G) is 2.64, maximum dry density (MDD) is 15.19 kN/m^3, optimum moisture content (OMC) is 23.31% and natural moisture content is 7.11%. The liquid limit and plastic limit of expansive soil are 72% and 21% respectively. The soil is classified as clay of high plasticity (CH) as per ASTM D2487. The fly ash with low calcium content (class F) was obtained from the captive power plant of National aluminium company Ltd, Angul Odisha, India.

Table 1. Geotechnical Properties of Expansive Soil.

Properties	Value	ASTM standard
Specific gravity (G)	2.64	ASTM D854
Maximum dry density (MDD)	15.19 kN/m^3	ASTM D1557
Optimum moisture content (OMC)	23.31%	ASTM D1557
Natural moisture content	7.11%	ASTM D2216
Liquid limit	72%	ASTM D4318
Plastic limit	21%	ASTM D4318
Classification of soil	CH	ASTM D2487

The individual morphology and particle chemistry were studied in a Jeol-840-A model scanning electron microscope (SEM) fitted with electron dispersive X-ray (EDX) analyser. The mineralogy of the materials were studied using X-ray diffraction (XRD) analysis on a Rich-Siefert X-ray diffractometer using copper target and Ni filter.

The X-ray diffraction (XRD) pattern of the expansive soil as shown in Fig. 1 shows presence of quartz, illite, and Montmorillonite as major minerals, indicating that the soil is expansive. Similarly, XRD analysis of fly ash (Fig. 2) shows presence of quartz and mullite as the major minerals with alumino-silicate glassy phase (as hump position in between 18–26^0). The glassy phase is responsible for development of pozzolanic

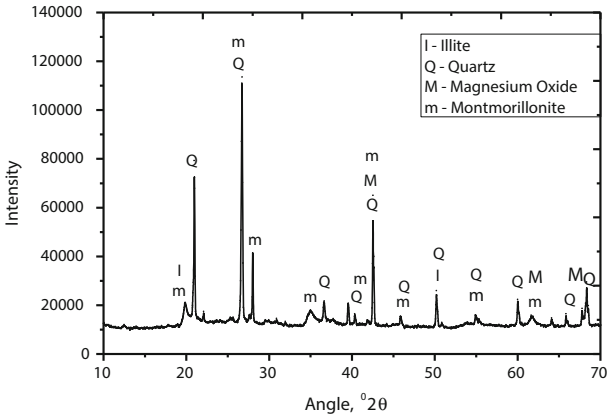

Fig. 1. XRD analysis of Black cotton soil.

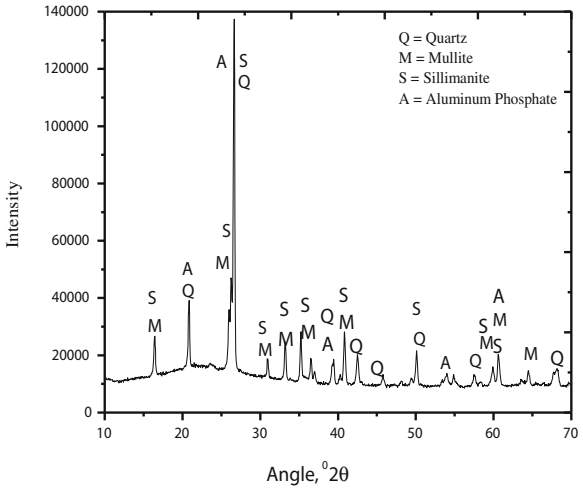

Fig. 2. XRD analysis Fly ash.

reaction. The fly ash is found to composed of spherical particles of different sizes as shown in Fig. 3 and surface chemistry as determined using electron dispersive X-ray (EDX) shows, that it consist of 41.65% of SiO_2, 22.38% of Al_2O_3, 15.04% of Fe_2O_3, 4.76% of MgO, 4.75% of CaO, 5.82% of K_2O and 4.72% of Na_2O.

The alkaline activator solution used was a combination of sodium silicate ($Na_2 Si O_3$) and sodium hydroxide (NaOH). The sodium silicate was originally in powder form and having molecular weight of 284.20 gm/mole and specific gravity of 1.5. While the

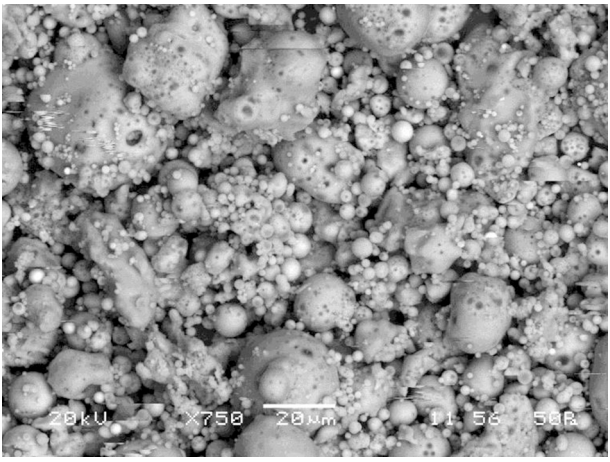

Fig. 3. Scanning electron microscope result for fly ash.

sodium hydroxide was originally in flake form with a molecular weight of 40 gm/mole, and specific gravity of 2.13 at 20º C and 95–99% purity.

1 mol of sodium silicate solution was prepared by adding 284.20 gm of sodium silicate powder to 1 litre of distilled water. NaOH of different concentrations of 10, 12.5, and 15 molal were prepared before testing. In the present study the ratio of sodium silicate to sodium hydroxide solution by mass was kept as 2 as per Hardjito and Rangan (2005), Criado et al. (2007) and Villa et al. (2010) as a guide line.

2.2 Sample Preparation and Testing

The experimental investigation includes the evaluation of the effect of the fly ash/soil ratio (by dry mass) on mechanical strength. Three different fly ash percentages, regarding the total solids (soil + fly ash) weight, were used: 20, 30 and 40%, corresponding to ash/soil ratios of 0.25, 0.43 and 0.67. Moreover to study the effect of activator on the gain in mechanical strength, the activator/total solids ratios are kept as 0.15, 0.2 and 0.25, respectively with each percentage of fly ash mixed with soils.

However, Cristelo et al. (2013) conducted experiments on the 10, 12 and 15 molal alkali activated fly ash treated soft soils by evaluating the unconfined compressive strength of samples having ash/soil ratio of 0.25, 0.43 and 0.67, having varying activator/ash ratio for each percentage of fly ash used in the sample and curing periods. The activator solution was prepared at least 24 h before being used, so that the temperature increase due to the exothermic reaction between the silicate and hydroxide was dissipated and the activator was back to room temperature, which in this case was 33 ± 2º C.

Initially the soil and the fly ash were homogenized and then the activator was added to the mixture. After mixing for 3 min in a mechanical mixer, the samples were cast into 50 mm diameter and 100 mm high moulds by tapping the moulds on the lab counter as per Terashi and Kitazume (2011) and then kept in a sealed container. Some difficulties were encountered during the preparation of samples with 15 molal activator solutions, as they showed high viscosity. Cristelo et al. (2013) also reported similar problem with samples prepared with 15 molal activator solutions. The samples were removed from the moulds and wrapped in cling films after 48 h and then are kept in ambient temperature and humidity conditions (50–60% relative humidity (RH) and 32–35º C). Every single result obtained was the average of three tested samples. Nomenclature of alkaline activated fly ash samples in Table 2. For the soil sample with only fly ash without any activator, water to solid of 15, 20, 25 and 30% were added.

In terms of fly ash percentage in the mixtures, values of 20, 30 and 40% of the total dry weight were used. These values are used so as to have a direct comparison with the activated fly ash. The nomenclature of different type of fly ash mixtures are shown in Table 3. In order to explain the mechanism of strength gain and determine the structure of the final product, some selected samples at 3, 7 and 28 days curing were micro-structurally studied by X-ray diffraction (XRD).

Table 2. Nomenclature of Alkaline Activated Fly Ash Samples.

Sample Designation	Hydroxide Concentration	Fly ash content (%)	Activator to Solid (%)	Activator/Fly ash ratio
S1	10 molal	20	15	0.75
S2		30	15	0.5
S3		40	15	0.375
S4		20	20	1
S5		30	20	0.667
S6		40	20	0.5
S7		20	25	1.25
S8		30	25	0.83
S9		40	25	0.625
S10	12.5 molal	20	15	0.75
S11		30	15	0.5
S12		40	15	0.375
S13		20	20	1
S14		30	20	0.667
S15		40	20	0.5
S16		20	25	1.25
S17		30	25	0.83
S18		40	25	0.625
S19	15 molal	20	15	0.75
S20		30	15	0.5
S21		40	15	0.375
S22		20	20	1
S23		30	20	0.667
S24		40	20	0.5
S25		20	25	1.25
S26		30	25	0.83
S27		40	25	0.625

Table 3. Nomenclature of Different Type of Fly Ash Mixture

Sample	Water to Solid (%)	Fly ash content (%)	Water/Fly ash ratio
M1	15	20	0.75
M2	15	30	0.5
M3	15	40	0.375
M4	20	20	1.0
M5	20	30	0.667
M6	20	40	0.5
M7	25	20	1.25
M8	25	30	0.83
M9	25	40	0.625

The rheological studies include measurement of density and viscosity of both cement and alkali-activated grouts and comparison between the two. For this Marsh funnel viscometer confirming to IS 14343:1996 was used to calculate the viscosity of both the grouts. By using this viscometer we can measure the time taken for a known volume of liquid to flow from the base to the bottom end of the inverted funnel. The liquid was poured through the top of the funnel, until it reached the top level, which used approximately 1.5 L. The bottom exit was then released and the liquid flowed into a measuring container, while the time elapsed was recorded. The cement grout was prepared with a water/cement ratio of 1:1 and the Activated ash grout was prepared with the activator/ash ratio of 0.89. The activator/ash ratio of 0.89 is chosen so as to have a direct comparison with the results obtained by Cristelo et al. (2013). Setting time was ascertained by using Vicat's apparatus. Each grout was poured in the mould in the view point of calculating its initial and final setting time.

3 Results and Discussions

3.1 Unconfined Compressive Strength of Expansive Soil Fly Ash Mixture

Figure 4 shows the UCS values of all samples treated with fly ash, obtained after 3, 7 and 28 days curing. It is evident from the results depicted that the Mix M5 is giving more 3 day strength as compared to other mixes. But the Mix M1 is giving more strength at 7 day and 28 days of curing as compared to others. Strength of the Mix M9 obtained after 3, 7 and 28 days curing is the least among all others. The 3 day strength of M5 is near about 2.2 times more than that of M9.

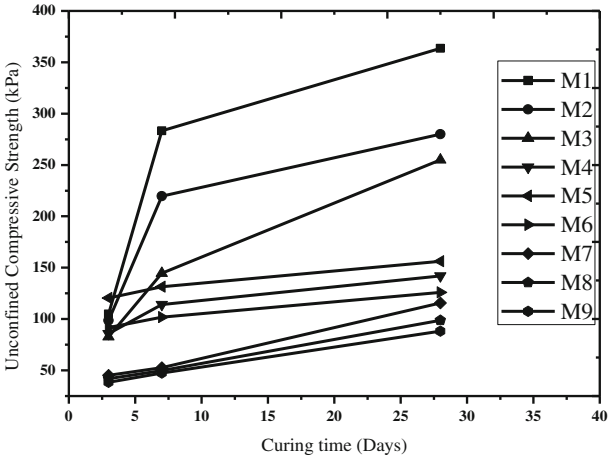

Fig. 4. UCS results of fly ash treated samples.

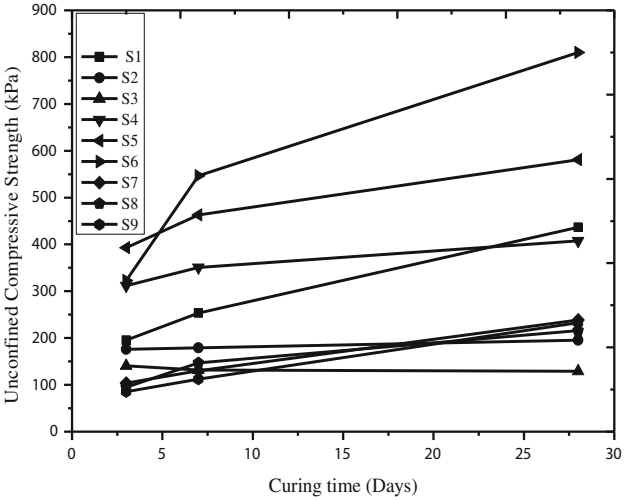

Fig. 5. UCS results of 10 molal samples.

3.2 Unconfined Compressive Strength of Alkaline-Activated Fly Ash Treated Samples

All total 81 samples were tested with different combinations of fly ash percentage and activator percentage. The variations of UCS value of the mixture obtained with 10 and 12.5 molal solution with different curing periods are shown in Figs. 5 and 6, respectively. It can be seen that as per Fig. 5, UCS of mixture activated with 10 molal

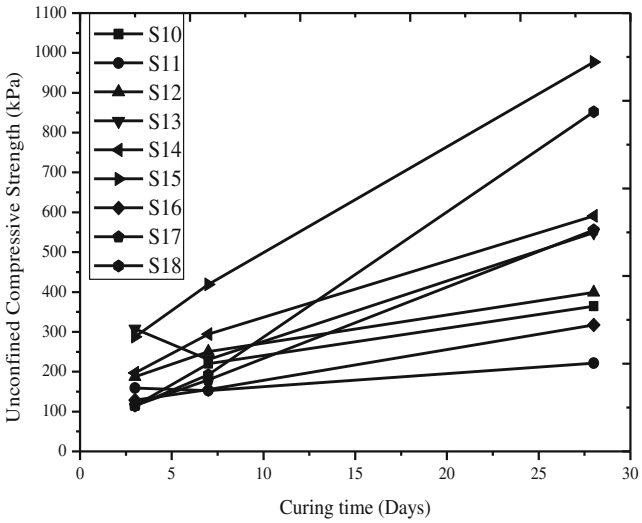

Fig. 6. UCS results of 12.5 molal samples.

solution decreases with increases in fly ash content and the strength increases with curing period. It is evident that the 3 days strength is more in case of Mix S5, while the 7 and 28 days strength is more in case of Mix S6. The least 3 and 7 days strength is exhibited by Mix S9, while Mix S8 exhibits least 28 days strength.

Similarly Fig. 6 shows results for 12.5 molal solution, it shows that the 3 days strength is more in case of Mix S13, while the 7 and 28 days strengths are more in case of Mix S15. The least 3 days strength was exhibited by Mix S18, while Mix S11 exhibit least 7 days strength and Mix S12 exhibit least strength after 28 days curing.

Among all the 81 number of mixes, the maximum strength obtained after 3 days of curing was attained by the Mix S23, while the strength attained by Mix S24 after 7 days of curing is more than all others. The Mix S24 outperforms all in respect of strength attained after 28 days of curing. This can be probably related to necessary time period required for the nucleation phase to occur, during which the products resulting from the dissolution of the raw silica and alumina accumulate before precipitation.

3.3 Effect of Percentage of Water on UCS of Fly Ash Treated Samples

Figure 7 shows Effect of water on UCS of 20%, 30% and 40% fly ash mixtures for 15 molal solution. It is evident from the figure that the amount of water added during preparation of sample has a significant effect in the strength acquired by the samples. It can be concluded from the above figures that the strength is decreasing with the increase in amount of water, irrespective of fly ash content and curing periods. Also the above figure gives us an idea about the optimum content of fly ash to be used, as sample containing 20% fly ash content are exhibiting more strength with respect to others, irrespective of days of curing and amount of water mixed during casting. This is

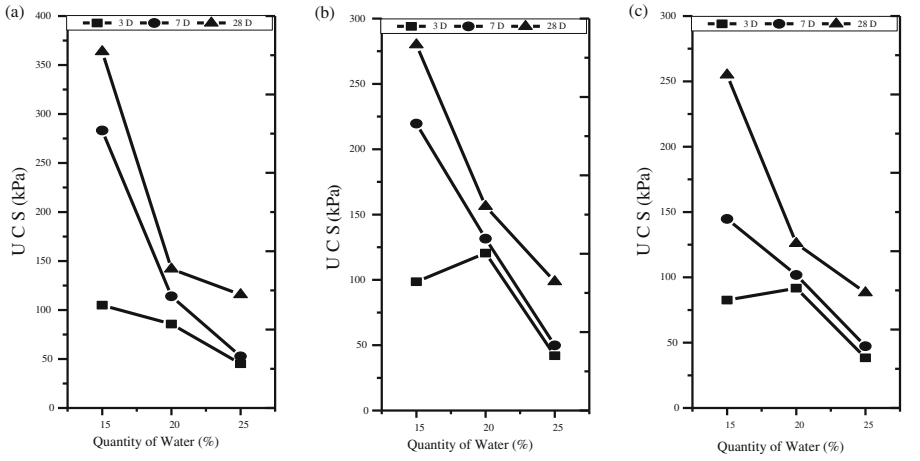

Fig. 7. Effect of water on UCS (a) 20% fly ash mixtures (b) 30% fly ash mixtures (c) 40% fly ash mixtures with 15 molal sample

in accordance to literatures, which suggested that the maximum strength of fly ash treated samples are obtained when the P^H of soil and fly ash mixed slurry is about 10 to 12.5, which is corresponding to fly ash content of 15 to 20%.

3.4 Effect of Activator/Ash Ratio

Figure 8 shows the variation of UCS at 7 days of curing with activator/ash ratio of samples across 10, 12.5 and 15 molal concentration of NaOH and 20, 30 and 40% fly ash content. The maximum strength obtained in this case was corresponding to activator/ash ratio of 0.3 to 0.6, and the maximum strength was gained by the samples corresponding to higher amount of fly ash content. S6 has gained the maximum strength after 7 days of curing. Unlike the 3 days cured samples these samples provide more strength with more fly ash content. This may be attributed to the time required to the development of the resulting amorphous aluminosilicate gel.

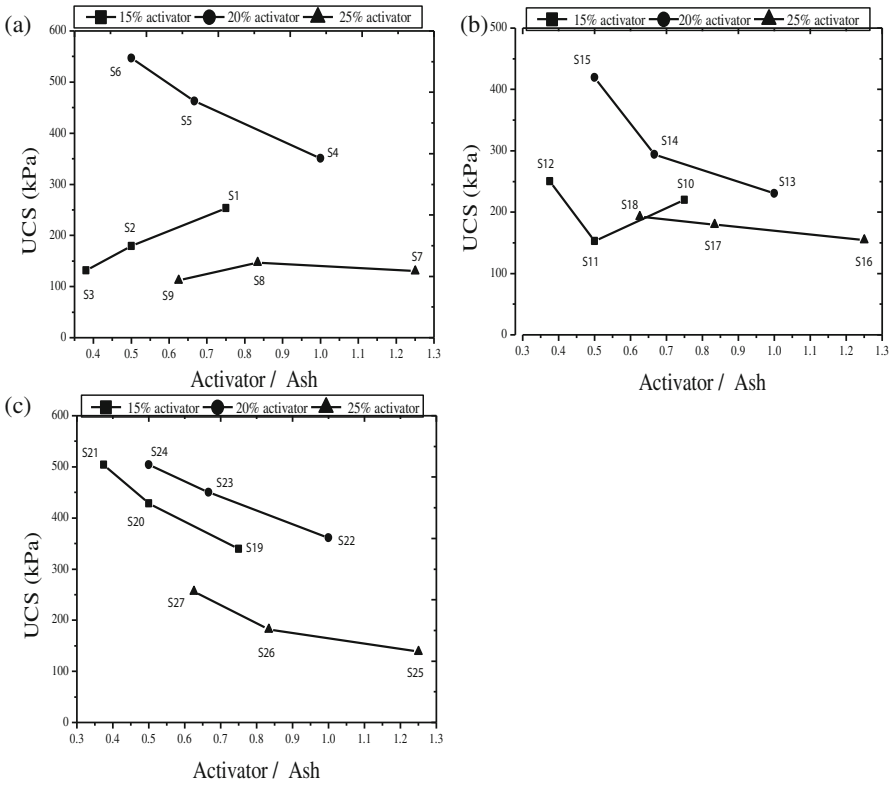

Fig. 8. UCS and activator/ash ratio relation at 7 days curing for (a) 10 molal samples. (b) 12.5 molal samples. (c) 15 molal samples.

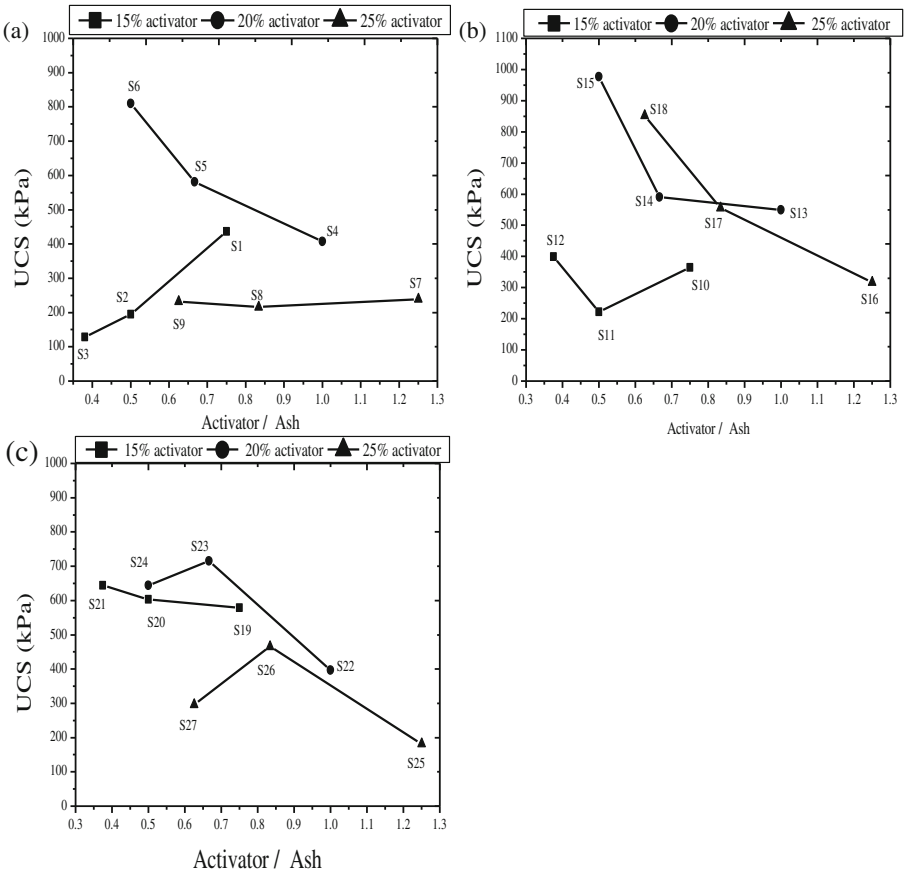

Fig. 9. UCS and activator/ash ratio relation at 28 days curing for (a) 10 molal samples. (b) 12.5 molal samples. (c) 15 molal samples with 40% fly ash

The effect of activator/ash ratio on the strength gained by the samples prepared from 10, 12.5 and 15 molal activator solution after 28 days of curing is shown in Fig. 9. In this case, the maximum strength is acquired by the samples, which have an activator/ash ratio lying in the range of 0.35 to 0.7, and the maximum strength is shown by sample S15. Another inference can be made that samples prepared from 12.5 molal NaOH concentrations are showing better strength as compared to others at 28 days curing. Overall the maximum strength was obtained at lower activator/ash ratio at every curing period except for an early stage, which makes this attempt economical. The lowering of strength at the early stages may be attributed to insignificant time for the reaction to occur as reported in literature. Also further test are needed to understand the mechanism as for 28 days curing period 12.5 molal samples are giving more strength as compared to 15 molal samples at an activator to ash ratio greater than 0.85. These results are agreeable with the results of a previous study by Cristelo et al. (2013).

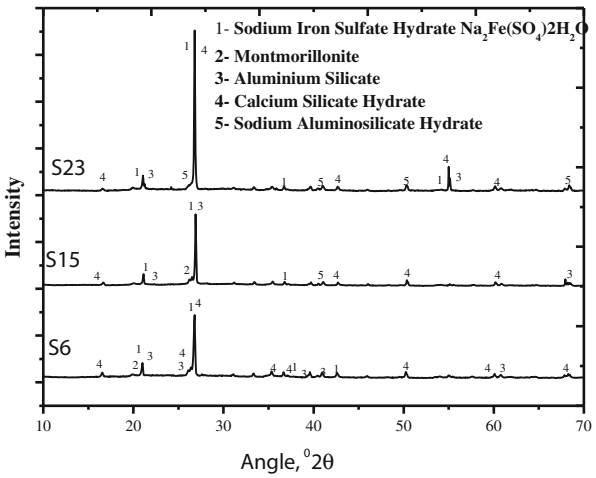

Fig. 10. XRD pattern of samples after 28 days curing.

3.5 Mineralogical Studies

The XRD analysis of alkali activated stabilized soils are presented in Fig. 10 after 28 days of curing. Sodium Iron Sulphate Hydrate, Montmorillonite, Aluminium Silicate, Calcium Silicate Hydrate (CSH) and Sodium aluminosilicate Hydrate (NASH) are the major minerals observed in the above studies. Comparing the XRD analysis results of expansive soil and the treated soil, it can be clearly visible that the montmorillonite minerals are less present in the treated sample, which is in support of increase in UCS value and will reduce the expansiveness. The formation of CSH gel is usually found out in the reaction of cement with the water and this CSH gel is also responsible for increase in the strength of the same. During analysis it was also observed that CSH gels are also forming in alkali activated fly ash treated samples, which could be responsible to the gain in strength. Along with the CSH gel sodium alumino-silicate hydrate (NASH) gels are also found out in the sample, which are believed to help in gaining strength. Villa et al. (2010) reached a similar conclusion when simultaneously evaluating mechanical strength and XRD development on natural zeolite with varying sodium silicate/hydroxide ratios.

3.6 Rheological Study

3.6.1 Setting Time

Due to very slow setting of mixtures the setting time of the alkaline grouts was not practically measurable. It was inferred during the investigations that the rate of setting of alkaline grouts are very slow than that of cement grout and it was found out that the setting process in alkaline grouts are non-homogenous in nature. This is due to the fact

Table 4. Density and Viscosity of cement and alkaline grout

Binder	Activator/ash ratio	Density (gm/cm^3)	Marsh funnel (S)
Cement grout	—	1.58	39
Alkaline grout, 10 molal	0.89	1.66	82
Alkaline grout, 12.5 molal	0.89	1.76	95
Alkaline grout, 15 molal	0.89	1.88	128

that the upper layer of the alkaline grout mass was able to get hardened at a relatively higher rate than the adjacent bottom layers. Again it was also observed that when the Vicat's needle was punctured into the grout mass, the fresh material underneath the top layers were getting exposed, which gets mixed up with the upper layers, thereby resulting in the loss of the already achieved hardness. Therefore, it was concluded that this test is not appropriate for evaluating the setting time of activated fly ash grouts.

Table 4 shows the density and Viscosity of cement and alkaline grout obtained from Marsh cone test. Results shows that the alkaline grouts are more viscous than the cement grout and also it can be observed that the flow time of grouts are clearly dependent on the density of the grouts and as explained earlier the strength is also governed by the viscosity and fluidity of the activator solution. Another inference is that if the grout will be too much viscous it will be very difficult to use the mixture as a grouting material. Hence care should be taken to measure the effective activator/ash ratio, for a desired viscosity and strength of the mixture.

4 Conclusions

Based on the results obtained and discussion thereof, the following conclusions can be made.

The unconfined compressive strength soil is found to vary with concentration of chemical in the activated fly ash and curing period. The 10 molal samples are giving better 3 and 7 days strengths than 12.5 and 15 molal samples, which make it economical as compared to 12.5 and 15 molal samples. Long term strength is more in case of 12.5 molal samples. Maximum 3 day strength attained by activated sample is 3.25 times more than that attained by fly ash treated samples. Maximum 7 day strength attained by activated sample is 2 times more than that attained by fly ash treated samples. Maximum 28 day strength attained by activated sample is 2.7 times more than that attained by fly ash treated samples. The activator/ash ratio of a mixture is directly related to the mechanical strength acquired by the mixture. The outcome of this experimental investigation also shows that the mixture containing less activator/ash

ratio are showing more strength as compared to the mixture containing higher activator/ash ratio. This also proves to be economical and cost effective. Since the final strength of the mixture is governed by the viscosity and fluidity of the mixture prepared, it is not advisable to lower the viscosity of alkaline grouts to a level of cement grouts, which will eventually have a negative effect on the final strength. Alkali-activated fly ash can be used effectively as a chemical stabiliser for stabilising expansive soils, but the challenge lies in its effective application.

References

Chen, F.H.: Foundations on expansive soils. Elsevier Science, Amsterdam (1975)

Cokca, E.: Use of class C fly ash for the stabilization of an expansive soil. J. Geotech. Geoenv. Eng. **127**(7), 568–573 (2001). ASCE

Criado, M., et al.: An XRD study of the effect of the SiO_2/Na_2O ratio on the alkali activation of fly ash. Cem. Concr. Res. **37**(5), 671–679 (2007)

Cristelo, N., et al.: Effects of alkaline-activated fly ash and Portland cement on soft soil stabilization. Acta Geotech. **8**, 395–405 (2013)

Desai, I.D., Oza, B.N.: Influence of anhydrous calcium chloride on shear strength of clays. In: Symposium on Expansive Soils, vol. 1, pp. 17–25 (1997)

Duxson, P., et al.: Understanding the relationship between geopolymer composition, microstructure and mechanical properties. Colloids Surf. A: Physicochem. Eng. Aspects **269**(1–3), 47–58 (2005)

Hardjito, D., Rangan, B.V.: Development and properties of low-calcium fly ash-based geopolymer concrete. Research Report GC 1. Perth (2005)

Mutaz, E., et al.: Evaluation of chemical stabilization of a highly expansive clayey soil. Transp. Res. Rec. J. Transp. Res. Board **2204**(2011), 148–157 (2011)

Pacheco-Torgal, F., et.al.: Durability of alkali-activated binders: a clear advantage over Portland cement or an unproven issue. Constr. Build Mater. **30**, 400–405 (2012)

Palomo, A., et al.: Alkali-activated fly ashes a cement for the future. J. Cem. Concr. Res. **29**, 1323–1329 (1999). Elsevier Science Ltd.

Phani Kumar, B.R., et.al.: Volume change behavior of fly ash-treated expansive soils. In: Proceedings of the 2nd International Conference on Civil Engineering, vol. 2, pp. 689–695. Indian Inst. of Science, Bangalore, India (2001)

Saylak, D.S., et.al.: Fly ash-calcium chloride stabilization in road construction. Transp. Res. Rec. J. Transp. Res. Board **2053**, 23–29 (2008)

Terashi, M., Kitazume, M.: QA/QC for deep-mixed ground: current practice and future research needs. In: Proceedings of ICE Ground Improv. **164**(3), 161–177 (2011)

Villa, C., et.al.: Geopolymer synthesis using alkaline activation of natural zeolite. Constr. Build Mater. **24**(11), 2084–2090 (2010)

Xu, H., Deventer, J.S.V.: The geopolymerisation of alumino-silicate minerals. Int. J. Miner. Process. **59**, 247–266 (2000)
Xu, H., Deventer, J.S.V.: Effect of source materials on geopolymerization. Ind. Eng. Chem. Res. **42**(8), 1698–1706 (2003)

Determination of Shrinkage Properties of Clayey Soils by the Image Analysis Technique

Houcem Trabelsi[1(✉)] and Wissem Frikha[2]

[1] Laboratoire de Génie Civil, Ecole Nationale D'ingénieurs de Tunis, Université Tunis El Manar, Tunis, Tunisia
[2] Ecole Nationale D'ingénieurs de Tunis, LR14ES03, Ingénierie Géotechnique, Université Tunis El Manar, Tunis, Tunisia

Abstract. The present paper involves a study the shrinkage properties during the drying of two types of Tunisian clayey soils under different initials hydraulic conditions and stress histories. A method of measuring the volumetric shrinkage using the image analysis technique is presented. Two procedures of sample preparation are used: slurry and consolidated. The evolution of the height and Crack Intensity Factor of the slurry and consolidated samples permit to define the dryings phases experienced by each soil. The shrinkage curves of consolidated and slurry samples are determined. Drying of saturated soil follows the saturation line until air entry value, which is the limit between the saturated and unsaturated soil. The air entry value depend in soil condition. The stress histories can reduce the kinetics of shrinkage and decreases the void ratio.

1 Introduction

In the context of climate change, the characteristics of the frequency and the intensity of precipitation and dryness may varied. In Tunisia, desiccation phenomena caused considerable damage to structures built on initially quasi-saturated soils. Especially the dams and the clayey landfills may experience shrinkage with different intensities as function of the stress histories, initial hydraulic conditions, grain-size distributions of the used materials, permeability, etc. (Trabelsi et al. 2012). The shrinkage can also be affected by chemical interactions (Thyagaraj et al. 2016).

Most studies are restricted to fixed boundary conditions, but it was proved that there are three stages in soils desiccation process, given initially saturated or unsaturated states (pendular, funicular and capillary regimes) (Urso et al. 1999). Desiccation cracking in drying soil is a common natural phenomenon, and it significantly impacts the soil's mechanical and hydraulic behaviours. In the present study, experimental desiccation tests were conducted on clayey soils to study several aspects of the hydraulic soil behaviour (water evaporation, volumetric shrinkage) (Zhang et al. 2013).

The present work deals with the effect of the dryness on the thermo-hydro-mechanical (THM) behaviour of two types of Tunisian clayey soils. During desiccation processes, multiple mechanisms are involved, which induce volumetric variation and cracks causing considerable damages on buildings (Trabelsi et al. 2014; Nowamooz et al. 2016).

L.R. Hoyos and J. McCartney (eds.), *Advances in Characterization and Analysis of Expansive Soils and Rocks*, Sustainable Civil Infrastructures,
DOI 10.1007/978-3-319-61931-6_5

The main scope of this paper is then to study the shrinkage properties during the drying of clayey soils under different initials hydraulic conditions and stress histories. The current laboratory methods for measuring the soil shrinkage are performed by the use of mercury or displacement point sensors (Zhang et al. 2013). A method of measuring the volumetric shrinkage using the image analysis technique is presented. Two procedures of sample preparation are used: slurry and preconsolidated. The results are interpreted and discussed.

2 Materials and Methods

The two tested soil are extracted from two regions in Tunisia: Soil 1 from the North East and Soil 2 from Tunis City. Table 1 summarises the liquid (ω_l) and plastic (ω_p) limits, plasticity index (I_p) and clay fraction of both tested soils. The grain size distributions of the two soils are depicted in Fig. 1.

Table 1. Physical properties of used soils

	ω_l	ω_p	IP	Clay fraction (%)	Origin
Soil 1	58	26	32	32%	Extracted from Jandouba City at surface
Soil 2	65	37	28	61%	Extracted from center of Tunis City at depth of 1 m

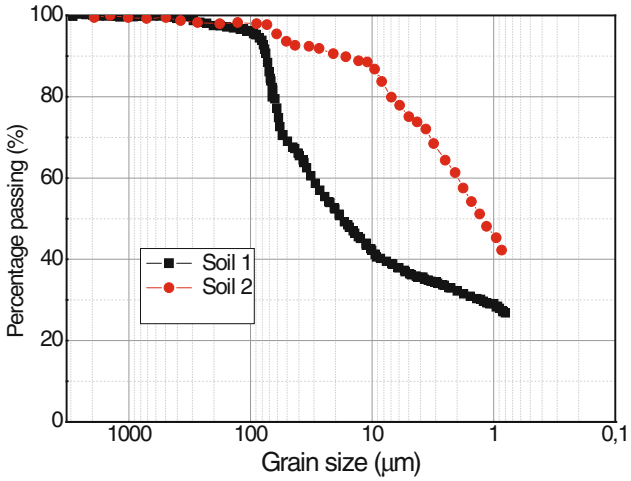

Fig. 1. Grain size distribution of soils

To measure the shrinkage proprieties of these soil, all samples are mixed with distilled water until reaching a moisture content of approximately $1.5\omega_l$. Two procedures are adopted to prepare the specimens. The first one consists in placing the saturated soil in a glass container of 7 cm height and 5 cm diameter. The in the glass

container slurry specimen is then placed in a climate chamber. The evaporation is limited in this case to the upper surface.

The second procedure consists of a vertical consolidation under applied stress of 70 kPa, of the obtained slurry sample, in a specific cylindrical mould. The specimen is subjected to a K_0 vertical pre-consolidation pressure in a container placed in a cell of consolidation apparatus. The mould container is a metallic cylinder with 5 cm internal diameter and 25 cm in height (Fig. 2). The inner surface of the cylindrical metallic mould is lubricated with silicone grease prior to the slurry placement in order to reduce the effects of roughness, and therefore, allow an easy unmoulding of the specimens. The slurry is then carefully placed into the mould, using a spoon, where it is frequently tamped with a plastic tamper to avoid the formation of air during the filling phase. When the predetermined specimen height is attained, the consolidation loading cap is placed to start the loading phase. The specimens are consolidated under a vertical stress of 70 kPa for at least ten days. At the end of the consolidation phase, the specimen height is 4 cm and the diameter is 5 cm. During the pre-consolidation phase, drainage is allowed at the top and bottom of the specimen through the installed upper and lower porous stones. A dial gauge on the loading cap is used to measure the axial deformation of the tested specimen. The consolidation is considered to be complete when quasi-constant axial deformation is recorded. The pressure is then reduced to zero, the loading cap is removed, and the soil sample is placed in the climatic chamber. After unmoulding, the consolidated sample is placed in the climate chamber. The evaporation is allowed on the upper and the laterals surfaces.

Fig. 2. Consolidometer apparatus

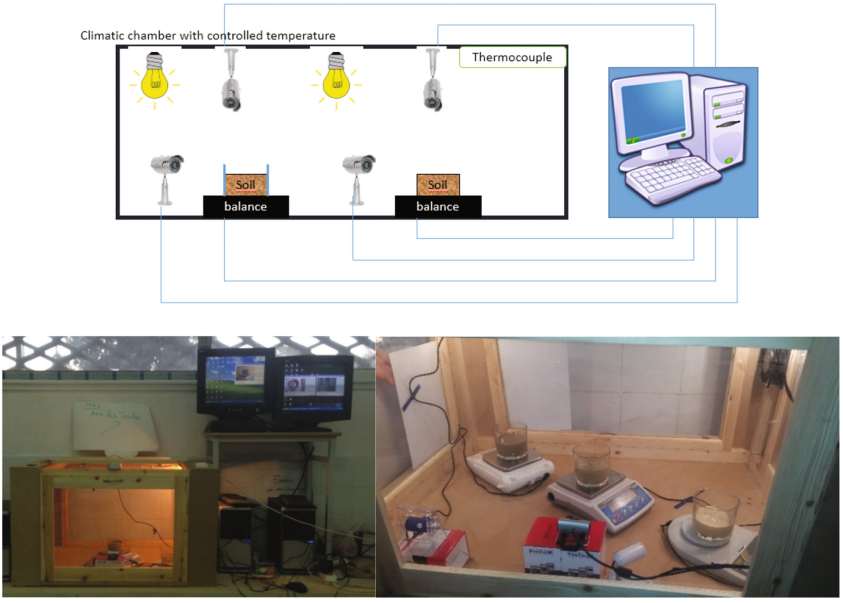

Fig. 3. Climatic chamber

In what follows, specimens obtained applying first and second procedures are referred to as "slurry samples" and "consolidated samples" respectively. The two cylindrical specimens are placed in a climatic chamber at controlled temperature. The climatic chamber was designed in the laboratory of soil mechanics at the National School of Engineering of Tunis (ENIT). It was equipped with a box, digital cameras, balances with an accuracy of 0.01 g, thermocouples and bulbs (Fig. 3). The surveillance digital cameras are installed in front of the upper and side surfaces of the samples to monitor their longitudinal and transverse withdrawals (height and surface) evolution during desiccation (crack pattern evolution). Images were taken and used subsequently for image analysis.

During drying, specimens were weighted using the balance which enables to record the water loss in time. The water content ω and the water evaporation rate Re [mm per unit hour] (Konrad et al. 1997a, b; Tang et al. 2010) variation can then be calculated with respect to elapsed drying time. The two cameras and the balances are connected to a computer. During the test the weight of specimen is recorded and the photos are saved every 30 min. The test is achieved when the weight became quasi-constant. Equilibrium is reached between five to fifteen days as function of type of soil and initial conditions. The temperature is applied by using bulbs and is controlled through thermocouple attached to the climatic chamber (box). It is fixed in all tests at a temperature of 30° (Fig. 3).

Figure 4 represents an example of initial (before desiccation) and final (after desiccation) states images captured for slurry and consolidated samples. Image analysis allows to determine the longitudinal and transverse withdrawals (height and surface)

Fig. 4. Example of photos of soil 2 (before and after desiccation) in both procedures: free and in a container samples

evolution during desiccation. ImageJ software (Ledesma et al. 2009) is used for the image processing (treatment). The recorded images were converted to 8-bit, and the background were subtracted. Finally, these images are converted to binary images, the set of white pixels represents the clayey aggregates and the black ones represents the cracks network (Fig. 5). Using Crack Intensity Factor CIF defined as the ratio of S_c (crack surface) and S (total sample surface) and the specimen height, the volumetric deformation and the void ratio variation are determined (Bottinelli et al. 2016).

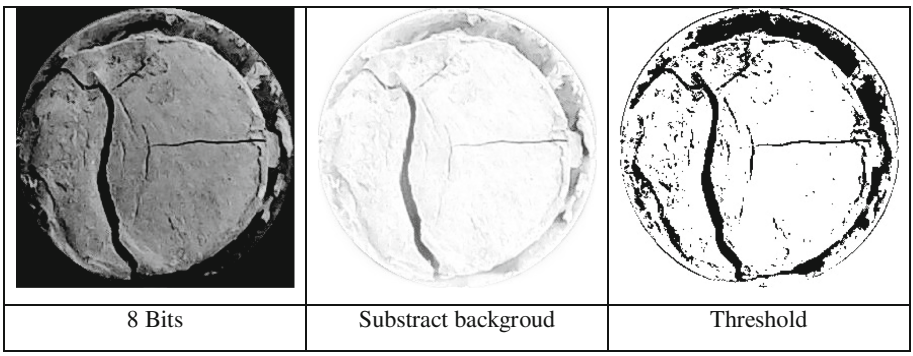

Fig. 5. Example of performed image treatment

According to the evaporation rate variation during drying, the water content decreases continuously until reaching constant residual values at the end of test. The required time to reach the residual values corresponds also to the time of apparition of cracks. Generally, the evaporation rate can be considered as an efficient indicator of the crack pattern progression (Nachshon et al. 2012).

To study the desiccation phenomenon during the crack propagation process, the evaporated flux is measured. The evaporation rate, derivative of the flux rate with time, was determined and was related to the crack propagation and the void ratio. The effect of initial conditions on the evaporation kinetic, and on the crack pattern development is also investigated. All the tests started from saturated conditions under the same dimensions and the same climatic conditions.

3 Results and Discussion

Figure 6 shows the obtained results for slurry and consolidated samples of soils 1 and 2 tested under different hydraulic boundary conditions. The results are presented in terms of moisture content and degree of saturation decrease versus time. In the case of slurry sample, the soil 1 required 10 days to obtain hydric equilibrium whereas the soil 2 required just 3 days. The consolidated sample of Soil 1 didn't reach hydric equilibrium, but the evolution of both consolidated soils samples (1 and 2) required less time than slurry ones to obtain hydric equilibrium. The rate of evaporation Re is defined as (Ritchie et al. 1974; Konrad et al. 1997a, b; Tang et al. 2010):

$$Re = \frac{\Delta m}{S.\Delta t} \tag{1}$$

Where:
Δm is the weight variation
Δt is the consider time
S is the section of the specimen

As depicted in Fig. 6, the rate of evaporation is quasi-linear with the saturation degree. Figure 7 show the decrease of the CIF (crack intensity factor) and the height of slurry samples versus time for soil 1 and soil 2. The evolution of the height and CIF of the slurry specimen shows five phases (Fig. 7):

- Phase of over-saturation, the layer of water over the soil is evaporated (0–1.3 day for soil 1, inexistent for soil 2)
- Phase of consolidation, the soil remain saturated. The withdrawal of sample is basely horizontal. The end of this phase corresponds to a moisture content of limit of liquidity. Desiccation process (1–3.6 days for soil 1, 0–0.6 days for soil 2)
- Phase of shrinkage, a vertical withdraw and tensile stress take place until soil cracking. In this phase, the horizontal withdrawal is prevented by initial friction between the inner walls of the container and the sample. The end of this phase corresponds to a moisture content of plasticity limit (3.6–6 days for soil 1, 0.6–2.6 days for soil 2)

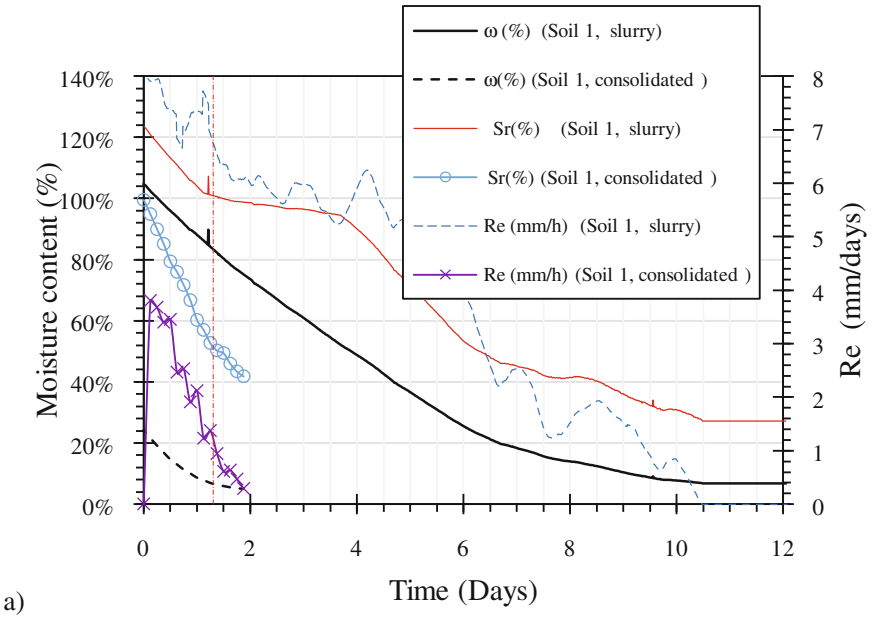

a)

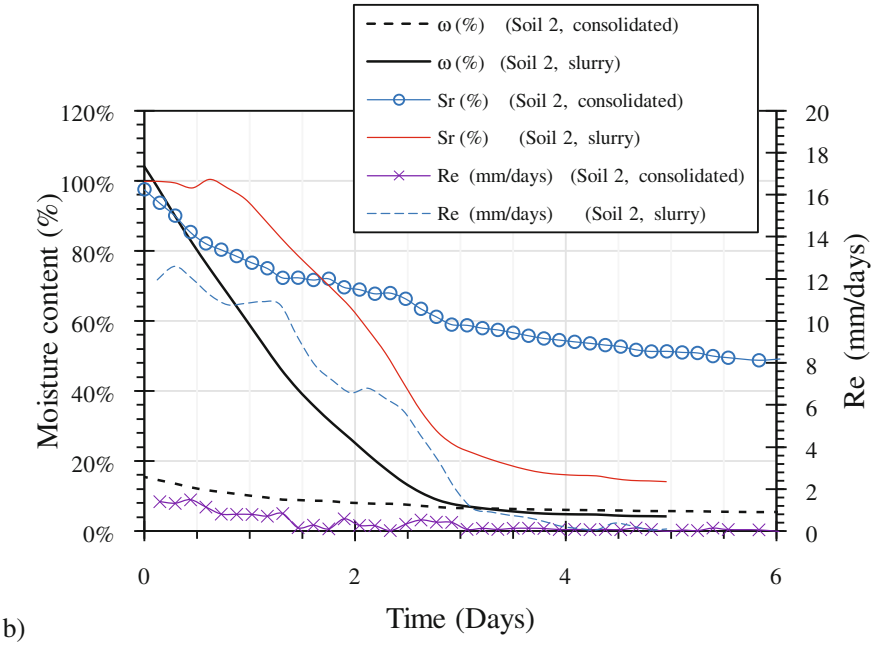

b)

Fig. 6. Evolution of Moisture content, saturation degree and rate of evaporation Re versus time for (a) Soil 1 and (b) Soil 2

(a)

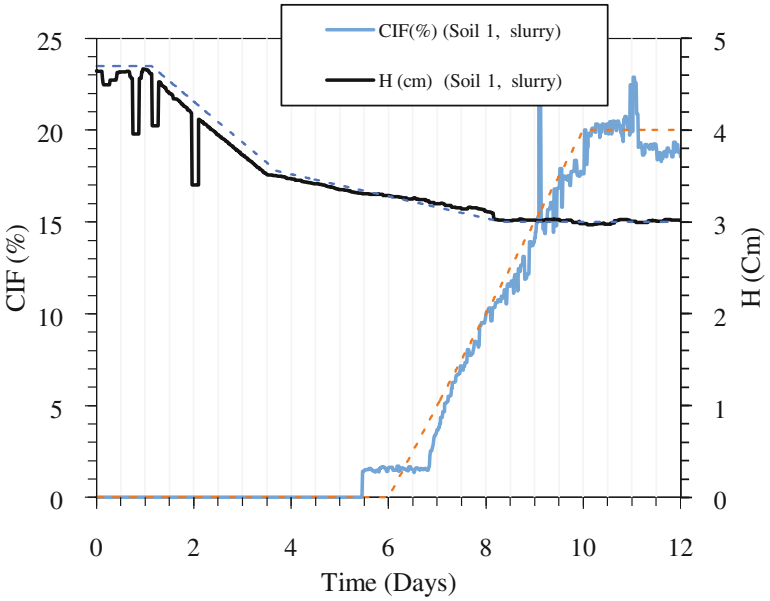

(b)

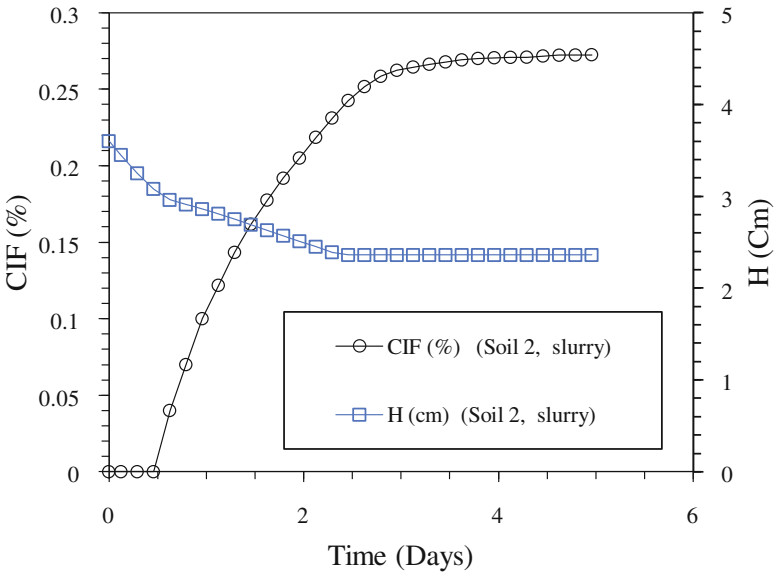

Fig. 7. Evolution of CIF and height of specimen versus time in the case of slurry (a) Soil 1 and (b) Soil 2

- Phase of cracking, characterized by the decrease in the evaporation and occurrence of cracks. The end of this phase corresponds to a water content of shrinkage limit, the height of specimen remains constant (6–10 days for soil 1 and 2.6–3.6 days for soil 2)
- Phase of hydric equilibrium, no shrinkage is observed (>10 days for soil 1 and >3.6 for soil 2)

Figure 8 shows the decrease of the CIF (crack intensity factor) and the height of consolidated sample versus time for soil 1 and soil 2. The initial water content is lower but both consolidated and slurry are initially saturated. However, for consolidated samples, surface interchange area (contact area with air) is more important. Nevertheless no significant change in withdrawal rate is observed. In this case, only three phases are distinguished: shrinkage (0–0.7 days for soil 1 and 0–1.3 days for soil 2), cracking (0.7–1.5 days for soil 1 and 1.3–2.0 days for soil 2) and hydric equilibrium (>1.5 days for soil 1 and >2 days for soil 2) phases.

The major difference between the consolidated and slurry specimen is mainly the equilibrium time. Both initial and final void ratios are lower for consolidated samples. In fact, the void ratio decreases in large fraction inside the mould (consolidometer) under saturation condition and load resulting in the decrease of the macro-porosity and final void ratio and the increase of tensile strength. Whereas, during desiccation of the slurry sample, the soil is close fitting to glass container and a tensile stress is generated. In addition, this tensile stress can increase the crack, the macro-porosity and the final void ratio. The tensile strength is higher for consolidated sample. Figure 9 show the shrinkage curve which represent the evolution of void ratio versus moisture content (%) in the cases of consolidated and slurry samples. The shrinkage curve provides an important link between change in the stress state and the consistency of a soil. The water content and void ratio of the soil are measured when the soil is gradually dried until a residual water content (hydraulic equilibrium with climatic conditions). The air entry value and residual suction are the two primary variables required for unsaturated soil properties. The two variable define the extent of the capillary zone and the residual zone.

The grain-size distribution and stress history are the main factors conditioning shrinkage behaviour. Drying of saturated soil follows the saturation line until air entry value, which is the limit between the saturated and unsaturated soil.

The air entry value depend in initial condition (Fig. 9): For slurry, initial condition the air-entry value is near the liquid-limit but for consolidated specimen it is near the plastic-limit. The transition zone is combined with significant withdrawal in the first part and cracking in second part; the cracking is more pronounced in the case of soil 2, whereas the withdrawal is more important in the case of soil 1. The residual condition is given in the end of shrinkage curve, the soil dray without any shrinkage. The histories of stress (consolidation) can reduce the kinetics of shrinkage and decreases the dried porosity (final porosity).

a)

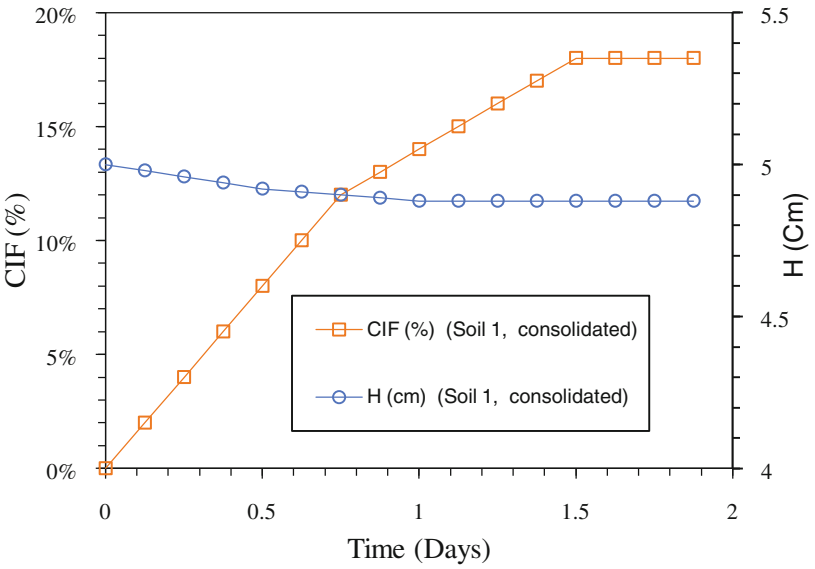

b)

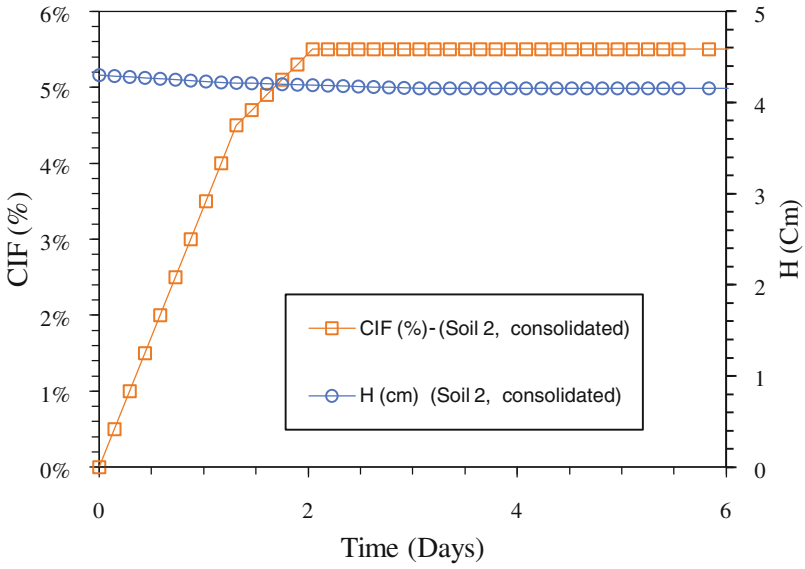

Fig. 8. Evolution of CIF and height of specimen versus time in the case of consolidated (a) soil 1 and (b) soil 2

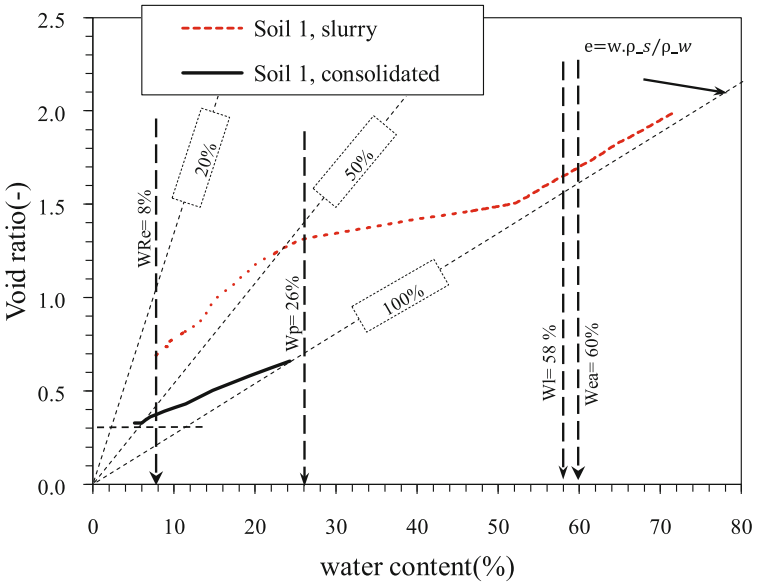

a)

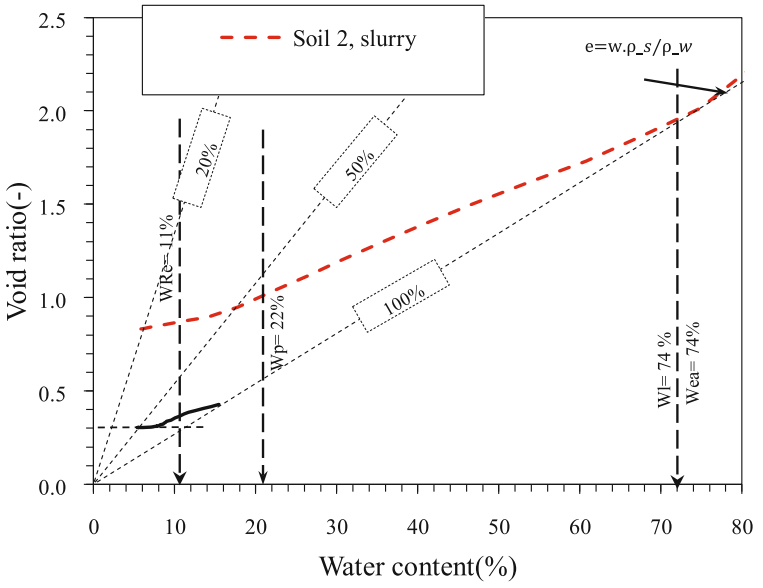

b)

Fig. 9. Evolution of void ratio of specimen versus moister content (a) Soil 1 and (b) Soil 2

4 Conclusion

The present paper descripts a dryness test performed on two types of Tunisian clayey soils. The volumetric shrinkage measure is made by using the image analysis technique. A climatic chamber is designed and made-up for perform the test. Two procedures are adopted to prepare the specimen: slurry and preconsolidated.

The evolution of the height and CIF of the slurry sample shows five phases: over-saturation, consolidation, shrinkage, cracking and hydric equilibrium. Nevertheless, in the case of consolidated sample no significant change in withdrawal rate is observed. Only three phases are distinguished: shrinkage, cracking and hydric equilibrium phases. In this case, the sample under predefined consolidation stress and a more important area contact with air, the withdrawal curve starts from the saturation curve, to attend the shrinkage limit.

The shrinkage curves (water content and void ratio) of consolidated and slurry samples are determined when the soil is gradually dried until a residual water content. The grain-size distribution and stress history are the main factors conditioning shrinkage behavior. Drying of saturated soil follows the saturation line until air entry value, which is the limit between the saturated and unsaturated soil. The air entry value depend in initial condition. For slurry, initial condition the air-entry value is near the liquid-limit but for consolidated specimen it is near the plastic-limit. The stress histories (consolidation) can reduce the kinetics of shrinkage and decreases the dried porosity (final porosity).

References

Bottinelli, N., Zhou, H., Boivin, P., Zhang, Z.B., Jouquet, P., Hartmann, C., Peng, X.: Macropores generated during shrinkage in two paddy soils using X-ray micro-computed tomography. Geoderma **265**, 78–86 (2016)

Konrad, J.M., Ayad, R.: Desiccation of a sensitive clay: field experimental observations. Can. Geotech. J. **34**(6), 929–942 (1997a)

Konrad, J.M., Ayad, R.: An idealized framework for the analysis of cohesive soils undergoing desiccation. Can. Geotech. J. **34**(4), 477–488 (1997b)

Ledesma, A., Lakshmikantha, M.R., Prat, P.C.: Image analysis for the quantification of a developing crack network on a drying soil. Geotechn. Test. J. **32**(6), 1–11 (2009). ASTM International

Ritchie, J.T., Adams, J.E.: Field measurement of evaporation from soil shrinkage cracks. Soil Sci. Soc. Am. J. **38**(1), 131–134 (1974)

Thyagaraj, T., Thomas, S.R., Prakash Das, A.: Physico-chemical effects on shrinkage behavior of compacted expansive clay. Int. J. Geomech (2016). American Society of Civil Engineers, 06016013. 10.1061/(ASCE)GM.1943-5622.0000698

Tang, C.S., Cui, Y.J., Tang, A.M., Shi, B.: Experiment evidence on the temperature dependence of desiccation cracking behavior of clayey soils. Eng. Geol. **114**(3), 261–266 (2010)

Trabelsi, H.: Etude expérimentale et numérique du comportement des argiles soumissent à des conditions de dessiccation. Thèse de doctorat ENIT, Tunisie (2014)

Trabelsi, H., Jamei, M., Zenzri, H., Olivella, S.: Crack patterns in clayey soils: experiments and modeling. Int. J. Numer. Anal. Meth. Geomech. **36**(11), 1410–1433 (2012)

Nachshon, U., Dragila, M., Weisbrod, N.: From atmospheric winds to fracture ventilation: cause and effect. J. Geophys. Res. **117**, 1–11 (2012)

Nowamooz, H., Jahangir, E., Masrouri, F., Tisot, J.-P.: Effective stress in swelling soils during wetting drying cycles. Eng. Geol. **210**, 33–44 (2016)

Urso, M.E., Lawrence, C.J., Adams, M.J.: Pendular, funicular, and capillary bridges: results for two dimensions. J. Colloid Interface Sci. **220**(1), 42–56 (1999). doi:10.1006/jcis.1999.6512

Zhang, Z.B., Peng, X., Wang, L.L., Zhao, Q.G., Lin, H.: Temporal changes in shrinkage behavior of two paddy soils under alternative flooding and drying cycles and its consequence on percolation. Geoderma **192**, 12–20 (2013)

Effect of Cement on Suction and Pore Size Distribution Before and After Swelling of a Natural Clay from Algeria

Souad Amel Bourokba Mrabent[1(✉)], Ramzy Djelloul[1], Abdelkader Hachichi[1], and Jean Marie Fleureau[2]

[1] Laboratoire Matériaux Sol et Thermique (LMST), University of Sciences and Technology Mohamed Boudiaf Oran, Bir El Djir, Algeria
sa_bourok@yahoo.fr
[2] Laboratoire MSS-Mat, CentraleSupélec & CNRS UMR 8579, Châtenay-Malabry, France

Abstract. This paper presents an experimental work on natural clay from the town of Mers El Kebir located in the suburbs of the city of Oran (West of Algeria). The aim of the study is primarily to determine suction using the filter paper method. Secondly the pore distribution was determined using the mercury intrusion porosimetry before and after swelling. The treated and untreated samples were compacted at Standard Optimum Proctor (SOP). The results of the cumulative intrusion curves show that the pore volume of the treated samples is a little higher than that of untreated ones before swelling and a little lower after swelling. This study, which was performed in LMST (Laboratoire Matériaux Sol et Thermique) laboratory (Algeria) with the collaboration of MSSMAT (Laboratoire de Mécanique des Sols, Structures et Matériaux) laboratory (France), is a contribution to the understanding of the swelling phenomena.

1 Introduction

Highly plastic soils are one of the major sources of problems in roads, railways and buildings. Cement is widely used in the treatment of clayey soils to improve their strength and workability, and reduce their suction and swelling potential. For instance in road construction; it improves the mechanical properties and hydraulic conductivity of soils. Many studies (Osula 1996; Balasubramaniam et al. 1998; Cabane 2004; Chew et al. 2004; Al-Rawas et al. 2005; Al Rawas and Goosen 2006; Sariosseiri and Muhunthan 2009; Venkatarama and Prasanna 2011; Portelinha et al. 2012; Pakbaz and Alipour 2012; Ikhlef et al. 2014; Aparna 2014) confirm that cement addition has a positive effect on the stiffening of compressible soils. The negative pore water pressure (suction) is the main factor governing the behavior of over-consolidated and unsaturated soil. This pressure can be related to swelling.

Depending on the chemical composition of the added cement and the mineralogical composition of the soil, chemical reactions may occur between calcium hydroxide of cement and silicas and aluminas soluble in the clay. These reactions lead to a change in

L.R. Hoyos and J. McCartney (eds.), *Advances in Characterization and Analysis of Expansive Soils and Rocks*, Sustainable Civil Infrastructures,
DOI 10.1007/978-3-319-61931-6_6

the particle structure after a short time by allowing granular rearrangement due to flocculation and afterwards, pozzolanic reactions result in the formation of cementitious compounds, binding soil particles between them resulting in the stiffening of the soil on the long term.

To better understand the arrangement of grains in the mixture, microstructural studies using mercury intrusion porosimetry tests were undertaken by many researchers (Cook and Hover 1999; Bin et al. 2007; Millogo and Morel 2012; Lemaire et al. 2013). They showed that the initial porosity of the untreated soil was characterized by two peaks related to micro and macro-porosity. Cement treatment lead to an increase in the micropore volume.

The main objective of this article was to study the effect of cement on the suction, swelling potential and also to evaluate the effect of cement on the pore size distribution of the untreated and treated samples using mercury intrusion porosimetry before and after swelling.

2 Site Location and Geotechnical Identification

The studied soil is an expansive clay from Mers El Kébir in North-Western Algeria. It comes from a site located in a depression zone and forms a marine sediment layer 300 m thick. This soil was previously studied by Hachichi and Fleureau (1999), Hachichi et al. (2007), Bourokba et al. (2010), Bourokba (2011), Bourokba and Hachichi (2011), Hachichi et al. (2011) and Bourokba et al. (2015).

2.1 Clayey Soil Identification

The results of identification tests conducted on the studied soil are summarized in Table 1. According to the Unified soil classification system (USCS), the clay of Mers El Kébir is somewhat plastic (CL). Its activity (Ac) is normal with 26% of particles smaller than 2 μm. The total specific surface area, derived from the blue Methylene test and the formula of Tran (1977) is 189 m^2/g. At the Standard Optimum Proctor (SOP), the maximum dry density is 1.63 g/cm^3 and the optimum water content is 20%.

The X-Ray diffractogram (Fig. 1) shows that the clay contains montmorillonite, illite, kaolinite, quartz and calcite. Mineralogy was derived quantitatively from the X-ray diffractogram (Table 1), following the method of Parrot et al. (1985).

2.2 Cement

The cement used as a clay stabilizing agent is: CPJ-CEM II/A 32.5 from Zahana factory (Algeria), which has pozzolan as cementitious additive. Table 2 shows the chemical and physical characteristics of this cement.

Table 1. Physical and chemical parameters of the studied clayey soil.

Parameters	Denomination	Measured value
Physical	Density of solids grains (g/cm^3) (ASTM D-854)	2.67
	Liquid Limit, LL (%) (ASTM D-4318)	49
	Plastic Limit, PL (%) (ASTM D-4318)	21.5
	Plasticity Index (%) (PI = LL−PL)	27.5
	Natural Water content (%) (ASTM D-2216)	15–17
	Shrinkage limit (%) (ASTM D-4318)	7,36
	Shrinkage Index (%) (SI = LL−PL)	41,64
	Percentage of elements smaller than 2 µm, F2 (%) (ASTM D-2217)	26
	Activity (PI/F2)	1.10
	Organic matter Content MO (%)	3,54
	Value of Methylene blue (%) (NF P94-068)	9.0
	Total Specific Surface Area = 21VBS (m^2/g) (Tran 1977)	189
	Calcium carbonate content (%) (NF X31-106)	18–28
	Cation exchange Capacity (meq/100 g)	26,86
Mineralogy (%)	Quartz	48.1
	Calcite	28.1
	Kaolinite	10.2
	Illite	6.8
	Montmorillonite	6.8

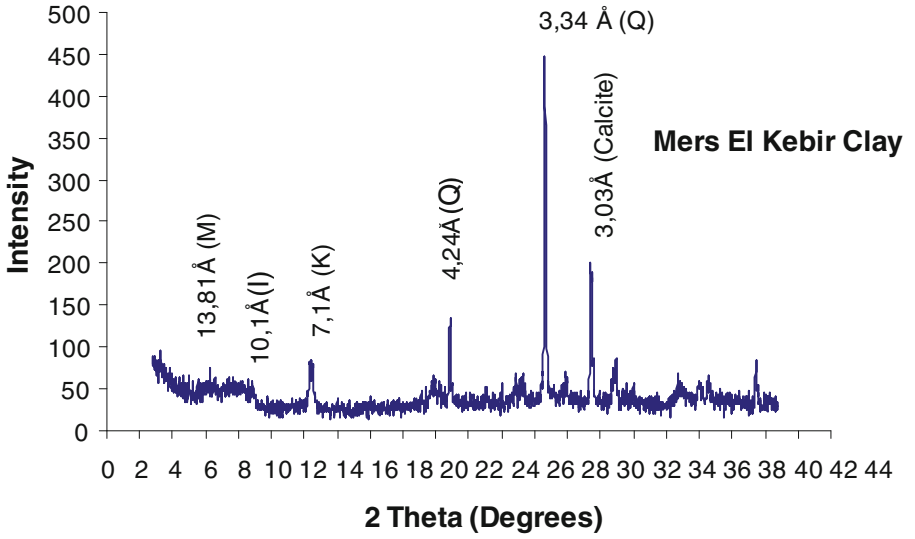

Fig. 1. X-ray diffractgram of Mers El Kébir clay.

Table 2. Physical and Chemical parameters of the cement.

Parameters	Denomination	Notation and units		Value
Physical	Total specific weight	Mv	g/cm^3	3.1
	Specific Surface	SSB	m^2/g	0.27
	Initial setting time	t		2 h 40 min
	Final setting time	t		3 h 45 min
Chemical Minerals		SiO_2	%	22,17
		CaO	%	64,05
		AL_2O_3	%	5,99
		Fe_2O_3	%	2,47
		MgO	%	0,27
		SO_3	%	1,86
	Loss on Ignition		%	2,47
	Carbonic anhydrite	CO_2	%	1,6
	Insoluble		%	0,5

3 Sample Preparations

The clayey soil was dried in an oven at approximately 105 °C to prepare the mixtures of clayey soil and cement. First, the required amounts of clayey soil and cement were measured and mixed together. The amounts of cement were selected as 2%, 4% and 6% of the total weight of the clayey soil–cement mixtures. Then, soil and cement were mixed with the required amount of water to reach the optimum water content. All mixing was done manually. Cylindrical metal moulds of 50 mm in diameter and 100 mm in height were used to statically compact the samples of clayey soil and clayey soil–cement mixtures. The values of the optimum water content and maximum dry density of treated and untreated soil were determined from the compaction curves in accordance with ASTM D 698 (2000) (Table 3).

Table 3. Values of maximum dry density and optimum water content of untreated and treated soil

Cement content (%)	0	2	4	6
Maximum Dry density	1,65	1,62	1,60	1,59
Optimum water content (%)	19,5	20	22,42	23,13

4 Results and Discussion

4.1 Effect of Cement on Suction

Matrix suction (s) is defined as the difference between the pressure in the air phase (ua) and the pressure in the water phase (uw). At a microscopic level, the concept of matrix suction involves both the capillary properties of the medium (characterised by

the radius of the pores) and the adsorption properties of the minerals, which depend on the type of minerals and surface ions (Fleureau et al. 1993).

Matrix suction measurements were made with a filter paper (ASTMD 5298-94 (1994)) in contact with the clay sample. This method is applicable for suctions ranging from 0.05 to 10 MPa.

For dry filter paper:

$$\log\ s = 5,327w_f - 0,0779w_f \rightarrow w_f < 45,3\% \quad (1)$$

$$\log s = 2,412w_f - 0,01359w_f \rightarrow w_f > 45,3\% \quad (2)$$

For wet filter paper:

$$\log s = 5,4018w_f - 0,0718w_f \rightarrow w_f < 47,3\% \quad (3)$$

$$\log s = 2,6995w_f - 0,01147w_f \rightarrow w_f > 47,3\% \quad (4)$$

where: s is the suction in kPa and w_f is the percentage of water content of filter paper (Whatman n°42).

Figure 2 shows the effect of different cement percentages on the matrix suction.

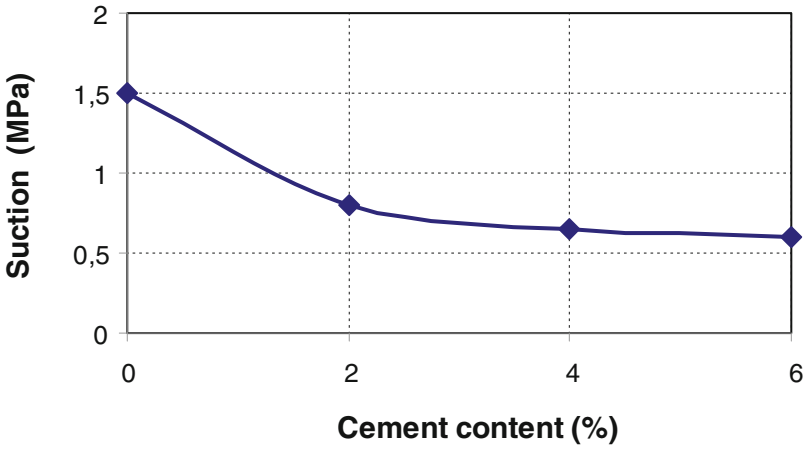

Fig. 2. Effect of added cement on suction.

For an untreated sample the suction is 1.5 MPa, this value decreases with the increase in cement percentage to reach 0.6 MPa for 6% of cement. This decrease is explained by the drop of the density observed after the addition of cement. This is due to the reorganization of the particles induced by the flocculation phenomenon, which agree with the observations of many researchers (Chu and Mou 1981; Pile 1983; Lloret et al. 2003).

4.2 Effect of Cement on Swelling

Swelling potential tests were performed in a standard one-dimensional oedometer in accordance with ASTM D 4546-90 (1990). The samples were confined in the consolidation ring of 50 mm in diameter and 20 mm in height. The natural and stabilized clayey soil samples were submerged in water. The samples were allowed to swell under the initial load. The dial gauge readings were recorded periodically until there was no further change in swelling. The swelling percentage can be expressed as:

$$G(\%) = \frac{H_f - H_0}{H_0} \tag{5}$$

where G is the swelling percentage, H_f is the final thickness of the sample in mm, and H_0 is the original thickness of the sample in mm.

The reduction of swelling can be expressed as:

$$\frac{\Delta G}{G} = \frac{G_0 - G_{added}}{G_0} \tag{6}$$

where:

G_0: The swelling without treatment.
G_{added}: The swelling of the soil treated with cement.

The results of the measurements of the swelling potential of the soil treated with different percentages of cement are shown in Fig. 3. It can be noted that the effect of cement is significant, and the reduction of the swelling potential reaches 65% for the clay treated with 6% of cement. It can be also observed that 4% of cement is sufficient to reach a reduction of 52% of the swelling potential. This is in agreement with the

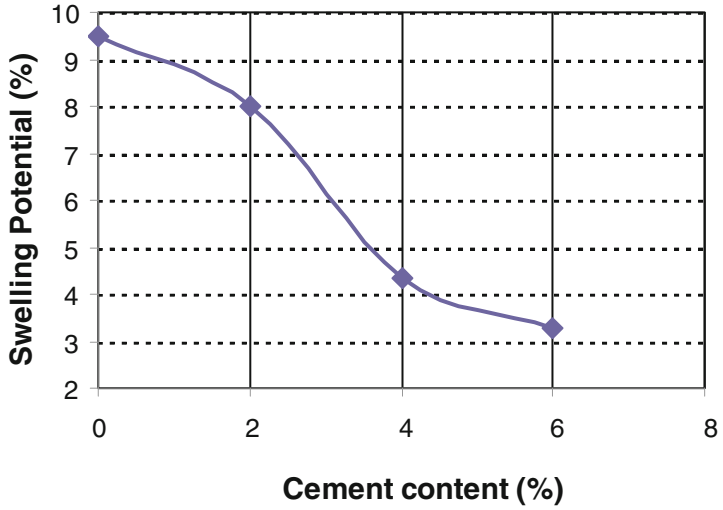

Fig. 3. Effect of added cement on swelling potential.

observations of several researchers (Cabane 2004; Al-Rawas et al. 2005; Al Rawas and Goosen 2006).

The hypothesis that could explain this decrease is that chemical reactions may occur between the calcium hydroxide of the cement and silicas and aluminas soluble in the clay. These reactions give a change in the particle structure after a short time by allowing granular rearrangement by flocculation and afterwards, pozzolanic reactions result in the formation of cementitious compounds binding soil particles.

4.3 Effect of Cement on Pore Distribution Before and After Swelling

Cement-treated samples were first compacted under standard Proctor conditions. To keep their microstructure unchanged and to be analysed with their initial fabric, water was removed from the samples using the freeze-drying technique (compact Flexi-dry). This technique is used to avoid shrinkage of the samples. The samples were introduced into liquid nitrogen (Delage and Pellerin 1984) and sublimation of ice was done in a lyophilizer. Samples of about 1 cm^3 volume were extracted from the freeze-dried specimen by simple cutting

Mercury intrusion porosimetry tests were performed on the freeze-dried specimens, in order to obtain information about the variation of the pore space according to time and treatment.

The porosimeter (Micromeritics Auto Pore IV 9500) software provides the porosity and distribution of the pore size of samples. The interpretation is based on Laplace-Young law (Eq. (5)) that connects the capillary pressure (P_c) to the capillary radius (r).

$$P_C = \frac{2y \cos\theta}{r} \tag{7}$$

where θ is the contact angle between the three immiscible phases: liquid mercury - mercury vapour-mineral grain (usually θ = 140°: Delage and Lefebvre 1984), and y is the surface tension of mercury (y = 0.482 N/m). Thus, by varying the pressure applied to mercury and measuring the volume of mercury that enters the specimen, the relationship between the access radius and pore volume is deduced. The apparatus can measure down to a radius of 3 nm for a mercury pressure of 200 MPa.

The pore distribution in the compacted soil of Mers El Kébir treated with cement at different percentages before and after swelling is shown in Figs. 4 and 5.

Before swelling (Fig. 4a), the untreated soil has a dominant pore diameter of about 20 μm and another intra-aggregate pore diameter around 0.04 μm. The cement-treated soil has a diameter of small pores between 0.03 μm and 0.09 μm and a diameter of large pores (inter-aggregate) between 4 and 30 μm, which explain the drop of dry density with the increase of cement percentage.

The results of the cumulative intrusion curves show that the pore volume of the treated soil samples is slightly higher than that of the corresponding untreated soil sample (Fig. 5a). For the untreated clay, the volume of mercury injected is 0.19 ml/g, and that of the treated clay at 6% of cement is 0.21 ml/g. This can be explained by the lower dry density after treatment.

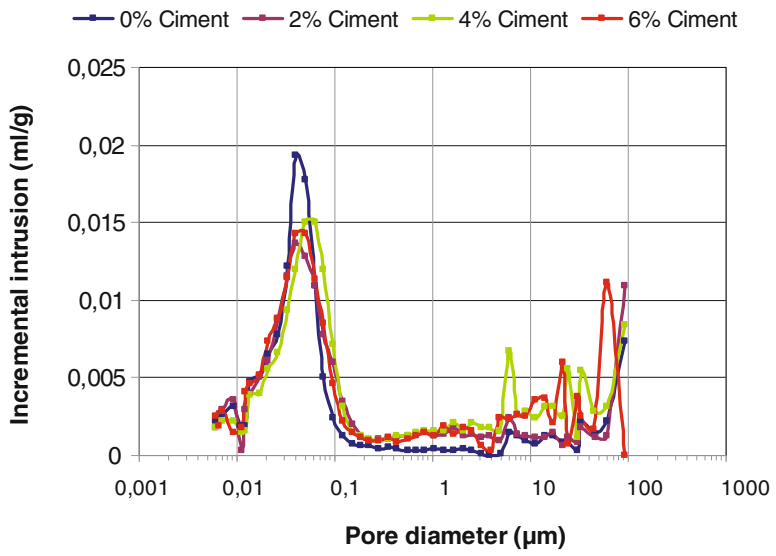

(a)

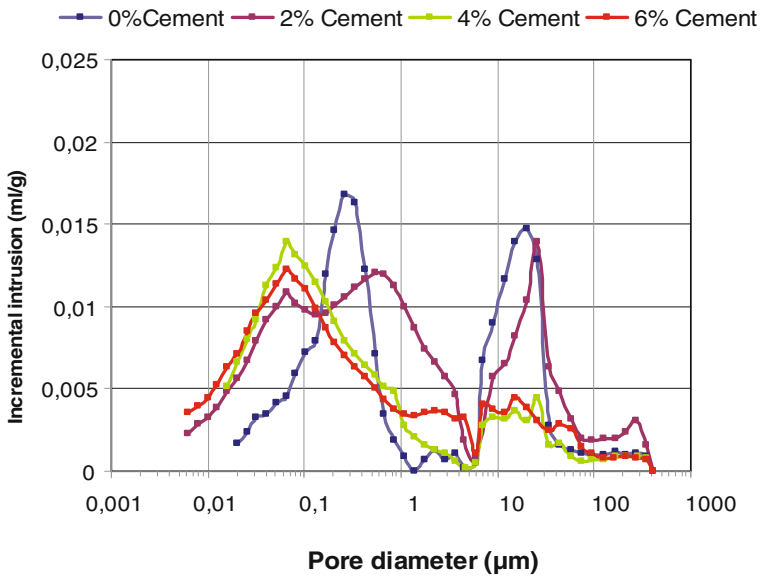

(b)

Fig. 4. Pore distribution Curves of Mers El Kébir clay treated with cement before swelling (a) and after swelling (b).

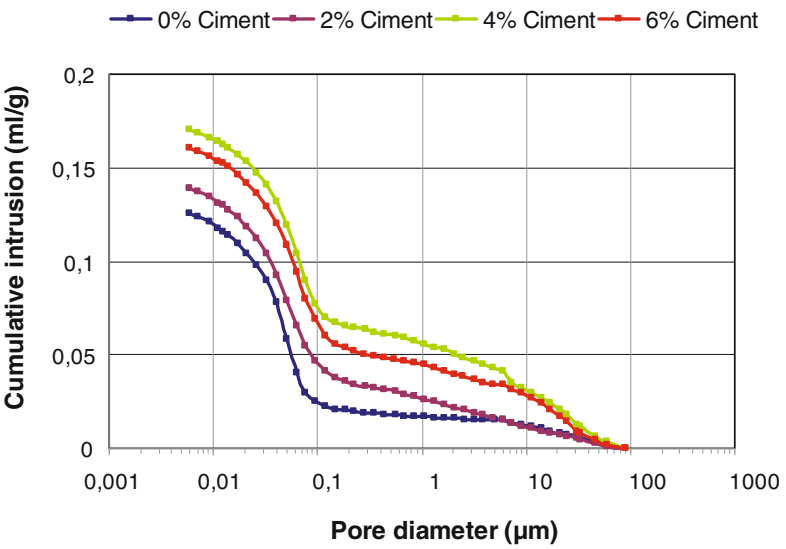

(a)

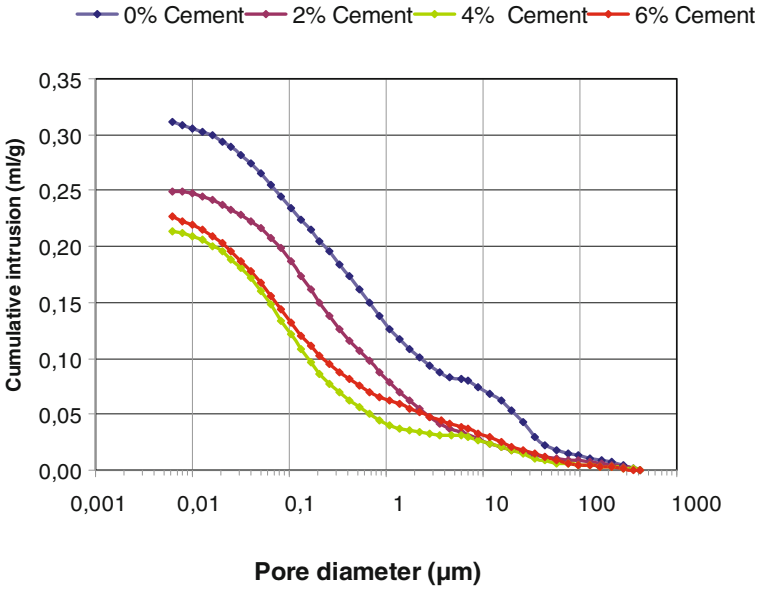

(b)

Fig. 5. Cumulative intrusion curves of Mers El Kébir clay treated with cement before swelling (a) after swelling (b).

After swelling (Fig. 4b), for the untreated soil, the small pore diameter increases up to 0.26 µm, and there is also the appearance of an inter-aggregate pore diameter of about 20 µm. The diameter of the small pores in the treated soils remains unchanged, while the diameter of the large pores decreases, which explains the decrease in the diameter of the pores of the soil treated with 4% and 6% of cement after swelling.

For the untreated clay, the volume of injected mercury is 0.31 ml/g and, for the treated soil at 4% and 6% of cement, it is 0.22 ml/g (Fig. 5b). This phenomenon can be explained by the bonding of particles together, and by the flocculation. The particles are coated by the cement, forming larger particles, which leads to a decrease in the porosity of the treated clay. This is confirmed by the decrease in the volume of mercury injected into the pores. This is in agreement with the studies of Cook and Hover (1999); Chew et al. (2004); Bin et al. (2007); Horpibulsuk et al. (2010); Millogo and Morel (2012); Lemaire et al. (2013).

5 Conclusion

From the tests conducted on the influence of the cement addition on suction, swelling and pore distribution, several conclusions can be made:

- The suction of Mers El Kebir clay measured by the filter paper method decreases with the percentage of added cement, which can be explained by the decrease in dry density;
- Cement is an efficient swelling reducer for the clay of Mers El Kébir. The higher the percentage of cement, the lower its swelling potential. This is probably due to the development of cementitious bonds produced by the cement-clay reactions and the continuous cation exchange;
- The results of the mercury intrusion porosimetry tests show that the pore volume of the treated soil samples is slightly higher than that of the corresponding untreated soil samples before swelling. These tests show the existence of large pores in the untreated clay after swelling. The treatment at a high percentage of cement substantially reduces the average pore diameter of the treated clay. This can be explained by the cement-clay reactions, including flocculation, which lead to the formation of larger particles and a decrease in porosity.

References

Al Rawas, A.A., Goosen, M.F.A.: Expansive Soils - Recent Advances in Characterization and Treatment. Taylor & Francis Group, Balkema, London (2006)

Al-Rawas, A.A., Hagoa, A.W., Hilal, A.-S.: Effect of lime, cement and Sarooj (artificial pozzolan) on the swelling potential of an expansive soil from Oman. Build. Environ. **40**(5), 681–687 (2005)

Aparna, R.: Soil stabilization using rice husk ash and cement. Int. J. Civil Eng. Res. **5**(1), 49–54 (2014). ISSN 2278-3652

ASTM D-4546: Standard test method for one-dimensional swell or settlement potential of cohesive soils. Annual Book of ASTM Standards, vol. 04.08. American Society for Testing and Materials, Easton, Philadelphia (1990)

ASTM D-5298: Standard test method for measurement of soil potential (suction) using filter paper. ASTM International, West Conshohocken, PA (1994). www.astm.org

ASTM D-698: Standard test method for laboratory compaction characteristics of soil using standard effort. Annual Book of ASTM Standards, vol. 04.08. American Society for Testing and Materials, Easton, PA (2000)

Balasubramaniam, A.S., Kamruzzaman, A.H., Uddin, K., Lin, D.G., Phienwij, N., Bergado, D. T.: Chemical stabilization of Bangkok clay with cement, lime, and fly ash additives. In: 13th Southeast Asian Geotechnical Conference, pp. 253–258 (1998)

Bin, S., Zhibin, L., Yi, C., Xiaoping, Z.: Micropore structure of aggregates in treated soils. J. Mater. Civil Eng. **19**, 99–105 (2007). ASCE

Bourokba, S.A., Hachichi, A., Taibi, S., Fleureau, J.-M.: Conductivité hydraulique non saturée de l'argile de Mers El Kébir (Algérie). EJECE **14**, 1297–1315 (2010)

Bourokba, S.A.: Étude de la conductivité hydraulique et de la stabilisation par ajouts de liants hydrauliques de l'argile de Mers El Kébir. Doctoral thesis, University of Science and Technology, Med Boudiaf, Oran, Algeria (2011)

Bourokba, S.A., Hachichi, A., Fleureau, J.-M.: Influence du cement sur le gonflement et la microstructure d'une argile naturelle. XXIXe Rencontres Universitaires de Génie Civil, Tlemcen, Algeria (2011)

Bourokba, S.A., Hachichi, A., Soulib, H., Taibi, S., Fleureau, J.M.: Effect of lime on some physical parameters of a natural expansive clay from Algeria. Eur. J. Environ. Civil Eng. **21**, 108–125 (2015)

Cabane, N.: Sols traités à la chaux et aux liants hydrauliques Contribution à l'identification et à l'analyse des éléments perturbateurs de la stabilisation. Ph.D. thesis, École Nationale Supérieure des Mines de Saint-Étienne, France (2004)

Chew, S.H., Kamruzzaman, A.H.M., Lee, F.H.: Physicochemical and engineering behavior of cement treated clays. J. Geotech. Geoenviron. Eng. **130**(7), 696–706 (2004)

Chu, T.Y., Mou, C.H.: Soil-suction approach for evaluation of swelling potential. In: Transportation Research Record 790, pp. 54–60 (1981). Géotechnique **53**(1), 27–40

Cook, R.A., Hover, K.C.: Mercury porosimetry of hardened cement pastes. Cem. Concr. Res. **29**, 933–943 (1999)

Delage, P., Lefebvre, G.: Study of the structure of a sensitive Champlain clay and of its evolution during consolidation. Can. Geotech. J. **21**, 21–35 (1984)

Delage, P., Pellerin, M.I.: Influence de la lyophilisation sur la structure d'une argile sensible du Quebec. Clay Miner. **19**, 151–160 (1984)

Fleureau, J.-M., Kheirbek-Saoud, S., Soemitro, R., Taibi, S.: Behavior of clayey soils on drying–wetting paths. Can. Geotech. J. **30**, 287–296 (1993)

Hachichi, A., Bourokba, S.A., Fleureau, J.-M.: Stabilisation chimique des sols gonflants de la région d'Oran. Revue Française de Géotechnique **118**, 3–11 (2007)

Hachichi, A., Fleureau, J.-M.: Caractérisation et stabilisation de quelques sols gonflants d'Algérie. Revue Française de Géotechnique **86**, 37–51 (1999)

Hachichi, A., Bourokba, S.A., Bengraa, L., Fleureau, J.-M.: Influence de l'ajout de chaux sur le potentiel gonflement et la microstructure d'une argile naturelle d'Algérie. INVACO2: Séminaire International, Innovation et valorisation en génie civil matériaux et construction, Rabat, Morroco (2011)

Horpibulsuk, S., Rachan, R., Chinkulkijniwat, A., Raksachon, Y., Suddeepong, A.: Analysis of strength development in cement-stabilized silty clay from microstructure considerations. Constr. Build. Mater. **24**, 2011–2021 (2010)

Ikhlef, N.S., Ghembaza, M.S., Dadouch, M.: Effect of cement and compaction on the physicochemical behavior of a material in the region of Sidi Bel Abbes. Eng. Technol. Appl. Sci. Res. **4**(4), 677–680 (2014)

Lemaire, K., Dimitri, D., Bonnet, S., Legret, M.: Effects of lime and cement treatment on the physicochemical, microstructural and mechanical characteristics of a plastic silt. Eng. Geol. **166**, 255–261 (2013)

Lloret, M., Villar, M., Sanchez, A., Gens, X., Pintado, E., Alonso, E.E.: Mechanical behaviour of heavily compacted bentonite under high suction changes (2003)

Millogo, Y., Morel, J.-C.: Microstructural characterization and mechanical properties of cement stabilised adobes. Mater. Struct. **45**, 1311–1318 (2012)

Osula, D.O.A.: A comparative evaluation of cement and lime modification of laterite. Eng. Geol. **42**(1), 71–81 (1996)

Pakbaz, M.S., Alipour, R.: Influence of cement addition on the geotechnical properties of an Iranian clay. Appl. Clay Sci. **67, 68**, 1–4 (2012)

Parrot, J.F., Verdoni, P.A., Delaune-Mayere, M.: Analyse modale semi-quantitative d'après l'étude des rayons X [Semi quantitative modal analysis from XRD study]. Analusis **13**, 373–378 (1985)

Pile, K.C.: The relationship between matrix and solute suction, swelling pressure, and magnitude of swelling in reactive clays. In: Webater, J.A. (ed.) Third Australia New Zealand Conference on Geomechanics, vol. 1, pp. 197–201 (1983)

Portelinha, F.H.M., Lima, D.C., Fontes, M.P.F., Carvalho, C.A.B.: Modification of a lateritic soil with lime and cement: an economical alternative for flexible pavement layers. Soils Rocks **35** (1), 51–63 (2012). São Paulo

Sariosseiri, F., Muhunthan, B.: Effect of cement treatment on geotechnical properties of some Washington State soils. Eng. Geol. **104**(2), 119–125 (2009)

Tran, N.L.: Un nouvel essai d'identification des sols: l'essai au bleu de méthylène. Bulletin de Liaison des Ponts et Chaussées **88**, 136–137 (1977)

Venkatarama, R., Prasanna, K.: Cement stabilized rammed earth. Part A: compaction characteristics and physical properties of compacted cement stabilised soils. Mater. Struct. **44**, 681–693 (2011)

Treatment of Collapsible Soils by Cement Using the Double Consolidation Method

Abbeche Khelifa[1(✉)], Lahmadi Azeddine[2], and Bahloul Ouassila[1]

[1] Laboratory of Applied Hydraulic Research (LARYHA), Department of Civil Engineering, University of Batna 2, Fesdis, Algeria
abbechek@yahoo.fr
[2] Department of Civil Engineering, University of M'sila, M'Sila, Algeria

Abstract. The stability of civil engineering constructions is a statically indeterminate problem when they were built on collapsible soils. These soils present significant changes due to sudden decrease in volume after wetting with or without loading. This paper is aimed at studying the treatment by cement of a collapsible soil, which was reconstituted in laboratory. Oedometer tests were carried out by using the double consolidation method. The main aim of this experimental study is to investigate the influence of this kind of treatment and the initial conditions on the collapse of the soils. The results obtained show that it is possible to reduce the soil collapse potential to an acceptable level by adding low cement contents to a test specimen at various initial water contents and under the effect of several compacting energies. These experimental results contribute in solving the problems of soil collapse by treating to enhance its resistance.

1 Introduction

Collapsible soils are metastable soils with a highly porous structure in the form of deposits, formed by sand, silt and clay particles located in the arid and semi-arid regions. In dry state, a cementation between the particles is responsible for an important internal connection forces and which can support very high loads. In order to estimate the possibility of collapse, we must see the loads intensity that causes the collapse of the soil's porous structure. This loads intensity was influenced by the grain size distribution, the dry density, the water content and the power of cementation. Nevertheless, if the soil becomes saturated with or without loads the soil structure will collapse due to the loss of binder strength of particles Reginatto and Ferrero (1973); Clemence and Finbarr (1981); Rogers (1995); Alawaji (2001); Abbeche et al. (2007, 2009, 2010); Abbeche and Laouar (2013). This type of changes generally causes structural damage with cracks appearance.

The literature revealed that the majority of research was devoted to the collapse identification, mechanisms, prediction, and methods of treatment. Momeni et al. (2012) defined the collapsible soils are any unsaturated soils generally characterized by the sudden and the considerable reduction in volume that occurs when subjected to inundation under constant stress.

L.R. Hoyos and J. McCartney (eds.), *Advances in Characterization and Analysis of Expansive Soils and Rocks*, Sustainable Civil Infrastructures,
DOI 10.1007/978-3-319-61931-6_7

This paper presents the results of a series of double oedometer tests. The main object is to measure directly the collapse potential of the reconstituted soil treated with cement. The experimental tests aim to determine the ideal conditions to treat the collapsing soil generally located in arid and semi-arid regions where minimization of humidification and compaction are require. The results obtained show that the relationship between the collapse potential and the parameters used in this study: (1) cement content varying from 1 to 5% (by weight) (2) initial water content, and (3) compacting energy (expressed by the number of blows). The following compacting efforts were used 20, 40, and 60 blows, which were corresponding to compacting energies of 5.56×10^{-3} kJ, 11.12×10^{-3} kJ, and 16.68×10^{-3} kJ, respectively.

2 Experimental Work

2.1 Materials

The samples used in the experimental program were prepared from a reconstituted soil, which is composed of 80% of sand and 20% of kaolin. This proportion is chosen in order to obtain a sample that meets the conditions of collapse, reported by Abbeche et al. (2010). Likewise, Lahmadi et al. (2012) and Abbeche and Laouar (2013) show that this reconstituted soil is collapsible. The reconstituted soil was classified as SM – silty sand according to ASTM D 2487-06 (2006).

The sand used to reconstitute the soil is a fine sand with a particle diameter less than 2 mm, taken from Liwa stream which is located in the region of Biskra (arid region) in Algeria. The amount of material more than 2 μm was less than 3%. The kaolin used in this kind of soil (grains size $\leq$ 80 μm) is extracted from the El Milia mine in the region of Jijel in Algeria. The geotechnical characteristics of the materials used in this investigation are presented in Table 1. The Grains size distribution curve of the reconstituted soil is shown in Fig. 1.

Chemical and mineralogical analysis

The chemical composition of the materials is given in Table 2. The results showed that the silica represents the main component in the sand and the kaolin.

The mineralogical content of the reconstituted soil is determined by X-ray diffraction (XRD). The recorded XRD pattern for the reconstituted soil is shown in Fig. 2. The crystal phases are quartz, calcite, corundum, chromium and bornite. Examination of XRD intensity, although qualitative, indicates that the proportion of quartz is very high compared to other phases. It is noted that the silica is crystallized in quartz form.

Characterization of cement

The cement used to stabilize reconstituted soil is Portland cement type CEM I with strength class 42.5.

Sample preparation and program tests

The principle consists to reconstitute a collapse soil sample then place it in the oedometer ring. The dimensions of the ring were 20 mm in height and 70 mm in diameter. Two types of reconstituted soil are prepared. One is treated with cement,

Table 1. Geotechnical properties of materials

Material	Characteristics	Values
Sand	Sand equivalent, *ES* (%)	75.34
	% of particles $\leq$ 80 µm	2.92
	Uniformity coefficient, C_u	2.70
	Coefficient of curvature, C_c	1.04
	Specific gravity, G_S	2.56
Kaolin	Liquid limit, w_L (%)	46.42
	Plastic limit, w_P (%)	29.01
	% of particles $\leq$ 2 µm	34.10
	Specific gravity, G_S	2.65
Reconstituted soil	Liquid limit, w_L (%)	18.20
	Plastic limit, w_P (%)	14.53
	Uniformity coefficient, C_u	24.50
	Coefficient of curvature, C_c	4.07
	Maximum dry density, $\gamma_{d\ max}$ (g/cm^3)	2.02
	Optimum water content, w_{opt} (%)	8.30
	% of particles $\leq$ 2 µm	7.12
	Specific gravity, G_S	2.61
	Soil classification (USCS)	SM

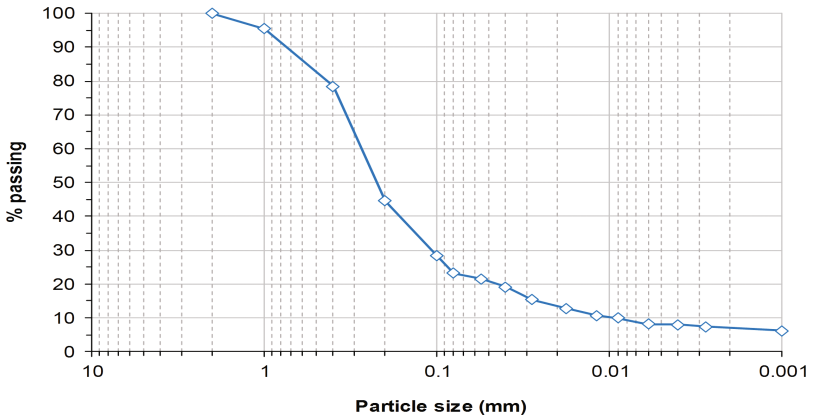

Fig. 1. Grains size distribution curves of the reconstituted soil

the other remains without treatment. All used samples have a given initial water and initial dry density which are obtained upon the variation of compacting energy. The confection of all samples are carried out according to the procedure described by Ayadat and Belouahri (1996); Abbeche et al. (2007, 2009, 2010), Ayadat and Hanna (2007, 2008, 2013) and Lahmadi et al. (2012); Abbeche and Laouar (2013).

Table 2. Chemical composition of sand and kaolin

Constituent	Percentage (%)	
	Sand	Kaolin
SiO_2	87.39	54.33
Al_2O_3	0.93	30.89
Fe_2O_3	1.90	2.10
CaO	1.77	0.43
MgO	0.28	<0.01
SO_3	0.04	0.03
K_2O	0.29	4.26
Na_2O	<0.01	0.06
Loss on ignition	6.45	7.36

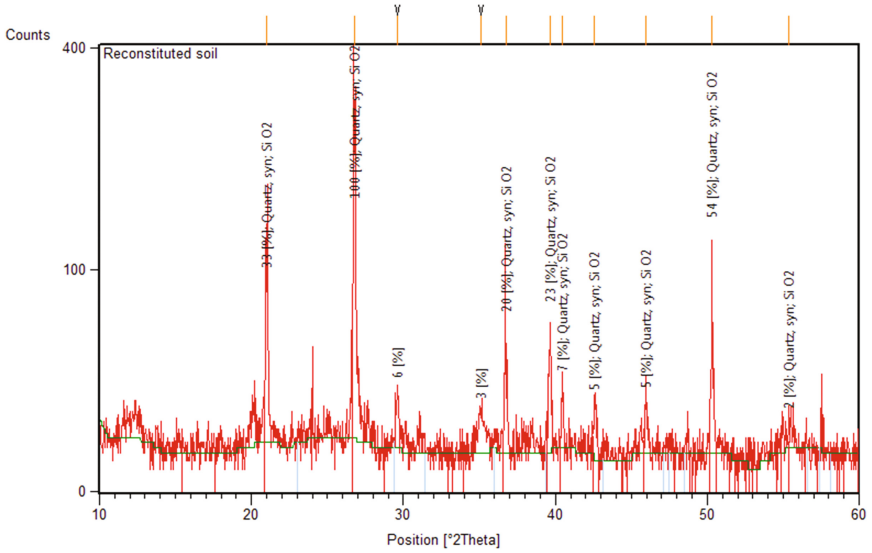

Fig. 2. XRD pattern of the reconstituted soil

In the case of untreated samples, the preparation of the sample was initiated by mixing the two components (sand and kaolin) then adding the initial water content to obtain a homogenized soil. However, in the case of samples treated with cement, the preparation was carried out as follows: (1) sand and kaolin are mixed before adding initial water content. The second step is to compact the sample with a tamper as shown in Fig. 3. The tamper is similar to that used by Abbeche et al. (2010) in their work. The tamper is composed of a disc having a small thickness fixed to a rod, which permits a free fall of a hammer of 152 g. The hammer dropped from 15 cm high on the fixed disc. In this manner, the sample placed in the oedometer ring will be compacted.

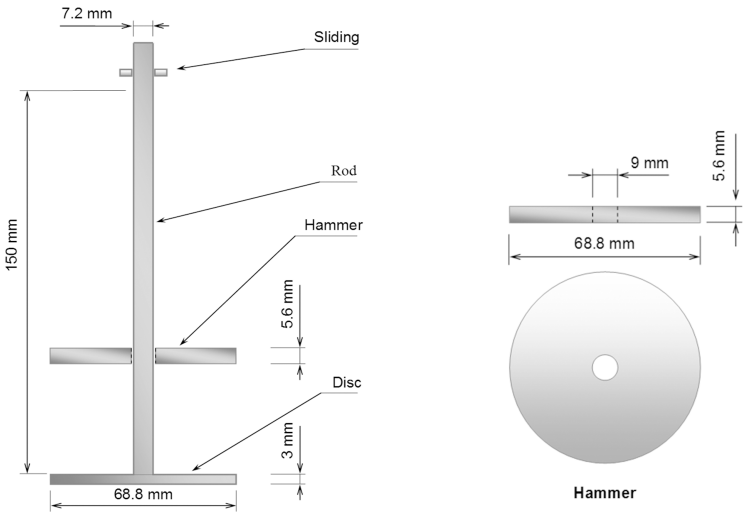

Fig. 3. Compaction tamper

Because of the limited thickness of the ring (20 mm), only one layer can be used and compacted according the test programs. The reconstituted soil shows good mechanical characteristics when it is compacted with a low initial water content ($w_0 < w_{opt}$). However, if more water is added, even without any additional load, the reconstituted soil collapses and the material becomes denser. Ayadat and Belouahri (1996); Abbeche et al. (2007, 2009, 2010); Ayadat and Hanna (2007, 2008, 2013); Lahmadi et al. (2012); Abbeche and Laouar (2013).

The samples are obtained by varying the cement content (*CC*), the initial water content (w_0), and the compacting energy (*CE*) under different conditions. Table 3 shows the program of these principal tests which were carried out on the reconstituted soil.

Test and procedure

After preparing and weighting, the sample was put in the one-dimensional oedometer to carry out the compressibility test, in order to determine the collapse potential. In this experimental study two identical oedometer samples, which can be simultaneously elaborated, have been used. One sample is tested under dry conditions; the other is tested under saturated conditions. A strength of 10 kPa have been applied for 24 h. Collapse stresses ranging from 10 kPa to 1600 kPa have been used during testing. The results of the measurement of the collapse potential are illustrated in Fig. 4.

The collapse potential (*CP*) is defined by the following formula:

$$CP(\%) = \left[\frac{\Delta e}{1 + e_0}\right] \times 100 \tag{1}$$

where Δe is the change in void ratio between the dry sample and the wet sample, and e_0 is the initial void ratio.

Table 3. Tests program

Treatment type		Initial water content, w_0 (%)	Initial dry density, γ_d (g/cm^3)		
			20 blows	40 blows	60 blows
Untraited	–	2	1.504	1.563	1.602
		4	1.545	1.591	1.627
		6	1.603	1.634	1.654
Cement	1%	2	1.502	1.559	1.597
		4	1.543	1.588	1.615
		6	1.582	1.617	1.628
	3%	2	1.497	1.543	1.581
		4	1.529	1.562	1.586
		6	1.568	1.587	1.593
	5%	2	1.491	1.528	1.563
		4	1.512	1.531	1.557
		6	1.533	1.548	1.553

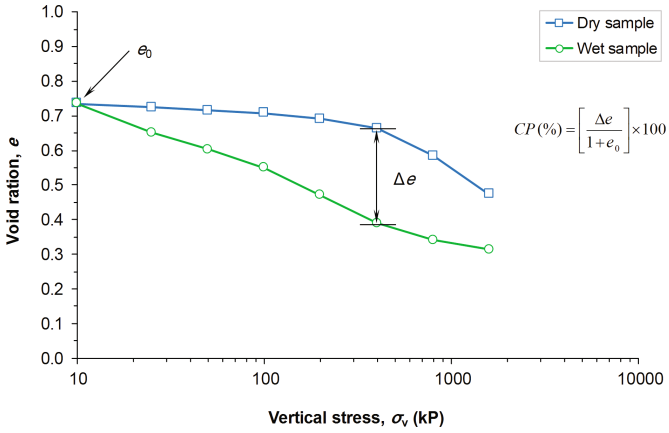

Fig. 4. Typical double oedometer test result

Jennings and Knight (1975) have suggested some values for collapse potential as shown in Table 4. These values can only indicate qualitatively the severity of the problem.

In addition, ASTM D 5333-3 (2003) proposed a relationship between the collapse index I_e (relative magnitude of collapse determined at 200 kPa) and the degree of specimen collapse (Table 5).

Table 4. Potential severity of collapse (Jennings and Knight 1975)

Collapse potential *CP* (%)	Severity of problem
0–1	No problem
1–5	Moderate trouble
5–10	Trouble
10–20	Severe trouble
>20	Very severe trouble

Table 5. Degree of specimen collapse vs. collapse index (ASTM D 5333-3 2003)

Degree of specimen collapse	Collapse index I_e (%)
None	0
Slight	0.1 to 2
Moderate	2.1 to 6
Moderately severe	6.1 to 10
Severe	>10

3 Results and Discussion

3.1 Untreated Samples

The results obtained from the oedometer tests carried out on the untreated samples are showed in Fig. 5. The maximum value of collapse potential CP_{max}, which is equal to 15.36%, is obtained under a vertical stress of about 400 kPa, with the minimal initial water content of 2% and under the minimal value of compacting energy of 20 blows (Fig. 5a). Figure 6 shows the maximum values of *CP* for various untreated samples versus the variation of compacting energy and initial water content.

The results show a tendency to the collapse of the untreated soil, which corresponds to the classification of Jennings and Knight (1975) given in Table 4 with a collapse potential of 1.86 to 15.36%, which corresponds to the headings active between "moderate troubles" and "severe troubles". Also, according to ASTM D 5333-3 (2003), the results showed that the index of collapse varied between "slight" and "severe" (Table 5).

The influence of the compacting energy on the collapse potential is presented in Fig. 6. It can be seen that CP_{max} decreases when the compacting energy increases, whatever the initial water content value. It is also noticed that for a given compacting energy, the collapse potential increases when the initial water content decreases. When the initial water content increases, the collapse potential decreases. It is also noted that, at a given initial water content, the collapse potential decreases with the increase of the initial dry density. Figure 7 shows the relationship between initial dry density and compacting energy. These results are in agreement with those obtained by several studies e.g. Lawton et al. (1989); Lefebvre and Ben Belfadhel (1989); Abbeche et al. (2007, 2009, 2010); Ayadat and Hanna (2007, 2008, 2013); Lahmadi et al. (2012); Abbeche and Laouar (2013).

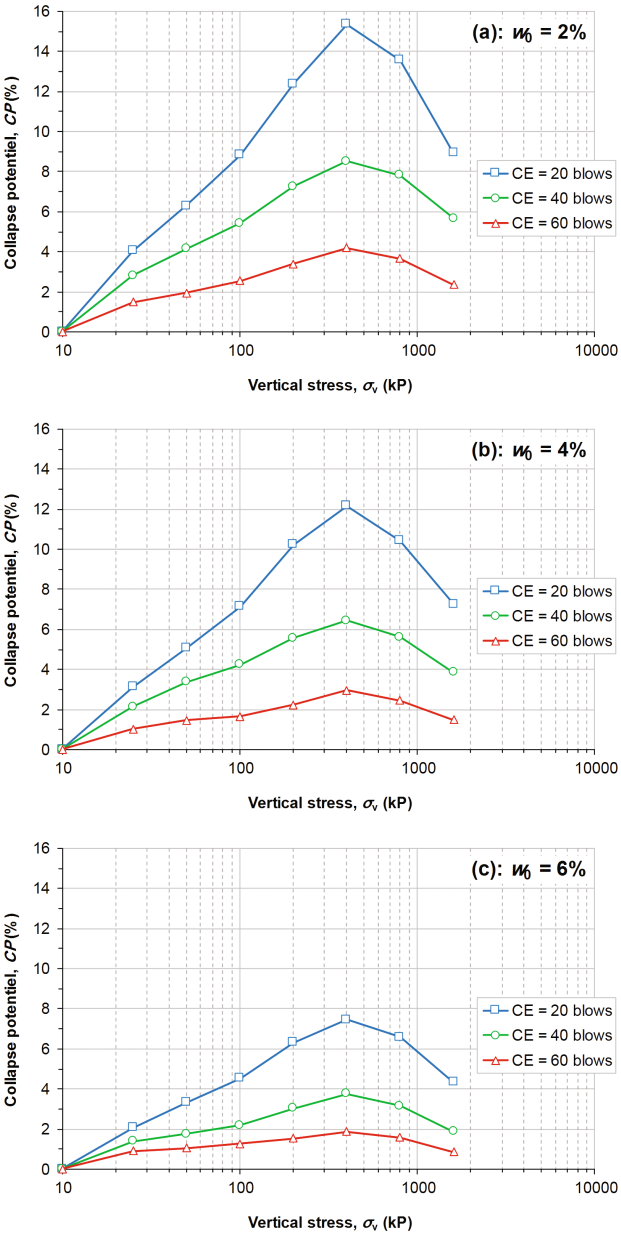

Fig. 5. Collapse potential variation vs. vertical stress, (a) for w_0 = 2, (b) for w_0 = 4, (c) for w_0 = 6%

In addition, Fig. 8 shows that CP_{max} decreases in a progressive manner, when the initial void ration increases and the compacting energy increases as well as the initial water content.

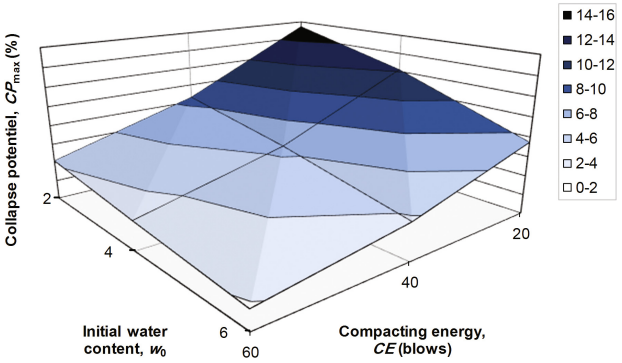

Fig. 6. Maximum collapse potential variation vs. compacting energy and initial water content

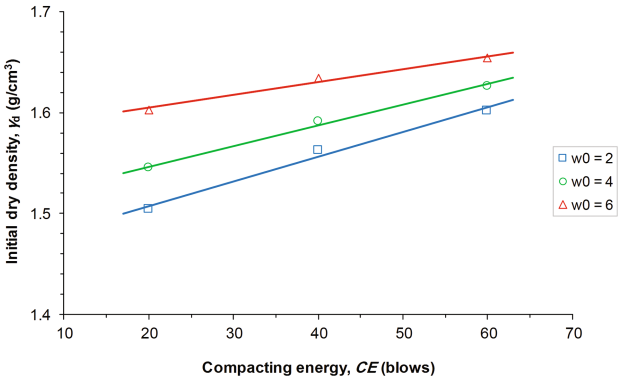

Fig. 7. Relationship between initial dry density and compacting energy

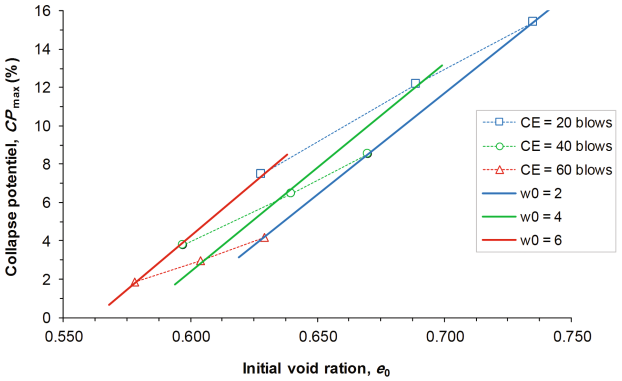

Fig. 8. Collapse potential vs. initial dry density

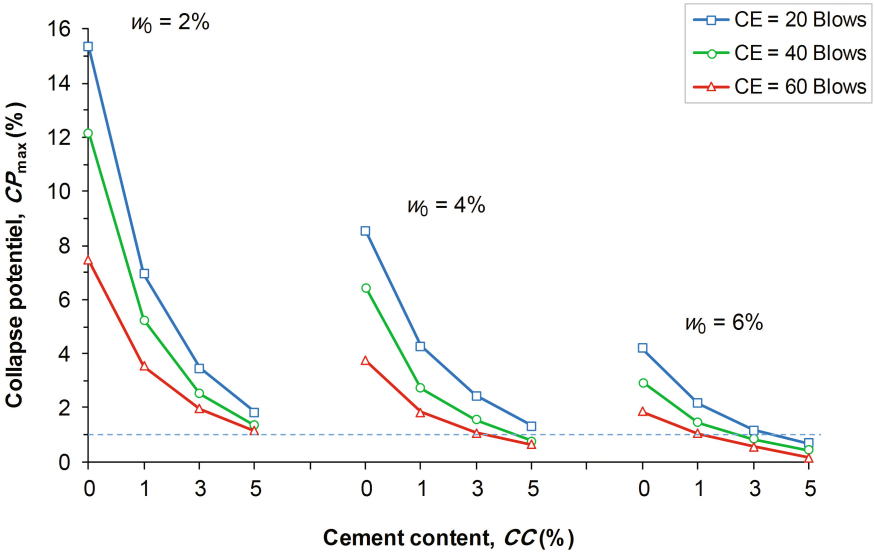

Fig. 9. Influence of cement content on $CP_{\max}$

Treated sample

The influence of the variation of the initial water content, for various cement contents and compacting energies is clearly visible on Fig. 9. It reaches the value of 0.26% for a maximum cement content associated with the maximum compaction level.

As it is shown in Fig. 9, the collapse potential decreases with increasing of one of the following parameters: initial water content, cement content and compacting energy. So that, the non-collapsible soil is obtained when the initial water content is 4% with 5% of cement and compacting energy of 40 blows, as well as, for 6% of initial water content with 3% of cement and compacting energy of 40 blows. It is noted that the humidification of the soil with 2% is not sufficient to treat the soil with a considered cement content and energy of compaction. Indeed, for a minimal compacting energy of 20 blows, a minimum of 5% of cement and 6% of initial water content are needed. However, increase in the compacting energy with 60 blows, for an initial water content of 6% allows the reduction of cement content to 3%.

The relationship between the compacting energy and collapse potential indicates that the decrease of CP_{max} is related to the increase of compacting energy. According to the results obtained, as shown in Fig. 9, it can be concluded that for a cement content of 1%, the compacting energy does not affect the reduction in the initial water content in order to obtain a non-collapsible soil.

The collapse reduction ratio (CRR) is defined by the following formula:

$$CRR(\%) = \left[1 - \frac{CP_{\text{Treated sample}}}{CP_{\text{Untreated sample}}}\right] \times 100 \tag{2}$$

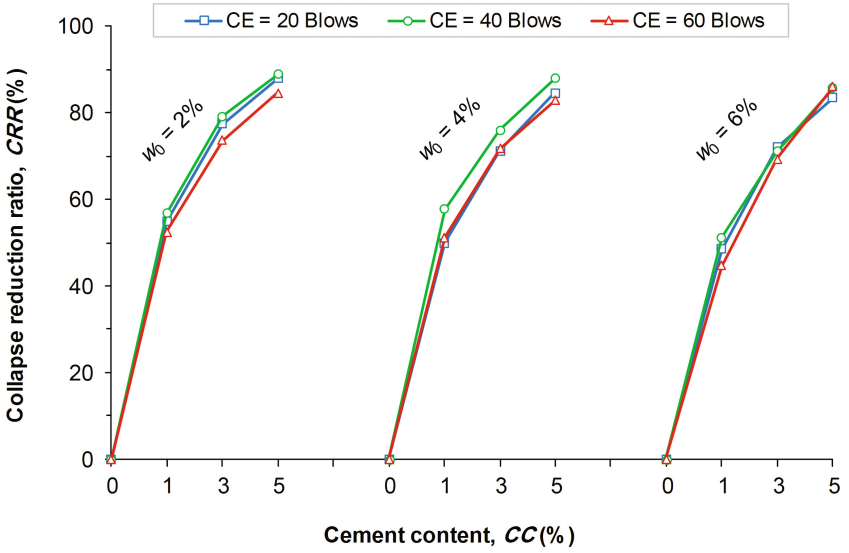

Fig. 10. Collapse reduction ratio vs. *CC*

Figure 10 shows the different values of collapse reduction ratio (*CRR*) vs. the initial water content, for various compacting energies and cement contents.

As it can be seen from Fig. 10, the collapse reduction ratio varies between 45% and 58% for 1% of cement content, from 69% to 79% for 3% of cement content and between 83% and 89% for 5% of cement content. It is noticed that the compacting energy does not have a great influence on collapse reduction ratio. Thus, the *CCR* is constant for such a cement value with the variation of initial water content.

When water is added to the soil-cement mixture, chemical reactions can occur. Cement quickly rigidifies the soil in an irreversible way. The hydrated components of cement connect the grains of the soil between them forming solid bridges, and this results in an increase in the bearing capacity and the mechanical resistance. This increase is due to the reaction between the calcium of the cement and the alumina or silica existed in the soil.

The soil-cement mixture was carefully wetted to a minimum value of water to cement ratio (W/C) of 0.8. Experience has shown that the amount of water after this value is sufficient to produce the hydration reaction.

4 Conclusions

Based on the results obtained from this experimental study, about the collapsing soil phenomenon, the following conclusions can be drawn:

It is possible to prepare a collapsible soil in the laboratory by mixing sand with kaolin, at various proportions, and then compacting them with a certain energy after adding a content of water inferior to the Proctor optimum.

The results obtained by the use of double consolidation method show clearly the influence of certain parameters such as: cement content, initial water content and compacting energy on the collapse potential.

There is a significant influence of the initial water content and the compacting energy on the behavior of collapsible soils. It is approved that collapses could be excessive, when these two parameters are weak.

The results show also that in order to obtain a non-collapsible soil treated by cement and a minimum energy, it is necessary to use 5% of cement and 6% of water. However, reducing the quantity of water to 4% while preserving the same percentage of cement leads to use a high compacting energy. Thus, it is possible to obtain a non-collapsible material by increasing the compacting energy or the quantity of water, which is not the aim of this.

The mechanical properties of a collapsible soil are significantly improved when it is treated with cement. The results show that any treated soil will be considered as non-collapsible soil after a short time treatment operation.

Finally, it is recommended to treat superficial and thin layers of collapsible soils with cement due to economical reasons and reliability.

Acknowledgments. The authors want to express their sincere gratitude to all members of laboratory LNHC Batna and Adwan Chemicals Industries Cie. (Algeria).

References

Abbeche, K., et al.: Influence of relative density and clay fraction on soils collapse. In: Schanz, T. (ed.) Experimental Unsaturated Soil Mechanics. Springer Proceedings in Physics, vol. 112, pp. 3–9. Springer, Heidelberg (2007). doi:10.1007/3-540-69873-6_1

Abbeche, K., et al.: Lime stabilisation of a collapsible soil. In: Proceedings of the 1st International Seminar Innovation and Valorization in Civil Engineering. Hammamet, Tunisia, pp. 161–168 (2009)

Abbeche, K., et al.: Treatment of collapsible soils by salts using the double consolidation method. In: Hoyos, L.R., Zhang, X., Puppala, A.J. (eds.) Experimental and Applied Modeling of Unsaturated Soils. ASCE Geotechnical Special Publication, vol. 202, pp. 69–78 (2010). doi:10.1061/41103(376)10

Abbeche, K., Laouar, M.S.: Ultrasound as a new approach for the prediction of collapsible soils. In: Zhang, L., Wang, Y., Wang, G., Dianqing, L. (eds.) Geotechnical Safety and Risk IV, pp. 529–537. CRC Press, London (2013). doi:10.1201/b16058-81

Alawaji, H.A.: Shear induced collapse settlement of arid soils. Geotech. Geol. Eng. **19**, 1–19 (2001). doi:10.1023/A:1012223622250

ASTM D 2487-06. Standard practice for classification of soils for engineering purposes (Unified Soil Classification System) (2006). doi:10.1520/D2487-06

ASTM D 5333-03. Standard test method for measurement of collapse potential of soils (2003). doi:10.1520/D5333-03

Ayadat, T., Belouahri, B.: Influence du coefficient d'uniformité sur l'amplitude et le taux de l'affaissement des sols. Revue Francaise de Géotechnique 76, pp. 25–34. Presses de l'Ecole Nationale des Ponts et Chaussées, Paris (1996)

Ayadat, T., Hanna, A.: Prediction of collapse behaviour in soil. Revue Européennede Génie Civil **11**(5), 603–619 (2007). doi:10.1080/17747120.2007.9692947

Ayadat, T., Hanna, A.: Effects of hydraulic shear stress and rate of erosion on the magnitude, degree, and rate of collapse. Geomech. Geoeng. Int. J. **3**(1), 59–69 (2008). doi:10.1080/17486020701759644

Ayadat, T., Hanna, A.: Design of foundations built on a shallow depth (less than 4 m) of Egyptian macro-porous collapsible soils. Open J. Geol. **2013**(3), 209–215 (2013). doi:10.4236/ojg.2013.33024

Clemence, S.P., Finbarr, A.O.: Design considerations for collapsible soils. Geotech. Eng. Div. ASCE **107**(GT3), 305–317 (1981). doi:10.1016/0148-9062(81)91226-2

Jennings, J.E., Knight, K.: A guide of construction on or with materials exhibiting additional settlement due to collapse of grain structure. In: Proceedings of the 6th Regional Conference for Africa of Soil Mechanics and Foundation Engineering, pp. 99–105 (1975)

Lahmadi, A., et al.: Prediction of collapsible soils by proctor tests. In: CD-ROM of the 10th International Congress on Advances in Civil Engineering, Ankara, Turkey (2012)

Lawton, E.C., et al.: Collapse of compacted clayey sand. J. Geotech. Eng. **115**(9), 1252–1267 (1989). doi:10.1061/(ASCE)0733-9410(1989)115:9(1252)

Lefebvre, G., Ben Belfadhel, M.: Collapse at permeation for a compacted non-plastic fill. In: Proceedings of the 12th International Conference on Soil Mechanics and Foundation Engineering, Rio de Janeiro, pp. 619–622. Balkema, Rotterdam (1989)

Momeni, W.M., et al.: Evaluation of soil collapse potential in regional scale. Nat. Hazards **64**, 459–479 (2012). doi:10.1007/s11069-012-0252-z

Reginatto, A.R., Ferrero, J.C.: Collapse potential of soils and soil-water chemistry. In: Proceedings of the 8th International Conference on Soil Mechanics and Foundation Engineering, Moscow, vol. 2, pp. 177–183 (1973)

Rogers, C.D.F.: Types and distribution of collapsible soils. In: Derbyshire, E., Dijkstra, T., Smalley, I.J. (eds.) Genesis and properties of collapsible soils, pp. 1–17. Kluwer Academic Publishers/Springer, Netherlands (1995). doi:10.1007/978-94-011-0097-7_1

Prediction of Swelling Pressure of Compacted Bentonite with Respect to Void Ratio Based on Diffuse Double Layer Theory

Haiquan Sun(✉)

Faculty of Science, Charles University, Prague, Czech Republic
haiquan.sun@natur.cuni.cz

Abstract. Compacted bentonite was chosen as the buffer and backfill material in high level nuclear waste disposal due to its high swelling pressure and low permeability. The estimation of swelling pressure is essential in design and construct the nuclear repositories. The swelling pressure model of compacted bentonite has been developed by former researchers based on Gouy-Chapman diffuse double layer theory. It is effective in predicting low swelling pressure (low compaction dry density), while it is invalidated in simulating high swelling pressure (high compaction dry density). Based on the published literature data of MX80 bentonite, the new relationship between nondimensional midplane potential function, u, and nondimensional distance function, Kd, is established. The new relationship is based on the Gouy-chapman theory by considering the variation of void ratio. The proposed equations are applied to compute swelling pressure of other bentonites (FEBEX, Bavaria bentonite, Bentonite S-2, FoCa bentonite and GMZ bentonite) based on the reported experimental data. Results show that the predicted swelling pressure has a good agreement with the experimental swelling pressure.

1 Introduction

Compacted bentonite is often planned as buffer and backfill material used in high level nuclear waste repositories all around the world thanks to its low hydraulic conductivity, high-ion adsorption capacity and high swelling pressure (Bucher and Muller Vonmoos 1989; ENRESA 2000; Schanz and Tripathy 2009). The function of compacted bentonite is that the material can hold the canister tightly when subjected to water, simultaneously limit the access of water to waste container and prevent the migration of radionuclide into the nature. Thus, the estimation of swelling pressure is essential and crucial for safe design of backfill materials and buffer in nuclear repositories. Swelling pressure determined by laboratory tests have been studied by many researchers (Pusch 1982; Dixon and Gray 1985; ENRESA 2000 and Komine 2004). Here the swelling pressure was measured by constant volume of compacted bentonite when adsorbing distill water.

Compacted bentonites are clays with high content of montmorillonite. The interaction of clay-water-electrolyte systems is the main reason for bentonite swelling (Bolt 1956). The double layer repulsive pressure is caused by physical-chemical effects at

L.R. Hoyos and J. McCartney (eds.), *Advances in Characterization and Analysis of Expansive Soils and Rocks*, Sustainable Civil Infrastructures,
DOI 10.1007/978-3-319-61931-6_8

particle scale level and can be determined by the diffuse double layer (DDL) theory. The repulsive pressure contributes to swelling pressure (Verwey and Overbeek 1948). The basic form of DDL was proposed by Gouy-Chapman (Gouy 1910; Chapman 1913). This theory can predict the swelling behavior of bentonites by consideration of variations in clay-water-electrolyte systems. According to DDL theory, the interaction pressure between double layers depends on the potential and ion concentration at mindplane between the two parallel clay platelets and its value equals to the osmotic pressure in that plane (Bolt 1956). However, the hydration energy due to surface and ion hydration are the major contributing factors to swelling pressure at close separation of clay platelets (Verwey and Overbeek 1948; Van Olphen 1963 and Yong 1999). Many researchers have applied the Gouy-Chapman diffuse double layer theory for predicting the swelling pressure of clays and pointed out some difference between theoretical predictions and experimental data. The reasons of the difference summarized by researchers (Bolt 1956; Sridharan and Jayadeva 1982; Mitchell 1993 and Tripathy et al. 2004) as following: (1) ion size and particle size, (2) deviation of soil structure and fabric, (3) existence of electrical attractive forces, (4) hydration energy at close particle distances, (5) anion adsorption, (6) presence of minerals other than montmorillonite in the clay.

2 Theory

The swelling pressure is the difference between the osmotic pressure in the central plane between two clay platelets and the osmotic pressure in the equilibrium solution (Bolt 1956). The osmotic pressure at the central plane between clay platelets can be calculated from Gouy-Chapman diffuse double layer theory which original presented by Bolt (1956) and Van Olphen (1963) and later improved by Sridharan and Jayadeva (1982). The following equations are used to establish the theoretical relationship between swelling pressure and dry density:

$$e = GY_wSd \times 10^6 \tag{1}$$

$$Y_d = \frac{GY_w}{1 + e} \tag{2}$$

$$\int_z^u \frac{1}{\sqrt{(2\text{coshy} - 2\text{coshu})}}dy = \int_0^d dx = -Kd \tag{3}$$

$$-\frac{dy}{d\xi} = \sqrt{(2\text{coshz} - 2\text{coshu})} = \frac{B}{S}\sqrt{\frac{1}{2\varepsilon_0 Dn_0 kT}} \text{ at } x = 0,\ y = z \tag{4}$$

$$p = 2n_0 kT(\text{coshu} - 1) \tag{5}$$

$$K = \left(\frac{2n_0 e'^2 v^2}{\varepsilon_0 DkT}\right)^{\frac{1}{2}} \tag{6}$$

Where e is void ratio of compacted bentonite, G is specific gravity, Y_w is density of water, Y_d is the dry density of bentonite, S is the specific surface area (m^2/g), d is the half of the distance of clay platelets (m), u is the nondimensional midplane potential, y is the nondimensional potential at a distance x from the clay surface, z is the nondimensional potential function at the surface (x = 0), ξ is the distance function ($\xi = Kx$), B is the base cation exchange capacity (meq/100 g), ε_0 is the permittivity of vacuum (8.8542×10^{-23} $C^2J^{-1}m^{-1}$), D is the dielectric constant of bulk fluid (80.4 for water), n_0 is the ionic concentration of the bulk fluid in ions/m^3, k is the Boltzmann's constant (1.38×10^{-23} J/K), K is the diffuse double layer parameter (1/m), T is the absolute temperature in Kelvin, p is the swelling pressure (Pa), e' is the elementary electric charge (1.602×10^{-23} C), v is the weighted averaged of valence of exchangeable cations (Tripathy et al. 2004).

Sridharan and Jayadeva (1982) summarized the u-Kd relationships for different values of $(dy/d\xi)_{x=0}$ shown in Fig. 1. A linear relationship between u and log(Kd) was suggested to compute u value for known Kd. Tripathy et al. (2004) established new relationship between the nondimensional midplane potential function, u and the distance function, Kd for several bentonites, which is based on comparing the experimental results and swelling pressure derived from diffuse double layer theory.

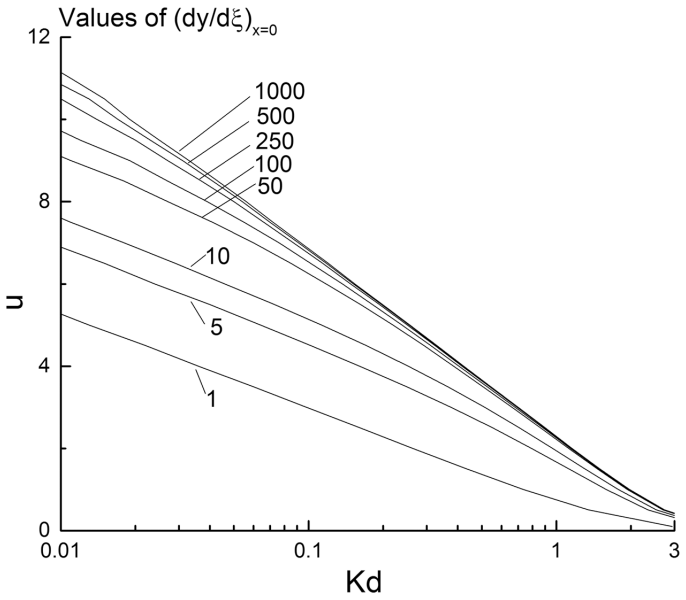

Fig. 1. Theoretical u–Kd relationship (Sridharan and Jayadeva 1982)

The swelling pressure can be predicted by relating the value of u obtained from Eq. (5) and Kd for any given properties of bentonite and by given bulk fluid properties (Sridharan and Jayadeva 1982; Tripathy et al. 2004). For a range of assumed swelling pressure, the value of u can be obtained from Eq. (5) and the value of z can be

calculated from Eq. (4). The value of Kd also can be calculated from Eq. (3) by knowing u and z. The value of K can be determined by Eq. (6), so the value of d can be obtained from Eq. (3). Knowing d, Eq. (1) can be used to calculate e. The dry density can be calculated from Eq. (2). The integration of Eq. (3) is evaluated numerically using the "quad" MATLAB method. Thus the theoretic relationship between swelling pressure and dry density can be obtained.

3 Materials

Various bentonites were studied as buffer materials for nuclear waste disposal all over the world. One of the bentonites, MX80 bentonite, original from Wyoming, USA, have been investigated in the past several years. The montmorillonite content is around 75%, which is the average value among all the compacted bentonite in the publish papers. Another kind of bentonite, Kunigel bentonite, original from Japan, have been planned as backfill materials in Japan high level nuclear waste disposal. The swelling pressure determined by distill water under constant specimen volume are only considered in this paper. Table 1 shows the physical properties and montmorillonite content and Table 2 shows the cation exchange capacity of MX 80 bentonite and Kunigel bentonite. MX80 bentonite have a wide range of swelling pressure compare to Kunigel bentonite, in other words, the swelling pressure of kunigel bentonite is much lower than MX80 bentonite at the same dry density. Part of the reasons is that the montmorillonite content of MX80 bentonite is higher than Kunigel bentonite.

Table 1. Physical properties and Montmorillonite content of MX80 and Kunigel

Bentonite	Montmorillonite content (%)	Specific gravity, G	Specific area, m^2/g	Liquid limit, $w_L(\%)$	Plastic limit, $w_p(\%)$	Reference
MX80	75	2.76	562	411 ± 10	47	Muller-Vonmous and Kahr 1982, 1983
Kunigel	48	2.73	388.8	473.9	26.6	Komine and Ogata 1996

Note: na. is not available

Table 2. Cation exchange capacity of MX80 and Kunigel

Bentonite	Cation exchange capacity (meq/100 g)				Base exchange capacity (meq/100 g)	Valency of cation, v	Reference
	Na	Ca	Mg	K			
MX80	62	7.4	3	0.2	73	1.14	Muller-Vonmous and Kahr 1982
Kunigel	na	na	na	na	76	2	Komine and Ogata 1996

Note: na. is not available

4 Swelling Pressure Calculated from DDL Theory

To calculate the swelling pressure, the u-log(Kd) relationship must be established as mentioned before. According to Sridharan and Jayadeva (1982) and Tripathy et al. (2004), the distilled water has a molal concentration of approximately 10^{-4} M, so the concentration n_0 is assumed to 10^{-4} M in this paper. The following procedures were suggested to established the u-Kd relationship of MX80 bentonite and Kunigel Bentonite: (i) assumed the pressure range which is from 50 to 40 000 kPa increased by step, u values can be obtained by Eq. (5); (ii) the value of z can be calculated from Eq. (4) by given the value of B, S; (iii) The value of Kd also can be calculated from Eq. (3) by given the value of u and z. The calculated u and Kd values are shown in Table 3.

Table 3. Values of u, z, $(dy/d\xi)_{x=0}$ and Kd for MX80 bentonite and Kunigel bentonite

Pressure/KPa	u	MX80 bentonite			Kunigel bentonite		
		z	$(dy/d\xi)_{x=0}$	Kd	z	$(dy/d\xi)_{x=0}$	Kd
$n_0 = 10^{-4}$ M							
50	5.32	10.710	211.17	0.211	11.525	311.79	0.214
100	6.01	10.714	211.17	0.146	11.527	311.79	0.150
200	6.70	10.723	211.17	0.101	11.531	311.79	0.104
400	7.39	10.741	211.17	0.069	11.539	311.79	0.072
800	8.08	10.775	211.17	0.046	11.554	311.79	0.049
1000	8.30	10.792	211.17	0.040	11.562	311.79	0.043
2000	9.00	10.872	211.17	0.026	11.600	311.79	0.029
4000	9.69	11.015	211.17	0.016	11.671	311.79	0.019
8000	10.38	11.250	211.17	0.010	11.800	311.79	0.012
10000	10.61	11.350	211.17	0.008	11.859	311.79	0.010
20000	11.30	11.739	211.17	0.005	12.111	311.79	0.006
40000	11.99	12.236	211.17	0.002	12.478	311.79	0.003

From Table 3, the value of $(dy/d\xi)_{x=0}$ is 211.17 and 311.79 for MX80 and Kunigel respectively. According to Sridharan and Jayadeva (1982), it was noted that u plotted against log(Kd) is linear for larger values of $(dy/d\xi)_{x=0}$ and for u > 1.0. The u-log(Kd) relationship are shown in Fig. 2. From Fig. 2, the linear relationship of u and Kd can be observed. Thus, the swelling pressure of theoretic DDL prediction of MX80 and Kunigel bentonite are presented by Eqs. (7) and (8) respectively:

$$p = 2n_0kT[\cosh(-3.462\log(Kd) + 3.292) - 1] \tag{7}$$

$$p = 2n_0kT[\cosh(-3.737\log(Kd) + 3.063) - 1] \tag{8}$$

Figures 3 and 4 show the theoretical DDL prediction and experimental swelling pressure of MX80 and Kunigel bentonite respectively. It shows a good agreement

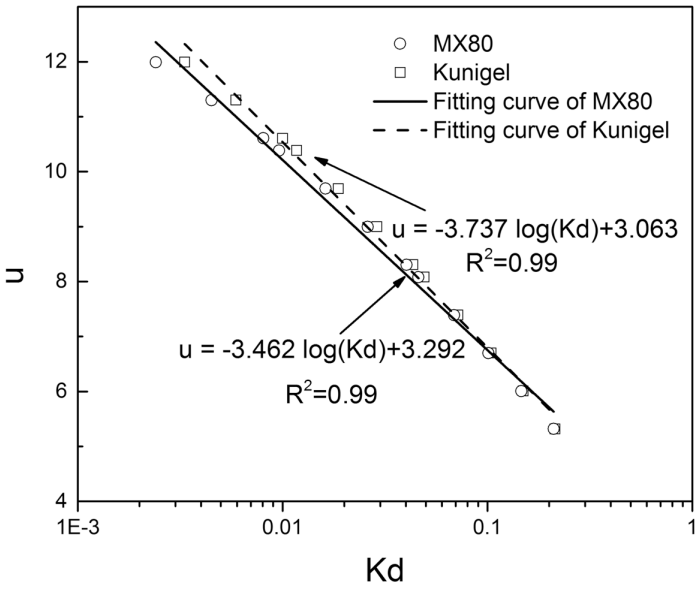

Fig. 2. Theoretic u-Kd relationships of MX80 and Kunigel bentonite

between the theoretical and experimental data for MX80 bentonite at low dry density (<1.6 g/cm^3). The swelling pressure predicted by theoretical DDL is much lower than the experimental results at high dry density. However, the swelling pressure determined by theoretical DDL is well consistent with the experimental data for Kunigel bentonite.

It is known that swelling of bentonite (montmorillonite) has two mechanisms. One is the crystalline swelling and the other is the diffuse double layer swelling (Van Olphen 1963). Swelling of montmorillonite takes place in two distinct ways. At closed clay platelet distance (<2.2 nm), the expansion was primary dependent on the exchangeable cation and the hydration energy of the cation. Upon further ingress of water, when the clay platelet distance is greater than 3.5 nm, the hydrated cations will move into the solution to form the electrical diffuse double layer. The montmorillonite was thought to develop the rest of the micelle fluid and the swelling was essentially osmotic (Norrish 1954). At lower dry density, a possible dissociation of ions from the clay particle surface contributed to the diffuse double layer repulsion. While at higher dry density, the adsorptive forces due to surface and ion hydration dominated the swelling pressure. The hydration energy due to surface and ion hydration are the major contributing factors to swelling pressure at close separation of clay platelets (Verwey and Overbeek 1948; Van Olphen 1963 and Yong 1999). The swelling pressure can be regard as equivalent to the double layer repulsive pressure only when double layer repulsion is the dominated force. It is clearly to see that there are some limited conditions when using the DDL theory. The effects of ion and surface hydration energy may be influence the swelling pressure of compacted bentonite at very close separation distance. However, the DDL theory doesn't consider this influence.

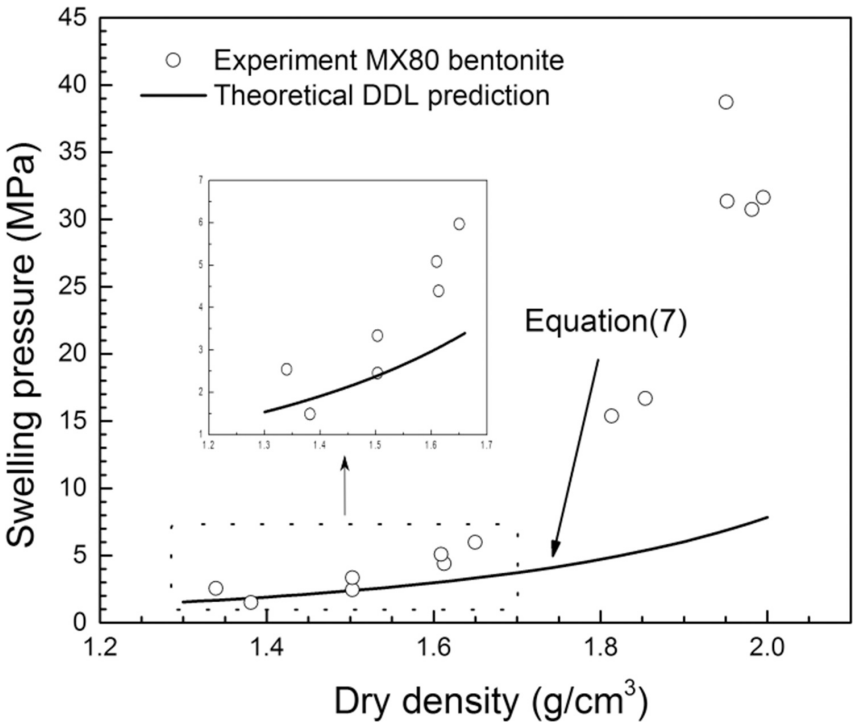

Fig. 3. Theoretical DDL prediction and experimental swelling pressure of MX80 bentonite

It can be seen that several factors may significantly influence the swelling pressure of compacted bentonite other than the one predicted by diffuse double layer theory. There are different kinds of cations existing in compacted bentonite, which has different hydration radius and hydration energy, and they can contribute to swelling pressure. For higher dry density, the distance between clay platelets is much closer, even their respective force fields overlap and have a great influence on the behavior of the system. Therefore, it needs developed of the basic DDL theory used for predicting the swelling pressure.

5 Suggested New Relationship Between u-log(Kd)

The effects of ion and surface hydration energy can deeply influence the swelling pressure of compacted bentonite at very close separation distance as previous analysis. The swelling pressure is predicted by Eq. (5). The parameter $n_{0,}$ k and T in Eq. (5) is assumed to be constant in this paper, the theoretical swelling pressure only depends on the non-dimensional mid-plane potential u. It can be concluded that the value of u is the reason for the difference between theoretical DDL prediction and experimental data. It is necessary to find the difference of theoretical and experimental u. From experimental results, the u values can be calculated by knowing the swelling pressure by Eq. (5).

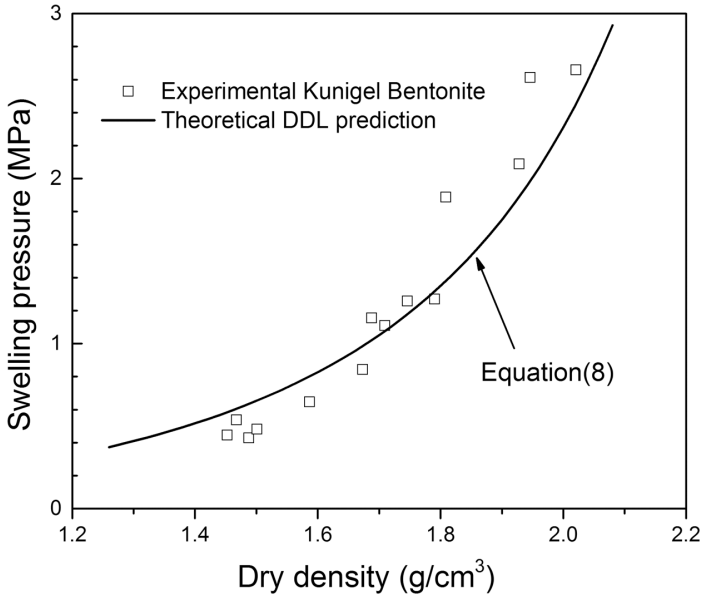

Fig. 4. Theoretical DDL prediction and experimental swelling pressure of bentonite

K values can be obtained by Eq. (6). The values of d can be calculated by Eq. (1), thus Kd values can be calculated. The void ratio corresponding to each dry density also can be calculated by Eq. (1). Figure 5 shows the actual experimental relationship of u and log(Kd). It can be seen from Figs. 2 and 5 that the slope of fitting curve of experimental results is lower than that of theoretical DDL equation. This confirm the previous discussion.

The type of bentonite and the amount of exchange cations can affect the swelling pressure. Considering the big difference of preserve cations in different bentonite and the difference between theoretical and measured swelling pressure (Fig. 8), an attempt was made to revise the relationship between u and log(Kd). Generally speaking, the content of montmorillonite is an obvious indicator of swelling pressure. Because the MX80 bentonite has an average content of montmorillonite among all the bentonites, so it will be used for the basic analysis. It can be seen that the difference between the DDL predicted and experimental swelling pressure has an exponential increase relationship with the dry density for all bentonites. From the expression of Eq. (5), an idea came out that the difference of experimental and theoretical non-dimensional mid-plane potential, Δu, should follow the same trend with dry density. The growth form of hyperbolic function coshu and exponential function follows the same style. Based on this, it is assumed that the Δu has an exponential increased with dry density. Considering the relationship between dry density and void ratio, the Δu shows a natural logarithm decreased with increased of void ratio. Here we choose the void ratio instead of dry density considering the non-dimension of void ratio. Based on the experimental information of MX80 bentonite, the relationship between Δu and e of MX80 bentonite was established.

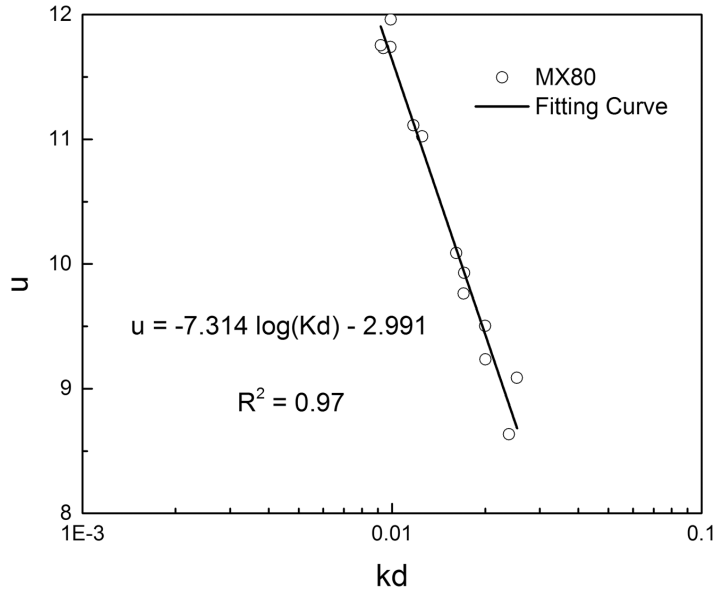

Fig. 5. Experimental u-kd relationship of MX80 bentonite

Once the experimental u and log(Kd) relationship was obtained, the difference in u values, Δu, can be calculated using experimental u values minus theoretical DDL prediction u values. The Δu versus void ratio (e) presented in Fig. 6. The values of Δu

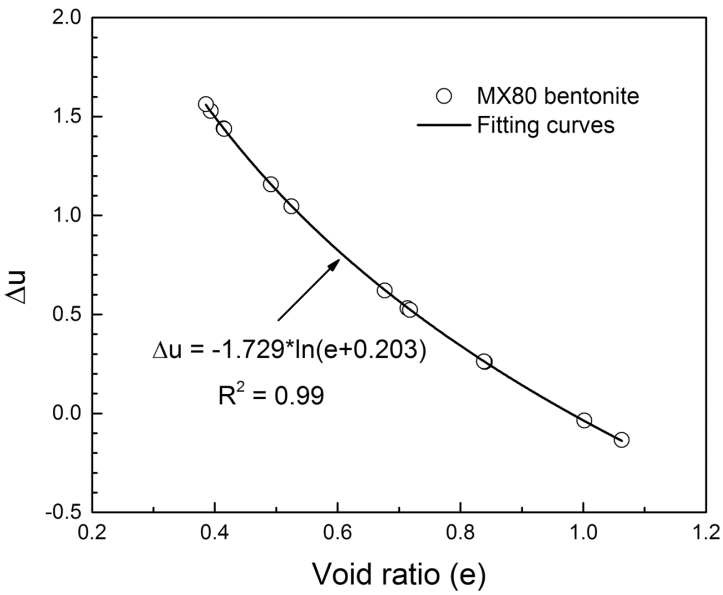

Fig. 6. Relationship between Δu and void ratio of MX80 bentonite

decrease with the increased of void ratio. The natural logarithm relationship between Δu and e can be obtained. The modified nondimension midplane potential can be got by added Δu to theoretical u. And the swelling pressure can be computed by Eq. (9). Figure 7 shows swelling pressure vs. dry density of MX80 bentonite by the experimental, theory and proposed equation. As expected, the proposed equation has a good agreement with the experimental data.

$$p = 2n_0kT[\cosh(u_{theory} + \Delta u) - 1] \tag{9}$$

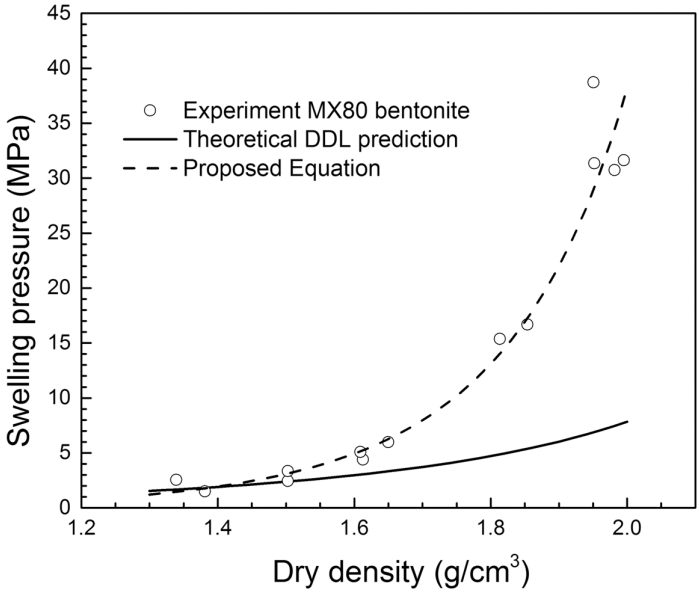

Fig. 7. Theoretical DDL prediction, experimental and proposed equation for swelling pressure of MX80 bentonite

6 Verification of Proposed Equations for Swelling Pressure

The modified swelling pressure Eq. (9) is derived based on experimental MX80 bentonite data and double layer theory. And later this equation will be applied in other nuclear waste barrier materials. Experimental swelling pressure data of FEBEX bentonite (ENRESA 2000) from Spain, Kunigel V1 (Japan Nuclear Cycle Development Institute 1999) from Janpan, bentonite S-2 (ENRESA 2000) from Spain, Bavaria Bentonite (Schanz and Tripathy 2009) from Germany, FoCa bentonite (Imbert and Villar 2006) from France, GMZ bentonite (Schanz and Al-Badran 2014) from Gaomiaozi County (Inner Mongolia, China) were selected for the verification of this new modified swelling-pressure equations. The u-kd relationship can be obtained by assumed the known pressure as mentioned before. For all the bentonites, the theoretical u and log(Kd) relationship are shown in Eqs. (10)–(14).

$$u = -3.265\log(Kd) + 3.496\,(\text{FEBEX}) \tag{10}$$

$$u = -3.555\log(Kd) + 3.217\,(\text{bentonite S - 2}) \tag{11}$$

$$u = -3.373\log(Kd) + 3.360\,(\text{Bavaria bentonite}) \tag{12}$$

$$u = -3.958\log(Kd) + 2.868\,(\text{FoCa}) \tag{13}$$

$$u = -3.501\log(Kd) + 3.260\,(\text{GMZ}) \tag{14}$$

Tables 4 and 5 show the physical properties and cation exchange capacity of all the compacted bentonite. The montmorillonite content varies from 48% to 96%, the FoCa bentonite contents 50% beidellite and 50% kaolinite. The specific gravities are around 2.75. The plastic limit varies from 21 to 56 and 105 to 276 of liquid limit. The base exchange capacity varies from 73 to 102 meq/100 g.

Table 4. Physical properties and Montmorillonite content of compacted bentonite

Bentonite	Montmorillonite content (%)	Specific gravity G	Specific area m^2/g	Liquid limit, $w_L(\%)$	Plastic limit, $w_p(\%)$	Reference
FEBEX	92 ± 3	2.7	425 ± 47	102 ± 4	53 ± 3	ENRESA 2000, Lajudie et al. 1996
Bentonite s-2	92 ± 4	2.78	614 ± 74	105 ± 10	na	ENRESA 2000
Bavaria bentonite	na	2.8	650	178	56.1	Schanz et al. 2009
FoCa	50% beidellite + 50% kaolinite	2.67	300	112	50	Marcial et al. 2002, Imbert and Villar 2006
GMZ	75.4	2.71	570	276	38	Wen 2006

Note: na. is not available

Table 5. Cation exchange capacity of compacted bentonite

Bentonite	Cation exchange capacity (meq/100 g)				Base exchange capacity (meq/100 g)	Valence of cation v	Reference
	Na	Ca	Mg	K			
FEBEX	25	42	32	3	102	1.73	ENRESA (2000)
Bentonite s-2	na	na	na	na	97	1.66	ENRESA (2000)
Bavaria bentonite	9	33	32	na	74	1.88	Schanz et al. 2009
FoCa	3.6	73.1	6.5	0.8	84	1.94	Van Geet et al. 2009
GMZ	43	29.1	12.3	2.5	78.3	1.47	Wen 2006

Note: na. is not available

The swelling pressure, reported by experimental tests, calculated by theoretical DDL prediction and recalculated by proposed equations, versus dry density relationship are plotted in Fig. 8. It can be seen that the proposed equation can predict the swelling pressure more accuracy than the DDL prediction. In order to discuss the accuracy of the developed model, the root mean square error (RMSE) will be used for the evaluation of the developed model.

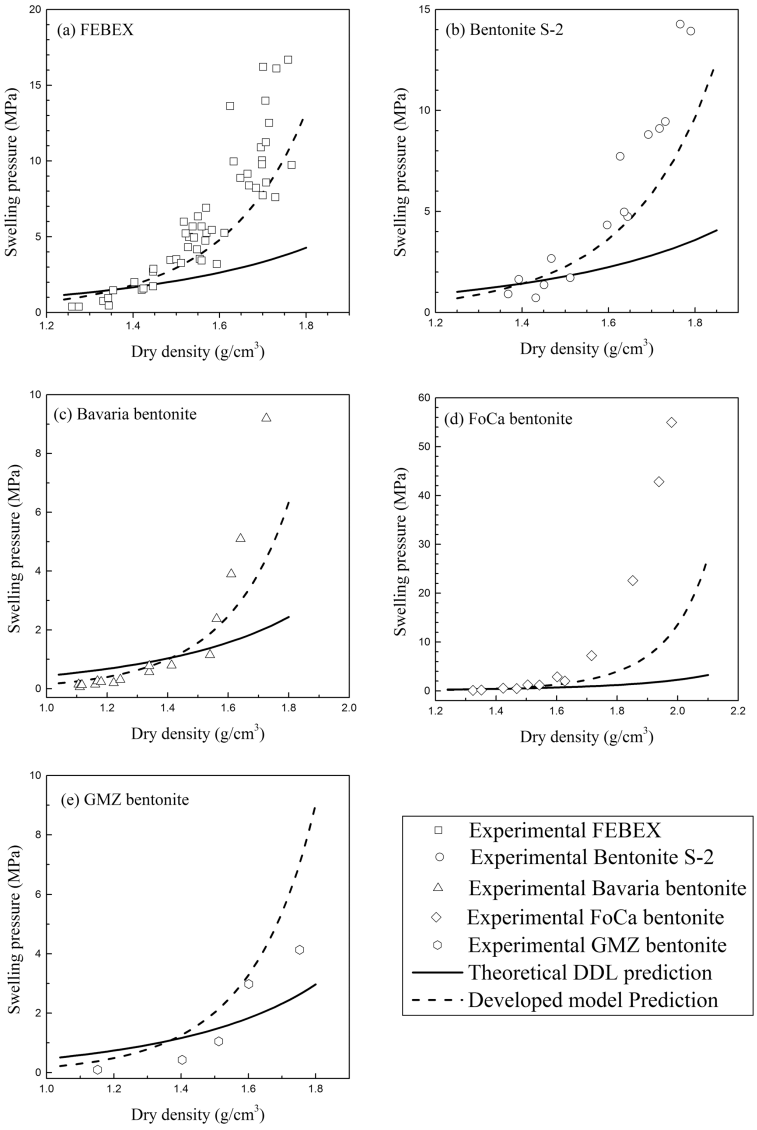

Fig. 8. Theoretical DDL prediction, experimental and proposed equation for swelling pressure of (a) FEBEX bentonite, (b) Bentonite S-2, (c) Bavaria bentonite, (d) FoCa bentonite, (e) GMZ bentonite

The root mean square error (RMSE) is a frequently used measure of the difference between values predicted by a model and the values actually observed from the environment that is being modelled. The RMSE can be calculated from the observation values and predicted values based on the observation times. The calculation of RMSE shows in Eq. (15).

$$\mathrm{RMSE} = \sqrt{\frac{\sum_{i=0}^{n}\left(x_{obs,i} - x_{model,i}\right)^2}{n}} \tag{15}$$

where $x_{obs,i}$ and $x_{mod,i}$ is the observation value and the model predicted value at i stage, respectively.

It can be seen that RMSE equals to zero when the observation value equals to model predicted value. This means that the model work quite well. The lower the RMSE value, the better the model can predict. The swelling pressure predicted by the proposed equations are compared with their experimental data. The RMSE values of each compacted bentonite are shown in Fig. 9. It is clearly that RMSE value of MX 80 is the minimum which is lower than 1. The RMSE value of FoCa bentonite is the maximum which is more than 16. The RMSE value of GMZ and Bavaria bentonite is around 2, while for FEBEX and Bentonite S-2 is around 3.

The swelling pressure data of the experimental and predicted value of all the bentonites were drawn in abscissa and ordinate respectively as shown in Fig. 10. The nearer the points closed to the 1:1 line (dash line in Fig. 10), the more accuracy the model predicted. It can be seen that the proposed equation has defects to predict the swelling pressure (<1 MPa) of FEBEX. This also can be confirmed by the RMSE value of FEBEX. It also can be observed that the FoCa data is far from the dash line, which

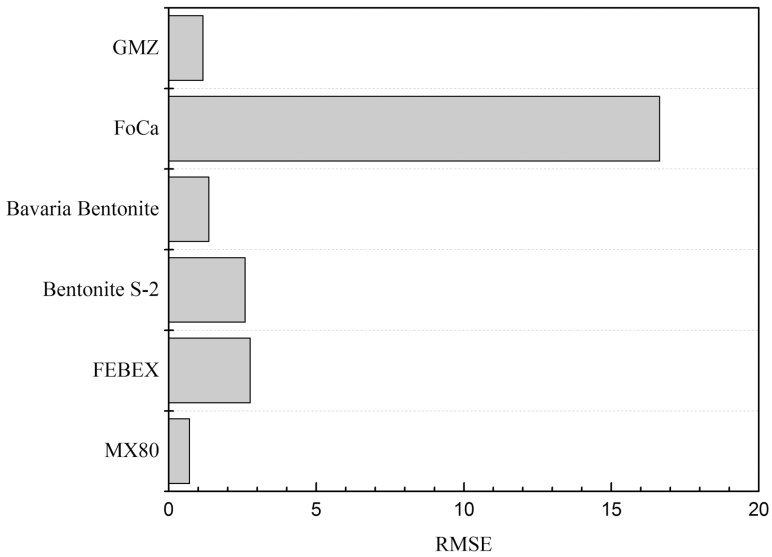

Fig. 9. RMSE values of all compacted bentonites

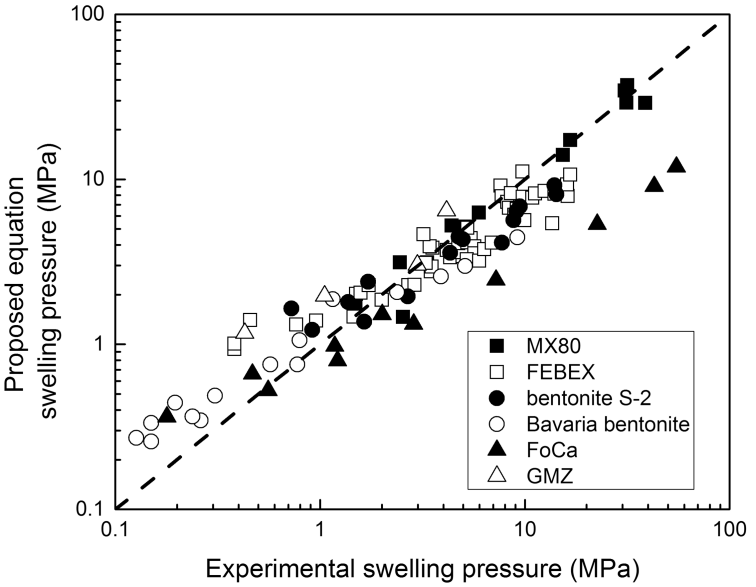

Fig. 10. Proposed equation versus experimental swelling pressure

means the proposed model can't predict the FoCa bentonite well. This can be confirmed by the highest RMSE value of FoCa bentonite. This disagreement is attributed to the 50% beidellite and 50% kaolinite which consists of significant amount of divalent exchangeable cations Ca^{2+} that produced greater hydration energy at close clay platelet distance. For other bentonites, the developed model can predict well.

7 Conclusions

The swelling pressure of MX80 bentonite determined from the Gouy-Chapman diffuse double layer theory was compared with the experimental data. Results show that the swelling pressure of theoretical DDL prediction is consistent with experimental swelling pressure at low dry density, while the theoretical value is much lower than that of experimental swelling pressure at high dry density. Based on the MX80 bentonite, a modified new relationship between nonodimension midplane potential, u, and distance function, Kd, were derived. And the proposed swelling pressure equation was established. The proposed equation was verified with five other bentonites that have been selected as barrier material in high level nuclear waste disposal from different countries. The swelling pressures calculated by proposed equation indicated a good agreement with the experimental swelling pressures. The proposed equation is valid in predicting of swelling pressure of compacted bentonite.

Acknowledgments. The financial support by the research grant No. 846216 of Charles University Grant Agency is greatly appreciated. The author is grateful to Dr. S. Tripathy for discussion.

References

Bolt, G.H.: Physico-chemical analysis of the compressibility of pure clays. Géotechnique **6**(2), 86–93 (1956). doi:10.1680/geot.1956.6.2.86

Bucher, F., Müller-Vonmoos, M.: Bentonite as a containment barrier for the disposal of highly radioactive waste. Appl. Clay Sci. **4**(2), 157–177 (1989). doi:10.1016/0169-1317(89)90006-9

Chapman, D.L.: A contribution to the theory of electro-capillarity. Philos. Mag. **25**, 475–481 (1913). doi:10.1080/14786440408634187

Dixon, D.A., Gray, M.N.: The engineering properties of buffer material. Technical report TR-350, Fuel Waste Technology Branch, Whiteshell Laboratories, Pinawa, Man (1985)

ENRESA. FEBEX project — full scale engineered barriers experiments for a deep geological respiratory for high level radioactive waste in crystalline host rock. Final report, Publicación téechnica 1/2000, Empresa Nacional de Residuos Radiactivos SA (ENRESA), Madrid, Spain (2000)

Gouy, G.: Electric charge on the surface of an electrolyte. J. Phys. **4**(9), 457 (1910)

Imbert, C., Villar, M.V.: Hydro-mechanical response of a bentonite pellets/powder mixture upon infiltration. Appl. Clay Sci. **32**, 197–209 (2006). doi:10.1016/j.clay.2006.01.005

Komine, H., Ogata, N.: Prediction for swelling characteristics of compacted bentonite. Can. Geotech. J. **33**, 11–22 (1996). doi:10.1139/t96-021

Komine, H.: Simplified evaluation for swelling characteristics of bentonites, 507. Eng. Geol. **71** (3–4), 265–279 (2004). doi:10.1016/S0013-7952(03)00140-6

Japan Nuclear Cycle Development Institute. H12: project to establish the scientific and technical basis for HLW disposal in Japan: supporting report 2 (respiratory design and engineering Technology). Japan Nuclear Cycle Development Institute, Tokyo (1999)

Lajudie, A., Raynal, J., Petit, J.-C., Toulhoat, P.: Clay-based materials for engineered barriers: a review. Mater. Res. Soc. Symp. Proc. **353**, 221–229 (1996). doi:10.1557/PROC-353-221

Marcial, D., Delage, P., Cui, Y.J.: On the high stress compression of bentonites. Can. Geotech. J. **39**, 812–820 (2002). doi:10.1139/t02-019

Mitchell, J.K.: Fundamentals of Soil Behaviour, 2nd edn. Wiley, New York (1993)

Müller-Vonmoos, M., Kahr, G.: Bereitstellung von Bentonit für Laboruntersuchungen. Nagra Technischer Bericht 82-04. Nagra, Wettingen, Switzerland (1982)

Müller-Vonmoos, M., Kahr, G.: Mineralogische Untersuchungen von Wyoming Bentonit MX-80 und Montigel. Nagra Technischer Bericht 83-12 (1983)

Norrish, K.: The swelling of montmorillonite. Discuss. Faraday Soc. **18**, 120–134 (1954). doi:10.1039/DF9541800120

Pusch, R.: Mineral–water interactions and their influence on the physical behaviour of highly compacted Na bentonite. Can. Geotechn. J. **19**, 381–387 (1982). doi:10.1139/t82-041

Schanz, T., Al-Badran, Y.: Swelling pressure characteristics of compacted Chinese Gaomiaozi bentonite GMZ01. Soils Found. **54**(4), 748–759 (2014). doi:10.1016/j.sandf.2014.06.026

Schanz, T., Tripathy, S.: Swelling pressure of a divalent-rich bentonite: diffuse double-layer theory revisited. Water Resources Res. **45**(2), W00C12 (2009). doi:10.1029/2007WR006495

Sridharan, A., Jayadeva, M.S.: Double layer theory and compressibility of clays. Géotechnique **32**(2), 133–144 (1982). doi:10.1680/geot.1982.32.2.133

Tripathy, S., Sridharan, A., Schanz, T.: Swelling pressures of compacted bentonites from diffuse double layer theory. Can. Geotech. J. **41**, 437–450 (2004). doi:10.1139/t03-096

Van Olphen, H.: An Introduction to Clay Colloid Chemistry: for Clay Technologists, Geologists and Soil Scientists. Interscience, New York (1963). doi:10.1126/science.143.3610.1023-a

Van Geet, M., Bastiaens, W., Volckaert, G., Weetjens, E., Sillen, X., Maes, N., Imbert, C., Billaud, P., Touzé, G., Filippi, M., Plas, F., Villar, M.V., García-Gutiérrez, M., Mingarro, M., Gens, A., Vallejan, B.: A large-scale in situ demonstration test for repository sealing in an argillaceous host rock – Phase II, Technical report NO. EUR 24161 EN, European Commission, Contract No. FIKW-CT-2000-00010 (2009)

Verwey, E.J.W., Overbeek, J.: Theory of the stability of lyophobic colloids. Elsevier, Amsterdam (1948). doi:10.1021/j150453a001

Wen, Z.J.: Physical property of China's buffer material for high-level radioactive waste Repositories. Chinese J. Rock Mech. Eng. **25**(4), 794–800 (2006)

Yong, R.N.: Soil suction and soil-water potentials in swelling clays in engineered barriers. Eng. Geol. **54**, 3–13 (1999). doi:10.1080/14786440408634187. Amsterdam

Penetration Characteristics of Expansive Soil: A Probabilistic Study

K.V.N.S. Raviteja[1(✉)], K. Ramu[2], and R.D. Babu[3]

[1] Indian Institute of Technology Hyderabad, Hyderabad, India
kvnsravi.teja@gmail.com
[2] University College of Engineering, JNTUK Kakinada, Kakinada, India
kramujntu@gmail.com
[3] Department of Civil Engineering, KITS Divili, Divili, India
baburdll08@hotmail.com

Abstract. The requisite for a careful design of pavement subgrades and subbases has been stressed by the failures caused by fallacy in understanding the variability and uncertainty associated with material properties (Jung et al. 2012). This study emphasizes the improvement of California bearing ratio (CBR) found in the expansive soil after treating with lime and fly ash through probabilistic evaluation. The variability associated with the CBR values is studied for twenty soil specimens stabilized with lime and fly ash at varying proportions. A comprehensive analysis has been carried out in a probabilistic framework for a complete understanding of the variability range. The aftermath of the investigation can be suitably beneficial for a reliable and reasonably economical design of pavement subgrades.

1 Introduction

The performance of pavement subgrades mostly depends on strength of the subgrade soil that is been used. Pavements on expansive soils often subjected to distress, waviness and proved unsuccessful in meeting the service limits. Stabilization of these expansive soils using lime and fly ash is substantiated to be one of the economical and reliable ground improvement technique. Specifically, the California bearing ratio (CBR) of expansive soils can be significantly improved by treating them with lime and fly ash. The CBR is a critical parameter in assessing the mechanical strength of the natural ground, pavement subgrades, and base courses. The test was initially developed by California state highway department and later adopted by US army corps and ASTM 2000. It typically measures the resistance offered by the soil against the penetration of the standard CBR plunger. However, the CBR experimentation is influenced by a number of variabilities viz. moisture content, compaction effort, grain size, the density of the soil and etc. These variables are vulnerable spatially and temporally. Therefore, a single or some multiple CBR tests cannot reflect the penetration characteristics of the entire soil strata in the case of large-scale projects. Pavement subgrades that are designed by snubbing the variabilities often vulnerable to failures.

The existing deterministic methodologies are based on unique pavement system for the set of unique input variables. These methods don't account for the variability

L.R. Hoyos and J. McCartney (eds.), *Advances in Characterization and Analysis of Expansive Soils and Rocks*, Sustainable Civil Infrastructures,
DOI 10.1007/978-3-319-61931-6_9

associated with the material properties and end up resulting an untrue quantitative estimate of overall design reliability. A probabilistic design method is, therefore, necessary in order to consider the material variability within a reliability framework. (Witczak et al. 1983). A methodology for considering the material variability in flexible pavement design in the probabilistic framework was developed (Chou 1986). Further, the complex Taylor series expansion was simplified using an advanced Rosenbluth method and design has been extended using elastic layer method (Chou 1987). It is experimentally proved that the density of the soil is need not to be proportional to its actual strength (Al-Amoudi et al. 1995).

The sensitivity analysis of CBR values has shown considerable variability which has an intense effect on the pavement reliability (Bourdeau 1990). The analysis indicated that coefficient of variation (COV) of CBR values ranging from 20–40% are the major source of uncertainty in the assessment of subgrade bearing capacity (Bourdeau 1990). However, it can be noted that the COV is not constant always and therefore the standard deviation gives the better representation of variability. The pavement performance incorporating the analyzed material variability is considered in the designer's selection of CBR value (Chou 1989). An extension to the empirical equation of AASHO road tests for the design of flexible pavements has been developed (Bourdeau 1990). Further, a generalized CBR equation was developed in probabilistic approach to account the parameter variability and uncertainty for accurate prediction of future conditions (Divinsky 1996). It is suggested that the variability associated with CBR values can be appropriately represented by beta distribution (Freeman and Grogan 1997). This consideration is due the mean value of the CBR may near to zero for virgin/untreated soils. However, this consideration is need not to be applicable in the current study as it deals with the variability of improved CBR values of treated soil-matrix. The developed probabilistic approach is applied successfully in the field conditions for flexible pavements (Divinsky 1998). Finally, the CBR data is statistically analyzed and the best regression model was developed based on the results (Al-Amoudi et al. 2002). Convinced from the above reasons, an attempt has been made to address the variability associated with the penetration characteristics of treated expansive soil through probabilistic evaluation of experimental data.

2 Objective

CBR experimentation is a much tedious and time-consuming task and it cannot be easily installed in field conditions (Habib-ur-Rehman 1995). It is obvious that the number of experimental tests that one can perform in the laboratory are limited. It is a hectic task to perform hundreds of tests to derive accurate results and it is not possible in all the cases. In general, most of the laboratory experiments are carried out at certain predetermined mix proportions. The behavior of the soil-matrix will be analyzed on the basis these experiments for rest of the proportions by correlating them linearly or non-linearly. However, the results derived from these correlations cannot reflect the exact behavior of the soil-matrix. Moreover, the correlations cannot predict the extent of variability that can be associated with the properties of soil-matrix. This espousal is merely based on a reasonable approximation or generalized assumption.

Instead, a probabilistic analysis can serve better in assessing the exact mean value and the extent of variability associated with the material property. Therefore, the current study is focused on the probabilistic analysis of the experimentally determined CBR values to evaluate the concomitant variability.

3 Methodology

3.1 Experimentation

CBR tests have been conducted on the untreated and treated soil specimens compacted at optimum moisture content and maximum dry density conditions as per IS: 2720 (Part XVI)-1987. Experiments were conducted on untreated and soil treated with different proportions of lime and fly ash. Fly ash is used as an admixture which replaces the equal amount of soil from the mix. Whereas, lime is used as an additive and its percent is constant for one complete cycle. The specimens are prepared for mix proportions in which fly ash if varying from 0–40% and lime is varying 3–9%. These specimens are compacted at optimum moisture and maximum dry density to study the resistance offered against penetration of CBR plunger. A twenty samples with different soil-lime-fly ash proportions have been tested in the laboratory to assess their CBR characteristics. The geotechnical properties of untreated soil are summarized in Table 1. The variable mix proportions that are experimented are presented in Table 2.

Table 1. Geotechnical properties of untreated soil

S.No.	Property	Value
1.	Specific gravity	2.66
2.	Liquid limit	85.4%
3.	Plastic limit	33.1%
4.	Plasticity index	52.3%
5.	Shrinkage limit	11.2%
6.	Sand	5%
7.	Silt and Clay	95%
8.	Differential free swell	140%
9.	IS classification	CH
10.	Optimum moisture content	31%
11.	Max. dry density	1.48 g/cc
12.	Unsoaked CBR	2.01%
13.	Soaked CBR	0.74%
14.	Cohesion	54 kPa
15.	Angle of friction	0 degrees

3.2 Probabilistic Analysis

The results of the experimental studies are compiled and evaluated statistically. Table 2 provides the soaked and unsoaked CBR values at different mix proportions.

Table 2. Experimental observations of soaked and unsoaked CBR

Mix proportion (Soil + Fly ash + Lime)	Soaked CBR (%)	Unsoaked CBR (%)
100 + 0 + 0	0.74	2.01
90 + 10 + 0	2.69	3.36
80 + 20 + 0	4.48	5.15
70 + 30 + 0	4.71	5.40
60 + 40 + 0	4.93	5.61
100 + 0 + 3	1.34	2.47
90 + 10 + 3	3.62	4.01
80 + 20 + 3	5.6	5.82
70 + 30 + 3	5.84	6.08
60 + 40 + 3	5.87	6.23
100 + 0 + 6	2.20	3.10
90 + 10 + 6	4.69	4.95
80 + 20 + 6	6.70	6.93
70 + 30 + 6	7.17	7.41
60 + 40 + 6	7.39	7.66
100 + 0 + 9	3.15	3.85
90 + 10 + 9	5.85	6.02
80 + 20 + 9	7.39	8.07
70 + 30 + 9	7.65	8.29
60 + 40 + 9	7.84	8.50

Random variables have been generated within the lower and upper bounds of CBR values for fly ash percentage varying from 1–40 with an increment of 1%. The percentage of soil in the mix is programmed to decrease at corresponding equal proportions with an increase in fly ash content. As lime being used as an additive, the percentage would be constant for on complete cycle.

Histograms are plotted to understand the variation of the parameter with reference to mean value. A histogram plots the number of measurements falling within specific intervals of value as a vertical bar. The histogram divides the entire data into fixed intervals known as bins. The size of the bin can be chosen arbitrarily, but they should be of uniform width and have convenient end points. In general, geotechnical properties exhibit histograms with unimodal distributions, but rarely shows multimodal quoting heterogeneity in the data. In this study, bin size is chosen in such a way to curtail the multimodality of the distributions. Histograms plotted for four different cycles by centered on the appropriate bin size. The frequency density is calculated from the bin count as given in Eq. (1).

$$\text{frequency density} = \frac{\text{bin count}}{\text{total number of data points}} \tag{1}$$

For predictive purposes, it is desirable to understand the shape of the underlying distribution of the interface friction angle. To determine this underlying distribution, it

is common to fit the observed distribution to a theoretical distribution by comparing the frequencies observed in the data to the expected frequencies of the theoretical distribution. The distribution of probability mass over a finite sample space is known as probability Density Function (PDF). PDF fitting of interface friction angle is the fitting of a probability distribution to a series of observed data concerning the repeated measurements of a friction angle. The aim of distribution fitting is to predict the probability or to forecast the frequency of occurrence of the magnitude of the phenomenon in a certain interval. There are many types of PDFs among which some can be fitted more closely to the observed frequency of the data than others, depending on the characteristics of the phenomenon and of the distribution. The PDF giving a close fit is supposed to lead to better predictions. In distribution fitting, therefore, one needs to select a distribution that suits the data well.

In the present study, normal PDF is fitted for all the four sets of cycles at the optimized mean and standard deviation values that are found to be best suitable through a trial and error procedure. The form of PDF distribution has been carefully chosen depending on the skewness of the observed data. Further, the goodness of the distribution at the fitted optimized mean and standard deviation are successfully verified through normality tests. Though the data can be suitably fitted with another type of PDFs like uniform distribution, this is focused on delivering a practical output, which can have gainful usability in the reliability-based analysis. The mean and standard deviation (σ) are computed with the help of trial and error method in such a way that the skewness of the observed values of CBR matches with the PDF, which is a close fit. Then, the coefficient of variation (COV) associated with CBR has been calculated from the equation as given below:

$$COV = \frac{\sigma_{CBR}}{\mu_{CBR}} \tag{2}$$

It is obvious to note that certain types of variables follow specific distributions. Variables whose values are determined by an infinite number of independent random events can be distributed following the normal distribution as shown below:

$$f(CBR) = \frac{1}{\sigma_{CBR}\sqrt{2\pi}} \exp\left\{ -\frac{1}{2}\left(\frac{CBR - \mu_{CBR}}{\sigma_{CBR}} \right)^2 \right\} \tag{3}$$

4 Results and Discussion

The swell index of the untreated soil sample is found to be 140% resulting in a weak resistance against penetration as 2.01% and 0.74% for unsoaked and soaked CBR tests respectively. Based on the experimental studies, a percentage improvement of 322.89% and 959.46% were observed in the case of unsoaked and soaked CBR values respectively when treated with lime and fly ash. Further, a considerable range of variability is evidenced by every change in the matrix mix proportions. The causes for the variability concomitant with the material properties can be attributed to proper

material proportions, workability of the matrix, the extent of chemical action triggered by C-S-H gel, etc. The average values of mean, standard deviation and coefficient of variation (COV) are computed using statistical analysis. The probability density function (PDF) plotted from the computed data shows a high degree of variability associated with the CBR values at every different proportion.

It can be observed from Figs. 1, 2, 3, 4, 5, 6, 7 and 8 that the CBR values are plotted on the abscissa and the frequency density, *f* (CBR) on the primary ordinate for better representation. For 0% lime, as shown in Figs. 1 and 2, the variability is found to be very high which is more than 45% in case of soaked and more than 30% for unsoaked. It can be noted that the optimized normal mean (μ) and standard deviation (σ) for soaked CBR are 2.84 and 2.99. Nevertheless, they are found to be 3.81 and 3.90 for unsoaked CBR. Similarly, the mean, standard deviation, and COV are determined for all the other cases.

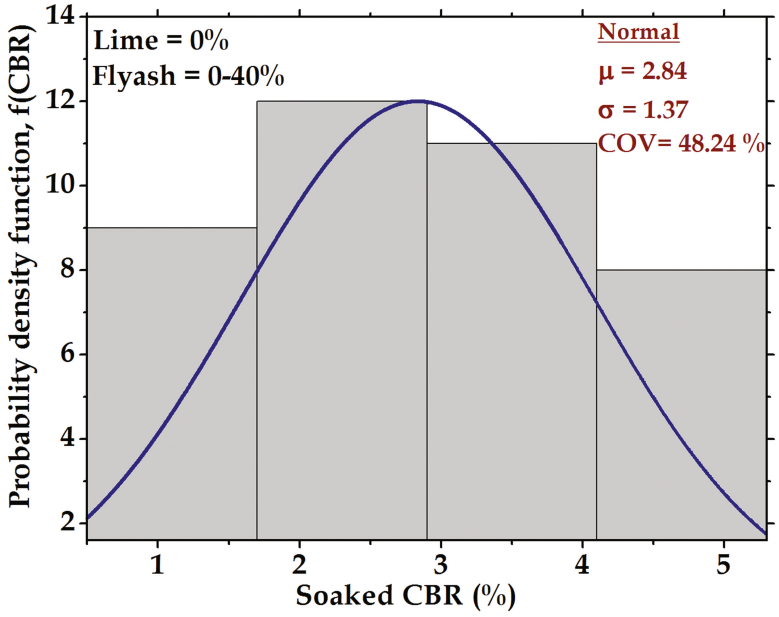

Fig. 1. Variability of soaked CBR values with 0% lime and 0–40% fly ash

It is obvious to note the increment in the mean value with increased lime contents from 0–9% due to the improvement in strength of the soil-matrix. Whereas, the standard deviation and COV doesn't follow any particular trend. Moreover, in the case of 3% and 6% of lime, multimodality is observed in the histogram despite the care taken to avoid them. From the shape of the bell curve of the PDFs, it can be noted that the data have a central tendency with mean, median and mode are all approximately on the same line. The histogram shows the symmetric variation with zero skewness

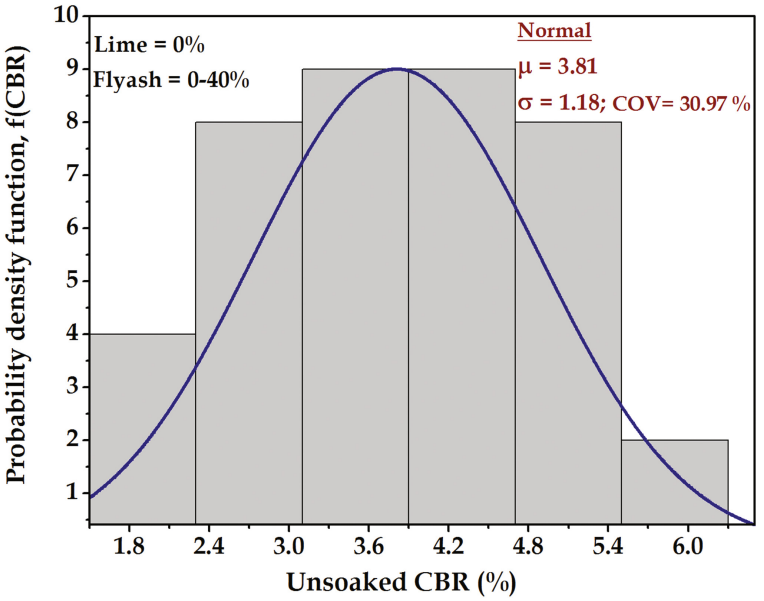

Fig. 2. Variability of unsoaked CBR values with 0% lime and 0–40% fly ash

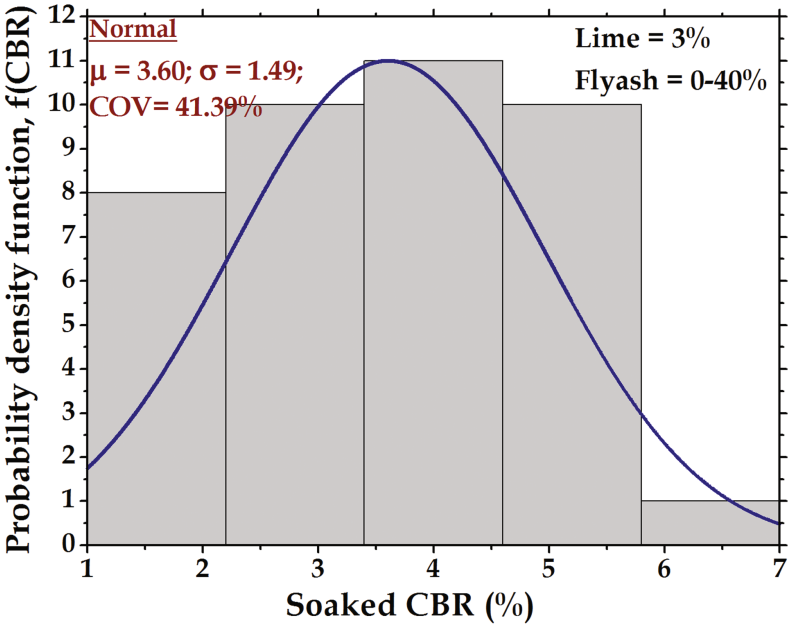

Fig. 3. Variability of soaked CBR values with 3% lime and 0–40% fly ash

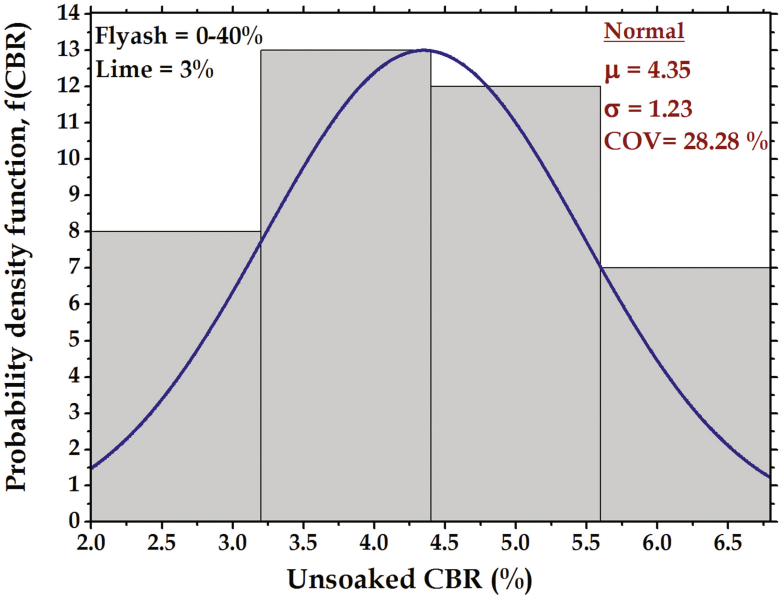

Fig. 4. Variability of unsoaked CBR values with 3% lime and 0–40% fly ash

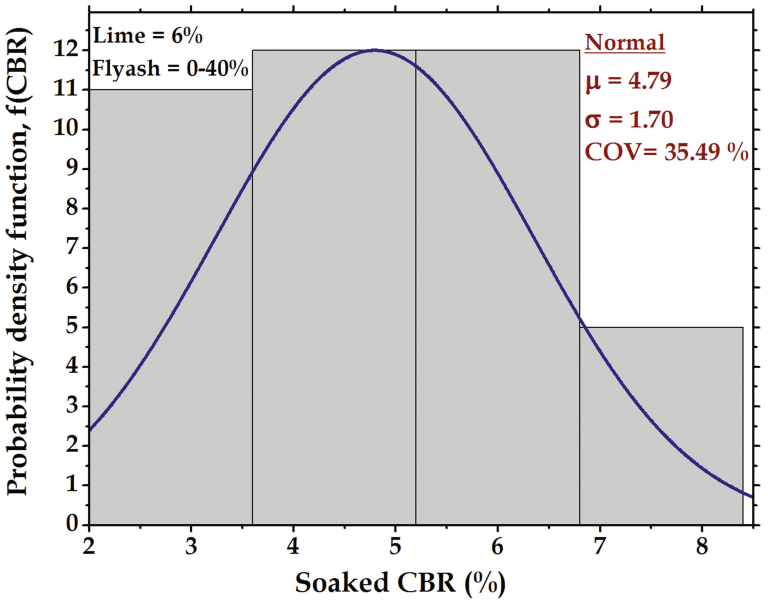

Fig. 5. Variability of soaked CBR values with 6% lime and 0–40% fly ash

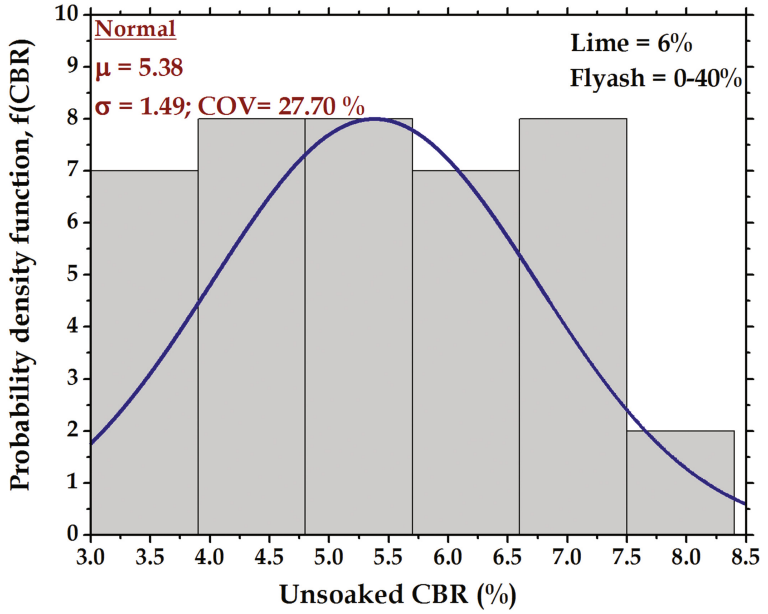

Fig. 6. Variability of unsoaked CBR values with 6% lime and 0–40% fly ash

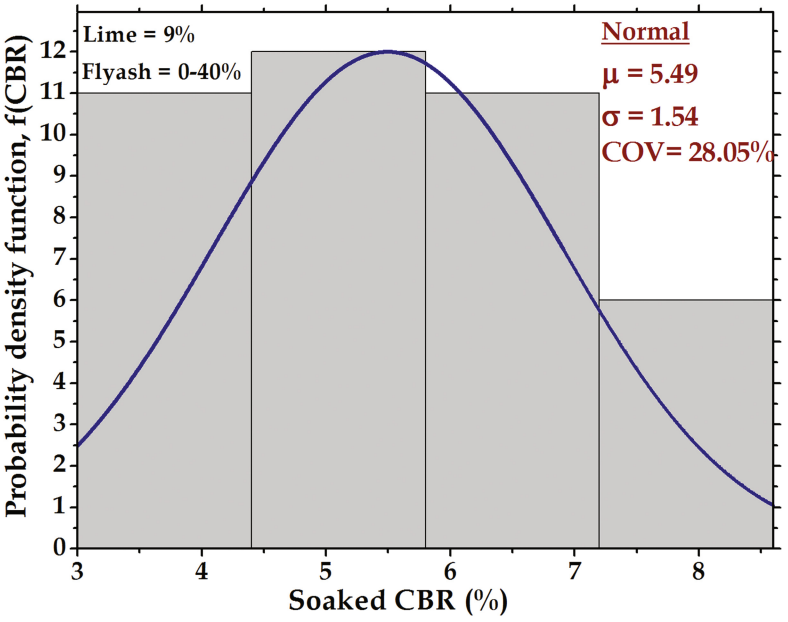

Fig. 7. Variability of soaked CBR values with 9% lime and 0–40% fly ash

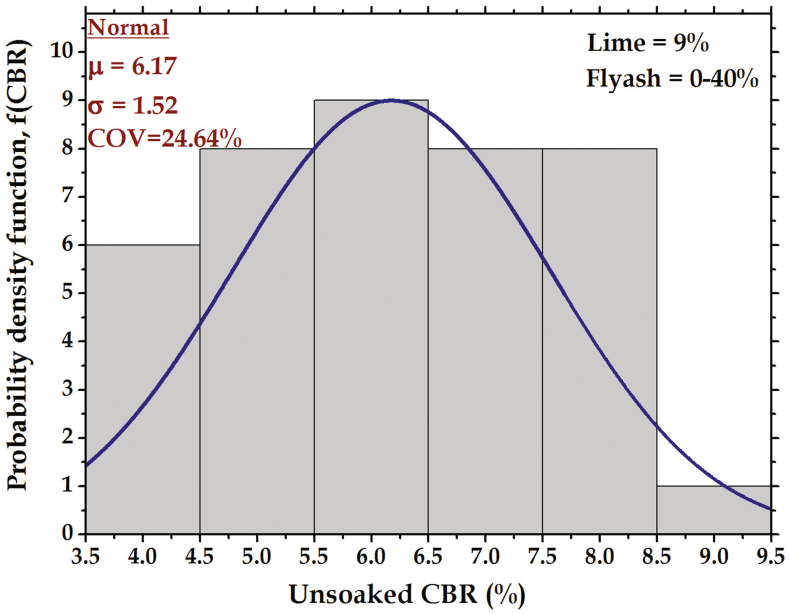

Fig. 8. Variability of unsoaked CBR values with 9% lime and 0–40% fly ash

specifying that most of the CBR values have found to be accumulated at the center i.e. in the range of 1.5–4.5. The width of each bin in the histogram proposes the scale of variation of the data.

5 Conclusions

A study has been conducted to analyze the variability associated with the friction angle of the CBR values of treated expansive soil. It can be concluded from the probabilistic analysis of the experimentally determined CBR values is that the value of 0.74–7.84% for soaked condition and 2.01–8.5% for the unsoaked condition with varying lime and fly ash contents of 0–9% and 0–40% respectively. Interestingly, the maximum COV is observed at 0% lime cycle and minimum COV is found at 9% lime cycle. It can also be observed that normal distribution is fitted to the data at the best suited mean and standard deviation values that are determined through trial and error method. To obtain an accurate estimation of the probability of failure associated with the pavement performance w.r.t CBR values, the design would require the consideration of variability associated with CBR values. The results produced by this study can be gainfully useful for reliability based design optimization of flexible pavements.

References

Al-Amoudi, O.S.B., Asi, I.M., Hamad, I., Wahhab, A.: Clegg Hammer—California-Bearing Ratio Correlations. J. Mater. Civ. Eng. **14**(6), 512–523 (2002)

Al-Amoudi, O.S.B., Asi, I.M., El-Naggar, Z.R.: Stabilization of an arid, saline soil using additives. Q. J. Eng. Geol. **28**(4), 369–379 (1995)

Bourdeau, P.L.: Probabilistic modeling of flexible pavements. Transp. Res. Rec., TRB **1286**, 184–191 (1990)

Chou, Y.T.: Probabilistic and Reliability Analysis of the California Bearing Ratio (CBR) Design Method for Flexible Airfield Pavements. US Army Corps of Engineers, Washington (1986)

Chou, Y.T.: Probabilistic and Reliability Design Procedures for Flexible Airfield Pavements-Elastic Layer Method, pp. 1–75. US Army Corps of Engineers, Washington (1987)

Chou, Y.T.: Reliability design procedures for flexible pavements. J. Transp. Eng. **116**(5), 602–614 (1989)

Divinsky, M., Ishai, I., Livneh, M.: Probabilistic approach to pavement design based on generalized California bearing ratio equation. J. Transp. Eng. **124**(6), 582–588 (1998)

Divinsky, M., Ishai, I., Livneh, M.: Simplified generalized California bearing ratio pavement design equation. Transp. Res. Rec., TRB **1539**, 44–50 (1996)

Freeman, R.B., Grogan, W.P.: Statistical Analysis and Variability of Pavement Materials, pp. 1–165. US Army Corps of Engineers, Washington (1997)

Habib-ur-Rehman, A.: Characterization and stabilization of eastern Saudi marls. M.S. Thesis report (King FAhd University of Petroleum and Minerals), pp. 1–100 (1995)

Jung, Y.S., Zollinger, D.G., Cho, B.H., Won, M., Wimsatt, A.J.: Subbase and subgrade performance investigation and design guidelines for concrete pavement. FHWA Report No: 6037-2. Texas Transportation Institute, US (2012)

Witczak, M.W., Uzan, J., Johnson, M.: Development of probabilistic rigid pavement design methodologies for military airfields. Technical report (US Army corps of Engineers) AD-A138212, pp. 1–219 (1983)

Influence of Applied Boundary Condition During Wetting on Volume Change Characteristics of a Compacted Highly Expansive Soil

Mohamed Farid Abbas(✉), Mosleh Ali Al-Shamrani, and Tamer Yehia Elkady

Bugshan Research Chair in Expansive Soils, Civil Engineering Department, College of Engineering, King Saud University, Riyadh, Saudi Arabia
mabbas@ksu.edu.sa

Abstract. Different methods are available for determining the swell pressure of expansive soils. Selecting the appropriate method depends on the prevailing boundary condition in situ. Two boundary conditions (constant stress and constant volume) applied during wetting were investigated in this paper. The influence of examined boundary condition on volume change characteristics is presented in this research. The evaluated volume change characteristics include axial and mean swell pressures as well as compression and swelling indices. Three methods for evaluation of swell pressures were utilized in current research, namely; swell under load, swell-load and constant volume methods. Findings show that the boundary condition applied during wetting has a considerable effect on swell pressures estimated and to some extent affect the estimated compression index while it has no impact on the predicted swell index.

1 Introduction

Expansive soils may naturally exist or used as a compacted material, in different engineering projects such as: subgrades, backfill material, engineered clay barrier and buffer materials for radioactive waste disposal. In this regard, there is a variety of stress, boundary and wetting conditions that may exist in the field. Consequently, its behavior should be examined under conditions simulating real field conditions. With respect to boundary condition that may exist in the field, there are an infinite possible field boundary conditions, however, the most realistic ones are constant stress (CS) and constant volume (CV).

Swell pressure is considered one of the critical factors that control making accurate prediction of field heave (Fredlund et al. 1980; Nelson and Miller 1992; Singhal et al. 2011). With respect to estimation of swell pressure, many methods have been developed by various researchers, however only three have been standardized, popularly used and documented in the literature (Brackley 1973; El Sayed and Rabba 1986; Sridharan et al. 1986; Erol et al. 1987; Dhowian 1990; Feng et al. 1998; Di Maio 2001;

L.R. Hoyos and J. McCartney (eds.), *Advances in Characterization and Analysis of Expansive Soils and Rocks*, Sustainable Civil Infrastructures,
DOI 10.1007/978-3-319-61931-6_10

Thompson et al. 2006; Kayabali and Demir 2011; Singhal et al. 2011). These methods are; swell-load method, constant volume method and swell under load method.

The first alternative defines the swell pressures as the stress at which the specimen experienced no wetting strains after wetting (swell under load method). In this method the axial swell pressures (σ_s) are obtained from the trend of variation of axial wetting strain versus axial wetting stress. Second, axial or mean swell pressure (σ_s or p_s) is defined as the stress (axial or mean, respectively) required to return the specimen back to its original state (height or void ratio) before swell and is obtained from wetting under constant axial stress condition (CS) (swell-load method). The constant volume method defines the third definition in which it considers axial or mean swell pressure (σ_s or p_s) as the equilibrium stress (axial or mean, respectively) at the end of wetting that is required to maintain the volume of specimen and the swell pressures (σ_s or p_s) are obtained from wetting under constant volume condition (CV).

Feng et al. (1998) examined the variation of swell pressure, as obtained from different test methods, with applied axial stress as shown in Fig. 1. Two opposite trends were observed for swell pressure obtained under both constant stress (i.e., swell-load method) and constant volume conditions. Swell pressure versus axial stress relations obtained under constant stress condition (i.e., swell-load method) showed descending trend, while those obtained under constant volume condition (either uncorrected or corrected values) showed ascending trend. Komornik and David (1969) arrived at a similar trend of variation for swell pressure obtained under constant volume condition.

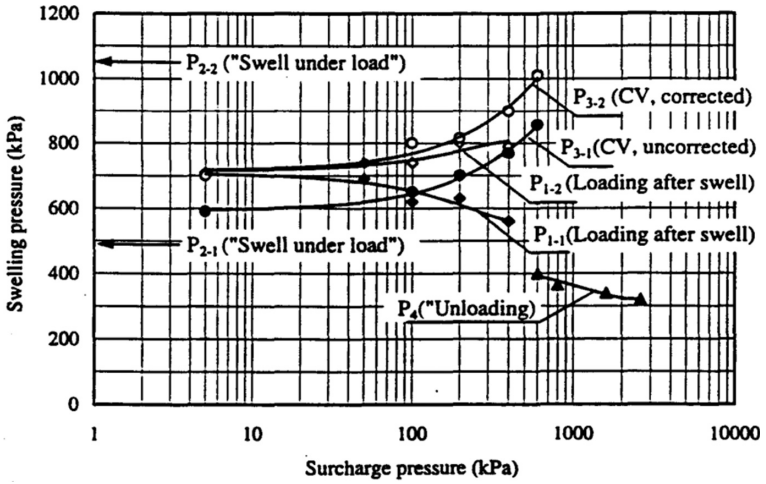

Fig. 1. The relationship between swell pressure and axial stress for different test methods (Feng et al. 1998)

Singhal et al. (2011) investigated the effects of testing procedures (initial applied stress level and wetting boundary condition) on the laboratory determination of swell pressure of expansive soils and concluded the same as Feng et al. (1998).

The dependence of swell pressure on wetting boundary condition (i.e., constant stress and constant volume) was overall attributed to the differences in fabric resulting from boundary conditions applied during wetting. When swell is allowed to occur (i.e., CS condition), water enters certain interstices that might not have been accessible if swell were being prevented (i.e., CV condition). Clay particle surfaces are hydrated during swell, even more so under low than under high applied stress level. In addition, they suggested that the sorption of water during swell under low initial applied stress may disturb the soil structure in contrast to at high stress level or under CV condition as has been found in previous studies (ASTM D4546 2003; Sridharan et al. 1986). In this regard, it is of paramount importance to select the appropriate test method for expansive soils.

The compression index (C_c) and swelling index (C_s) are the main parameters, in saturated soil mechanics, needed for calculating the anticipated settlement or swelling due to changing applied stress. It is therefore important to examine the effect of testing method, or in other words the boundary condition applied during wetting, on such parameters. To the authors' knowledge, there is a lack of researches that examined the impact of testing procedure (i.e., wetting boundary condition) on such indices.

The primary goal of this research is to experimentally investigate the influence of applied boundary condition during wetting on the volume change characteristics (swell pressure and compression and swelling indices) of a typical compacted highly expansive soil.

2 Material Used

A highly expansive soil was selected in order to be able to substantiate the influence of loading and wetting conditions. The soil used in this study was brought from Al-Qatif town located in the eastern province of Saudi Arabia (latitude 26° 56' N and longitude 50° 01' E). Al-Qatif clay represents a typical expansive soil generally encountered in the Arabian Gulf coastal region. Based on the documented review of Al-Qatif clay minerals (Abduljauwad and Al-Sulaimani 1993; Azam et al. 1998; Al-Shayea 2001; Azam 2003), it is considered as highly expansive in nature due to the high presence of smectite minerals.

The sampled material chosen for this study was calcareous grayish silty clay obtained from a field test pit at a depth of about three meters located at the border of Iskan district – Al Qatif town. Bulk disturbed specimens were collected in big plastic bags and transported to the laboratory where it was air dried, then pulverized and screened through sieve No. 40. Screened soil was mixed thoroughly to be homogeneous and stored in big sealed buckets until needed to be prepared for testing. A summary of physical properties of selected soil are provided in Table 1.

Table 1. Physical properties of Al–Qatif soil

Physical property	Value
Specific gravity, G_s	2.74
Liquid limit, LL (%)	137
Plastic limit, PL (%)	45
Shrinkage limit, SL (%)	18
Plasticity index, PI (%)	92
% Finer than 200 μm	70
USCS classification	CH

3 Specimen Preparation

Compacted specimens were used in the testing program to minimize heterogeneity in test results. Disturbed samples obtained from the field were air dried, pulverized and screened through sieve No. 40 to produce clay powder. The clay powder was thoroughly mixed with target water content and placed in air-tight plastic bags and stored in humid desiccators for about 72 h to allow for uniform distribution of moisture content. After the homogenization period, the soil was transferred to the thin-walled oedometer ring and statically compacted using a compaction rate of 3 mm/min. Final specimen dimensions were 16.0 mm high and 50.0 mm diameter with a dry unit weight of 11.77 kN/m^3 and water content of 31.5%. These values correspond to the maximum dry unit weight and 4% dry-of-optimum moisture content obtained from standard compaction test ASTM D 698 (2000).

4 Equipment Used

The experimental device used in this study was a thin-walled oedometer which is similar in principle to that developed by Ofer (1980). The advantage of this device is its ability to monitor changes in lateral stresses, and hence the mean stresses, developed by specimens during the test. The main component of the thin-walled oedometer is a brass ring of diameter 50.0 mm and wall thickness of 1.5 mm. The ring was instrumented with four electrical resistance strain gauges attached to the outer surface of the ring at an angular spacing of 90°. Each strain gauge was oriented such that the change in strain in the circumferential direction (ε_c) of the ring can be measured. The thin-walled oedometer cell was fitted with a linear variable differential transformer (LVDT) with an accuracy of 0.001 mm for axial strain measurement. All strain gauges and LVDT were connected to a portable data logger (TDS-303) for the continuous recording of strains during the test. Figure 2 provides a detailed diagram showing the different components of the thin walled oedometer cell. Through circumferential strain measurements, the lateral stresses generated during the test can be calculated via an appropriate calibration factor. Detailed discussion about the utilized thin-walled oedometer cell, calibration and corrections to be applied to raw data is provided in Abbas et al. (2015).

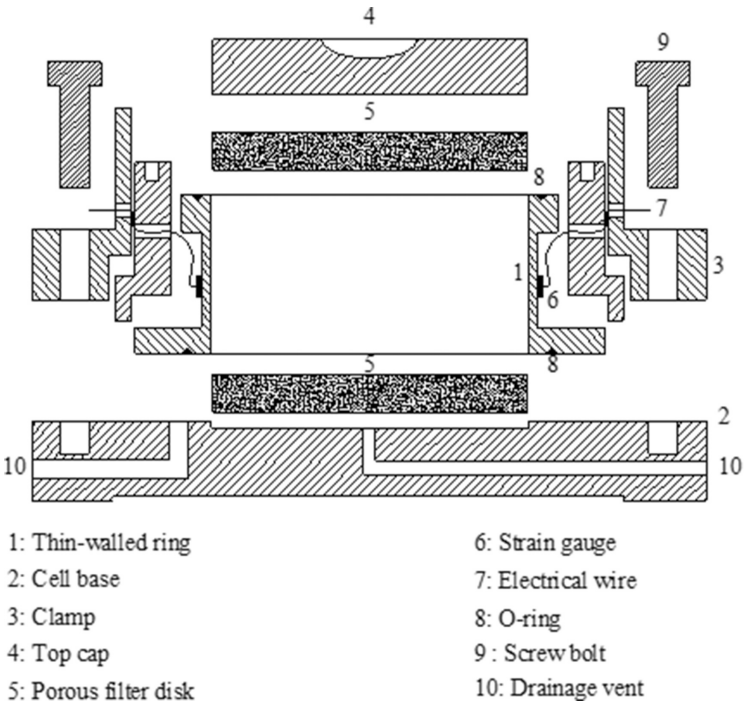

Fig. 2. Schematic diagram showing the components of the thin-walled oedometer cell

5 Experimental Program

In order to examine the influence of applied boundary condition during wetting on volume change characteristics, two test series were performed according to the boundary condition applied in axial direction during wetting stage.

The first group (constant axial stress method) represents wetting under one-dimensional constant axial stress condition (CS condition). The volume change potential due to wetting under different axial wetting stresses (σ_{aw}) varied from 50 kPa to 900 kPa was estimated. In addition, the swell pressure (axial or mean) corresponding to the stress (axial or mean, respectively) that returns the specimen back to its original state (height or void ratio) before swelling was obtained.

The second group (constant volume method) represents wetting under one-dimensional constant volume condition (CV condition). In this group, specimens were refrained to experience volume change in axial direction as well as lateral direction. From this group, the swell pressure (axial or mean) defined as the equilibrium stress (axial or mean, respectively) at end of wetting required to keep the specimen at its pre-wetting volume, was obtained. Specimens were wetted at axial wetting stresses (σ_{aw}) ranging from about 50 to 1000 kPa.

Both test series primarily comprised of four phases: dry loading, inundation, wet loading and unloading. A summary of the tests performed including test reference

(ID) and testing conditions is provided in Table 2. Each test ID represents the testing method (i.e., applied boundary condition during wetting) and applied axial wetting stress (σ_{aw}). For instance, CS_230 refers to a specimen wetted under constant axial stress condition with axial wetting stress (σ_{aw}) of 230 kPa.

6 Results and Analysis

This section summarizes the results of the experimental program described earlier. The effect of examined boundary conditions on both swell pressures as well as compression and swelling indices is discussed. A summary of the main test results is provided in Table 2.

The stress-strain behavior of tested specimens wetted under different axial wetting stresses for both considered boundary conditions (CS and CV) is presented in Figs. 3 and 4, respectively. It is observed that the specimen wetted under constant stress (CS) condition may undergo swell or collapse behavior depending on the magnitude of the axial wetting stress (σ_{aw}). In case of specimens experiencing swell, the swell strain

Table 2. Summary of testing program conditions and results

Specimen ID	Test conditions				Test results		
	Water content, (%)	Unit weight, kN/m^3	Wetting stresses (kPa)		Axial wetting strain, (%)	Swell pressure, (kPa)	
	w_c	γ_b	σ_{aw}	σ^*_{Lw}	ε_{aw}	σ_s	σ^{**}_{Ls}
CS_50	31.1	11.77	50	29	13.2	400	104
CS_110	31.8	11.77	110	8	7.2	350	121
CS_230	31.6	11.77	230	32	2.4	335	172
CS_335	31.7	11.77	335	53	−0.6	N. A.	187
CS_450	31.9	11.67	450	60	−2.9	N. A.	190
CS_600	31.5	11.77	600	50	−5.3	N. A.	237
CS_900	31.4	11.77	900	180	−7.7	N. A.	379
CV_50	31.4	11.77	50	44	zero	257	160
CV_150	31.4	11.77	150	52	zero	275	186
CV_275	31.4	11.77	275	86	zero	275	213
CV_350	31.4	11.77	350	100	zero	299	212
CV_515	31.4	11.77	515	128	−0.21	313	223
CV_630	32.0	11.67	630	114	−0.31	358	237
CV_1000	31.4	11.77	1020	222	−0.75	450	259

* The value of lateral stress corresponding to axial wetting stress

** The equilibrium lateral stress at the end of wetting

N.A. means “not applicable”

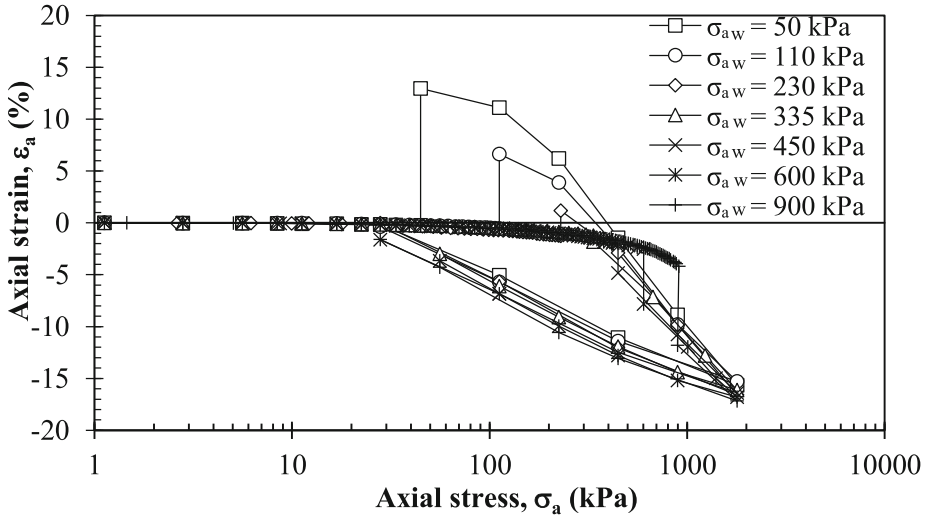

Fig. 3. Stress-strain curves for wetting under constant axial stress condition

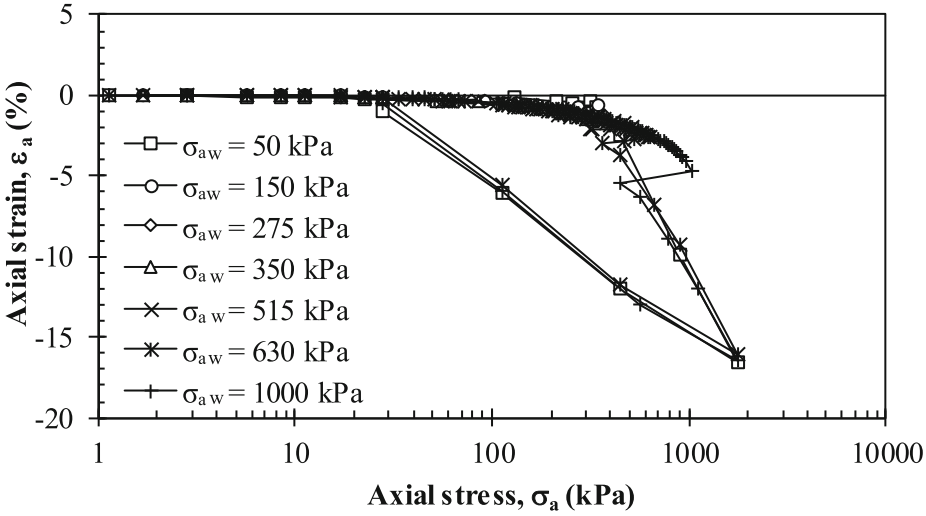

Fig. 4. Stress-strain curves for wetting under constant volume condition

is observed to decrease with the increase in axial wetting stress (σ_{aw}). On the other hand, the collapse behavior is observed for specimens wetted at axial wetting stress (σ_{aw}) higher than a limiting value, referred as axial swell pressure (swell under load method), after which the collapse strain increased with increasing axial wetting stress (σ_{aw}). Variation of axial wetting strain (ε_{aw}) with axial wetting stresses (σ_{aw}) obtained under constant stress (CS) condition is illustrated in Fig. 5.

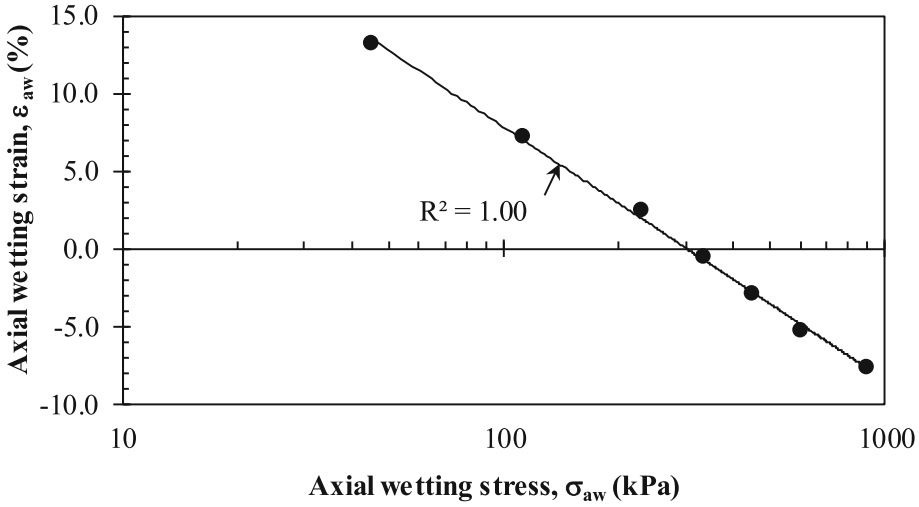

Fig. 5. Axial wetting strain vs. axial wetting stress trend

6.1 Swell Pressures

With respect to the axial swell pressure (σ_s) estimated based on the swell under load method, it can be seen that it has a unique value estimated as the point of intersection of the ($\varepsilon_{aw} - \sigma_{aw}$) trend of variation, plotted in Fig. 5, with the x-axis (310 kPa). On the other hand, Table 2 shows that the axial swell pressures (σ_s), estimated from swell-load and constant volume methods, vary with axial wetting stress (σ_{aw}). Figure 6 presents a comparison between axial swell pressures (σ_s) estimated from swell-load and constant volume. The axial swell pressure (σ_s) is observed to be dependent on boundary condition applied during wetting (i.e., CS or CV). The observed dependency of (σ_s) on boundary condition applied during wetting is in agreement with findings of previous researches (Brackley 1973; El Sayed and Rabba 1986; Sridharan et al. 1986; Erol et al. 1987; Dhowian 1990; Edil and Alanazy 1992; Thompson et al. 2006; Singhal et al. 2011).

It is observed from Fig. 6 that axial swell pressures (σ_s) estimated under CS condition, at low axial wetting stress, is higher than that predicted under CV condition. This is attributed, in general, to the differences in fabric resulting from boundary conditions applied during wetting. When swell is allowed to occur (i.e., CS condition), water enters certain interstices that might not have been accessible if swell were being prevented (i.e., CV condition). Clay particle surfaces are hydrated during swell, even more so under low σ_{aw} than under high σ_{aw}. The stress required to expel this absorbed water during clay particle hydration is more than that required to prevent its uptake. Thus, axial swell pressure (σ_s) estimated under CS condition exceeds that predicted under CV condition. In addition, sorption of water during swell under low σ_{aw} may disturb the soil structure in contrast to at high or under CV condition as has been found in previous studies (ASTM D4546 2003; Sridharan et al. 1986).

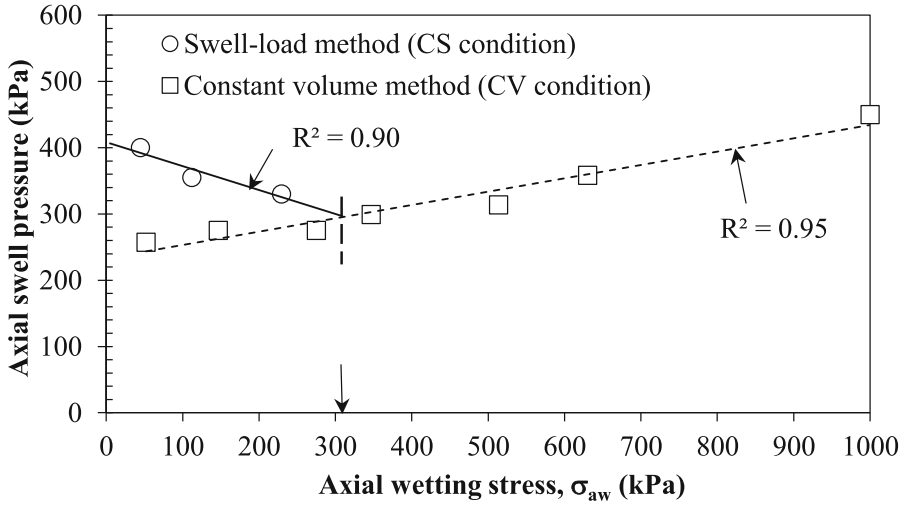

Fig. 6. Comparison of axial swell pressures (σ_s) obtained from swell-load and constant volume methods

The axial swell pressure (σ_s) is related to axial wetting stress (σ_{aw}) with linear relations, Fig. 6, either with descending trend (under CS condition) or ascending trend under (CV condition). The descending trend is attributed to the decrease of water absorbed at higher stress and subsequently reduction of stress required to expel this absorbed water as discussed formerly. On the other hand, the ascending trend for CV condition is ascribed to the decrease in pre-wetting void ratio (i.e., increase in dry density) with increase σ_{aw} and hence increase in stress required to prevent swell. Similar observation was reported by Feng et al. (1998); Singhal et al. (2011). The intersection between the two trends (i.e., point of equality of σ_s obtained from CS and CV conditions) is at σ_{aw} of 310 kPa which is equal to σ_s obtained based on the swell under load method (Fig. 5). This emphasizes the role played by specimen fabric in altering axial swell pressures (σ_s). Specimen wetted under CS and CV condition at σ_{aw} equals to σ_s obtained from swell under load method (i.e., 310 kPa) did not experienced any disturbance in its structure where no deformation after wetting is to be initiated and hence the estimated σ_s from both methods is equal.

The mean swell pressure (p_s) obtained from swell-load and constant volume methods (i.e., under CS and CV conditions, respectively) are compiled in Fig. 7. It is seen that the relationship between mean swell pressure (p_s) and mean wetting stress (p_w) are affected by the boundary condition applied during wetting.

6.2 Compression and Swelling Indices

The compression and swelling indices, C_c and C_s respectively, obtained for specimens wetted under both constant axial stress (CS) and constant volume (CV) conditions are plotted in Figs. 8 and 9, respectively, against the axial wetting stress (σ_{aw}).

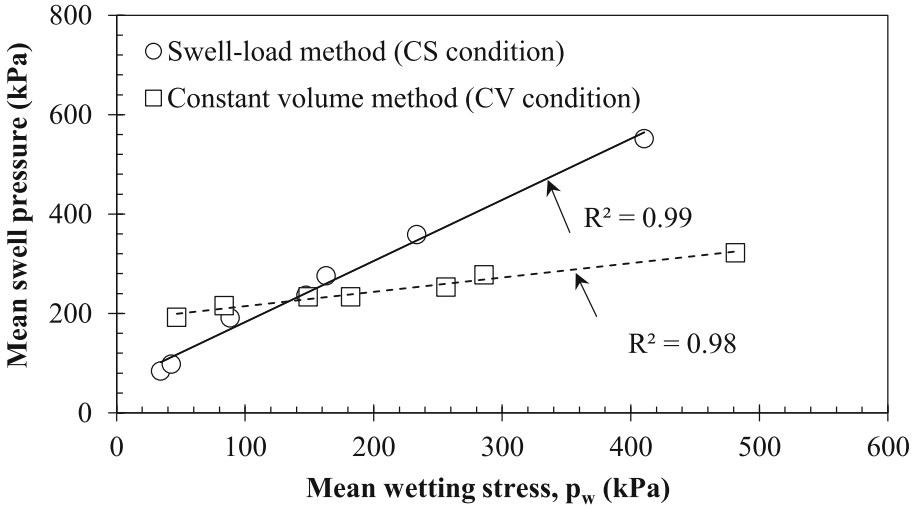

Fig. 7. Comparison of mean swell pressures (p_s) obtained from swell-load and constant volume methods

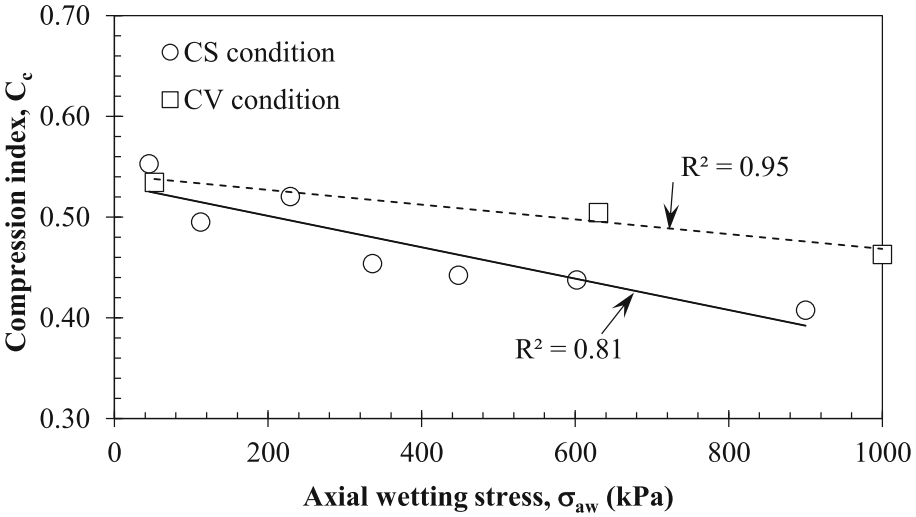

Fig. 8. Variation of compression indices with axial wetting stress

It is observed that irrespective of boundary condition applied during wetting, the compression index (C_c) exhibited similar trends with the C_c decreasing with increasing axial wetting stress. However, at the same value for axial wetting stress (σ_{aw}), the value of compression index (C_c) obtained from constant axial stress method is lower than that obtained from constant volume method, and the discrepancy between the two values increase with increasing axial wetting stress.

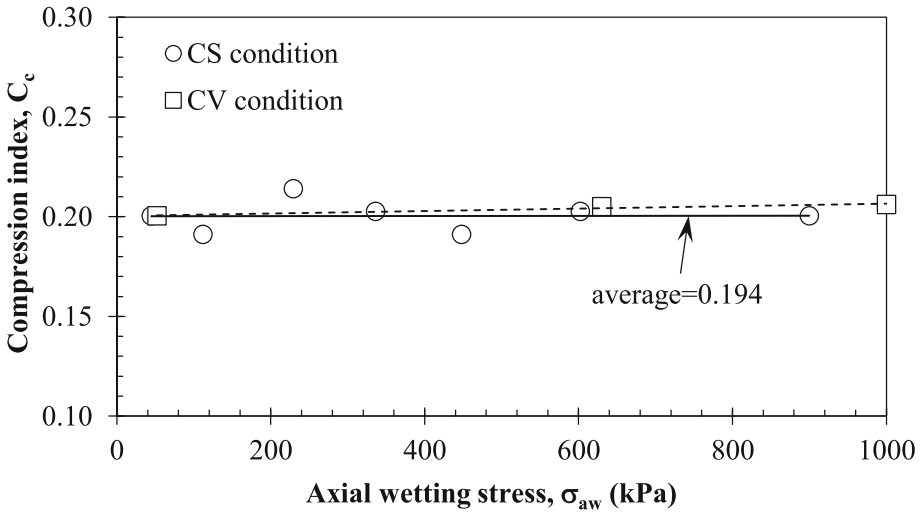

Fig. 9. Variation of swelling indices with axial wetting stress

The specimens wetted under CS condition and low axial wetting stress (σ_{aw}) experienced high swell and absorbed more water during hydration compared to those wetted under relatively high constant axial wetting stress (σ_{aw}). Subjecting tested specimen to an axial wetting stress (σ_{aw}) higher than the axial swell pressure (σ_s) (swell under load method) resulted in a final collapse of tested specimens. The amount of final collapse strain increases with increasing σ_{aw}. Hence, the dry density prior to wet loading increases with the increase in σ_{aw}. In turn, the stiffness of wetted specimens prior to wet loading, increases with the increase in σ_{aw} and consequently the compression index (C_c) decreases with increasing axial wetting stress (σ_{aw}).

Based on previous interpretation, the values of compression index (C_c), for specimens wetted under CV condition, is expected to be constant for the examined range of axial wetting stress (σ_{aw}) since the specimens are supposed to have almost the same dry density after complete wetting. However, the actual condition is that tested specimens were subjected to slightly collapse during wetting under CV condition and high axial wetting stress as depicted in Table 2. So, there is a slight reduction in the values of C_c with increasing σ_{aw} compared to the case of wetting under CS condition. The low values of C_c at high axial wetting stress for specimens wetted under CS condition compared to those wetted under CV condition is because the specimens wetted under CS condition experienced a high magnitude of collapse compared to the slight one inflicted under CV condition, see Table 2.

Regarding the variation of swelling index (C_s) with axial wetting stress (σ_{aw}) plotted in Fig. 9, it is seen that swelling index (C_s) is almost constant with a mean value of 0.194. This is attributed to the fact that all specimens prior to wet unloading have almost the same void ratio (as deduced from Figs. 3 and 4).

7 Conclusions

The effect of the method of determination (or in other words boundary condition during wetting) on measured swell pressure and compression and swelling indices were presented. The results indicated that axial and mean swell pressures (σ_s and p_s) are not a material constant but rather are dependent on method of determination (i.e., boundary condition applied during wetting and definition used for determination). When the axial swell pressure (σ_s) was estimated based on the swell under load method, it was found that it has a unique value. However, when it was obtained from either the swell-load or constant volume method it was observed to depend also on axial wetting stress (σ_{aw}). The same conclusion is also applied to the mean swell pressure (ps).

With respect to the influence of method of determination on compression and swelling indices (C_c and C_s, respectively), findings showed that the compression index (C_c) was to some extent affected by method of determination, whereas, method of determination has no impact on the predicted swell index (C_s).

Acknowledgments. The project was financially supported by King Saud University, Vice Deanship of Research Chairs.

References

Abbas, M.F., Elkady, T.Y., Al-Shamrani, M.A.: Evaluation of strain and stress states of a compacted highly expansive soil using a thin-walled oedometer. Eng. Geol. J. **193**, 132–145 (2015)

Abduljauwad, S.N., Al-Sulaimani, G.J.: Determination of swell potential of Al-Qatif clay. Geotech. Test. J. **16**(4), 469–484 (1993)

Al-Shayea, N.: The combined effect of clay and moisture content on the behavior of remolded unsaturated soils. Eng. Geol. **62**, 319–342 (2001)

ASTM. D 4546-03: Standard Test Methods for One-Dimensional swell or settlement potential of cohesive soils. West Conshohocken, PA (2003)

ASTM. D 698-00a$^{\varepsilon}$1: Standard Test Methods for Laboratory Compaction Characteristics of Soil Using Standard Effort. West Conshohocken, PA (2000)

Azam, S.: Influence of mineralogy on swelling and consolidation of soils in eastern Saudi Arabia. Can. Geotech. J. **40**, 964–975 (2003)

Azam, S., Abduljauwad, S.N., Al-Shayea, N.A., Al-Amoudi, O.S.B.: Expansive characteristics of gypsiferous/anhydritic formations. Eng. Geol. **51**, 89–107 (1998)

Brackley, I.J.: Swell pressure and free swell in compacted clay. In: Proceedings of 3rd International Conference on Expansive Soils, Haifa, vol. 1, pp. 169–176 (1973)

Dhowian, A.W.: Heave prediction techniques and design consideration on expansive soils. J. King Saud Univ. Eng. Sci. **2**, 355–377 (1990)

Di Maio, C.: Swelling pressure of clayey soils: the influence of stress state and pore liquid composition. Ital. Geotechn. J. **3**, 22–34 (2001)

El-Sayed, S.T., Rabbaa, S.A.: Factors affecting behaviour of expansive soils in the laboratory and field – a review. Geotech. Eng. **17**(1), 89–107 (1986)

Erol, O., Dhowian, A., Youssef, A.: Assessment of oedometer methods for heave prediction. In: Proceedings 6th International Conference on Expansive Soils, New Delhi, India, vol. 1, pp. 99–103 (1987)

Feng, M., Gan, J., Fredlund, D.G.: A laboratory study of swelling pressure using various test methods. In: Proceedings of the 2nd International Conference on Unsaturated Soils, UNSAT2, Beijing, China, pp. 350–355 (1998)

Fredlund, D.G., Hasan, J.U., Filson, H.: The prediction of total heave. In: Proceedings of the Fourth International Conference on Expansive Soils, Denver, CO, pp. 1–17 (1980)

Kayabali, K., Demir, S.: Measurement of swelling pressure: direct method versus indirect methods. Can. Geotech. J. **48**(3), 354–364 (2011)

Komornik, A., David, D.: Prediction of swelling pressure of clays. J. Soil Mech. Found. Div. ASCE **95**(SM1), 209–225 (1969)

Nelson, J.D., Miller, D.J.: Expansive Soils, p. 295. Wiley, New York (1992)

Ofer, Z.: Instruments for laboratory and in-situ measurement of the lateral swelling pressure of expansive clays. In: Proceedings of the 4th International Conference on Expansive Soils, ASCE, New York, pp. 45–53 (1980)

Singhal, S., Houston, S.L., Houston, W.N.: Effects of testing procedures on the laboratory determination of swell pressure of expansive soils. Geotech. Test. J. **34**(5), 476–488 (2011)

Sridharan, A., Rao, A.S., Sivapullaiah, P.V.: Swelling pressure of clays. Geotech. Test. J. **9**(1), 24–33 (1986)

Thompson, R.W., Perko, H.A., Rethamel, W.D.: Comparison of constant volume swell pressure and oedometer load-back pressure. In: 4th International Conference on Unsaturated Soils, Arizona, EE, UU, pp. 1787–1798 (2006)

Co-relation Between Electrical Resistivity and Index Properties of Periodic Hydrocarbon Contaminated Bentonite Clay

M.V. Shah[1(✉)] and Preeti Tiwari[2]

[1] Applied Mechanics, L.D College of Engineering, Ahmedabad 380015, India
[2] Department of Civil Engineering, Indus University, Ahmedabad 382115, India

Abstract. Present papers deals with determination of electrical resistivity of hydrocarbon contaminated bentonite clay and to establish correlation between electrical resistivity and index properties for periodic contamination. Research work focuses on studying the hydrocarbon-bentonite interaction through electrical resistivity which is one of the perturbed geo-physical method of analysis and is non-destructive in nature. Bentonite clay, which is expansive in nature with high montmorillonite mineral content usually have resistivity range between 10 Ω–20 Ω. The resistivity range for hydrocarbon contaminated bentonite clay for each period is determined and obtained in the laboratory. The impact of hydrocarbon contamination on electrical resistivity of bentonite clay is studied through passing 30 V–40 V DC voltage through compacted sample in a resistivity box in accordance with ASTM G-187. CEC, EDAX tests were performed to evaluate the effect of ions of montmorillonite clays and their penetrability into hydrocarbon-clay matrix. The above study reveals that there is a major influence of hydrocarbon contamination on engineering behavior of clays. This leads us advance assessment of influence of both percentage contamination and periodic contamination on strength characteristics of such marine clays.

1 Introduction

The past few years have witnessed tremendous growth in petroleum sector all over the world. This has led to hydrocarbon contamination of soil situated in the vicinity of the petroleum spillage areas which is a serious problem for the environment as it adversely affects the soil inherent properties viz. index properties and strength properties. Hydrocarbons contaminated clay resulting in large amounts from the treatment of crude-oil produced from large Oil Refineries represents a great geo-environmental pollution threat. Hydrocarbon soil contamination is very common in marine clays. Petrochemicals, hydrocarbons (oil spills), are extensively liberated onto the surrounding soil and get penetrated into the deep ground soil further affecting its physico-chemical properties. With this process of large-scale exploitation of coastal and offshore oil, coastal soils have encountered oil pollution. And this legacy of industrialization which has resulted in a prevalence of hydrocarbons contamination of surrounding soils, necessitates the evaluation and analysis of the hazardous effects (such as differential settlement and structure failures due to the change in engineering properties) of these contaminants on soils as well.

L.R. Hoyos and J. McCartney (eds.), *Advances in Characterization and Analysis of Expansive Soils and Rocks*, Sustainable Civil Infrastructures,
DOI 10.1007/978-3-319-61931-6_11

Electrical resistivity is one of the perturbed properties in the presence of hydrocarbons in the soil. Many authors have correlated Electrical resistivity with varied soil parameters viz. Moisture content, Specific gravity, Atterberg's limit, C and ϕ. Many researchers have worked on correlating electrical resistivity of soil with index properties and engineering properties of soil but very few researches have been done in analyzing the impact of rate of contamination, rate of degradation (soil exposed to shorter period or longer period of contamination), change in soil structural, physical and chemical properties due to these contaminants and weather these contaminants impede some electrical potential into the soil strata due to their interaction with various soil minerals and pore water. They all have studied the various geotechnical properties of soil which is being contaminated by various chemicals, salts, radioactive materials and compounds and have suggested the remediation methods to improve the performance and quality of contaminated soils through different tests, methods and chemicals, but they lack in making the above measurements as well as very less information is dispersed between soil-contaminant interaction with electrical resistivity. So to overcome above limitations, a detailed laboratory programme was framed to study the electrical resistivity of contaminated marine clay (with montmorillonite as the basic mineral) at various rate of contamination (3%, 6% and 9%) and for various period of degradation (15, 30 and 45 days) due to the presence of these contaminants in soil.

The correlations developed between the electrical resistivity and index properties of soil have been used to analyze the impact of periodic contamination due to hydrocarbon which leads to change in physical, chemical and engineering properties of marine clay.

2 Material and Experimental Setup

2.1 Soil Resistivity Box

Soil resistivity is obtained in laboratory by fabricating soil resistivity box (10 cm 5 cm × 5 cm) in accordance with ASTM G187 (Fig. 1). For laboratory test an individual soil sample is compacted in the resistivity box in a predetermined unit weight and moisture content. LCR meter, D.C voltage and current source, can be utilized for the resistivity measurements. To obtain the correlations, soil resistivity tests are conducted using different geotechnical considerations. Using Ohm's law,

Electrical resistance, $R = \Delta V/I$

Electrical resistivity, $\rho = AR/L = \Delta V A/IL$

Thus electrical resistivity of the soil sample can be obtained using the above equation.

2.2 Sample: Clay & Hydrocarbon

Source of the Bentonite clay was identified and procured commercially from Baroda, Gujarat. The disturbed soil samples were put in plastic bags, and then transported to the soil laboratory. The natural soil was classified visually and experimentally as clay of high plasticity (CH) according to unified classification soil system (IS classification).

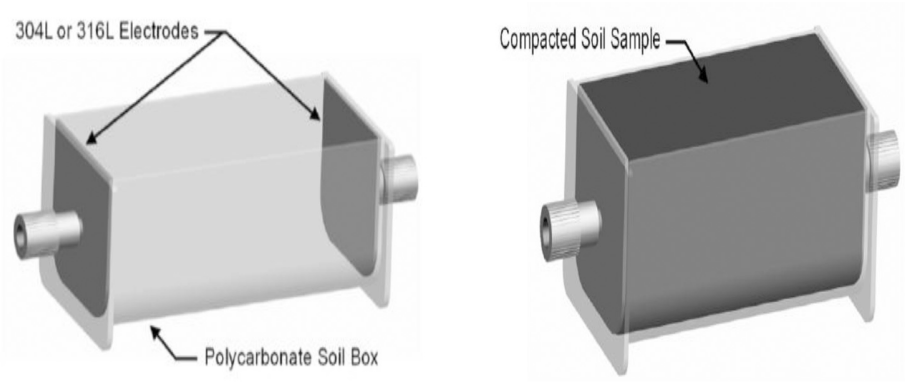

Fig. 1. Typical two-electrode soil box (Empty and Full)

For the present study the hydrocarbon contaminated soil was procured from one of the major petroleum unit. The sample was in saturated form mixed with various hydrocarbons.

2.3 Theoretical Validation of Experimental Results and Co-relations

Electrical resistivity is been co-related with index properties and engineering properties of non-contaminated and hydrocarbon contaminated bentonite clay. To analyze and validate the co-relations obtained in the laboratory statically, a statistical model called lineal regression analysis has been used.

3 Laboratory Testing

3.1 GC-MS (Gas Chromatography & Spectroscopy)

To identify the type of hydrocarbon, GC-MS test was performed at Department of Chemistry, Gujarat University and the hydrocarbon was identified as Dodecane ($C_{12}H_{26}$)

3.2 Index Properties

The index properties of non-contaminated bentonite clay (with montmorillonite as basic mineral) and periodic (15, 30, 45 and 60 days) hydrocarbon contaminated clay was obtained in accordance with IS code for each percentage of contamination i.e., 3%, 6% and 9%. The overall percentage variation in various index properties of hydrocarbon contaminated clay from non-contaminated clays is shown in Table 1.

Table 1. EDAX results summary for % weight of elements present in pure bentonite clay after hydrocarbon contamination

% weight of elements present in bentonite clay after contamination	Elements		C	O	Na	Mg	Al	Si	K	Ti	Fe
	60 days hydrocarbon contamination	0%	9.08	48.1	2.5	1.4	9.19	23.25	0.51	–	6.2
		3%	11.5	51.6	1.5	1.1	8.85	22.83	0.64	0.98	5.7
		6%	11.8	53.6	2.1	1.1	7.38	18.48	0.7	0.99	6.5
		9%	12	50.6	1.4	1	7.75	19.15	0.74	0.85	6.7

3.3 Electrical Resistivity

The electrical resistivity is obtained in accordance with ASTM G187 (Fig. 2) and the values are obtained for non-contaminated and hydrocarbon contaminated marine clay at the rate of 3%, 6% and 9% using constant DC source having voltage of 35 V (provides most desirable and comparable results) for the purpose of setting correlations and evaluation of various geotechnical properties. The overall percentage variation in electrical resistivity of hydrocarbon contaminated clay from non-contaminated clays is shown in Table 1.

Fig. 2. Measurement of electrical resistivity

4 Results and Discussion

4.1 Electrical Resistivity v/s Period of Contamination and Rate of Hydrocarbon Contamination

Electrical resistivity value increases when percent of hydrocarbon contamination increases from 3% to 6% as hydrocarbon hinders with ion-exchange mechanism leading to higher resistivity values. But when % of contamination further increases from 6% to 9%, there is a decrease in resistivity which can be explained by the following philosophy: when hydrocarbon comes in contact with clay-water system, it acts as a barrier for ion exchange process. Increasing the rate of hydrocarbon

contamination further i.e. from 3% to 6% increases the resistivity. But with further increase in rate of hydrocarbon, i.e. from 6% to 9%, there is a decrease in resistivity value as the abundance of hydrocarbon layer compels or pushes the un-exchanged ion present at distance from clay surface which leads to exchange of those positively charged ions with that of negatively charged clay ions and thus reducing resistivity value (Fig. 3).

4.2 Liquid Limit v/s Electrical Resistivity

Electrical resistivity decreases with increase in liquid limit as with high water content allows free movement of ions and thus conductivity increases and resistivity reduces (Fig. 4). Electrical resistivity reduces by 28% for every 13.4% overall increase in Liquid limit. Hence we can conclude on an average that for increase in liquid limit the Electrical resistivity reduces twice the increment value of liquid limit. Liquid limit of non-contaminated clay is higher than that of hydrocarbon contaminated clay and it decreases by 13.43%, 25.37% and 18% for 3%, 6% and 9% of hydrocarbon contamination respectively. The mineralogical composition of hydrocarbon (Dodecane) comprises of long chains of carbon-hydrogen atoms, which when comes in contact with water leads to decrease in inter-molecular bond and leads to development of viscous layer over the clay mass as hydrocarbon has low density in comparison to water, it tends to float and thus leads to reduction in liquid limit. But with increase in period of contamination, the effect of hydrocarbon is seen to be degrading due to its either conversion into gaseous form or due to its degradation by micro-organisms.

4.3 Plastic Limit v/s Electrical Resistivity

Electrical resistivity is increasing with increase in plastic limit (Fig. 5). The plastic limit of non-contaminated clay is the lowest having lowest resistivity value. There is an increment by 21.7% of electrical resistivity for an increment in plastic limit by 5.8% which is not very considerable. However, it can be predicted that higher plastic limit leads to higher resistivity in clay.

Plastic limit for hydrocarbon contaminated bentonite clay is higher than that of non-contaminated clay by 5.8%, 11.57% and 9% for each percentage of contamination. The C-H layer of hydrocarbon when interacts with clay-water, prevents rapid development of cracks over the clayey surface of the thread and thus causes increment in plasticity of clay-hydrocarbon-water mixture. Increase in period of contamination gradually leads to decrease in plastic limit. The reason can be attributes to the fact that Dodecane being less reactive compound in itself loses further its reactivity with time or due to its degradation with micro-organisms.

4.4 Shrinkage Limit v/s Electrical Resistivity

Electrical resistivity reduces with increment in shrinkage limit for each percent of contamination (Fig. 6). Shrinkage limit of non-contaminated clay is highest having lowest electrical resistivity. There is an increment in electrical resistivity value by 28% for 17.5% reduction in shrinkage limit. Shrinkage limit for hydrocarbon contaminated bentonite clay is lower than that of non-contaminated clay by 70.17%, 33.33% and 63.15% for each percentage of contamination i.e. 3%, 6% and 9% respectively. Shrinkage limit for hydrocarbon contaminated clay increases with increase in period of contamination for each percent of contamination. The hydrocarbon layer which tends to float over clay mass due to its low density gets adsorbed over the clay-water system and forms diffused double layer having considerable thickness which in turn prevents, the suction of moisture content to the atmosphere and thus the loss of moisture is reduced which leads to lower shrinkage limit.

4.5 Specific Gravity v/s Electrical Resistivity

Referring Fig. 7, electrical resistivity reduces with increment in specific gravity. Specific gravity of non-contaminated clay is highest having lowest electrical resistivity. There is an increment in electrical resistivity value by 13.5% for 2% reduction in specific gravity. Specific gravity tends to increase with increase in period of contamination. Specific gravity for hydrocarbon contaminated bentonite clay is higher than that of non-contaminated clay by 17%, 26.3% and 26.8% for 3%, 6% and 9% respectively. Specific gravity for hydrocarbon contaminated clay increases with increase in period of contamination for each percent of contamination. Since the specific gravity of hydrocarbon is much lower than that of water, it tends to float over water layer. Bentonite when contaminated with hydrocarbon and water, the specific gravity tends to decrease significantly as hydrocarbon has low specific gravity and it tends to reduce the specific gravity of clay when contaminated.

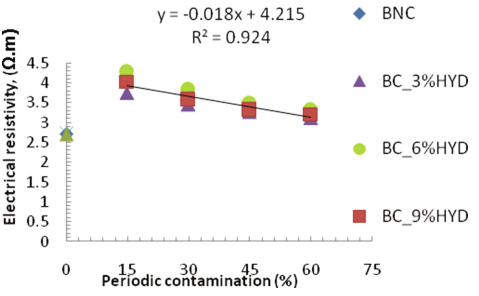

Fig. 3. Electrical resistivity v/s % of contamination

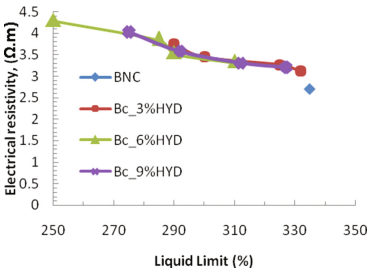

Fig. 4. Electrical resistivity v/s Liquid limit

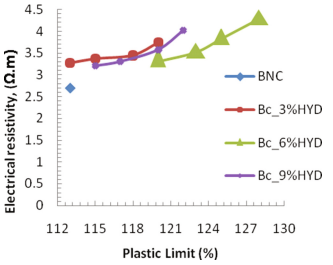

Fig. 5. Electrical resistivity v/s plastic limit for each % of hydrocarbon contamination

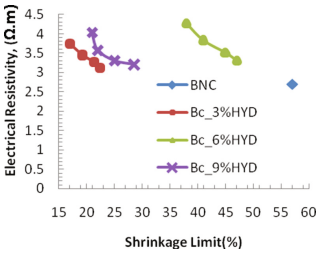

Fig. 6. Electrical resistivity v/s shrinkage limit for each % of hydrocarbon contamination

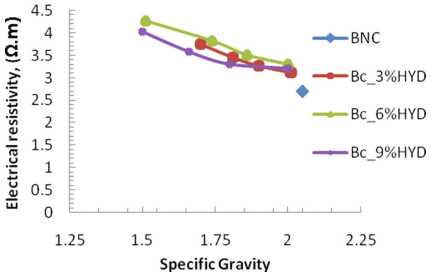

Fig. 7. Electrical resistivity v/s shrinkage limit for each % of hydrocarbon contamination

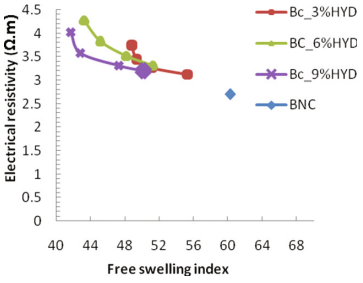

Fig. 8. Electrical resistivity v/s FSI for each % of hydrocarbon contamination

4.6 Free Swell Index v/s Electrical Resistivity

Referring Fig. 8, electrical resistivity reduces with increment in FSI. FSI of non-contaminated clay is highest having lowest electrical resistivity. For decrease in FSI by 8%, there is an increase in electrical resistivity by almost 13.5%.

Free swell index for hydrocarbon contaminated bentonite clay is lower than that of non-contaminated clay by 20%, 28% and 30.83% for 3%, 6% and 9% of hydrocarbon contamination respectively. Free swell index for hydrocarbon contaminated clay, than increases with increase in period of contamination for each percent of contamination i.e. 3%, 6% and 9%. There is a considerable decrease in swelling as the percentage of K ions in the system increases. % weight of K ions in non-contaminated clay is 0.51 and for hydrocarbon contaminated clay; it is 0.64, 0.70 and 0.74 according results obtained from EDAX test for 3%, 5% and 9% (Table 1) respectively. Thus, for hydrocarbon contaminated clay, percentage of K-ions is increasing significantly, leading to reduction in swelling characteristics.

5 Conclusions

The above study aimed at correlating index properties of non-contaminated marine clay and hydrocarbon contaminated marine clay with electrical resistivity. From the plots and results, it can be seen that hydrocarbon contamination leads to change in electrical properties, index properties and consolidation properties. Although the reactivity of Dodecane is not very high but when it contaminates the clay, some reactions however take place leading to physical alterations of clay property. Low reactivity of Dodecane can be attributed to the fact that it consists of long chain of carbon atom whose tetra-valence is satisfied by each hydrogen atom and thus satisfying charges. Dodecane however has a huge structure and thus it leads to physical alternations in clay structure. Chemical changes are not very considerable.

- Electrical resistivity value for 3% hydrocarbon contaminated bentonite increases by 28% in comparison to non-contaminated clay. The linear equation, using linear regression model, obtained for 3% of hydrocarbon contamination for electrical resistivity v/s period of contamination is; $y = -0.0138x + 3.915$, $R^2 = 0.9726$. R^2 value is close to 1 which states that it is a good co-relation. And through the equation, it can be inferred that by increasing value of x, y value will decrease by 0.0138 times.
- Electrical resistivity value for 6% hydrocarbon contaminated bentonite increases by 40% in comparison to non-contaminated clay. The linear equation, using linear regression model, obtained for 6% of hydrocarbon contamination for electrical resistivity v/s period of contamination is; $y = -0.0215x + 4.540$, $R^2 = 0.9728$. R^2 value is close to 1 which states that it is a good co-relation. And through the equation, it can be inferred that by increasing value of x, y value will decrease by 0.0215 times.
- Electrical resistivity value for 9% hydrocarbon contaminated bentonite increases by 33% in comparison to non-contaminated clay. The linear equation, using linear regression model, obtained for 9% of hydrocarbon contamination for electrical resistivity v/s period of contamination is; $y = -0.0182x + 4.215$, $R^2 = 0.924$. R^2 value is close to 1 which states that it is a good co-relation. And through the equation, it can be inferred that by increasing value of x, y value will decrease by 0.0182 times.

  Electrical resistivity value increases when percent of hydrocarbon contamination increases from 3% to 6% as hydrocarbon hinders with ion-exchange mechanism leading to higher resistivity values. But when % of contamination further increases from 6% to 9%, there is a decrease in resistivity which can be explained by the following philosophy: when hydrocarbon comes in contact with clay-water system, it acts as a barrier for ion exchange process. Increasing the rate of hydrocarbon contamination further i.e. from 3% to 6% increases the resistivity. But with further

increase in rate of hydrocarbon, i.e. from 6% to 9%, there is a decrease in resistivity value as the abundance of hydrocarbon layer compels or pushes the un-exchanged ion present at distance from clay surface which leads to exchange of those positively charged ions with that of negatively charged clay ions and thus reducing resistivity value.

- The linear equation obtained for electrical resistivity v/s liquid limit; $y = -0.0130x + 7.4593$ ($R^2 = 0.9223$), $y = -0.0165x + 8.4079$ ($R^2 = 0.951$), $y = -0.0156x + 8.2297$, ($R^2 = 0.9347$) for 3%, 6% and 9% of hydrocarbon contamination respectively. It can be thus inferred that y value (electrical resistivity) will decrease for increase in value of x variable by 0.0130, 0.0165 and 0.0156 for 3%, 6% and 9% of hydrocarbon contamination respectively.
- The linear equation obtained for electrical resistivity v/s plastic limit; $y = 0.0853x - 6.5452$ ($R^2 = 0.9589$), $y = 0.1232x - 11.546$ ($R^2 = 0.951$), $y = 0.1129x - 9.8498$ ($R^2 = 0.9171$) for 3%, 6% and 9% of hydrocarbon contamination respectively. The linear equation obtained for electrical resistivity v/s shrinkage limit; $y = -0.1134x + 5.6635$ ($R^2 = 0.9926$), $y = -0.1035x + 8.1591$ ($R^2 = 0.9797$), $y = -0.0954x + 5.8339$ ($R^2 = 0.7714$) for 3%, 6% and 9% of hydrocarbon contamination respectively. The linear equation obtained for electrical resistivity v/s specific gravity; $y = -2.0298x + 7.1627$ ($R^2 = 0.9744$), $y = -2.024x + 7.3326$ ($R^2 = 0.9938$), $y = -1.6302x + 6.369$ ($R^2 = 0.8909$) for 3%, 6% and 9% of hydrocarbon contamination respectively. The linear equation obtained for electrical resistivity v/s FSI; $y = -0.0805x + 7.5172$ ($R^2 = 0.755$), $y = -1159x + 9.1807$ ($R^2 = 0.9293$), $y = -0.0844x + 7.3716$($R^2 = 0.8215$) for 3%, 6% and 9% of hydrocarbon contamination respectively. The electrical resistivity increases with decrease in free swell index.
- Above study reveals that electrical resistivity can be used to correlate various index properties of non-contaminated and hydrocarbon contaminated marine clay being a non-destructive tool which can be economical as well as time saving and there is a major influence of hydrocarbon contamination on engineering behavior of clays. This leads us advance assessment of influence of both percentage contamination and periodic contamination on strength characteristics of such marine clays. India's coastal belt is highly influenced by oil and gas spillages and other volatile toxic and non-toxic intrusion of chemicals demands geotechnical engineer to study the engineering behavior of clays by adapting various types of geophysical methods simulating true field conditions.

Presently many coastal part of many countries are facing oil-gas spillage contamination problems, where such co-relations can be very much useful in interpretation of soil characterization. Further hydrocarbon contaminated soil samples collected through boreholes at varied depths can be brought to the laboratory and instead of extensive, conventional and destructive soil investigation methods, electrical resistivity is more handy and rapid tool to determine indirectly index and engineering properties of such

soft expansive marine clays. There are numerous types of hydrocarbons, some of which are very complex in nature, whose assessment should be done thoroughly so as to know its long term influence on engineering behavior of clays. Mostly, statistical analysis of such relevant data may not be useful every time unless the soil characterization is done through method like electrical resistivity which replicates soil-water-hydrocarbon interaction.

References

Oh, T.-M., Cho, G.-C., Lee, C.: Effect of soil mineralogy and pore-water chemistry on the electrical resistivity of saturated soils. J. Geotech. Geoenviron. Eng. ASCE, ISSN 1090-0241/06014012(5)

Influence of Hydrologic Information on Shallow Foundation Design and Analysis in Arid Climates

Nadarajah Ravichandran(✉), Ashok Mishra, Shweta Shrestha, and Parishad Rahbari

Glenn Department of Civil Engineering, Clemson University, 202 Lowry Hall, Clemson, SC 29634, USA
{nravic, ashokm}@clemson.edu, {shwetas, prahbar}@g.clemson.edu

Abstract. The hydrological parameters such as rainfall and water table depth influence the degree of saturation of the near surface soil which indeed alters the strength and deformation parameters of the soil. Therefore, geotechnical design of shallow foundation especially in arid climate must incorporate the hydrological parameters for designing and constructing economical and resilient infrastructure systems. In this study, a simplified approach based on a probabilistic method for computing the ultimate bearing capacity of shallow foundation considering site specific historical rainfall and water table data is proposed. The infiltration of water into an initially partially saturated soil was modeled using one-dimensional Richard's equation and the Vanapalli et al. (1996) equation, which incorporates both matric suction and degree of saturation, was used to compute the ultimate bearing capacity. The randomness in soil moisture due to seasonal variation over a long period of time was considered systematically using the Monte Carlo simulation technique. The results show that the ultimate bearing capacity computed using the proposed method is significantly larger than that computed assuming fully saturated soil condition.

Keywords: Unsaturated soil · Shallow foundation design · Coupled hydrological-geotechnical design · Monte carlo simulation · Ultimate bearing capacity

1 Introduction

Shallow foundations are commonly used for supporting small to medium size structures since they are economical and easy to design and construct. The design and analysis of shallow foundation require the properties of near surface soil and they are typically determined from subsurface exploration program. In most cases, the influence zone of shallow foundation for a medium to small structure lies above the water table and the soil in the influence zone is unsaturated. Researchers have proven that the properties of unsaturated soil are function of degree of saturation and are different from that of saturated or dry soils which are special cases of general soil condition. The unsaturated soil properties cannot be directly derived from these extreme special cases.

L.R. Hoyos and J. McCartney (eds.), *Advances in Characterization and Analysis of Expansive Soils and Rocks*, Sustainable Civil Infrastructures,
DOI 10.1007/978-3-319-61931-6_12

Hydrologic variables such as rainfall, evapotranspiration and groundwater depth play an important role in modulating unsaturated soil properties (e.g., hydraulic conductivity, shear strength and compression parameters) and ultimately affecting the performance of shallow foundations. The internal soil strength can be reduced due to increase in rainfall that infiltrates into the ground that destabilizes the soil mass by inducing positive pore pressures.

Similarly, the transition of extreme climates (e.g., extreme drought to extreme flood) is likely to alter the subsurface soil properties and may lead to foundation failures. For example, record historical rainfall extremes after severe drought during 2015 in South Carolina, USA, resulted in significant number of dam failures, structural distress due to differential settlement of supporting foundations at various locations and other structural and geotechnical system failures. Intense and prolonged rainfall events can cause shallow landslides as infiltrating water reduces soil strength and may lead to abrupt mass release. Similarly, the small scale rainfall variability may play a key role in shaping landslide patterns. The rapid shallow landslides in mountainous regions are attributed to high intensity and long duration rainfall events.

Since shallow foundations transfer structural load to near surface soil, the shear strength and compression parameters of the near surface soil influence the design outcomes i.e., the size of the footing. In practice, shallow foundations are designed for the worst case geotechnical conditions which assume that the soil is fully saturated with the water table at the ground surface. Although such assumptions are valid for many practical situations, there are locations in arid climates where the water table is well below the influence depth of the shallow foundation during the lifetime of the structure and the soil never gets fully saturated. The size and extent of the near-surface unsaturated soil zone are highly sensitive to perturbations in location or regional climate. Precipitation, evaporation and evapotranspiration are all the important natural environmental mechanisms that act to influence the depth and extent of the unsaturated zone. Figure 1 shows different components of hydrologic cycle that modulates unsaturated soil properties in the influence zone of a shallow foundation. For those situations, the assumption of fully saturated soil will obviously result in safe but uneconomical conservative designs. Therefore, a new design procedure that considers the near surface soil as unsaturated soil could be developed for economical designs.

The recent developments in understanding the unique hydro-mechanical behaviors of unsaturated soils support the idea of developing procedures and theories to design shallow foundations treating the near surface soil as unsaturated wherever applicable. In this study, we developed a new framework using theories associated with partially saturated soils to evaluate deformation properties of near surface partially saturated soils based on the hydrologic variables, such as rainfall events, evapotranspiration and depth of water table. The proposed framework is then applied for computing the ultimate bearing capacity of shallow foundations using hydrologic information, geotechnical and hydraulic properties of the supporting soil. Finally, design examples considering two sites in the United States are used to demonstrate the proposed procedure.

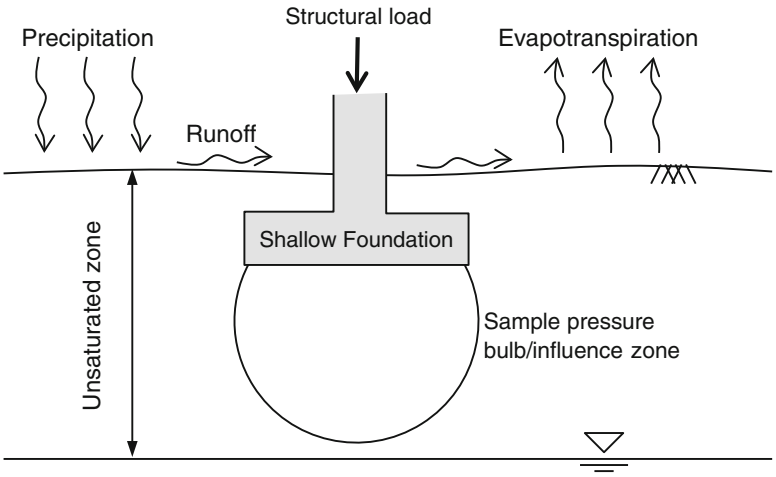

Fig. 1. Different components of hydrologic cycle that modulates soil properties in the influence zone of a shallow foundation

2 Methodology

2.1 Basic Theory

The ultimate bearing capacity of a shallow foundation for conventional design is typically computed using either Terzaghi's (Terzaghi 1943) ultimate bearing capacity equation or Meyerhof's (Meyerhof 1963) general bearing capacity equation presented in Eq. (1). In additional to bearing capacity factors, the general bearing capacity equation consists of shape, depth and load inclination factors to overcome the limitations of Terzaghi's equation.

$$q_u = c'N_c(F_{cs}F_{cd}F_{ci}) + qN_q\left(F_{qs}F_{qd}F_{qi}\right) + \frac{1}{2}B\gamma N_\gamma\left(F_{\gamma s}F_{\gamma d}F_{\gamma i}\right) \tag{1}$$

where c' is the cohesion of soil, γ is the unit weight of the soil, q is the effective overburden pressure at the bottom of the footing ($q = \gamma D_f$), B is the width of footing, N_c, N_q and N_γ are the bearing capacity factors that are non-dimensional and functions of the soil friction angle ϕ', and F_{-s}, F_{-d} and F_{-i} are the shape, depth and load inclination factors, respectively.

Both Terzaghi's and Meyerhof's equations were derived considering the general shear failure mechanism and resistance along the failure surfaces based on the saturated soil mechanics principles. However, recent studies show that the shear strength of soils (resistance along a failure surface) varies with degree of saturation (Steensen-Bach et al. 1987; Oloo et al. 1997; Costa et al. 2003; Rojas et al. 2007; Vanapalli and Mohamed 2007; Sheng 2011). The foundations designed using Eq. 1 are often conservative for sites which may not reach the fully saturated condition during the life time of the structure supported by it. Recently, the need for incorporating the unique features

of unsaturated soils, particularly the effect of matric suction in geotechnical engineering practice was summarized by many researchers (Fredlund 2006; Lu and Lokos 2004; Briaud 2013) with practical examples. In one of the notable experimental studies related to shallow foundation, Mohamed and Vanapalli (Mohamed and Vanapalli 2006) showed that the bearing capacity of a square model footing on a coarse-grained soil under a unsaturated condition is approximately five to seven times higher than the bearing capacity under fully saturated condition. Uchaipichat and Man-koksung (2011a) showed that the ultimate bearing capacity increases with matric suction for all ranges of suction based on their laboratory experiments on clayey soils. Another study on granular soils by the same authors Uchaipichat and Man-koksung (2011b) showed that the ultimate bearing capacity increases with increasing matric suction at low suction value but decrease at high level of suction. In order to take advantage of the higher capacity of the unsaturated soil, it is important to understand the unique concepts associated with unsaturated soil along with the rainfall, evapotranspiration and water table fluctuation data over a period of time.

The equation for the ultimate bearing capacity that considers the effect of suction in shear strength proposed by Fredlund and Rahardjo (Fredlund and Rahardjo 1993) is shown in Eq. 2.

$$q_u = \left[c' + (u_a - u_w)\ \tan\ \phi^b\right] N_c + qN_q + \frac{1}{2}\gamma B N_\gamma \tag{2}$$

The variable ϕ^b indicates the rate of increase in shear strength with respect to a change in matric suction. The direct application of Eq. 2 requires ϕ^b and matric suction. As the matric suction is related to the degree of saturation through the Soil Water Characteristics Curve (SWCC) and the availability of fitting parameters for many SWCC models, researchers have proposed to use SWCC in the bearing capacity equation to eliminate the need for calculating ϕ^b (Vanapalli et al. 1996; Vanapalli and Mohamed 2007). Particularly, Vanapalli and Mohamed (Vanapalli and Mohamed 2007) suggested a semi empirical equation modified from the initial equation proposed by Vanapalli et al. (Vanapalli et al. 1996) in the following form.

$$\begin{aligned} q_u = {} & \left[c' + (u_a - u_w)_b\left(\tan\phi' - S^\psi \tan\phi'\right) + (u_a - u_w)_{ave} S^\psi \tan\ \phi'\right] N_c F_{cs} F_{cd} \\ & + \gamma D_f N_q F_{qs} F_{qd} + 0.5\gamma B N_\gamma F_{\gamma s} F_{\gamma d} \end{aligned} \tag{3}$$

where $(u_a - u_w)_b$ = air entry value which can be computed from the SWCC of the soil, $(u_a - u_w)_{ave}$ is the average air-entry value, S is the degree of saturation and ψ is the bearing capacity fitting parameter given by:

$$\psi = 1.0 + 0.34\left(I_p\right) - 0.0031\left(I_p\right)^2 \tag{4}$$

where I_p is the plasticity index of the soil. The average matric suction in the above bearing capacity equation is given by:

$$(u_a - u_w)_{ave} = \frac{1}{2}\left[(u_a - u_w)_1 + (u_a - u_w)_2\right] \quad (5)$$

where $(u_a - u_w)_1$ is the matric suction at the bottom of the footing and $(u_a - u_w)_2$ is the matric suction at a depth equal to 1.5 times the width of the footing (1.5 * B).

2.2 Need for Integrating Hydrologic Data in Geotechnical Design of Shallow Foundation

Thorough examination of the above equations reveals that the ultimate bearing capacity of a shallow foundation varies with the degree of saturation (or matric suction) of the soil in the influence zone. If the design degree of saturation for the site is known, the ultimate bearing capacity can be calculated and the foundation can be designed accordingly using the above or other equations. Obtaining representative design degree of saturation value for a site requires incorporation of hydrologic data such as historical rainfall, evapotranspiration and depth of water table in a systematic manner. In this study, a simplified approach which takes into account the site specific hydrologic data is presented. It should be noted that the proposed framework uses the ultimate bearing capacity proposed by Vanapalli et al. (1996) but any other equation which is a function of matric suction can be used instead.

2.3 Integration of Hydrologic Information

General Framework

The hydrologic information affects the shallow foundation design indirectly through matric suction and/or degree of saturation of the soil within the influence zone as shown in Eqs. 2 through 5. The rain water infiltrates into the ground during rainy season resulting in downward movement of wetting front and evaporates during dry season resulting in downward movement of drying front. Therefore, the key component in developing accurate numerical procedure should incorporate the rate of infiltration considering precipitation, evaporation, surface runoff and ponding information and rate of flow through the unsaturated zone considering flow properties which vary with degree of saturation. It should also be able to model the rise and fall of water table location. Considering the infiltration as the top boundary condition, the change in hydraulic head (or matric suction) in the unsaturated zone can be computed using Richard's equation. Since hydrologic variables vary randomly over the lifetime of the foundation, a method that predicts their representative values considering the randomness in them must be employed. In addition, the unit weight of the soil within the influence zone which is a function of degree of saturation also changes with hydrologic data and must be considered as a random variable. In this study, the Monte Carlo simulation technique is employed to compute the matric suction considering the random variations in the hydrologic parameters and then to compute the ultimate bearing capacity of square and continuous shallow foundations at selected depths. The results are expressed as probability of failure for different return periods of rainfall. The

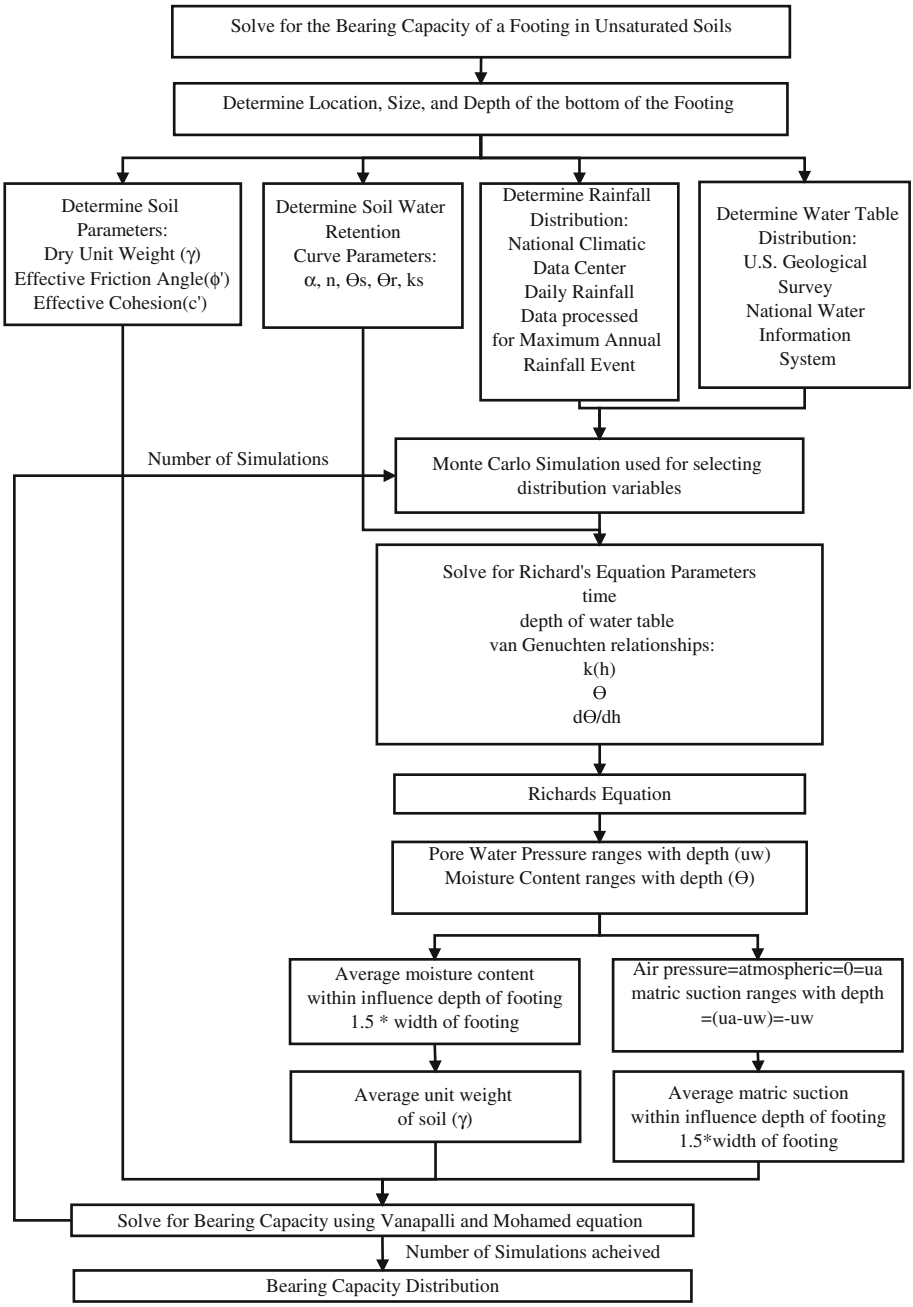

Fig. 2. Flow chart for the simulation

flowchart of the procedure employed in this study is presented in Fig. 2. The details of collection of hydrologic data and their incorporation in the design are presented in the succeeding sections.

Hydrologic Data Collection

The daily rainfall data obtained from the NOAA (National Oceanic and Atmospheric Administration) weather stations are utilized to derive precipitation frequency estimated by analyzing annual maximum series or partial duration series (Perica et al. 2011). Annual maximum series were used in this study and were constructed by extracting the highest precipitation amount for a particular duration in each successive year of record. A water-year starting on October 1 of the previous calendar year and ending on September 30 would be another typical option for selecting the maximum rainfall during a period of time. The data over a selected period of time can be fitted with widely used distributions such as the Frechet Distribution (Type II Extreme Largest), Gumbel Distribution (Type I Extreme Largest), Weibull Distribution (Type III Extreme Largest), Normal distribution and Lognormal distribution to determine the largest event, in this case for a selected returned period.

Temperature-based or radiation-based methods are commonly used to calculate the evapotranspiration which is the loss of moisture through the soil surface and through plants. Low resolution satellites such as NOAA-AVHRR and TERRA-MODIS can also provide daily evapotranspiration fluxes in a clear sky (Jhorar et al. 2004) which can be used to determine suction changes in the soil. It should be noted that the evapotranspiration near the foundation for small structures such as residential buildings may be significant because of dense plants and may also be neglected if the surface is paved as seen in commercial buildings.

The water table depth is used as the bottom boundary condition which affects the matric suction of an unsaturated soil. The U.S. Geological Survey (USGS), National Water Information System, provides data about the water table depths over numerous years at different locations (U.S. Geological Survey 2012). It is important to note that the water table data can only be determined in unconsolidated sand and gravel aquifers. There are over 26,135 sites in these types of aquifers with 50 or more data points. The locations of these wells are shown in Fig. 3. Fortunately, numerous wells are in locations with dry climates and unsaturated soils in the continental United States. Similar records may be available for other parts of the world.

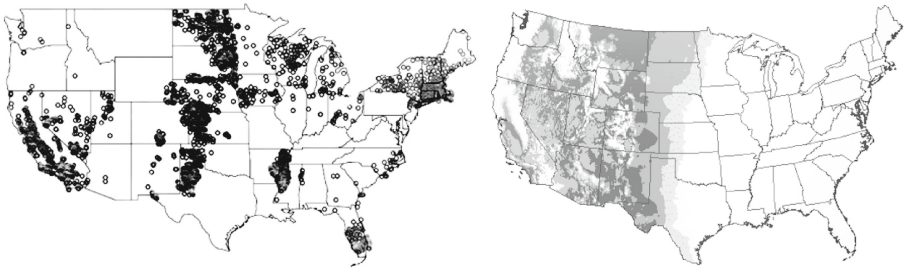

(a) (b)

Fig. 3. (a) Location of USGS wells in the continental US, and (b) Regions with dry climate

The data over a selected period of time can be fitted with widely used distributions such as the Frechet Distribution (Type II Extreme Largest), Gumbel Distribution (Type I Extreme Largest), Weibull Distribution (Type III Extreme Largest), Normal distribution and Lognormal distribution. They can then determine the largest event and the shallowest water table for a selected return period. The ground water table is treated as the bottom boundary condition for solving the Richard's equation. It should be noted that if the water table is too deep compared to the influence zone (pressure bulb) of the foundation, it may be ignored.

Computation of Matric Suction Using Richard's Equation by Incorporating Hydrologic Data

Considering the rainfall, evapotranspiration and surface runoff, the rate of infiltration (influx) can be computed and it can then be used to compute the matric suction in the soil using Richard's equation. With the distributions of infiltration and water table, variations in matric suction can be quantified. Matric suction is directly related to the hydraulic head (h_w) of the soil as follows:

$$(u_a - u_w) = 0 - (h_w - y)\rho_w g \tag{6}$$

where u_a is the atmospheric pressure, y is the gravitational head and ρ_w is the density of water.

The flow behavior of water in unsaturated soil is complex compared to the saturated soil because of the variation in hydraulic head with time and depth. The variation in hydraulic head with time and depth due to an infiltration event with the ground water table set at the datum can be solved using Richard's equation.

$$\frac{\partial\theta}{dh}\frac{dh}{dt} = \frac{\partial}{\partial z}\left[k(h)\left(\frac{dh}{dz} + 1\right)\right] \tag{7}$$

where $\frac{\partial\theta}{dh}$ is the water capacity function.

The hydraulic conductivity in Eq. 7 can be substituted by the equation proposed by van Genuchten (van Genuchten 1980) as shown below.

$$K(h) = \frac{\left\{1 - (\alpha h)^{n-1}\left[1 + (\alpha h)^n\right]^{-m}\right\}^2}{\left[\left[1 + (\alpha h)^n\right]^{-m}\right]^{m/2}} \tag{8}$$

$$\frac{d\theta}{dh} = \frac{-\alpha m(\theta_s - \theta_r)}{1 - m}\Theta^{1/m}\left(1 - \Theta^{1/m}\right)^m \tag{9}$$

where θ_r is the residual water content, θ_s is the saturated water content, α is the approximation of the inverse of the pressure head at which the SWCC becomes the steepest, Θ is the dimensionless water content and n and m are fitting parameters (typically $m = 1 - 1/n$) and are determined by fitting the experimental SWCC with the model.

With these parameters and initial hydraulic head, the Richard's equation can be solved numerically by the finite difference method. The one-dimensional simulation domain with spatial discretization is shown in Fig. 4. The Crank-Nicolson scheme

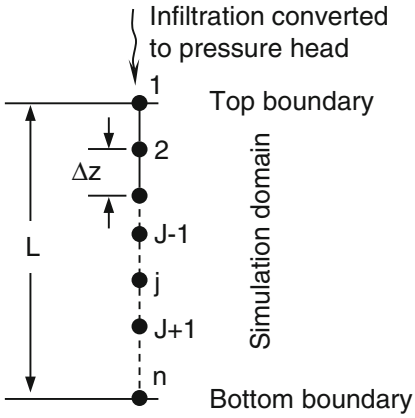

Fig. 4. Spatial discretization of simulation domain

implemented in Bolster and Raffensperger's Matlab program to solve Richard's equation was implemented in the Monte Carlo simulation algorithm in this study. The result is the variation in hydraulic head which can be used for computing $(u_a - u_w)_{ave}$ term in the bearing capacity equation.

The average air entry value,$(u_a - u_w)_B$ is the other type of suction that must be solved for. This is inversely proportional to the van Genuchten soil parameter α as given by the following equation.

$$(u_a - u_w)_B = \left[\frac{1}{\alpha}\right]\gamma_w \tag{10}$$

where γ_w is the unit weight of water.

Computation of Unit Weight by Incorporating Hydrologic Data

The unit weight of the soil which is another variable that affects the ultimate bearing capacity of a shallow foundation varies with degree of saturation of the soil. The following form of the van Genuchten (1980) equation can be used to relate the moisture content to the hydraulic head which is the solution from Richard's equation.

$$\theta = \theta_r + \frac{(\theta_s - \theta_r)}{[1 + (\alpha h)^n]^m} \tag{11}$$

Using the same method for calculating the $(u_a - u_w)_{ave}$, the average moisture in the soil within the influence depth of the footing (1.5* B) can be calculated by the following equation.

$$\theta = \left[\frac{(\theta)_1 + (\theta)_2}{2}\right] \tag{12}$$

Then, the average degree of saturation (S) in the influence area can be calculated by:

$$S = \left[\frac{\theta}{\theta_s}\right] \tag{13}$$

since θ_s can be considered equivalent to the porosity of the soil (ϕ).

Thus, the unit weight as a function of degree of saturation can be computed using the basic weight-volume relationship given below.

$$\gamma = \frac{(G_s + Se)\gamma_w}{1 + e} \tag{14}$$

where e is the void ratio and G_s is the specific gravity of the soil solids.

Computation of Ultimate Bearing Capacity, Risk and Probability of Failure

With the matric suction and unit weight values, Eq. 3 can be solved for with the predetermined number of Monte Carlo Simulations. Through numerous studies with different numbers of simulations, the location and shape parameters are checked for convergence. The converged data from the Monte Carlo simulation better represents the ultimate bearing capacity for the foundation. With the data collected from the Monte Carlo simulation, a cumulative distribution function (CDF) of the ultimate bearing capacity can be used to make risk assessments.

Design risk is quantified by the product of probability of failure and the consequence of failure. Calculating the consequences of failure is difficult for practicing engineers, thus current practice for foundations in reliability based design accounts for the consequence of failure indirectly by prescribing different target probabilities of failure (Kulhawy et al. 2012). The reliability index (β), which is the inverse standard normal cumulative function of the probability of failure is the prescribed value usually published. The Canadian Building Code uses a target β= 3.5 for superstructures and their foundations. AASHTO uses a target $\beta = 3.5$ for the superstructure and target β values from 2.0 to 3.5 for the foundations. For this paper a probability of failure of 10^{-4} was selected to enable the bearing capacity to be read from the CDF. This is equivalent to a $\beta = 3.7$, which exceed the Canadian Building Code and AASHTO target values. Figure 2 is a flow chart that outlines the method used to calculate the bearing capacity of unsaturated soil.

A cumulative distribution function (CDF) of the soil bearing capacity considering the uncertainty in the suction terms can be used to determine the failure probability of the footing. A bearing capacity with a probability of 10^{-4} can be selected from the CDF to follow traditional civil engineering probability of failure expectations for a typical structure. Failure of the footing is assumed to occur when the bearing capacity of the soil is less than the pressure caused by the column load. It should be noted that in addition to the variability in the suction terms, the inherent randomness of the soil parameters (e.g. friction angle and unit weight, due to spatial and testing variability)

also affects the bearing capacity. In this paper, soil parameter distributions are not considered since the primary interest is to understand how the unsaturated terms in the equation affect the selection of a bearing capacity for real world sites. Figure 2 is a flow chart that outlines the method used to calculate the ultimate bearing capacity of shallow foundation in unsaturated soil.

3 Applications to Two Different Geographical Locations

Two study areas were selected to show the effect of hydrologic data on the ultimate bearing capacity of shallow foundation in this paper. The geotechnical and hydrologic data for each site and their utilization are presented in the succeeding sections.

3.1 Study Area 1: Victorville, CA

Site Specific Geotechnical Data

Victorville, CA was selected due to its arid climate and the availability of the van Genuchten SWCC parameters for the Adelanto Loam present in this region. The van Genuchten parameters for the Adelanto Loam were taken from the report by Zhang (Zhang 2010). The soil strength parameters for the site were obtained from a geotechnical engineering report by Kleinfelder (Chowdhury 2006). For the soil, the dry unit weight at a depth of 1.52 m is 16.19 kN/m^3, friction angle is 33 degrees and cohesion is zero. The USCS soil classification for the soil at 1.52 m is SM. The SWCC and strength parameters are listed in Table 1.

Site Specific Water Table Data and the Largest Event

The water table data was taken from the U.S. Geological Survey National Water Information System: Web Interface (U.S. Geological Survey 2012). The water table depth was recorded between the years of 1930 and 1958. To determine the best-fit distribution for the water table data the probability paper plotting technique was used. For this case, the Gumbel Distribution (Type I Extreme Largest), Weibull Distribution (Type III Extreme Largest), Normal distribution, and Lognormal distribution were checked for the best fit. The Gumbel distribution had the best fit and used for return period analysis. The probability plot of the water table data for the Gumbel distribution is shown in Fig. 5(a). Using Eq. 15, it can be determined that the Gumbel distribution parameters are $\mu_n = 43.916$ and $\beta_n = 0.7912$.

$$-\ln\left(-\ln\left(\frac{i}{n+1}\right)\right)\beta_n + \mu_n = x_i \tag{15}$$

where x_i is the annual maximum water table data and n is the number of data points. The calibrated model can be used to compute the largest event for a selected return period.

Table 1. van Genuchten and strength parameters for the Victorville, CA and Levelland, TX sites

Parameters	Victorville, CA	Levelland, TX
Saturated volumetric water content, θ_s	0.423	0.385
Irreducible volumetric water content θ_r	0.158	0.117
Model parameter, α (m^{-1})	0.321	3.34
Model parameter, n	2.11	1.207
Hydraulic conductivity, k_s (cm/hr)	0.20952	0.043
Dry unit weight, γ_d (kN/m^3)	16.20	18.56
Void ratio, e	0.605	0.401
Friction angle, ϕ (deg)	33	25
Cohesion, c	0	0
Air entry value, $(u_a - u_w)_b$ (kPa)	14	1.5

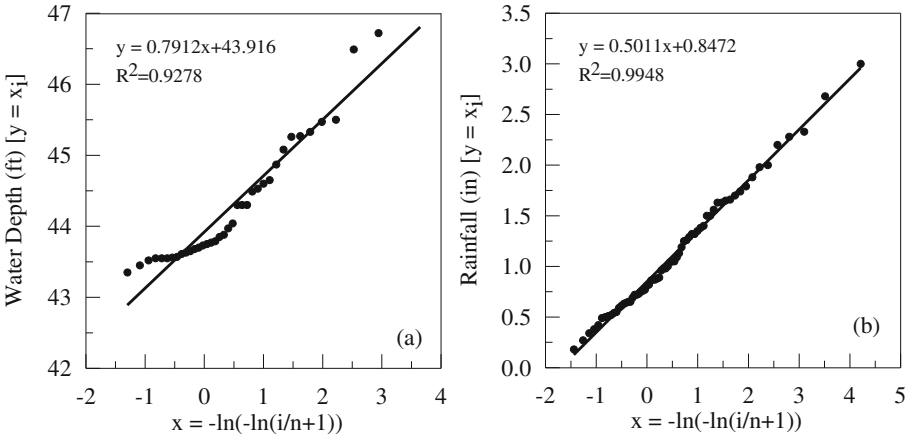

Fig. 5. Type I Extreme Largest (Gumbel distribution) for water table depth and rainfall data for Victorville, CA

Site Specific Rainfall Data and the Largest Event

The rainfall data from 1938 to 2014 was taken from the Victorville Pump Station within climate division CA-07. This station has been in service since November 1, 1938. The elevation of the station is 871 m (2858 ft) above mean sea level. The latitude and longitude of the station is 34° 32' 00" N and 117° 17' 34" W, respectively. The data for the pump station was processed from an ASCII file that was downloaded from the National Climatic Data Center (National Climatic Data Center 2012). The maximum rainfall in inches during a year was tabulated for each year from 1938–2014. Years where data was not recorded for all 365 days were removed from the data set. This prevents non-rainy season maximum yearly values from affecting the overall distribution. Out of 72 years, a total of 6 years was excluded from the data set. To determine the best fitting distribution for the rainfall data, the probability paper plotting

technique was used. The Type II Extreme Largest (Frechet distribution), Type I Extreme Largest (Gumbel distribution) and the Type III Extreme Largest (Weibull distribution) were checked for the best fit. The Gumbel distribution was deemed the best fit based on R^2 values. The probability plot of rainfall data for the Gumbel distribution is shown in Fig. 5(b). Using the Gumbel distribution, the CDF was transformed into a linear equation shown below. It can be determined that the location parameter, $\mu_n = 0.8472$ and the shape parameter $\beta_n = 0.5011$. The calibrated model can be used to compute the largest event for a selected returned period.

The worst case scenario was considered with no runoff or pooling of water (maximum infiltration) and no evapotranspiration (no loss of moisture from the simulation domain). However, surface runoff and evapotranspiration can be easily included in the proposed procedure easily by quantifying their values, subtracting from the total rainfall and then fitting with appropriate distribution to compute the largest event. This infiltration is the influx to the unsaturated zone and treated as the boundary condition at the top of the simulation domain for solving Richard's equation.

With the known initial conditions, rate of infiltration, water table location and hydraulic properties of the soil the moisture content in the soil was computed using Richard's equations. The moisture content was then used to compute the ultimate bearing capacity of the soil using Eq. 3. Finally the probability of failure was computed. Further detail is given below.

Monte Carlo Simulation

An example of the bearing capacity problem was calculated for a square 1.07 m (3.5 ft) footing embedded in the ground 0.61 m (2 ft) in Victorville, California. This example was extended to determine if the new dominating cohesion component $\left(\left[c' + (u_a - u_w)_b\left(\tan\ \phi' - S^{\psi}\tan\ \phi'\right) + (u_a - u_w)_{AVR}S^{\psi}\tan\phi'\right]N_c F_{cs} F_{cd}\right)$ in the bearing capacity equation was being controlled by the cohesion depth factor term:

$$F_{cd} = 1 + 0.4\left(\frac{D_f}{B}\right) \tag{16}$$

To determine influence of the depth of influence zone which is a function of the width and the depth of shallow foundation and the depth factor, the bearing capacity of three example footings were computed and compared. For the first example, the footing width, B, was increased from 1.07 to 1.52 m (3.5 to 5 ft). Another example kept the D_f/B ratio equal to the initial footing size and depth, thus B = 1.52 m, D_f = 0.87 m. The last example allowed B to remain equal to 1.07 m and increase the D_f to 0.87 m.

The convergence of the mean and the coefficient of variation for the bearing capacity distributions with the number of simulations are plotted in Fig. 6. At 10,000 simulations there is evidence of a convergence for each of the different example footings. The mean is the location parameter and the coefficient of variation takes into account the shape factor, with both of these measurements of the distribution converging, it can be understood that the empirical CDF created from the Monte Carlo simulations accurately represents the bearing capacity for the example footing in Victorville, California.

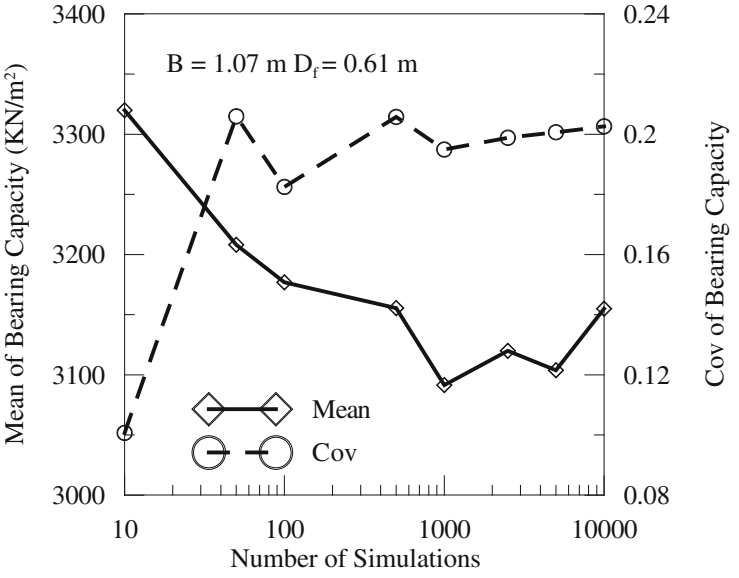

Fig. 6. Number of simulations versus the mean and coefficient of variation

Case 1: Evaluation of Bearing Capacity and Probability of Failure

The CDFs created for each of the example footings using 10,000 simulations are plotted in Fig. 7. The bearing capacity for the footing at a probability of failure of 10^{-4} is recorded in Table 2. To determine if taking into account unsaturated soils is meaningful to bearing capacity analysis, Meyerhof's equation was used to calculate the bearing capacity of the footing assuming the soil to be fully saturated (Table 1) and compared with the bearing capacity calculated with unsaturated soil mechanics principles. The percent increase in bearing capacity by taking into account unsaturated soils

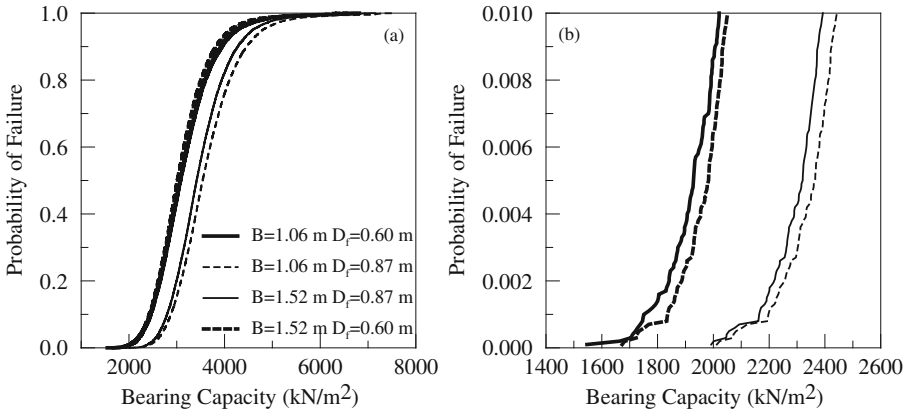

Fig. 7. Bearing capacity versus probability of failure for all systems in Victorville, CA

Table 2. Computed bearing capacities for Victorville, CA

Case	L (m)	B (m)	D_f (m)	Deterministic method assuming fully saturated condition (KN/m^2)	Monte Carlo simulation assuming unsaturated condition (KN/m^2)	Percent increase
1	1.07	1.07	0.61	419	1548	269
2	1.07	1.07	0.87	574	2013	251
3	1.52	1.52	0.61	455	1673	268
4	1.52	1.52	0.87	598	1992	233

are also recorded in Table 2. From the results tabulated in Table 2, it is evident that the depth factor in the cohesion term has a significant influence in the bearing capacity equation. The simulation with the highest bearing capacity was the footing with the 1.07 m width and the depth of 0.87 m (case 2). This is a larger bearing capacity than the larger footing at the same depth. This shows that a smaller depth factor has more influence than a larger footing. It is clearly evident that the bearing capacity of the soil is significantly affected by the matric suction and the variation of unit weight. All the bearing capacities for the different example footings have increased by over 233%.

Case 2: Effect of Return Period on Ultimate Bearing Capacity

To determine how the return period for a distribution affects the bearing capacity of a footing, the square 1.07 m footing embedded in the ground 0.61 m was tested by constraining the rainfall and water table data to return periods between: 1 yr and 2 yrs, 1 yr and 5 yrs, 1 yr and 10 yrs, 1 yr and 50 yrs, 1 yr and 100 yrs, 1 yr and 200 yrs and 1 yr and an infinite number of years.

The effect of the return period (RP) on the bearing capacity for the case 1 footing is plotted in Fig. 8(a). As expected, as the return period decreases the bearing capacity of the footing with a probability of failure of 10^{-4} increases. Figure 8(b) provides a plot

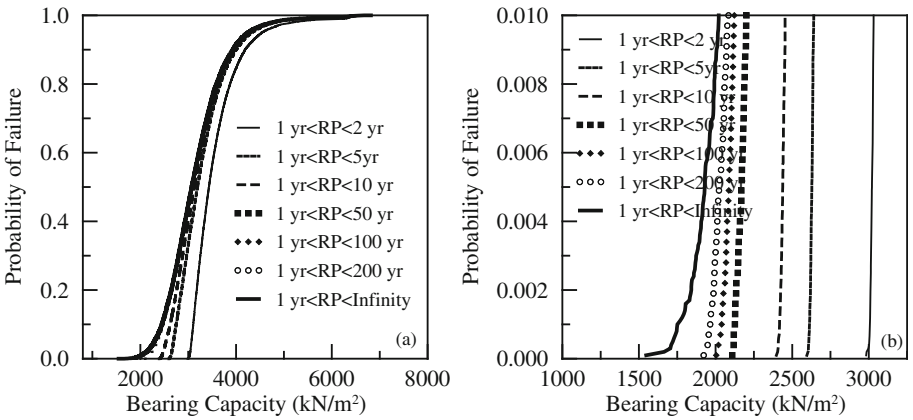

Fig. 8. Bearing capacity versus probability of failure for 1.07 m square footing at a depth of 0.61 m for different return periods in Victorville, CA

that an engineer could use to select a probability of failure for a foundation, the return period for the rain and water table event, and the bearing capacity for the site.

3.2 Study Area 2: Levelland, TX

The soil strength parameters were obtained from a geotechnical report made by Amarillo Testing and Engineering, Inc (Gonzalez 2009). Although the geotechnical engineering parameters were available for this site, the van Genuchten parameters were not available. In this study, the van Genuchten parameters for the Levelland, TX site were obtained from the class average value of hydraulic parameters for the twelve USDA textural classes from the program Rosetta (Schaap et al. 2000). The help index of the program provides a table with values determined through the TXT model, and the lowest of the hierarchical sequences in the model. The values in this table were generated by computing the average value for each textural class. The soil classification in the geotechnical report was used to determine which class the Levelland, TX soil fit best. The soil at the Levelland, TX site was considered to be in the sandy clay textural class. The associated van Genuchten parameters and strength parameters are presented in Table 1.

Presented in Fig. 9 are the Gumbel distribution of the rainfall and water table data at the Levelland, TX site generated following procedure similar to the one used for Victorville, CA.

The results from the first sensitivity analysis with a change in location are recorded in Table 3. The CDF for the simulation is plotted in Fig. 10. It is evident that the bearing capacity of the footing in Levelland, Texas is much lower than the bearing capacity in Victorville, California. To determine if the decrease in bearing capacity is primarily due to a change in the soil strength parameters, comparisons were made between the saturated and unsaturated soil bearing capacities. Even with increased rainfall the soil in Levelland, TX still had an increase in bearing capacity over 76%

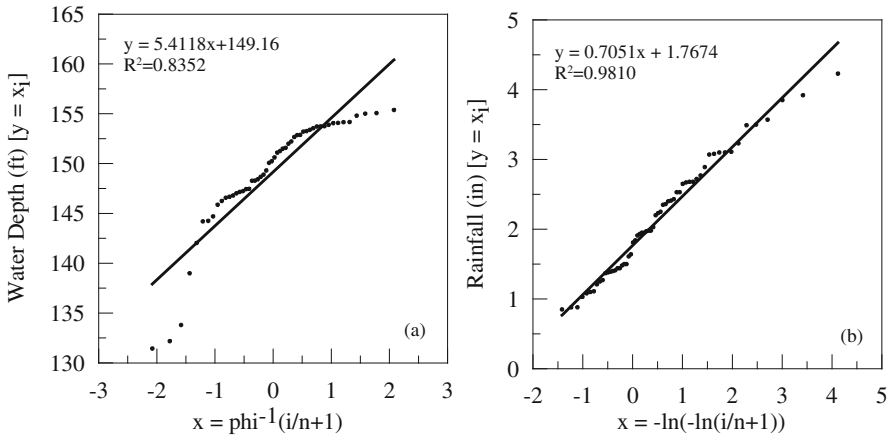

Fig. 9. Extreme Largest (Gumbel distribution) for water table depth and rainfall data for the Levelland, TX site.

Table 3. Computed Bearing Capacities for Levelland, TX

Case	L (m)	B (m)	D_f (m)	Deterministic method assuming fully saturated condition (KN/m^2)	Monte Carlo simulation assuming unsaturated condition (KN/m^2)	Percent increase
1	1.07	1.07	0.61	170	300	76
2	1.07	1.07	0.87	237	418	76
3	1.52	1.52	0.61	181	320	77
4	1.52	1.52	0.87	243	427	76

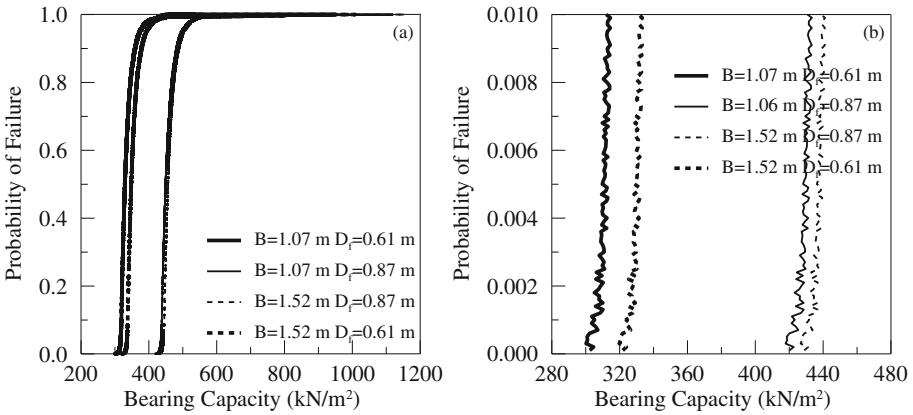

Fig. 10. Bearing capacity versus probability of failure for all systems in Levelland, TX

(Table 3) through the Monte Carlo simulation method. Thus this method is valuable to use in regions that are not excessive dry within the United States.

4 Parametric Study

A parametric study was conducted to further investigate the effect of key parameters other than the hydrological parameters. Although, the geotechnical parameters such as friction angle and cohesion are considered as random variables in the conventional foundation design, in this study the unsaturated soil parameters such as SWCC parameters and the depth of footing which affects the depth of zone of influence are considered as random variables. The details of the study and the results are presented in the succeeding sections.

4.1 Effect of van Genuchten Model Parameters

A sensitivity analysis was performed by testing each van Genuchten parameter determined by the textural class individually. Each parameter was increased by one

Table 4. Computed Bearing Capacities for Victorville and Levelland with Sensitivity Analysis

Site	Parameter	L (m)	B (m)	D_f (m)	Bearing capacity of soil using deterministic methods and assuming fully saturated (KN/m^2)	Bearing capacity of soil using monte carlo simulation (KN/m^2)	Percent increase in bearing capacity
Victorville*	θr	1.07	1.07	0.61	419	869	107
Victorville*	θs	1.07	1.07	0.61	419	879	110
Victorville*	α	1.07	1.07	0.61	419	1415	238
Victorville*	n	1.07	1.07	0.61	419	873	108
Levelland	θr	1.07	1.07	0.61	170	254	49
Levelland	θs	1.07	1.07	0.61	170	305	79
Levelland	α	1.07	1.07	0.61	170	379	123
Levelland	n	1.07	1.07	0.61	170	321	89

*Sandy Loam

standard deviation to determine which parameter plays the largest role in affecting the bearing capacity of shallow footings. Each parameter's one standard deviation increase for both the Victorville, CA site (Sandy Loam) and the Levelland, TX site is summarized in Table 4. This analysis also allows for a discussion of how important it is to have accurate SWRC for this type of method for calculating bearing capacity.

The sensitivity analysis of the van Genuchten parameters was tested by comparing the bearing capacities of the Victorville (Adelanto Loam) and the Victorville (Sandy Loam) sites. The bearing capacity for the case 1 footing for the Victorville (Adelanto Loam) is 1548 KN/m^2. The bearing capacity for the same footing for the Victorville (Sandy Loam) is 872 KN/m^2. All the footing sizes and depth have similar changes (refer to Tables 2 and 4). The changes in parameters also affected the distribution of bearing capacities computed form the Monte Carlo simulation. Comparing Figs. 7, 8, 9 and 10 it is noticeable that the CDFs are much steeper. Though the rainfall and water table distributions are very important, this sensitivity analysis revealed, as expected, that the SWRC parameters are equally important in accurately predicting the increase in bearing capacity in this probabilistic method.

Based on the individual sensitivity analysis for each parameter, the parameter with the greatest change in bearing capacity by increasing the parameter by one standard deviation was the alpha (α) parameter in Eq. 9 (refer to Table 4). It is reasonable that this parameter has a significant control since it describes the suction a soil has when it is almost completely saturated. The smaller the alpha value is; the greater the suction is at higher degrees of saturation. The rest of the van Genuchten parameters have similar sensitivities to the increase in bearing capacity when increased by one standard deviation (refer to Table 4). With this probabilistic method it is most important to accurately predict alpha while fitting a SWRC to the volumetric moisture content and hydraulic head data.

4.2 Effect of Footing Depth

The final sensitivity analysis observed the influence of the depth factor in the cohesion term of the bearing capacity. Once again the footing was tested with the four different variations of footing size and depth described in the sample application for both the mean values of Levelland, TX and Victorville, CA (Sandy Loam).

The influence of the depth factor was studied by comparing the percent increases in bearing capacity for two footings with different sizes at a specified depth. The difference between the percent increase for the deterministic method with fully saturated soil and the Monte Carlo simulation with unsaturated soil was calculated. Since the depth is the same, the effects of suction are constant. Considering this, the percent increase from the bearing capacity for both methods should only be a factor of the change in size from the footing. Thus the percent difference between the two methods for increased bearing capacity should be the same; this is not the case in Table 5. The important trend in Table 5 is that as the influence of suction increases in the bearing capacity equation, the influence of the depth factor increases. The percent increase difference for the two methods in bearing capacity due to an increase in footing size reduces by 1.70% at a depth of 0.87 m in Victorville, CA (Sandy Loam). For sites where suction has more influence such as Victorville, CA (Adelanto Loam), the percent increase difference for the two methods in bearing capacity due to an increase in footing size reduces by 5.18% for a footing at a depth of 0.87 m when comparing the two methods. The negative percent increase is due to the depth factor having more control than the increased footing size in Victorville, CA (Adelanto Loam), which is explained in the results section of the sample application section. From these results it is evident that the depth factor has influence on the bearing capacity calculated from the bearing capacity equation.

Table 5. The effect of the depth factor for the cohesion term in the bearing capacity equation

Site	Footing 1 (m)	Footing 2 (m)	Depth (m)	Percent increase		
				Deterministic methods assuming saturated condition	Monte Carlo simulation assuming unsaturated condition	Difference for two methods
Victorville*	1.07	1.52	0.61	8.705	6.192	2.51
Victorville*	1.07	1.52	0.87	4.138	2.435	1.70
Levelland	1.07	1.52	0.61	6.695	6.666	0.03
Levelland	1.07	1.52	0.87	2.223	2.153	0.07
Victorville**	1.07	1.52	0.61	8.705	8.074	0.63
Victorville**	1.07	1.52	0.87	4.138	−1.043	5.18

*Sandy Loam and **Adelanto Loam

5 Conclusion

A probabilistic modeling framework for computing the ultimate bearing capacity of a shallow foundation in arid climate considering hydrologic information is presented in this paper. The results of the sample study show that shallow foundations designed coupling the geotechnical (unsaturated soil mechanics principles) and climatic data can be economical for sites where the soil mostly remains unsaturated during the lifetime of the structure.

The sensitivity analysis reinforced the importance of having accurate SWCC parameters when working with methods that rely on the SWCC for computing hydraulic conductivity and relating moisture content to suction. The effect of the depth factor seems to have an important role from the sensitivity analysis. As suction increases the value of the cohesion term, the depth factor has a greater influence on the bearing capacity equation. This results in smaller factors of increase in bearing capacity when there is an increase in footing size which creates a conservative estimate of the bearing capacity of footings in high suction.

This study considered homogeneous soil with 1-D flow. However, the proposed method can be extended for 2-D and 3-D cases to replicate more complex practical situations. The proposed framework can also be extended to study the effect of rainfall on the stability of slopes for various surface conditions such as stability of slopes after a wild fire and effects of intermittency and special variability of rainfall on many geotechnical systems.

References

Briaud, J.: Geotechnical Engineering: Unsaturated and Saturated Soils. Wiley, Hoboken (2013)

Chowdhury, K.: Preliminary Geotechnical Investigation Report Victorville 2 Hybrid Power Project Victorville. Kleinfelder, California (2006)

Costa, Y.D., Cintra, J.C., Zornberg, J.G.: Influence of matric suction on the results of plate load tests performed on a lateritic soil deposit. Geotech. Test. J. **26**(2), 219–226 (2003)

Fredlund, D.G.: Unsaturated soil mechanics in engineering practice. J. Geotech. Geoenviron. Eng. **132**(3), 286–321 (2006)

Fredlund, D.G., Rahardjo, H.: Soil Mechanics for Unsaturated Soils. Wiley, New York (1993)

Gonzalez, O.E.: Geotechnical Investigation Proposed New Rail and Roads. Amarillo Testing and Engineering Inc, Levelland (2009)

Jhorar, R.K., van Dam, J.C., Bastiaanssen, W.G.M., Feddes, R.A.: Calibration of effective soil hydraulic parameters of heterogeneous soil profiles. J. Hydrol. **285**, 233–247 (2004)

Kulhawy, F.H., Phoon, K.K., Wang, Y.: Reliability-based design of foundations-a modern view. In: Geotechnical Engineering State of the Art and Practice, Geo Congress Oakland California 2012, pp. 102–121 (2012)

Lu, N., Lokos, W.J.: Unsaturated Soil Mechanics. Wiley, New York (2004)

Meyerhof, G.G.: Some recent research on the bearing capacity of foundations. Can. Geotechn. J. **1**(1), 16–26 (1963)

Mohamed, F.O., Vanapalli, S.K.: Laboratory investigations for the measurement of the bearing capacity of an unsaturated coarse-grained soil. In: Proceedings of the 59th Canadian Geotechnical Conference, Vancouver, pp. 219–226 (2006)

National Climatic Data Center. U.S Department of Commerce. NOAA Satellite and Information Service. National Environmental Satellite, Data, and Information Service (2012). http://www.ncdc.noaa.gov/oa/ncdc.html. Accessed Apr 2012

Oloo, S.Y., Fredlund, D.G., Gan, J.K.-M.: Bearing capacity of unpaved roads. Can. Geotech. J. **34**(3), 398–407 (1997)

Perica, S., Martin, D., Lin, B., Parzybok, T., Riley, D., Yekta, M.: Precipitation-Frequency of the United States. NOAA Atlas 14; **4**(3) (2011). http://www.nws.noaa.gov/oh/hdsc/PF_documents/Atlas14_Volume4.pdf. Accessed Apr 2012

Rojas, J.C., Salinas, L.M., Seja, C.: Plate-load tests on an unsaturated lean clay. Experimental unsaturated soil mechanics. In: Proceedings of the 2nd International Conference on Unsaturated Soils. Springer Proceedings in Physics, Weimar Germany, pp. 445–452 (2007)

Schaap, M.G.: Rosetta Version 1.2. U.S Salinity Laboratory ARS-USDA, Riverside (2000)

Sheng, D.: Review of fundamental principles in modeling unsaturated soil behavior. Comput. Geotech. **38**, 757–776 (2011)

Steensen-Bach, J.O., Foged, N., Steenfelt. J.S.: Capillary induced stresses—fact or fiction? In: Proceedings of the 9th European Conf. on Soil Mechanics and Foundation Engineering, Budapest, Hungary, pp. 83–89 (1987)

Terzaghi, K.: Theoretical Soil Mechanics. Wiley, New York (1943)

van Genuchten, M.T.: A closed Form Equation for Predicting the Hydraulic Conductivity of Unsaturated Soils. Soil Sci. Soc. Am. J. **44**(5), 892–898 (1980)

Vanapalli, S.K., Mohamed, F.M.O.: Bearing capacity of model footings in unsaturated soil. In: Schanz, T. (ed.) Experimental Unsaturated Soil Mechanics, Springer, Heidelberg, pp. 483–93 (2007)

Vanapalli, S.K., Fredlund, D.G., Pufahal, D.E., Clifton, A.W.: Model for the prediction of shear strength with respect to soil suction. Can. Geotechn. J. **33**, 379–392 (1996)

Uchaipichat, A., Man-koksung, E.: Variation of ultimate bearing capacity of unsaturated clay with suction. ARPN J. Eng. Appl. Sci. **6**(12), 62–65 (2011a)

Uchaipichat, A., Man-koksung, E.: Bearing capacity characteristic of unsaturated granular soils. Adv. Mater. Res. **261–263**, 989–993 (2011b). doi:10.4028/www.scientific.net/AMR.261-263.989

U.S. Geological Survey. National Water Information System: Web Interface (2012). http://waterdata.usgs.gov/nwis/current/?type=gw&group_key=state_cd. Accessed Apr 2012

Zhang, F.: Soil Water Retention and Relative Permeability for Full Range of Saturation. Prepared for US Department of Energy, Pacific Northwest National Laboratory (2010)

Strength Properties of Rock as an Index of Blastability

Hamza Azzouz Rached(✉), Korichi Talhi, and El Bahi Hannachi

Mineral Processing and Environmental Research Laboratory,
University of Badji Mokhtar, Annaba, Algeria
azzouzrached@hotmail.com

Abstract. The goal of this paper is the significance of the tensile strength as one of parameters determining the resistance of rocks to blasting has been emphasized within the field of blasting research. In the paper the applicability and interpretation of tensile strength tests in connection with rock characterization for blasting is discussed.

Brazilian tests, uniaxial tensile strength tests and point load tests have been performed on rock material drilled out from the vicinity of blasting operation prior to and after blasting. Both the Brazilian tests and the uniaxial tensile strength tests revealed no general decrease of the remaining rock material strength due to the blasting. RQD and fracture frequency calculations indicated a law degree of remaining rock damage in a part of the rock mass close to the blasts. The absence of damage and problems encountered at the blasting may, on the basis of the results from the tensile strength tests, is explained as a result of the state of fissuring of the rock material. On the basis of the results is suggested that more research should be aimed at the use of Brazilian and uniaxial tensile strength tests as methods for characterizing the rock strength for fragmentation.

1 Introduction

The significance of the tensile strength as one of the parameters determining the resistance of rocks to blasting has been emphasized within the field of blasting research. In an early attempt to classify blasting resistance (Hino 1959) suggested the use of a "blastability coefficient" defined as the ratio between the compressive and the tensile strengths. Later the tensile strength was included in a formula aiming at the characterization of the rock resistance to blasting in tunneling (Bergh-Christensen and Selmer-Olsen 1970). Among previous work performed by (Persson et al. 1970) explain the appearance of radial cracks in around a blasthole as a result of tangential tensile stresses first appearing one or two holes radii out from the blasthole wall. The propagation of these cracks in bench blasting is furthermore indicated to be affected by tensile waves reflected from the front of the bench (Field and Ladegaard-Pedersen 1969). Results from investigations of the remaining rock damage at blasting also encourage studies of the strength of rock materials.

Measurements indicate that displacements taking place in the remaining rock are results of both movements in existing joints and fracturing of rock that prior to blasting would be classified as intact (Holmberg and Persson 1979, Holmberg and Mäki 1982).

L.R. Hoyos and J. McCartney (eds.), *Advances in Characterization and Analysis of Expansive Soils and Rocks*, Sustainable Civil Infrastructures,
DOI 10.1007/978-3-319-61931-6_13

In the waiting for future characterization methods using dynamic strength tests and fracture mechanics principles it is the aim of this paper to discuss the interpretation and applicability of conventional tensile strength tests in connection with rock characterization for blasting. To provide a basis for a case history will finally form the basis for conclusions.

2 The Tensile Strength of Rocks

The rock mechanics literature contains a large number of papers on the subject of tensile testing of rocks. The two testing methods recommended by the International Society for Rocks Mechanics, (ISRM 1978), the Brazilian test and uniaxial tensile strength test, are discussed by (Hawkes and Mellor 1970, 1971).

The two testing methods are often subjected to criticism, the Brazilian test due to uncertainty concerning the point of failure initiation and the indirect testing procedure which assumes linear elastic material behavior. The main objection against the uniaxial tensile strength test is the problem of achieving a uniform stress distribution in the sample. Since most rocks are weak in tension. However, the tensile strength is considered as an important parameter and it is the author's opinion that tensile strength tests should not be avoided, provided that the testing procedures are critically analyzed and interpretations which are made with an ambition to control the uncertainties. Both the Brazilian test and the uniaxial tensile strength test must be regarded as rock material tests. Specimens are prepared from unfractured core parts. It is the expert's judgment that sufficient fragmentation rock material failure has to be achieved, at least in cases of competent rock with a low density of larger existing fractures.

In following the recommended testing procedures for Brazilian tests and uniaxial tensile strength tests will be discussed.

3 The Brazilian Test

The Brazilian test is performed by diametral compression of a cylindrical rock specimen. The knowledge is demanded of the stress distribution in the loaded specimen before the stage of failure which can be analyzed. A stress solution for a line loaded specimen of homogeneous, isotropic and linearly elastic material was first obtained by H.R. Hertz in 1883.

The stresses in such a specimen are also described by (Colback 1966). By applying a strength criterion to the Griffith fracture theory, contours were established showing the likelihood of failure in different parts of the specimen. The results indicate that failure is likely starts either close to the points of line loading or in the center of the specimen. Since the critical crack orientation in the specimen parts close to the loading points and is not in line with the loading diameter and those parts of the specimen also contain high compressive stress failure initiating close to the loading points not to be taken as an indication of tensile failure. According to Colback the Brazilian test can be regarded as a correct test only if failure is initiated in the center of the specimen.

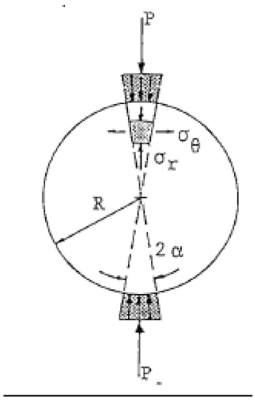

Fig. 1. Applied load and principal stress direction along the loading diameter in the Brazilian test.

This can be achieved by distributing the load over larger areas of cylindrical surface of the specimen (Fig. 1).

The distribution of the load was investigated by Colback in which was applied using several pieces of cardboard inserted between the specimen and the loading plates. According to (Mellor and Hawkes 1971) cardboard pieces should have a thickness equal to one percent of the specimen diameter. As another way of distributing the load Mellor and Hawkes used a curved-jaw loading jig like to present on (Fig. 2). The radius of the jaws should be 1.5 by specimen radius, thus giving an arc of contact (2α) of approximately 100 at failure.

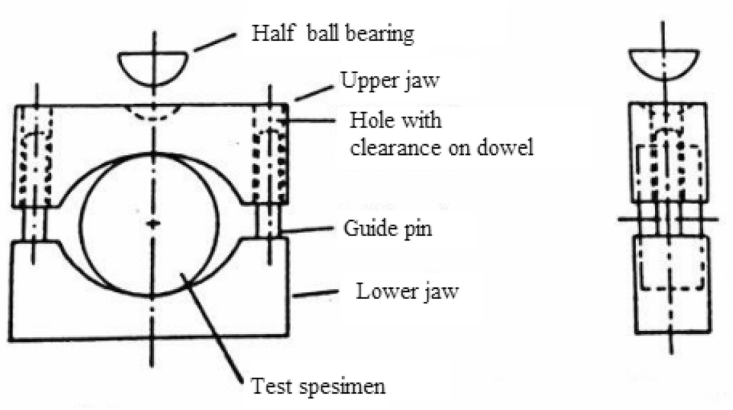

Fig. 2. Loading jig for Brazilian tests, after the (ISRM 1978).

The jig is recommended by the (ISRM 1978) who also suggest the use of a single of masking tape (thickness 0.2–0.4 mm) wrapped around the specimen by using the jig Mellor and Hawkess obtained fractured specimen. The propagation of the diametral fracture starts from the center of the specimen only if it contains a fracture in the center. The propagation of the fracture ceased before it reached the areas close to the points of loading.

A stress solution for the case of load distribution over finite arcs is given by (Hondros 1959).

The principal tensile stress in the center of the specimen is given by the equation:

$$\sigma_\theta = \frac{p}{\pi Rt}\left(\frac{\sin 2\alpha}{\alpha} - 1\right) \approx \frac{p}{\pi Rt} \tag{1}$$

Where t is the specimen thickness and the other parameters are defined in (Fig. 1).

With a 150 arc of contact the error introduced by use of the approximate expression for σ_θ is 2%. For specimens showing no fractures apart from the primary diametral fracture tensile strength may be calculated using Eq. (1).

Figures 3 and 4, after (Mellor and Hawkes 1971), Illustrate the influence of specimen geometry on the tensile strength for various rocks. The tensile strength is not indicated to be decisively affected by a change of specimen thickness for thicknesses greater than the specimen radius. Similarly the tensile strength is not indicated to be much affected by a change of specimen diameter provided that the diameter exceeds 2.5–3.0 cm. The influence of the specimen geometry on the tensile strength has also been investigated by (Tourenq and Denis 1970). The used cardboard must have an arc of contact of 23°. The results, reviewed by (Mäki 1983), are similar to those in (Figs. 3 and 4).

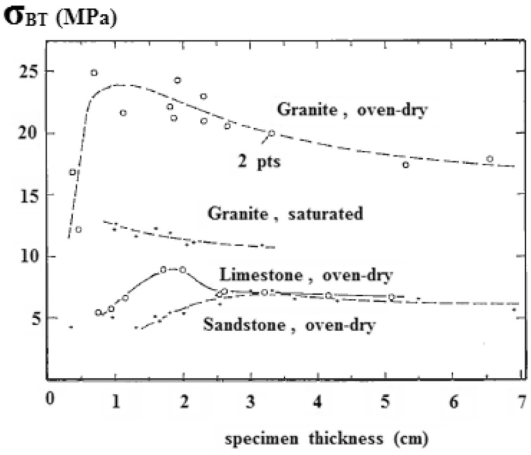

Fig. 3. The Brazilian tensile strength as a function of specimen thickness. Specimen diameter = 5 cm. After (Mellor and Hawkes 1971).

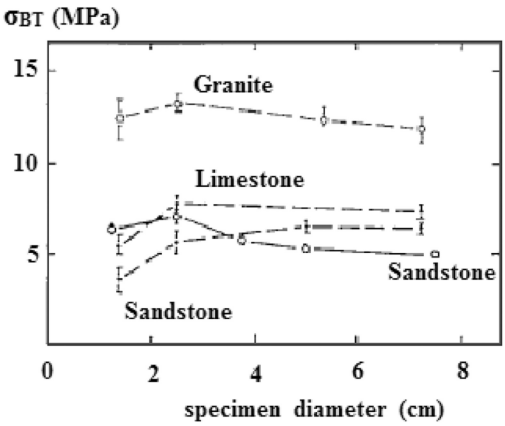

Fig. 4. The Brazilian tensile strength as a function of specimen diameter. Specimen thickness equal to the radius. After (Mellor and Hawkes 1971).

The influence of the loading rate is illustrated in (Fig. 5), after (Mellor and Hawkes 1971). The results indicate that the tensile strength is less affected by loading rate for a loading rate less than 0.1 cm/minute.

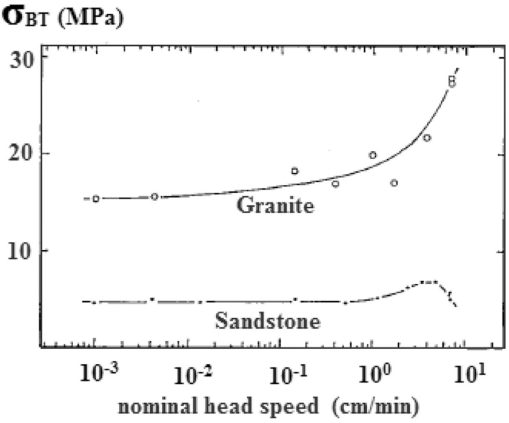

Fig. 5. The Brazilian tensile strength as a function of loading rate for two rock types. After (Mellor and Hawkes 1971).

In the recommendations for Brazilian tests published by the (ISRM 1978) it is stated that the specimen diameter should exceed 54 mm, the thickness should be equal to the specimen radius and the loading rate should be such that failure in the weakest rocks will occur within 15–30 s of loading. Alternatively a loading rate of 200 N/s is recommended. The ISRM also give recommendations on the preparation of the specimens.

4 The Uniaxial Tensile Strength Test

Various methods for the performance of the test are discussed by (Hawkes and Mellor 1970). Recommendations are given by the (ISRM 1978) and the American Society for Testing and Materials, (ASTM 1978). The testing procedure recommended by the ASTM is shown in (Fig. 6A).

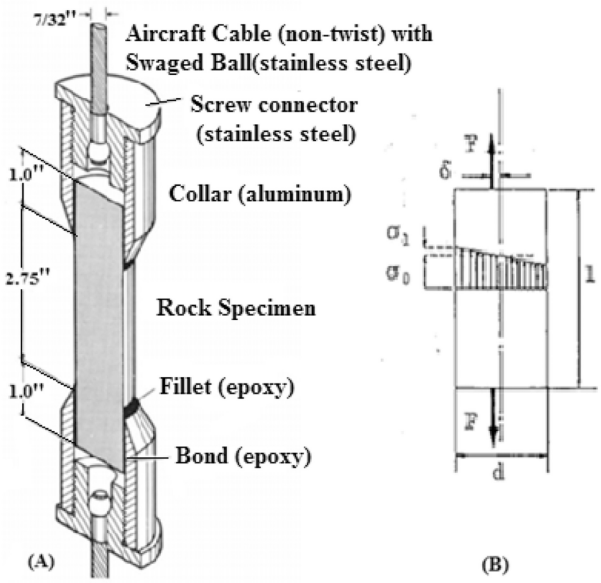

Fig. 6. A–B. Uniaxial tensile strength testing procedure. (A) Performance recommended by the (ASTM 1979). (B) Effect of excentric loading, after (Wijk 1979a).

According to the ISRM the length of the linkage system transferring the load from the metal caps to the pulling machine should on both sides of the specimen be at least twice the diameter of the metal caps. The diameter of the metal caps should not be less than the specimen diameter and not exceed it by more than 2 mm. Recommendations concerning specimen dimensions and loading rates are summarized in (Table 1). Careful preparation is a demand if a uniform stress distribution is to be achieved.

The influence of excentric loading has been investigated by (Wijk 1979a). For The case in (Fig. 6B) Beam theory gives:

$$\frac{\sigma_1}{\sigma_0} = \frac{8\delta}{d} = 4\,e \tag{2}$$

Where e is the excentricity defined as:

Table 1. Recommendations concerning specimen geometry and loading rate uniaxial tensile strength test

	ASTM (1978)	ISRM (1978)
Specimen length/diameter	2.0–2.5	2.5–3.0
Specimen diameter	48 mm	54 mm
	(min. 10 times largest grain size)	
Loading rate	Failure should occur after 5–15 min of loading	Failure should occur within 5 min. of loading (alternatively 0.5–1.0 MPa/s)

$$e = \frac{2\delta}{d} \tag{3}$$

To detect excentric loading in compression test strain measurements was performed by Wijk. Four axial gauges mounted with a 90° separation in the mid-plane of the specimens were used. Assuming a sinusoidal variation of axial strains around the specimen measured strains (ε_I to ε_{IV}), may be interpreted as a result of an average strain, ε_0 and a maximum additional strain ε_I, according to the equations:

$$\varepsilon_I = \varepsilon_0 + \varepsilon_I \sin\psi \tag{4}$$

$$\varepsilon_{II} = \varepsilon_0 + \varepsilon_I \sin\,(\psi + 90^\circ) \tag{5}$$

$$\varepsilon_{III} = \varepsilon_0 + \varepsilon_I \sin\,(\psi + 180^\circ) \tag{6}$$

$$\varepsilon_{IV} = \varepsilon_0 + \varepsilon_I \sin\,(\psi + 270^\circ) \tag{7}$$

Where ψ is an angle defines the position of maximum strain.

From the Eqs. (4), (5), (6) and (7), expressions for the strains $\varepsilon 0$ and $\varepsilon 1$, may be derived:

$$\varepsilon_0 = \frac{1}{2}(\varepsilon_I + \varepsilon_{III}) = \frac{1}{2}(\varepsilon_{II} + \varepsilon_{IV}) \tag{8}$$

$$\varepsilon_I^2 = \frac{1}{4}\left\{(\varepsilon_I - \varepsilon_{III})^2 + (\varepsilon_{II} - \varepsilon_{IV})^2\right\} \tag{9}$$

Assuming linearly elastic material the Eq. (3) then gives the excentricity:

$$e = \frac{\varepsilon_I}{4\varepsilon_0} \tag{10}$$

The uniaxial compression tests performed by (Wijk 1979a) revealed excentricities between 2 and 6% for 62 mm diameter specimens of granite.

5 Results from Tensile Strength Tests Performed on Rock Material from the Vicinity of a Blasting Operation and a Review of Blasting Results

In order to make a detailed study the strength and the fracturing of the surrounding rock, cores were drilled out prior to and after the blasting of a raise in the Kenadsa ore-body of the underground mine and with geological conditions. This mining underground is situated 12 miles on the outskirts of Bechar, see (Fig. 7a) variables profile such as that shown in (Fig. 7b), reflecting different rock materials that can have a significant effect on the underground mining operation. The performance of the blasting operation is presented in (Table 2), and which was undertaken by Onex in cooperation with the University of Badji Mokhtar Annaba, Department of mining as a part of research on the application of large holes in underground mining.

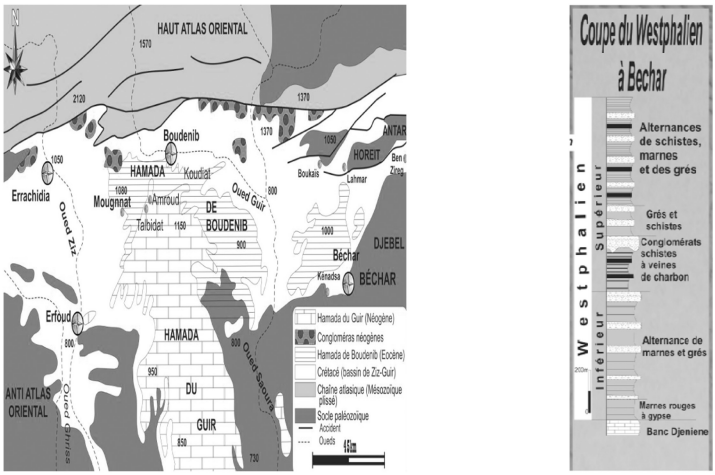

Fig. 7. a. Geographic situation of Kenadsa underground mine Bechar [Levy, Benyoucef] b. Geological profile of Kenadsa underground mine Bechar [DELEAU P, O.R.G.M]

The Location of the cores, drilled from the 494 m level, is shown in (Fig. 8).

The drilling was performed completely within the orebody and a representative Core piece containing 95% of magnetite with a very small amount of magnetic pyrite, quartz and biotite.

The cores were investigated with respect to fracture frequencies and RQD-values specimens for Brazilian tests and uniaxial tensile strength tests were prepared and tested. Finally point load tests were also performed. The primary aim was to in terms of fracture frequencies and RQD-values characterize the damage to the rock surrounding the raise and to by using the strength to test detect small scale rock damage. As a working hypothesis, it was assumed that a growth of the length of fissures and microcracks could be detected using results from uniaxial tensile Strength tests and Brazilian tests as indicated by the results in (Table 3) after (Tourenq and Denis 1970).

Table 2. Data from VCR-raising in the Kenadsa mine

Location of raise	Diameter of charge holes	Explosives
Between the 494 and 530 m levels	102 mm	Dynamex and ANFO

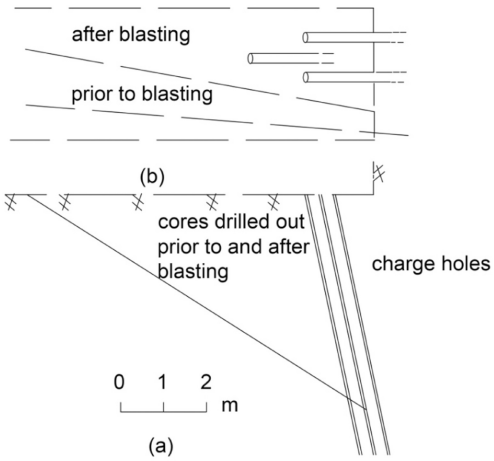

Fig. 8. a–b. Position of drill cores and charge holes at VCR-raising in the Kenadsa mine, (a) vertical section, (b) horizontal section.

Table 3. The influence of fissure length on the ratio. After (Tourenq and Denis 1970). Table also given by (Goodman 1976).

Rock type	Fissure length (mm)	σ_T/σ_{BT}
Limestone	0.2	1
	1–5	0.45
	3–5	0.47
	2–6	0.31
Granite	‹ 0.1	0.93
	0.3	0.7
	1–3	0.50
	2–5	0.34
	1–10	0.14
	3–20	0.07
Basalt	‹ 0.1	0.9
	2–20	0.15

Figure 9 shows the performance of the Brazilian and the uniaxial tensile strength tests. All tests were performed using an Instron servo hydraulic testing machine. A spherical seat was used to avoid non-uniform loading in the Brazilian tests. In the uniaxial tensile strength tests an epoxy resin of high strength was used for the fastening

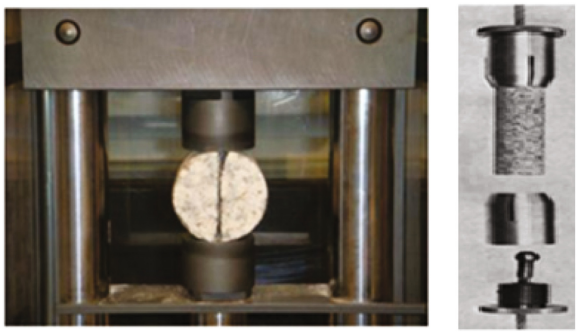

Fig. 9. a–b. Performance of Brazilian, (a), and uniaxial tensile strength, (b), tests.

of the specimens. Steel cylinders and fixtures containing thrust spherical plain bearings provided the load application system.

Prior to the uniaxial tensile strength tests the functioning of the load application system was studied using an aluminium specimen with tour axial gauges for strain measurements. Calculations of the excentricity for three tests performed up to a load corresponding to an average tensile stress of 6.4 MPa resulted in excentricities less than 2.5% at maximum load. Data on the performance of the Brazilian tests and uniaxial tensile strength tests are summarized in (Table 4). All details of the performance and the results have been reported by (Mäki and Holmberg 1980).

Table 4. Data on the performance of strength tests

	Brazilian tests	Uniaxial tensile strength tests
Specimen diameter	31.5 mm	31.5 mm
Specimen length	=radius	Twice the diameter
Speed of loading	0.12 cm/minute (failure within 15–30 s)	0.60 MPa/minute (9 MPa in 15 min)
Load distribution	Cardboard sheets, thickness = 0.3 mm (2α = 8–11°)	
Treatment of specimens	Stored for 24 h at a temperature of 100 °c before testing	

Figure 10 shows the results of the Brazilian tests performed prior to and after blasting. The results were possible to divide into groups referring to two modes of failure, here denoted stable and unstable failures:

Stable failure. Failure along the line of loading, extension of the fracture was limited to the central part of the specimen. Areas around points of loading only slightly or not at all fractured. Specimen halves not completely separated.

Unstable failure. Failure along the line of loading, fractures close to the points of loading and in other directions in the specimen. Specimen halves completely separated.

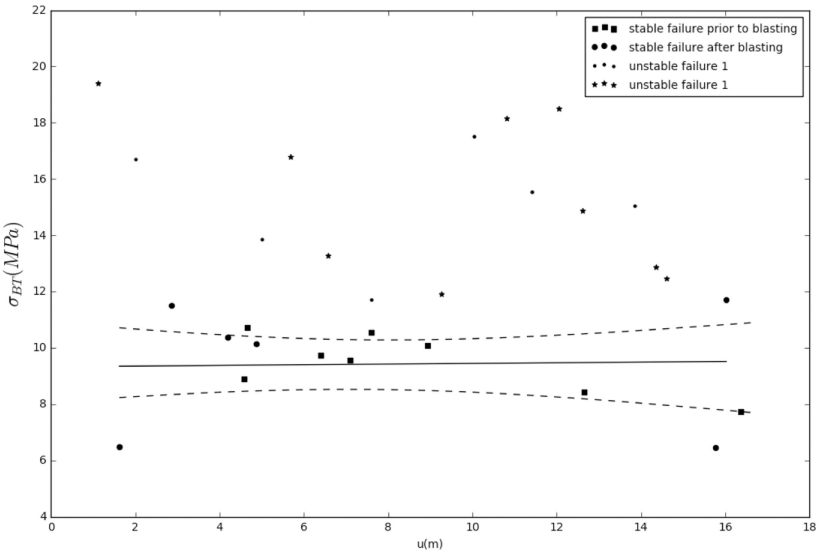

Fig. 10. Results from Brazilian tests.

Significance testing revealed a significant difference between the average tensile strengths σ_{BT}, for the two groups of results. The regression line and 95% confidence limits show the variation of σ_{BT}, along the cores for stable failures only. No significant difference was obtained between the results obtained prior to and after blasting.

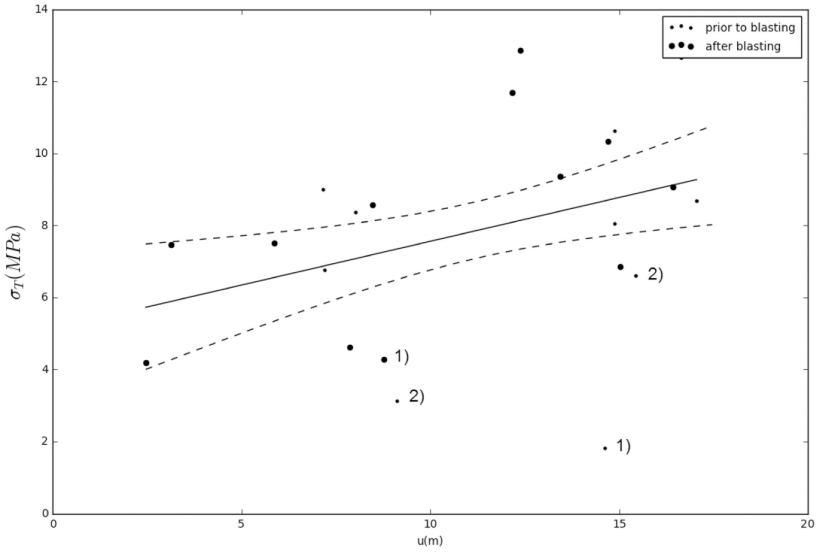

Fig. 11. Results from uniaxial tensile strength tests. (1) Failure along the plane of weakness, (2) Specimen containing non-ore minerals.

Figure 11 shows the results from the uniaxial tensile strength tests. Since no major difference between the uniaxial tensile strengths σ_T, prior to and after blasting was obtained, and the regression line and the confidence limits have been calculated based on all the results. Figure 11 indicates a variation of the point load strength index, which is much more similar with the results from the uniaxial tensile strength tests than with the results from the Brazilian tests.

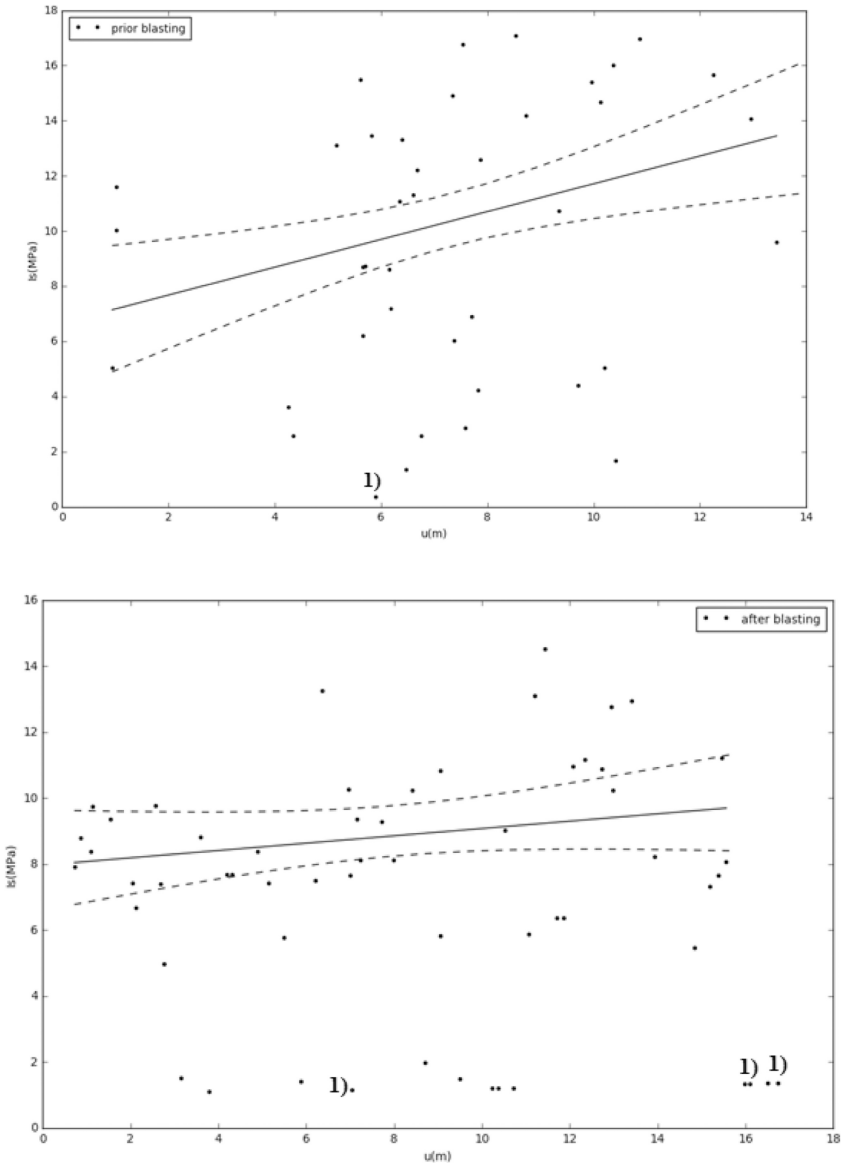

Fig. 12. The point load strength index I_S. (a) prior to blasting (b) after blasting (1) Loading along the plane of weakness.

I_S values less than 2 MPa were ignored in the calculation of regression and confidence limits.

From the results in Figs. 10 and 11 it was concluded that no general decrease of the tensile strength had occurred due to the blasting, it was however, noted that the variations of the tensile strengths along the cores as given by the regression lines result in (σ_T/σ_{BT}-ratios) agreeing with the ones obtained by (Tourenq and Denis 1970) which strengthened the idea of using tensile strength test results as a means of characterizing the state of fissuring of the rock (Fig. 12).

The results from the blasting of the raise are reported by (Holmberg et al. 1980). During the operation several problems were encountered. Charge hole deviations were larger than expected. In spite of the fact that some re-drilling was made this resulted in greater distances between corner holes and the center hole than was originally planned, particularly in the lower parts of the raise.

Problems were furthermore encountered in the measuring of the position of the rock surface after blasting and in the plugging of holes, the latter problem being partly caused by a tendency for the charge holes orifices to become conically shaped after blasting. Together with other possible factors of influence these problems were reflected in the blasting results. In the initial stage of the work where Dynamics cartridges (7 kg in each hole) were used, only approximately 25% of the craters obtained reached the stipulated depth of 1.4 m.

After changing the explosive to ANFO, larger crater depths were obtained. The amount of explosive was however also increased (5–24 kg in each hole). Identifying a single factor as the one causing the problems and the unexpectedly bad result of the blasting is a difficult task, it was however by (Holmberg et al. 1980) stated that to a major extent, the blasting results appeared to be depending on the structure of the rock.

A different approach to the study of the rock resistance to blasting is to investigate the remaining rock damage. Figure 13, after (Mäki and Holmberg 1980), shows the results from the determinations of RQD-values prior to and after blasting. In the calculations all fractures separating core parts were used.

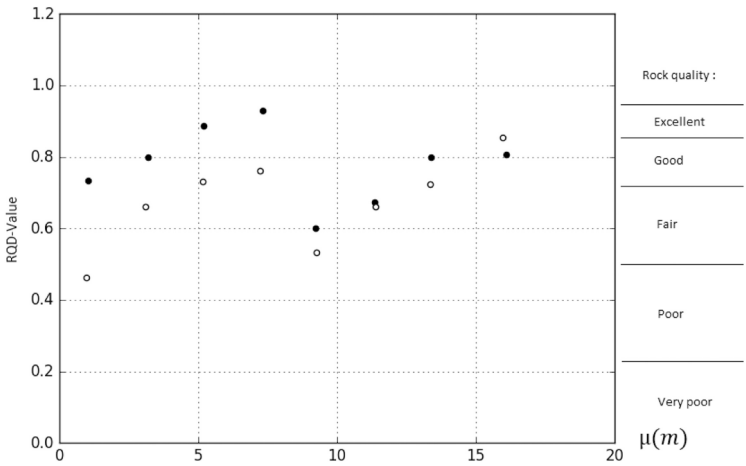

Fig. 13. RQD-values prior to and after blasting.

No major decrease of the rock quality was obtained for the rock mass closest to the raise. For the rock mass closer to the drift, however a decrease of the rock quality was noted. Similarly the results of fracture frequency calculations, (Figs. 14 and 15), indicated a low relative increase of the fracture frequency in the rock mass closest to the raise. On the basis of the results in (Figs. 13, 14 and 15) it was by (Mäki and Holmberg 1980) concluded that an unexpectedly low degree of damage was obtained close to the raise.

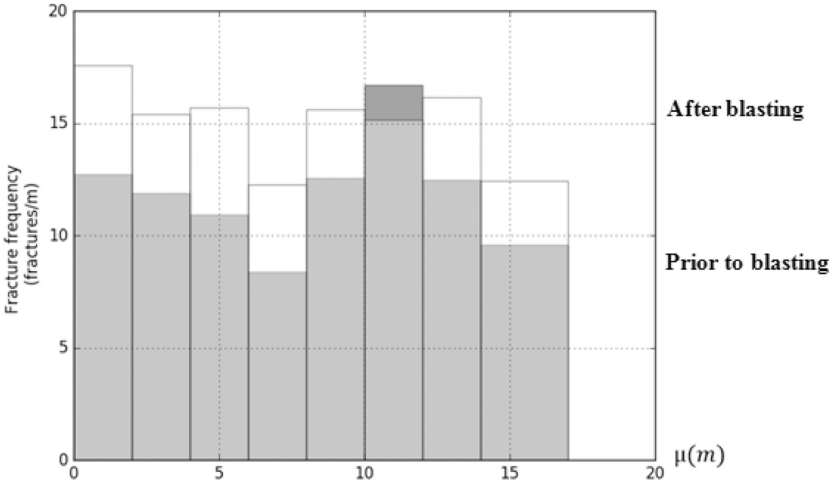

Fig. 14. Fracture frequencies prior to and after blasting

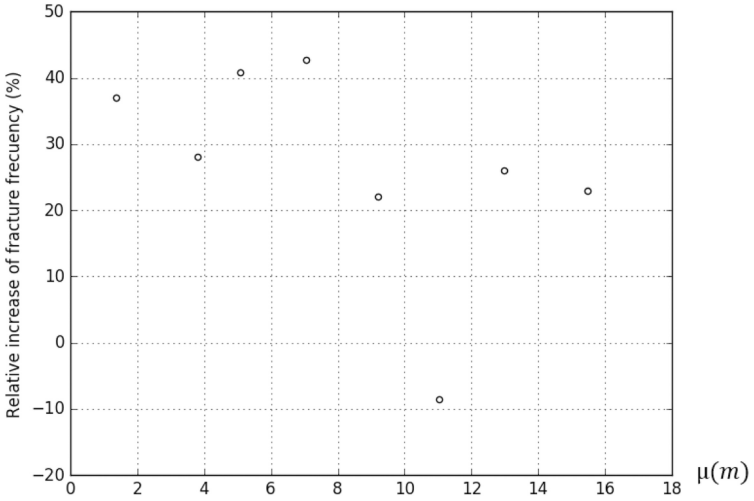

Fig. 15. Relative increase of fracture frequencies.

6 Discussion of Results

The general agreement between the results from the Brazilian tests and the Uniaxial tensile strength tests confirm the validity of the conclusions concerning the Brazilian test given by (Mellor and Hawkes 1971) and (Colback 1966). In a valid test only a diametral fracture should be obtained.

The experiments performed by (Tourenq and Denis 1970) resulting in σ_T/σ_{BT} ratios according to (Table 3), were performed under conditions to some extent differing from the ones followed at the experiments presented here. The Brazilian tests were, for instance performed on specimens with a diameter of 40 mm, a thickness equal to the diameter and with a load distribution angle of 23°.

An investigation of the effects the discrepancies, (Mäki 1983), does however not indicate that different results should be expected from the two methods of testing. It may thus be concluded that the results from the experiments give σ_T/σ_{BT}–ratios agreeing with the ones presented by Tourenq and Denis and may be interpreted as reflecting the state of fissuring of the rock material. Looking at the results of the blasting and from the investigation of the remaining rock damage, the experienced high resistance of the rock may be explained as a result of an existing state of fissuring characterized by short fissures rather than longer ones. In the parts of the rock mass closer to the drift a decreased rock quality was obtained. As would be expected from this line of reasoning, the tensile strength tests for this part of the rock mass indicated a state of fissuring more characterized by longer fissures.

The results from the investigations thus show that more attention should be paid to the conventional tensile strength tests due to the fact that they, apart from being strength tests, may be used to give information about the small scale structures of the rock. For future applications in connection with blasting more research could lead to useful results relating the tensile strength, the state of fissuring and the rock resistance to fragmentation.

Concerning the results from the point load tests an observation can be made. From the point load strength index the compressive strength of the rock material may be calculated using relations such as the one proposed by (Broch and Franklin 1972). The results, however, also exist indicating a relation between the point load strength index and the uniaxial tensile strength, (Wijk 1979b), and the results presented here form a support for such a relation.

7 Conclusion and Recommendations

The Brazilian tests reported in the paper gave approximately equal or higher average strength values than the uniaxial tensile strength tests, both before and after blasting.

In the paper, reference is given to a French investigation where similar relation between Brazilian and uniaxial tensile strength test results were obtained. As it point out, this indicates that the Brazilian test gives the strength of the unfissured rock matrix or in other words the intrinsic tensile strength. According to this line of reasoning, first suggested by the French scientists in question, the relation between the Brazilian

strength and uniaxial tensile strength may be regarded as reflecting a strength vs stressed volume relation given by the structuring of the rock material.

At this stage of development, however, we should not neglect any of the static tests due to the fact that the characterization is performed in tensile stress fields.

Acknowledgement. This research work was carried out at Annaba University, Algeria, under the sponsorship of the Mineral Processing and Environmental Research Laboratory, Whose financial and technical assistance is gratefully acknowledged.

References

ASTM. Standard test method for direct tensile strength of intact rock core specimens. ANSI/ASTM D 2936-78 (1978)

Bergh-Christensen, J., Selmer Olsen, R.: On the resistance to blasting in tunneling. In: Proceedings of 2nd Congress ISRM, vol. 3, pp. 5–7, Belgrade (1970)

Broch, E., Franklin, J.A.: The point-load strength test. Int. J. Rock Mech. Min. Sci. **9**, 669–697 (1972)

Colback, P.S.B.: Analysis of brittle fracture initiation and propagation in the Brazilian test. In: Proceedings of 1st Congress ISRM, pp. 385–391, Lisbon (1966)

Field, J.E., Ladegaard Pedersen, A.: The importance of the reflected shock wave in rock blasting. Swedish Detonic Research Foundation, Stockholm, Report DL, vol. 7 (1969)

Goodman, R.: Methods of Geological Engineering. West Publishing Co., St. Paul (1976)

Hawkes, I., Mellor, M.: Uniaxial testing in rock mechanics laboratories. Eng. Geol. **4**, 177–285 (1970)

Hino, K.: Theory and Practice of Blasting. Nippon Kayaku Co Ltd. (1959)

Holmberg, R., Mäki, K.: Case examples of blasting damage and its influence on slope stability. In: Proceedings of 3rd International Conference on Stability in Surface Mining, SME of AIME, Vancouver, pp. 773–793 (1982)

Holmberg, R., Persson, P.A.: Design of tunnel perimeter blasthole patterns to prevent rock damage. In: Proceedings of Tunne1ing 1979, Institute of Mining and Metallurgy, London (1979)

Holmberg, R., Rustan, A., Naarttijarvi, T., Mäki, K.: Crater blasting of a raise in the LKAB-Malmberget Mine. Swedish Detonic Research Foundation, Stockholm, Report DS 1980:12 (in Swedish) (1980)

Hondros, G.: The evaluation of Poisson's ratio and the modulus of materials of a low tensile resistance by the brazilian (Indirect Tensile) test with particular reference to concrete. Australian J. Appl. Sci. **10**, 243–268 (1959)

ISRM Commission on standardization of laboratory and field tests. Suggested methods for determining tensile strength of rock materials. Int. J. Rock Mech. Min. Sci. Geornech. Abstr. **15**, 99–101 (1978)

Mellor, M., Hawkes, I.: Measurement of tensile strength by diametral compression of discs and annuli. Eng. Geol. **5**, 173–225 (1971)

Mäki, K.: On the influence of fissures on rock fragmentation at blasting. Swedish Detonic Research Foundation, Stockholm, Report 1981:2 (in Swedish) (1983)

Mäki, K., Holmberg, R.: Rock damage from crater blasting of a raise. Swedish Detonie Research Foundation, Stockholm, Report 1980:8 (in Swedish) (1980)

Persson, P.A., Lundborg, N., Johansson, C.H.: The basic mechanisms in rock blasting. In: Proceedings of 2nd Congress ISRM, vol. 3, pp. 5–3, Belgrade (1970)
Tourenq, C., Denis, A.: La resistance a la traction des roches. laboratoire Central des Ponts et Chaussées, Rapport de Recherches 4 A, Paris (1970)
Wijk, G.: Extentricity in the uniaxial strength test on rock. Swedish Detonic Research Foundation. Stockholm, Report DS 1979:13 (1979a)
Wijk, G.: Some new aspects of the Brazilian test. Swedish Detonic Research Foundation, Stockholm, Report DS 1979:5 (1979b)

Thermo-poro-mechanics Modelling of Gypsum Dehydration

A. Karrech[1(✉)], F. Fusseis[2], C. Schrank[3], and K. Regenauer-Lieb[4]

[1] School of Civil Environmental, and Mining Engineering,
University of Western Australia, 35 Stirling Hwy, Crawley, WA 6009, Australia
[2] University of Edinburgh, West Mains Road, Edinburgh EH9 3JW, UK
[3] School of Earth, Environmental and Biological Sciences,
Queensland University of Technology, Brisbane, Australia
[4] School of Petroleum Engineering,
The University of New South Wales, Kensington, Australia

Abstract. Understanding the behaviour of natural calcium sulphates is important to ensure the sustainable integrity of civil structures. The phase transitions of these minerals are associated with considerable volume variations, creation of porosity with local defects, and water exchanges. Such changes can jeopardise the integrity of structures when the conditions that trigger the phase transitions are encountered. This paper uses advanced poromechanics to investigate the dehydration of gypsum when subjected to heating. The proposed approach includes the fundamental principles of non-equilibrium thermodynamics as well as the coupled multi-physics of thermal, hydraulic, mechanical and chemical (THMC) processes. A novel mathematical formulation is introduced to describe the coupled constitutive relationships in the reversible and dissipative regimes as well as the consequent partial differential equations that describe the THMC processes. The governing equations are integrated numerically using the finite element method. The obtained results show a significant correlation between gypsum dehydration and creation of fluid pathways. The proposed model can be generalised to describe the effects of dehydration in other minerals carrying water in their crystal structures.

1 Introduction

Numerous geohazards are associated with the poromechanics and phase transitions of calcium sulphates. For instance, the highly soluble nature of gypsum can generate local subsidences and the hydration of anhydrite can cause surface uplifts. Existing infrastructures including buildings, roads, railways, canals and dams can be affected severely under such conditions. Subsidence and collapse due to gypsum dissolutions have been encountered in urban areas around Paris (France), the Perm area (Russia), Madrid (Spain), Stuttgart (Germany), Ripon (England). Water leakage causing gypsum dissolution can lead to considerable damages in the foundations of civil structures. For example, several

L.R. Hoyos and J. McCartney (eds.), *Advances in Characterization and Analysis of Expansive Soils and Rocks*, Sustainable Civil Infrastructures,
DOI 10.1007/978-3-319-61931-6_14

dams have been affected by gypsum dissolution in the USA, China, Europe, and South America (Cooper and Calow 1998). The existence of gypsum karst areas resulted in reservoir leaking in France and difficult tunnelling conditions in Switzerland. What makes the risk management of calcium sulphates more complex is their abundance and difficult identification. For instance, the calcium sulphate alabasterine is commonly misidentified as limestone, which leads to important engineering disasters.

In this paper, we propose a mathematical model to describe the behaviour of gypsum under non-equilibrium thermodynamics conditions. Based on recent research work showing that the coupling between thermal, hydraulic, mechanical and chemical processes along with the basic principles of non-equilibrium thermodynamics can affect the stability of geomaterials significantly (Karrech 2013), we focus on gypsum dehydration characterised by large volume and porosity changes along with complex kinetics.

The following section describes the general background of gypsum dehydration. It discusses the thermodynamic properties of the minerals involved as well as the kinetics of the relevant reaction. The third section summarises the mathematical formulation, which is specifically cast for gypsum dehydration. The governing framework is detailed in terms of relationships between fluxes and forces as well as partial differential equations of energy and matter balances. The last part of this paper is dedicated to the solution method as well as the results and discussions.

2 Chemical Reactions

The system ($CaSO_4$,H_2O) forms several deposits around the globe (Cooper and Calow 1998). The most common minerals of this system are gypsum ($CaSO_4 \cdot 2H_2O$), bassanite ($CaSO_4 \cdot 0.5H_2O$, hemihydrate), and anhydrite ($CaSO_4$, anhydrous). These minerals have been investigated extensively to understand their behaviour under different loading conditions (Bezou et al. 1995; Charola et al. 2007; Christensen et al. 2008; Freyer and Voigt 2003; Jacques et al. 2009; Singh and Middendorf 2007). The chemical reactions that govern the phase transitions of these minerals can be summarised as follows:

$$CaSO_4 \cdot nH_2O + Heat \Leftrightarrow CaSO_4 \cdot mH_2O + (n-m)H_2O \tag{1}$$

where the subscripts m and n are positive real numbers. The dehydration of gypsum into hemihydrate (n = 0.5, m = 0) corresponds to the dehydration of hemihydrate into anhydrite. The opposite reactions are also possible as hydration and gypsum crystallisation takes place in the presence of water. As illustrated in Fig. 1, one mole of gypsum (molar volume $V_g = 74.69\, cm^3\, mol^{-1}$) produces one mole of hemihydrate (molar volume $V_h = 53.8\, cm^3\, mol^{-1}$) and one mole and a half of water (molar volume $V_w = 18.4\, cm^3\, mol^{-1}$). In other words, the solid content reduces by 30% but the overall volume (fluid water and bassanite) increases by 9%. The produced water creates fluid pathways and gets expelled out of the structure, which leaves pore spaces within the new material (Fusseis et al. 2012).

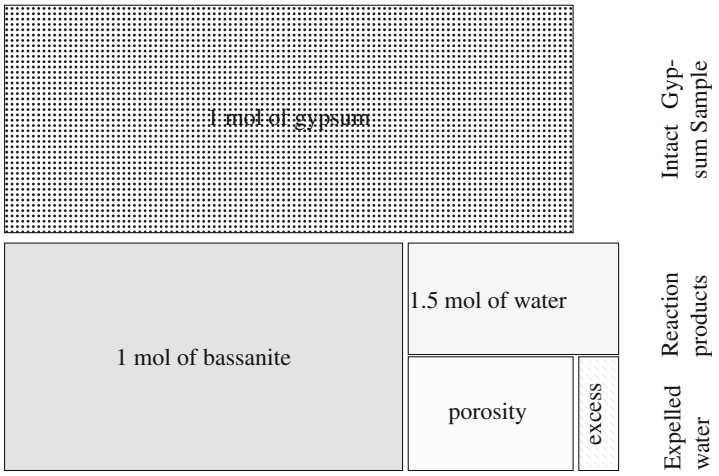

Fig. 1. Illustration of the reaction (1) of gypsum into bassanite and water after a temperature increase up to $388^o K$. 1 mol of Gypsum (molar volume $74.69\,cm^3\,mol^{-1}$) produces 1 mol of bassanite (molar volume $V_h = 53.8\,cm^3\,mol^{-1}$) and 1.5 mol of water ($V_w = 18.4\,cm^3\,mol^{-1}$). This figure illustrates how the the produced molar volume ($81.4\,cm^3\,mol^{-1}$) is higher than the initial. That is a total volume excess of 9% despite the solid phase shrinking by 30%. The difference in volume will be accommodated by deformation and/or creation of porosity.

3 Balance Equations

The dehydration reaction described in the last section involves gypsum, bassanite and the pore fluid water. The rate of mass change for each species k can be expressed as follows:

$$\int_\Omega \left\{ \frac{\partial \rho_k}{\partial t} + \boldsymbol{v}_k \cdot \nabla \rho_k + \rho_k \nabla \cdot \boldsymbol{v}_k \right\} d\Omega = \int_\Omega \overset{\circ}{m}_{\rightarrow k} d\Omega \tag{2}$$

where $\rho_k[kg.m^{-3}]$ is the mass concentration (mass per total volume), $\boldsymbol{v}_k[m.s^{-1}]$ is the velocity, and $\overset{\circ}{m}_{\rightarrow k}[kg.m^{-3}.s^{-1}]$ is the production rate of the species k due to dehydration. In the current configuration, the mass concentration, ρ_k, is related to the actual density, ρ_k, through $\rho_k = \phi_k \rho_k$, where ϕ_k is the volume fraction of a given species. The volume fractions satisfy the relationship $\phi_g + \phi_b + \phi_w = 1$. The current porosity is defined as the fraction of non solid volume over total volume, ϕ, which verifies $1 - \phi = \phi_g + \phi_b$. Defining $\tau = \phi_b/(1-\phi)$, it can be seen that $\rho_g = (1-\tau)(1-\phi)\rho_g$, $\rho_b = \tau(1-\phi)\rho_b$ and $\rho_w = \phi\rho_w$. In addition, the conservation of mass in chemical reactions states that:

$$\sum_k \mathscr{M}_k \nu_k = 0 \tag{3}$$

where $\mathscr{M}_k[kg.\,mol^{-1}]$ is the molar mass of k, ν_k is the stoichiometric coefficient of k as it appears in the reaction (it is negative for reactants and positive

for products). Locally, the equations of conservation (2) can also be written in terms of substantive derivative defined by $\frac{d^s(.)}{dt} = \frac{\partial(.)}{\partial t} + \boldsymbol{v}_s \cdot \nabla(.)$, for a given property. The continuity equations can be written as:

$$\begin{aligned}
&\frac{d^s(1-\phi)(1-\tau)\rho_g}{dt} + (1-\phi)(1-\tau)\rho_g \nabla \cdot \boldsymbol{v}_s = \mathscr{M}_g \nu_g \overset{\circ}{\xi} \\
&\frac{d^s(1-\phi)\tau\rho_b}{dt} + (1-\phi)\tau\rho_b \nabla \cdot \boldsymbol{v}_s = \mathscr{M}_b \nu_b \overset{\circ}{\xi} \\
&\frac{d^s\phi\rho_w}{dt} + \phi\rho_w \nabla \cdot \boldsymbol{v}_s + \nabla \cdot \boldsymbol{J}_w = \mathscr{M}_w \nu_w \overset{\circ}{\xi}
\end{aligned} \tag{4}$$

where $\boldsymbol{J}_w = \rho_k(\boldsymbol{v}_w - \boldsymbol{v}_s)$ is the flux of water and $\boldsymbol{v}_s$ is the velocity of the skeleton. In the above equations, we use $\overset{\circ}{m}_{\to k} = \mathscr{M}_k \nu_k \overset{\circ}{\xi}$, where $\overset{\circ}{\xi}[mol.s^{-1}.m^{-3}]$ is the rate of reaction.

In non-equilibrium thermodynamics, heat flow and work exchange are described by processes, which are well defined with respect to time. The process driven heat and work increments are well defined. Therefore, we derive a Clausius-Duhem inequality from the first and second principle of thermodynamics:

$$\begin{aligned}
Tr_s = &-\rho s \frac{d^s T}{dt} - \left(\frac{d^s \rho\psi}{dt} + \rho\psi \nabla \cdot \boldsymbol{v}^s \right) + \boldsymbol{\sigma} : \nabla \boldsymbol{v}_s - \frac{\nabla T}{T} \cdot \boldsymbol{J}_q + (\boldsymbol{f} - \boldsymbol{a}_w) \cdot \boldsymbol{J}_w \\
&+ T\nabla \cdot (s_w \boldsymbol{J}_w) - \nabla \cdot (u_w \boldsymbol{J}_w) - \nabla \cdot \left\{ \frac{p_w}{\rho_w} \cdot \boldsymbol{J}_w \right\} - \sum_k \frac{\overset{\circ}{m}_{\to k}}{2} \left(\boldsymbol{v}_k - \boldsymbol{v}_s \right)^2 \geq 0
\end{aligned} \tag{5}$$

where r_s is a positive function that denotes the rate of entropy production, ψ is the specific overall Helmholtz free energy, $\boldsymbol{\sigma}$ is the overall Cauchy stress, $\boldsymbol{J}_q$ is the heat flux on the periphery of the system, $\boldsymbol{f}$ is the body force, s_w is the specific vibrational (calorimetric) entropy of water, u_w is the specific internal energy of water, p_w is the partial pressure on water (or the pore pressure), and J is the gradient of deformation. The second principle expressed by (5) can be written as:

$$\begin{aligned}
Tr_s = &-\left(S_s \frac{d^s T}{dt} + \frac{d^s \Psi_s}{dt} \right) + \boldsymbol{\sigma} : \nabla \boldsymbol{v}_s + p_w \frac{d^s \Phi}{dt} - \boldsymbol{J}_q \cdot \frac{\nabla T}{T} \\
&+ \boldsymbol{J}_w \cdot (\boldsymbol{f} - \boldsymbol{a}_w - \frac{\nabla p_w}{\rho_w}) + \overset{\circ}{\xi} \mathscr{A} \geq 0
\end{aligned} \tag{6}$$

where $\Psi_s = J\psi_s$ and $\Phi = J\phi$ are, respectively, the specific Helmholtz free energy and porosity pushed back to the reference configuration, S_s is the volumetric entropy of the solid skeleton (solid phases and interfaces), $\mathscr{A} = -\sum_{k=0}^{n} \mathscr{M}_k \nu_k \left(g_k + \frac{1}{2} \left(\boldsymbol{v}_k - \boldsymbol{v}_s \right)^2 \right)$ is the chemical affinity of the reaction, and g_k is the specific Gibbs free energy of the species k. The Clausius-Duhem inequality (6) ensures that the second law of thermodynamics is respected, since the entropy production r_s is positive. However, as presented in the last subsection, the expression of entropy production involves reversible and irreversible quantities. It needs to be simplified further to identify the state laws as well as the

expression of dissipation. For this purpose, we express the elastic natural deformation as follows: $\boldsymbol{\epsilon}^e = \boldsymbol{\epsilon} - \boldsymbol{\epsilon}^p$, where the superscripts "e" and "p" refer to elastic and plastic, respectively. In addition, we consider that the determinant of the deformation gradient J is close to 1 and express the Helmholtz specific free energy as follows:

$$\psi_s = \psi_s(\boldsymbol{\epsilon}^e, T, \phi) \tag{7}$$

Substituting Eq. (7) in the Clausius-Duhem inequality (6) shows that:

$$\begin{aligned} Tr_s = &\left(\boldsymbol{\sigma} - \frac{\partial \psi_s}{\partial \boldsymbol{\epsilon}^e}\right) : \dot{\boldsymbol{\epsilon}}^e - \left(\frac{\partial \psi_s}{\partial T} + S_s\right)\frac{d^s T}{dt} + \left(p_w - \frac{\partial \psi_s}{\partial \phi}\right)\frac{d^s \phi}{dt} + \mathscr{A}\overset{\circ}{\xi} \\ &+\boldsymbol{\sigma} : \dot{\boldsymbol{\epsilon}}^p - \mathscr{V}_w \cdot (\nabla p_w - \rho_w \boldsymbol{f}) - \boldsymbol{J}_q \cdot \frac{\nabla T}{T} \geq 0 \end{aligned} \tag{8}$$

where $\mathscr{V}_w = \phi(\boldsymbol{v}_w - \boldsymbol{v}_s)$. The independence of the different processes results in the following relationship:

$$\mathscr{D} = Tr_s = \mathscr{A}\overset{\circ}{\xi} + \boldsymbol{\sigma} : \dot{\boldsymbol{\epsilon}}^p - \mathscr{V}_w \cdot (\nabla p_w - \boldsymbol{\rho}_w \boldsymbol{f}) - \boldsymbol{J}_q \cdot \frac{\nabla T}{T} \geq 0 \tag{9}$$

where $\mathscr{D}$ is the dissipation. Equation (9) shows that the entropy production is expressed as the sum of scalar products of dual thermodynamic fluxes with thermodynamic forces. Optimising the entropy production or dissipation under physical constraint can deliver relationships between dissipative fluxes and their duals.

4 Constitutive Laws

Apart from the expression of the entropy production (9), the independence of the processes involved in the Clausius-Duhem inequality (8) delivers reversible constitutive relations. Application of Legendre transformation to ψ_s with regard to ϕ can be written as $\Psi = \psi_s - p_w\phi$. Hence, the following expression can be obtained:

$$d\Psi = \boldsymbol{\sigma} : d\boldsymbol{\epsilon}^e - S_s dT - \phi dp_w \tag{10}$$

If we consider that the free energy function Ψ is continuous at least to the second order, with respect to its variables, Schwartz' theorem can be applied to deduce the following relationships, which describe the behaviour of isotropic materials:

$$\begin{aligned} d\boldsymbol{\sigma} &= (K - \frac{2}{3}G)d\vartheta \mathbf{1} + 2G d\boldsymbol{\epsilon}^e - 3\alpha K dT \mathbf{1} - b dp_w 1 \\ dS_s &= 3\alpha K d\vartheta + C_v \frac{dT}{T} - 3\alpha_\phi dp_w \\ d\phi &= b d\vartheta - 3\alpha_\phi dT + \frac{dp_w}{N} \end{aligned} \tag{11}$$

where $\vartheta = \mathrm{tr}\boldsymbol{\epsilon}$. The thermal-mechanical properties K, G, α, and C_v denote the bulk modulus, shear modulus, thermal expansion coefficient, and volumetric heat capacity. The thermal-hydraulic-mechanical properties b, N and α_ϕ are the Biot

coefficient, the Biot modulus, and the latent heat coefficient associated with the change of porosity. The specific Helmholtz free energy Ψ of the skeleton can be upscaled from the specific Helmholtz free energies of its components. Since we consider no plastic deformation, the Clausius-Duhem inequality (9) reduces to:

$$\mathscr{D} = Tr^s = \overset{\circ}{\xi}\mathscr{A} - \mathscr{V}_w \cdot (\nabla p_w - \rho_w \boldsymbol{f}) - \boldsymbol{J}_q \cdot \frac{\nabla T}{T} \geq 0 \tag{12}$$

where $\mathscr{V}_w = \phi(\boldsymbol{v}_w - \boldsymbol{v}_s)$ describes the filtration of fluids within the skeleton and $\boldsymbol{v}_w$ is the barycentric velocity of the fluid mixture. The above expression means that the entropy production (12) is of the common form $r^s = \sum_i \boldsymbol{\xi}_i \boldsymbol{\chi}_j$ where $\boldsymbol{\xi}_i$ and $\boldsymbol{\chi}_j$ are thermodynamic forces and fluxes respectively. Through proper constitutive models, which can be identified experimentally, the fluxes can be written as function of thermodynamic focus and state variables such as pressure, temperature, and composition $\boldsymbol{\xi}_i(\boldsymbol{\chi}_1, \boldsymbol{\chi}_2, ..., T, p, \varphi_1, \varphi_2, ...)$. A Taylor expansion to the first order shows that the fluxes can be expressed as $\boldsymbol{\xi}_i = \sum_j L_{ij}\boldsymbol{\chi}_j$, where L_{ij} are Onsager's phenomenological constants (Onsager 1931). As shown by (Truesdell and Noll 2004), the processes belonging to different tensorial ranks are decoupled (this concept is often referred to as the "Curie principle"):

$$\begin{aligned}
\boldsymbol{J}_q &= -L_{qf}\frac{\nabla p_w - \rho_w \boldsymbol{f}}{T} + L_{qq}\nabla\frac{1}{T} \\
\mathscr{V}_w &= -L_{ff}\frac{\nabla p_w - \rho_w \boldsymbol{f}}{T} + L_{fq}\nabla\frac{1}{T} \\
\overset{\circ}{\xi} &= L_\xi \frac{\mathscr{A}}{T}
\end{aligned} \tag{13}$$

We consider that the off diagonal terms L_{qf} and $L_{fq} = 0$ to comply with Fourier and Darcy laws. The first two diagonal Onsager' s coefficients can be identified as $L_{qq} = T^2\kappa_{TT}$ and $L_{ff} = T\frac{\kappa_{ff}}{\eta_w}$ where κ_{TT} is the thermal conductivity, κ_{ff} is the intrinsic permeability and η_w is the viscosity of water. The last Onsager coefficient is directly related to the rate of reaction.

4.1 Transport Equations

The balance of the fluid content can be derived from Eq. (4) as follows:

$$\frac{d^s\phi}{dt} + \phi\nabla\cdot\boldsymbol{v}_s + \frac{\phi}{\rho_w}\frac{d^s\rho_w}{dt} + \nabla\mathscr{V}_w + \mathscr{V}_w\frac{\nabla\rho_w}{\rho_w} = \rho_w^{-1}\mathscr{M}_w\nu_w\overset{\circ}{\xi} \tag{14}$$

As $\frac{d^s\phi}{dt} + \phi\nabla\cdot\boldsymbol{v}_s = \frac{d^s\phi}{dt} = b\frac{d^s\vartheta}{dt} - 3\alpha_\phi\frac{d^sT}{dt} + \frac{1}{N}\frac{d^sp_w}{dt}$, and $\frac{d^s\rho_w}{\rho_w} = \frac{d^sp_w}{K_w} - 3\alpha_w d^sT$, where K_w is the bulk modulus and α_w is the thermal expansion coefficient of the fluid mixture, it can be seen that:

$$\begin{aligned}
&\left(\frac{1}{N} + \frac{\phi_w}{K_w}\right)\frac{d^sp_w}{dt} + b\frac{d^s\vartheta}{dt} - 3(\alpha_\phi + \phi\alpha_w)\frac{d^sT}{dt} + \mathscr{V}_w\frac{\nabla p_w}{K_w} - 3\alpha_w\mathscr{V}_w\nabla T \\
&= V_w\overset{\circ}{\xi} + \tfrac{\kappa_{ff}}{\eta_w}(\nabla p_w - \rho_w\boldsymbol{f})
\end{aligned} \tag{15}$$

where $V_w = \rho_w^{-1}\mathscr{M}_w\nu_w$ is the molar volume of water. For small fluid velocities, the terms $\mathscr{V}_w\frac{\nabla p_w}{K_w} - 3\alpha_w\mathscr{V}_w\nabla T$ in Eq. (15) can be neglected. Therefore, the partial differential equation of hydraulic flow in porous media can be obtained:

$$\begin{aligned} &\frac{1}{M}\frac{dp_w}{dt} + b\frac{d\vartheta}{dt} - 3\alpha_m\frac{dT}{dt} = V_w\overset{\circ}{\xi} + \nabla\frac{\kappa_{ff}}{\eta_w}\left(\nabla p_w - \rho_w\boldsymbol{f}\right) \\ &\nabla p_w = \boldsymbol{q}_f \text{ at } \Gamma_{q_f}, \quad p_w = p_d \text{ at } \Gamma_p \end{aligned} \tag{16}$$

where $1/M = 1/N + \phi/K_w$ and $\alpha_m = \alpha_\phi + \phi\alpha_w$. Γ_{q_f} and Γ_p are the surfaces where the boundary conditions in terms of fluid flux $\boldsymbol{q}_f$ and pore pressure p_d are applied. Gypsum dehydration affects matrix morphology; the porosity changes due to the decrease of solid volume and increase of fluid content. In addition, the increase of pore pressure affects the compaction within the porous material. Therefore, the intrinsic permeability varies with respect to porosity, and it can be estimated based as follows:

$$\frac{\kappa_f f}{\kappa_0} = \left(\frac{\phi}{\phi_c}\right)^{n_\kappa} \tag{17}$$

where ϕ_c is a critical porosity, and n_κ is a fitting exponent. We consider $\kappa_0 = 2 \times 10^{-21}m^2$, $\phi_c = 0.2$, $n_\kappa = 2$ for $\phi > \phi_c$, and $n_\kappa = 6$ for $\phi \leq \phi_c$. Based on the conservation of energy, we also obtain the equation of heat transfer:

$$\begin{aligned} &\left(C_p + \phi C_w\right)\frac{dT}{dt} + C_w\nabla T.\mathscr{V}_w = \nabla\kappa_{TT}\nabla T + \mathscr{H}\overset{\circ}{\xi} \\ &\nabla T = \boldsymbol{q}_T \text{ at } \Gamma_{q_T}, \quad T = T_d \text{ at } \Gamma_T \end{aligned} \tag{18}$$

where Γ_{q_T} and Γ_T are the surfaces where the boundary conditions in terms of heat flux $\boldsymbol{q}_T$ and temperature T_d are applied. We express the equation of mechanical equilibrium as follows:

$$\begin{aligned} &\nabla\cdot\boldsymbol{\sigma} + \rho\boldsymbol{f} = 0, \\ &\boldsymbol{\sigma}\cdot\boldsymbol{n} = \boldsymbol{T}_d \text{ at } \Gamma_\sigma, \quad \boldsymbol{u} = \boldsymbol{u}_d \text{ at } \Gamma_u \end{aligned} \tag{19}$$

where and Γ_u and Γ_σ are the surfaces of the respective Dirichlet and Neumann boundary conditions, $\boldsymbol{u}_d$ and $\boldsymbol{T}_d$.

5 Solution Method

5.1 Numerical Model Setup

The purpose of this example is to model the response of a cylindrical gypsum sample of diameter 2.3 mm under thermal loading. The proposed model is comparable to the experimental set-up of (Fusseis et al. 2012) who studied the gypsum dehydration using synchrotron tomography. A plane strain quarter of the domain is considered for simulation, given the symmetric loading and boundary conditions. At $t = 0$, the sample is heated up by increasing its temperature from ambient conditions to 388 K at the outer surface, while keeping

the pressure atmospheric. The finite element program developed by (Karrech et al. 2012) is used to simulate the behaviour of the sample with respect to time. The involved minerals gypsum and bassanite are characterised by bulk moduli of 41 and 70 GPa, shear moduli of 16 and 30 GPa, and densities of 2310 and 2730 kgm^{-3}, respectively. The produced water is modelled using the equation of state proposed by the International Association for the Properties of Water and Stream (IAPWS 2007).

5.2 Results

Figure 2a shows that upon heating the sample externally, temperature diffuses towards the centre. The temperature equilibrates in about 10 seconds given the size of the domain, its heat capacity, thermal conductivity, and thermal feedbacks. Figure 2b depicts the variation of pore pressure with respect to time and space. The supplied heat results in the production of water, which first fills the available initial pore space and subsequently contributes to a pore pressure increase. Examining the pore pressure distribution at $t = 8.12\,\mathrm{s}$ shows the increase of pressure along the radius of the sample. It also shows a localised peak near the surface. This peak is due to the non-uniform temperature distribution at the beginning of dehydration process. The peak vanishes shortly after the temperature distribution stabilises. The pressure continues to increase and reaches more than 40 MPa, as can be seen from pressure distribution curve at $t = 582\,\mathrm{s}$. Pressures beyond 20 MPa result in a considerable increase of porosity within the whole sample. There is an increase of permeability that follows the porosity evolution as can be seen from Eq. (17). The permeability increase results in a pore pressure decay as shown in Fig. 2b at $t = 1.97\,\mathrm{ks}$ and later.

Figure 3a shows the variation of the overall porosity with respect to time. The numerical results obtained in this paper are comparable to those of (Fusseis et al. 2012), who considered similar loading conditions. Finally, the displacement that takes place within the domain is illustrated in Fig. 3b, which shows a residual displacement that remains within the reacted body.

5.3 Discussion

As can be seen in Fig. 2a, the temperature distribution is uniform beyond 10 s, which is mainly due to the thermal diffusivity (thermal conductivity over volumetric heat capacity) and the dimension of the sample. Like most geomaterials, the thermal diffusivity of gypsum is of the order of $1\,\mathrm{mm}^2\mathrm{s}^{-1}$. Since the radius of the sample is 1.15 mm, the time scale is of the order of $\pi\ 1.15^2\,\mathrm{s}$, which is close to the values that we obtained numerically. The enthalpy of the reaction does not significantly affect its distribution afterwards. Figure 2b shows the substantial increase of pore pressure immediately after the sample is heated up. The peak of pressure reaches around 45 MPa at $t = 582\,\mathrm{s}$, which is a relatively high value. After 582 s pressure decreases exponentially with respect to time as it is governed by a diffusion-like Eq. (16). The phenomenon of pore pressure diffusion is accelerated by the increase of permeability towards the periphery of the sample.

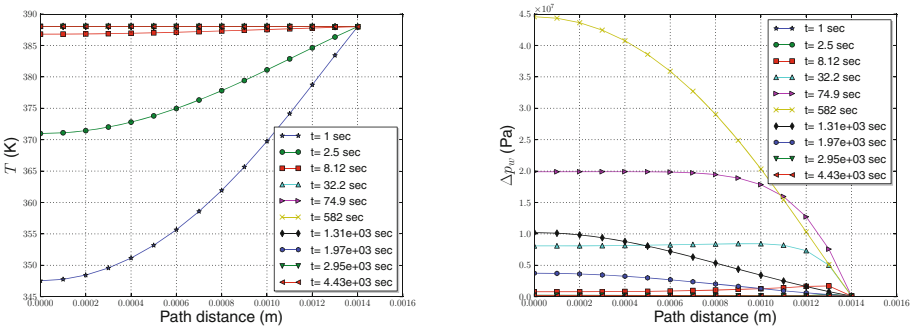

Fig. 2. Response of the sample in terms of (a) temperature an (b) pore pressure diffusion. The centre of the sample is located at the origin of the coordinate system.

The non-uniform variation of porosity with respect to time is depicted in Fig. 3a indicating that the porosity increases as the reaction front propagates towards the centre. This can be explained by the high pore pressure that builds up at the core due to water production, which suppresses the reaction. The results indicate that the maximum porosity stabilises at 30% about 10^3 s after initiation. Figure 3b describes the solid phase displacement within the sample. Apart from the non-linear behaviour that is due to multi-physics coupling used in the current framework, the results show that there is an overall increase of volume. Although there is a local volume decrease of volume because hemihydrate has smaller molecular volume than gypsum, there is a net displacement of the external surface. Along the radius the displacement increases gradually, reaches a maximum and starts decreasing as pore pressure is reduced. The displacement stabilises with a

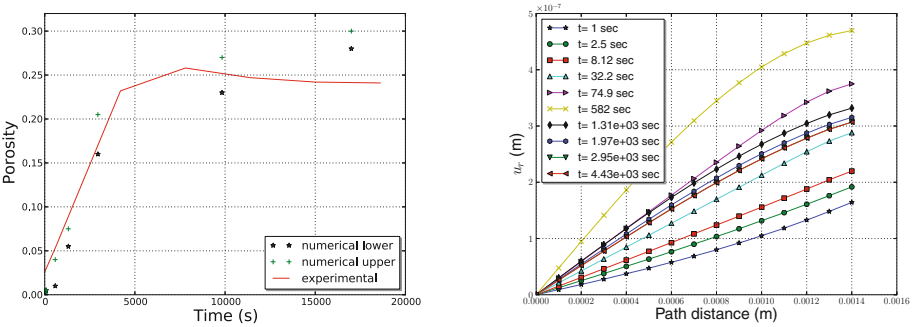

Fig. 3. (a) Experimental versus numerical results depicting the overall variation of porosity (b) Variation of displacement along the radius of the domain with respect to time.

net volume increase, although pore pressure continues to decrease due to drainage. The residual displacement that can be noticed in Fig. 3b are attributed to the increase of porosity, which is an irreversible process in the proposed model.

This contribution has been specifically formulated to capture the far from equilibrium processes that occur during the endergonic gypsum dehydration process which requires a positive flow of energy from the surroundings into the system to cause the dewatering reaction. The dehydration absorbs external power either through the application of deformational work with internal shear heating or through the application of heat. This latter case was investigated in the present manuscript.

The micro-physics underpinning this far from equilibrium dehydration process is quite complex as it involves an initial impermeable matrix which upon heating locally forms microscopic fluid pods that in turn need to form a connected network to be able to transport their fluid for the reaction to continue. Fluids can only be transported if the decreasing volume of the solid phase accommodates the fluid network, and the matrix can only deform if, upon heating, the increasing volume of fluid is able to flow by Darcy flow. If these tightly coupled thermo-hydro-mechanical-chemical (THMC) conditions for reaction are not fulfilled, the chemical reaction becomes metastable, and no phase change from gypsum to bassanite or anhydrite occurs. We have treated this complex fully coupled THMC problem through a thermodynamic averaging technique and appeal to the power of this energy- and entropy-based method. This is achieved through Onsager's relationships and by maximizing the product of the coupled diffusive fluxes times their driving thermodynamic forces. The thermodynamic averaging technique does not contradict a real case, where within the reference volume the reverse exothermic fluid precipitation reactions can take place locally to accommodate the necessary conditions for the bulk endergonic process. However, owing to the choice of the intrinsic maximum entropy production assumption, these processes are assumed to be vanishingly small. This may not be the case for more complex loading conditions.

Maximum entropy production is a strong assumption that underpins the foundations of plasticity theory. In our simple heating experiment it appeared to be a very good assumption as it can explain the data of the experiment. We observe a purely diffusive THMC coupled front propagating through the sample that maximises the entropy production. The current description, however, needs to be revised for the case of dewatering reactions under more general heating loads combined with mechanical deformation of the sample under generally applied shear or bulk deformation. Under shear conditions, for instance, the role of time dependent processes was found to be important (Alevizos et al. 2014; Poulet et al. 2014; Veveakis et al. 2014) for sufficiently high-applied shear loads. Under these conditions a multiplicity of steady states is possible. The current solution provides the stable end member for low loading rates. However, for a critical value of a constant shear force applied to the system, short oscillatory pulses of fluid release reactions were found to alternate with long periods of fluid precipitation. This solution does not fit the maximum entropy production

assumption. This is because for such cases the role of finite time must be explicitly considered (Veveakis and Regenauer-Lieb 2015) and the nonlinear THMC couplings require a thermodynamic approach, which allows assessment of the range of processes where the minimum of entropy production provides the correct (oscillatory) steady state.

6 Conclusions

This paper introduces a formulation of multi-physics processes involving thermo-hydro-chemo-mechanical interactions. It involves non-equilibrium thermodynamics to describe dehydration processes in geomaterials. The results show the importance of full coupling and exchange feedbacks. The heat supplied to the system induces a water release that fills pre-existing pores and induces over-pressure within the sample. The non-uniformity of the pore pressure, the small permeability, and the dependency of reaction rate on temperature and pressure play an important role in generating a slow and non-uniform porosity increase. The suggested approach is based on a comprehensive background that offers solving multi-physics processes within a thermodynamic framework. In this sense, the paper is the first to investigate the process of gypsum dehydration using a fully coupled numerical approach. In future work, the approach will be generalised to assess the impact of dehydration.

Acknowledgments. Christoph Schrank is grateful for funding by the German Research Foundation through grant SCHR 1262/1-1.

References

Alevizos, S., Poulet, T., Veveakis, E.: Thermo-poro-mechanics of chemically active creeping faults. 1: theory and steady state considerations. J. Geophys. Res. Solid Earth **119**(6), 4558–4582 (2014)

Bezou, C., Nonat, A., Mutin, J.C., Christensen, A.N., Lehmann, M.S.: Investigation of the crystal structure of $\gamma CaSO_4$, $CaSO_4 0.5 H_2O$, and $CaSO_4 0.6 H_2O$ by powder diffraction methods. J. Solid State Chem. **117**(1), 165–176 (1995)

Charola, A.E., Pühringer, J., Steiger, M.: Gypsum: a review of its role in the deterioration of building materials. Environ. Geol. **52**, 339–352 (2007)

Christensen, A.N., Olesen, M., Cerenius, Y., Jensen, T.R.: Formation and transformation of five different phases in the $CaSO_4 - H_2O$ system: Crystal structure of the subhydrate $\beta - CaSO_4 0.5 H_2O$ and soluble anhydrite $CaSO_4$. Chem. Mater. **20**(6), 2124–2132 (2008)

Cooper, A., Calow, R.: Avoiding gypsum geohazards: guidance for planning and construction. Technical report, British Geological Survey - Department for International Development, Nottingham (1998)

Freyer, D., Voigt, W.: Crystallization and phase stability of $CaSO_4$ and $CaSO_4$-based salts. Monatshefte für Chemie **134**(5), 693–719 (2003). doi:10.1007/s00706-003-0590-3

Fusseis, F., Schrank, C., Liu, J., Karrech, A., Llana-Fúnez, S., Xiao, X., Regenauer-Lieb, K.: Pore formation during dehydration of a polycrystalline gypsum sample observed and quantified in a time-series synchrotron X-ray micro-tomography experiment. Solid Earth **3**(1), 71–86 (2012)

IAPWS, Revised release on the IAPWS industrial formulation 1997 for the thermodynamic properties of water stream, Technical report, The International Association for the Properties of Water and Stream (2007)

Jacques, S.D.M., González-Saborido, A., Leynaud, O., Bensted, J., Tyrer, M., Greaves, R.I.W., Barnes, P.: Structural evolution during the dehydration of gypsum materials. Mineral. Mag. **73**(3), 421–432 (2009). doi:10.1180/minmag.2009.073.3.421

Karrech, A.: Non-equilibrium thermodynamics for fully coupled thermal hydraulic mechanical chemical processes. J. Mech. Phys. Solids **61**(3), 819–837 (2013)

Karrech, A., Poulet, T., Regenauer-Lieb, K.: Poromechanics of saturated media based on the logarithmic finite strain. Mech. Mater. **51**, 118–136 (2012)

Onsager, L.: Reciprocal relations in irreversible processes I and II. Phys. Rev. 37 and 38, 405–426 and 2265–2279 (1931)

Poulet, T., Veveakis, E., Regenauer-Lieb, K., Yuen, D.A.: Thermo-poromechanics of chemically active creeping faults. 3: the role of serpentinite in episodic tremor and slip sequences, and transition to chaos. J. Geophys. Res. Solid Earth **119**(6), 4606–4625 (2014)

Singh, N.B., Middendorf, B.: Calcium sulphate hemihydrate hydration leading to gypsum crystallization. Prog. Crystal Growth Charact. Mater. **53**(1), 57–77 (2007). doi:10.1016/j.pcrysgrow.2007.01.002

Truesdell, C., Noll, W.: The Non-Linear Field Theories of Mechanics. Springer, Heidelberg (2004)

Veveakis, E., Poulet, T., Alevizos, S.: Thermo-poro-mechanics of chemically active creeping faults: 2. transient considerations. J. Geophys. Res. Solid Earth **119**(6), 4583–4605 (2014)

Veveakis, E., Regenauer-Lieb, K.: Review of extremum postulates. Curr. Opin. Chem. Eng. **7**, 40–46 (2015)

A Comparative Evaluation of Indirect Methods to Estimate the Compressive Strength of Limestone (Chorgali Formation)

Sajid Ali[1,2(✉)], Sohail Akram[3], and Rashid Haider[4]

[1] Department of Earth Sciences,
COMSATS Institute of Information Technology, Abbottabad, Pakistan
[2] Neotectonics and Natural Hazards, RWTH Aachen University,
Lochnerstr. 4-20, 52056 Aachen, Germany
[3] Institute of Geology, University of the Punjab, Lahore, Pakistan
[4] Geological Survey of Pakistan, Lahore, Pakistan

Abstract. Evaluation of the strength of rockmass is very important to ensure the safety of the structures. The uniaxial compressive strength test (UCS), point-load index strength test (Is_{50}), Schmidt rebound hammer test (SRHN), tensile strength test (Ts), velocity test (Vp) and density have been commonly used for characterisation of the rockmass. The UCS is comparably expensive and time taking than other strength tests. Therefore, these tests have been correlated by various researchers for ease of evaluating the rock properties such as UCS. This study aims to correlate the UCS with Is_{50}, Vp, SRHN, Ts and density. The core samples were collected from different boreholes locations in the Salt Range, Pakistan. The lithology of the core samples was mainly Limestone of the Chorgali formation. Samples were prepared as per the ISRM standards. Afterwards, the strength tests have been performed in a laboratory followed by correlation of the UCS with Is50, Vp, SRHN, Ts and density. Then estimation capability of these correlations was checked by plotting actual UCS against the UCS estimated by correlation established. Plotted values were checked with reference to 1:1 diagonal. On the basis of which, it was concluded that all correlation were reasonable except UCS versus Is_{50} axial and UCS versus SRHN axial. The Is_{50} axial overestimated the UCS because of vertical variation in the lithology from limestone to argillaceous limestone while the SRHN axial underestimated the UCS value because of low rebound due to bedding surfaces encountered. It has been found that the data was scattered and the value of coefficient of variance was considerably high ranging from 29 to 59. These variations in the data were mainly due to mineralogical variation in the Chorgali Formation from limestone to argillaceous limestone.

Keywords: Point load strength · Uniaxial Compressive Strength · Schmidt Rebound Hammer Test · Tensile strength · Choregali formation

L.R. Hoyos and J. McCartney (eds.), *Advances in Characterization and Analysis of Expansive Soils and Rocks*, Sustainable Civil Infrastructures,
DOI 10.1007/978-3-319-61931-6_15

1 Introduction

The strength of rockmass is one of the basic parameters required for the design and stability analysis of the structures. The essential rock properties are Uniaxial Compressive Strength (UCS), Point-load Index Strength (Is_{50}), Schmidt Rebound Hammer Number (SRHN) and Tensile Strength (Ts) but UCS is the most important one. Due to some limitations: sophistication and unportability of apparatus, it is not easy to carry out the UCS in field. Therefore, other rock properties are often correlated with the UCS for evaluating rock properties particularly during preliminary design stage. Due to portability, cheapness and easiness to perform in the field, Is_{50} and SRHN have often been used to calculate the UCS by using previous correlations. In this paper, an attempt is made to establish correlations between the UCS and other mechanical properties of rockmass. The Laboratory tests have been performed on the core samples comprising of limestone of the Chorgali formation. These core samples have been collected from the drilling sites in Salt Range (Fig. 1).

Different studies were conducted by different researchers to show the relation of the UCS with other physical properties of the rock samples (Inoue and Ohomi 1970; Broch and Franklin 1972; Sheorey et al. 1984; Ulusay et al. 1994; 1999; Katza et al. 2000; Kahraman 2001; Yasar and Erdogan 2004; Kilic and Teymen 2008). Kahraman et al. 2012 has proposed a linear correlation between BT and the UCS having coefficient of determination 0.5 which is not reliable.

Farah (2011) also studied the Ocala limestone and found a better correlation between the UCS and Ts as compare to with Is_{50}. Altindag and Guney (2010) also established a strong relationship between the Ts and UCS.

D'Andrea et al. (1964) correlated the UCS and Is_{50} for various rock samples and found following regression model:

$$q_u = 16.3 + 15.3Is_{50} \tag{1}$$

Whereas:
q_u = Uniaxial Compressive Strength of rock.
Is_{50} = Point Load Index for 50 mm diameter core.

Gupta and Rao (2009) found a positive linear relationship between the UCS and Is_{50}, Ts but an exponential positive with SRHN. Kilic and Teymen (2008) ascertained a reasonable and a non-linear correlation between the UCS and Is_{50}, Ts, Vp and SHRN. Dincer et al. (2004) established a linear correlation between SHRN and the UCS. Chau and Wong 2012 developed a formula for the evaluation of the UCS by using simple methods. Akram and Bakar (2007) proposed to validate the correlations by plotting the estimated UCS values against actual ones.

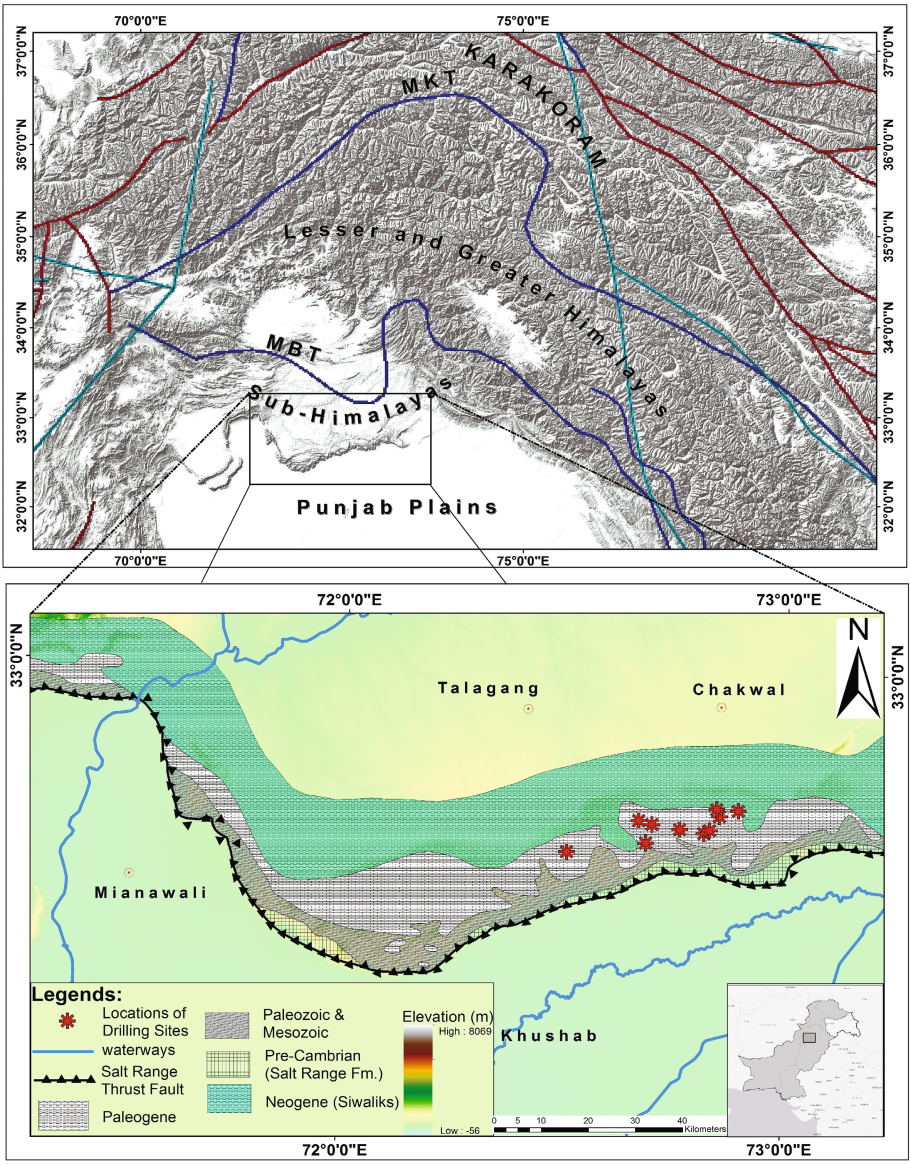

Fig. 1. Location and overview of geology of the study area: MBT-Main Boundary thrust, MKT-Main Karakorum Thrust

2 Geology of Study Area

The Upper Indus Basin possesses a unique tectonic setting. The youngest and highest mountain orogeny namely the Himalayan Orogeny is a result of continent to continent collision between northward drifting Indo-Pak Plate and southward drifting Eurasian Plate about 55 M.a ago. The Himalayas extends from the Punjab plains in south to the Karakorum in north. It is further classified into: Sub-Himalayas, Lesser Himalayas and Greater Himalayas. The Salt Range is a part of the Sub-Himalayas and is the most southern part of the orogeny (Fig. 1). It is an active thrust zone with about 1 km offset. The basement normal faults acted as a buttress that caused the Central Salt Range-Potwar Plateau thrust sheet to ramp to the surface, exposing the Mesozoic and Paleozoic strata (Lillie et al. 1987). Lack of internal deformation of the rear part of the thrust sheet is due to decoupling of sediments from the basement along this salt layer. The oldest strata (Infra-Cambrian) are exposed in south which gradually grades into the younger strata in the north (Quaternary). The closure of Neo-Tethys and rise of the Himalayas resulted in different stratigraphic sequences. The Eocene succession of Salt Range marks a complete transgressive-regressive system of deposition. The lower most Nammal Formation of Eocene (Early Ypreasian), shows a transgressive stacking of facies in a vertical sequence, the facies of Sakesser Limestone exhibits a Highstand system tract, while the Chorgali Formation reflects a system of deposition in which the Tethys Ocean was gradually receding. Predominantly, the Chorgali Formation consists of the alternating limestone and shale. Shales are rich in Eocene larger benthic foarms. Above the Chorgali Formation, the terrestrial sediments of Kamlial Formation (Miocene) are developed extensively. The development of Cal-rudite at the contact of Chorgali and Kamlial Formations shows a period of erosion during the final regression in the Upper Indus Basin. Internally, the Chorgali formation is composed of alternating limestone, shale and intermediate facies of argillaceous limestone (Fig. 2).

Fig. 2. Lithological variations in the samples: (a) limestone (b) argillaceous limestone (c) Alternate bedding of limestone and argillaceous limestone (d) Alternate bedding (e) Encircled part is argillaceous limestone

3 Methodology

Methodology involves collection of the core samples of 62 mm and 42 mm in diameter from different drilling sites in the Salt Range (Fig. 1). The core samples were comprised of limestone of the Choregali Formation. After collection, the samples were prepared as per the ASTM and ISRM standards 1985 (Fig. 3c). The background information of the core samples prior to testing was also recorded in prescribed performa. The dimensions of all the samples were kept in compliance with the ISRM standards for the UCS Test, Point Load Test (axial and diametral) and Rebound number (Rn) (axial and diametral). The purpose of these tests was to determine the rock strength. Afterwards values of $Is_{50,}$ TS, Rebound number (Rn) were correlated with the UCS and a correlation was established

Fig. 3. Collection of the core samples and the failed core samples during the UCS test: (a) Identification of the core samples belonging to the Choregali Fm. (b) Selected core samples of the Choregali Fm. from one of the drilling site (c) Prepared specimens for the UCS test (d) failed samples after UCS test.

4 Result and Discussions

4.1 Regression Analysis

The test results were analysed by using the method of least square regression. Indirect test values were correlated with the corresponding UCS values and among each other. The equation of the best fit line and the correlation co-efficient were determined for each regression.

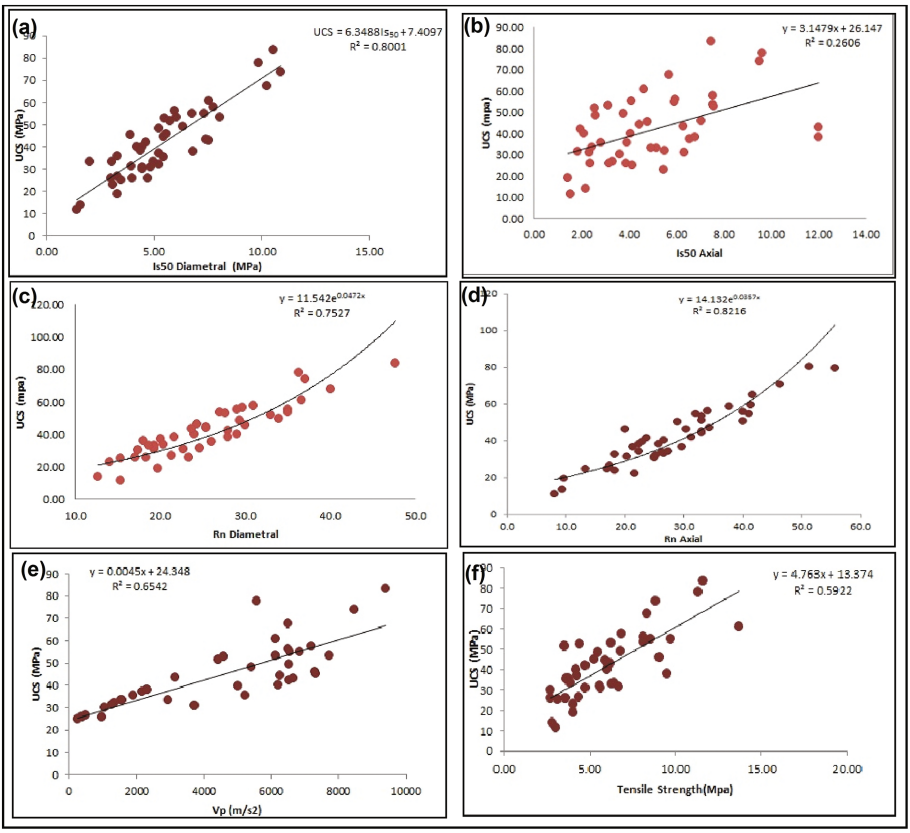

Fig. 4. Correlation between the UCS and other variables: (a) UCS versus Is50 (diametral) (b) UCS versus Is50 (axial) (c) UCS versus SRHN (diametral) (d) UCS versus SRHN (axial) (e) UCS versus Vp (f) UCS versus Tensile strength.

The relation between Is_{50}diametral, Is_{50}axial has been found linear (Fig. 4a and b) and equations of the lines are:

$$UCS = 6.3488 Is_{50} diametral + 7.4097 \quad \left(r^2 = 0.8001\right) \tag{2}$$

$$UCS = 3.1479 Is_{50} axial + 26.147 \quad \left(r^2 = 0.2606\right) \tag{3}$$

Exponential relations have been established between Rn diametral, Rn axial and UCS (Fig. 4c and d) and equations of curves are:

$$UCS = 11.542 e^{0.0472 Rn\ diametral} \quad \left(r^2 = 0.7527\right) \tag{4}$$

$$UCS = 14.132 e^{0.0357 Rn\ axial} \quad \left(r^2 = 0.8216\right) \tag{5}$$

The UCS values showed a linear relation with Ts and Vp values (Fig. 4e and f) and equations of lines are:

$$UCS = 0.0045Vp + 24.348 \quad \left(r^2 = 0.6542\right) \tag{6}$$

$$UCS = 4.763T_s + 13.374 \quad \left(r^2 = 0.5922\right) \tag{7}$$

It has been observed that the SRHN (axial) remained higher as compare to the SRHN (diametral) (Fig. 5a). On the basis of which it has been speculated that across bedding, there is less rebound impact due to presence of the discontinuities (bedding planes).

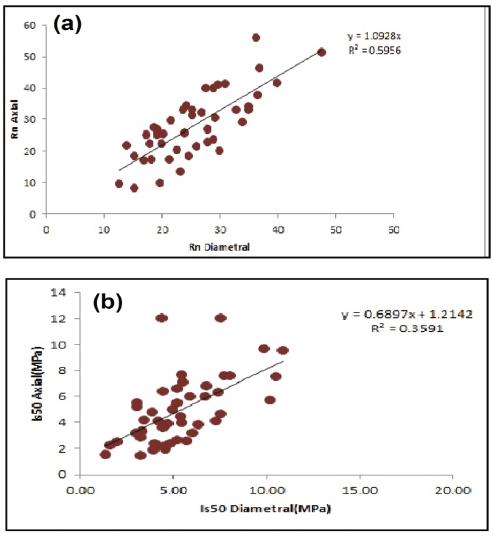

Fig. 5. Comparison of diametral and axial strength: (a) SRHN (diametral) versus SRHN (axial) (b) Is50 (diametral) versus Is50 (axial).

4.2 Estimation Capability of Correlations

The UCS values has been plotted against the estimated UCS values (from correlations) to check their estimation capability. The values of UCS were calculated by using Eqs. 2, 3, 4, 5, 6 and 7. Then, these values were plotted against the actual values of UCS. After plotting, the values, 1:1 diagonal lines were observed (Fig. 6).

The estimation capability of Eqs. 2, 4, 6 and 7 was found reasonable as values were found close to diagonal line (Fig. 6a, c, e and f). Whereas, diagonal lines for other Eqs. (3 and 5) were not suitable for estimation of the UCS as most of the values were away from diagonal lines. SRHN axial underestimated the UCS (Fig. 6d) as almost all points are above diagonal lines which may be due to presence of bedding surfaces (Fig. 3c) which decreased rebound impact by absorbing energy, whereas, Is_{50} axial overestimated the UCS (Fig. 6b). The scattering in data is due to the variations in lithology of sample (Fig. 3).

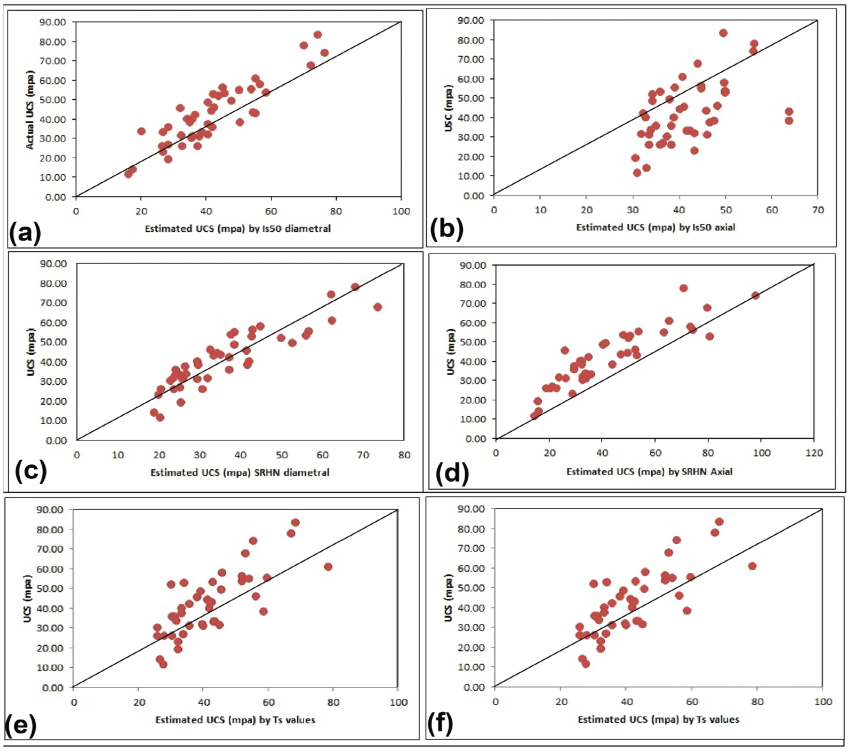

Fig. 6. Estimation capacity of correlations: (a) Estimated UCS versus Actual UCS for Eq. 2 (b) Estimated UCS versus Actual UCS for Eq. 3 (c) Estimated UCS versus Actual UCS for Eq. 4 (d) Estimated UCS versus Actual UCS for Eq. 5 (e) Estimated UCS versus Actual UCS for Eq. 6 (f) Estimated UCS versus Actual UCS for Eq. 7

4.3 Comparison of Correlations with Previous Studies

In the past, different researcher used different techniques to establish the correlations. Investigators used linear, exponential and power function techniques to evaluate the UCS. We used the linear regression techniques for establishment of correlations between $Is_{50,}$ Ts, Vp and the UCS. But, we used the exponential technique for SRHN and the UCS correlation. Then, correlation of Is_{50} (diametral and axial) was compared with previous studies. The derived equations (Eqs. 2 and 3) showed the same trend as observed in previous studies (Fig. 7). Further, the correlation of UCS with SRHN was compared with previous correlation. Equations 4 and 5 also showed same trend as of the previous equations (Fig. 8).

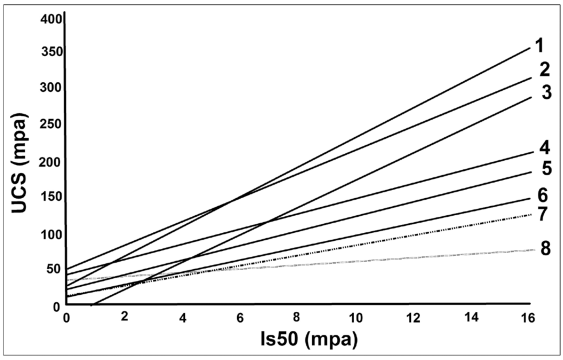

Fig. 7. Comparison of this study with the previous studies (UCS vs. Is_{50}): (1) Chargill and Shakoor (1990) (2) Kahraman (2001) (3) Singh (1981) (4) Ferner et al. (2005) (5) Grasso et al. (1992) (6) Kahraman (2001) (7) This study (UCS vs. Is_{50} (diametral) (8) This study (UCS vs. Is_{50} (axial).

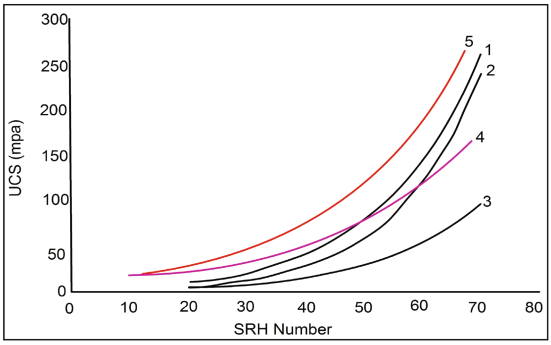

Fig. 8. Comparison of this study with the previous studies (UCS vs. SRHN): (1) Ferner et al. (2005) (2) Katz et al. (2000) (3) Yilmaz and Sendir (2002) (4) This study (UCS vs. SRHN axial) (5) This study (UCS vs. SRHN diametra).

4.4 Statistical Analysis of Data

SRHN (diameteral) has a mean value of 25.6 and lower value is 12.7. Also upper value is 47.70 (Table 1). These values show that there is a great variation in the results which is due to different mineralogical composition of the Chorgali Formation ranging from argillaceous limestone to limestone. The values of SD and CoV are 7.64 and 29.88 respectively. The same case is in SRHN (Axial) in which the values of mean, lower value, Upper value SD and CoV are 28, 8, 55.70, 10.62 and 37.95. The values of UCS test, Ts test results and Is_{50} are scattered as it shows high value of coefficient of variation.

Table 1. Statistical significance of data

Statistical Findings		Mean	Lower	Upper	SD	CoV (%)	Cl95
Schmidt rebound hammer test	Diametral	25.6	12.70	47.70	7.64	29.88	1.52
	Axial	28.00	8.00	55.70	10.62	37.95	1.04
Point load test	Is(50) Diametral	5.40	1.40	10.90	2.26	41.80	0.23
	Is(50) Axial	4.90	1.40	12.00	2.60	52.60	0.19
Brazilian test		6.00	2.70	13.70	2.62	43.24	0.31
Uniaxial compression test	UCS	41.50	11.20	80.07	15.73	37.93	2.99
Density		2.63	2.27	2.92	0.12	4.79	0.02
Sound velocity test	P-wave velocity	4389.15	253.13	9387.33	2618.84	59.67	452.42

5 Conclusion

The objective of the research was to correlate the UCS with Is_{50} (diameteral and axial), SRHN (axial and diameteral), Ts and Vp of the specimen. These parameters have been calculated by performing tests as per the ISRM standards. Forty seven samples were tested for evaluation of the strength. We have following conclusions from the data analysis:

a. The estimation capability of Eqs. 2, 4, 6 and 7 was found reasonable as values were found close to the diagonal line (Fig. 6a, c, e and f).
b. Eqs. (3 and 5) were not found suitable for estimation of UCS as most of the values were above or below the diagonal lines.
c. SRHN axial underestimated the UCS (Fig. 6d) as most of the points are above diagonal lines which may be due to presence of bedding surfaces (Fig. 3c) which decreased rebound impact by absorbing energy, whereas, Is_{50} axial overestimated the UCS (Fig. 6b).
d. Established correlations (Eqs. 2, 3, 4 and 5) showed the same trend as observed in the previous studies (Figs. 7 and 8).
e. Data was scattered and value of coefficient of variance was considerably high ranging from 29 to 59 (Table 1). Scattering in strength values was mainly due to the mineralogical variation in the Chorgali Formation as lithology was comprised of limestone and argillaceous limestone (Fig. 3).

Acknowledgement. The authors here are in acknowledgement of the Mine and Mineral Department, Government of the Punjab, for providing core samples from boreholes drilled for coal estimation project.

References

Akram, M., Bakar, M.Z.A.: Correlation between uniaxial compressive strength and point load index for Salt-Range rocks. Pak. J. Eng. Sci. **1**, 1–8 (2007)

ASTM. Standard test method of unconfined compressive strength in intact rock core specimens. Annual Book of ASTM standards, American Society of Testing Materials, Philadelphia ASTM Stand. 04.08 (D 2938) (1986)

ASTM. Standard testing method for determination of the point load strength index of rock. Annual Book of ASTM standards, American Society of Testing Materials, Philadelphia ASTM 04.08 (D5731-02) (2000)

ASTM. Standard testing method for determination of rock hardness by rebound hammer method. Annual Book of ASTM standards, American Society of Testing Materials, Philadelphia ASTM 04.09 (D5873-00) (2001)

Aufmuth, R.E.: A systematic determination of engineering criteria for rocks. Bull. Assoc. Eng. Geol. **11**, 235–245 (1973)

Broch, E., Franklin, J.A.: Point load strength test. Int. J. Rock Mech. Min. Sci. Geomech. Abstr. **9**, 669–697 (1972)

Cargill, J.S., Shakoor, A.: Evaluation of empirical methods for measuring the uniaxial compressive strength of rock. Int. J. Rock Mech. Min. Sci. **27**, 495–503 (1990)

Chou, K.T., Wong, R.H.C.: Uniaxial compressive strength and point load strength. Int. J. Rock Mech. Min. Sci. **33**, 183–188 (1996)

D'Andrea, D.V., Fisher, R.L., Fogelson, D.E.: Prediction of compression strength from other rock properties. Colorado Sch. Min. Q. **59**, 623–640 (1964)

Deere, D.U., Miller, R.P.: Engineering classification and index properties for intact rock. Air Force Weapons Lab. Tech. Report, AFWL-TR 65–116, Kirtland Base (1966)

Dincer, I., Acar, A., et al.: Correlation between Schmidt hardness, uniaxial compressive strength and Young's mudulus for andesite, basalt and tuffs. In: Brown, E.T. (ed.) Eng. Geol. Env., pp. 141–148. Pergamon Press, Oxford Bull (2004). doi:10.1007/s10064-004-0230-0

Dincer, I., Acer, A., et al.: Estimation of strength and deformation properties of Quaternary caliche deposits. Bull. Eng. Geol. Environ. 67: 353–366. doi:10.1007/s10064-008-0146-1

Fener, M., Kahraman, S., Bilgil, A., Gunayadin, O.: A comparative evaluation of indirect methods to estimate the compressive strength of rocks. Rock Mech. Rock Eng. **38**(4), 329–343 (2005)

Forster, I.R.: The influence of core sample geometry on the axial point-load test. Int. J. Rock Mech. Min. Sci. **20**, 291–295 (1983)

Ghose, A.K., Chakraborti, S.: Empirical strength indicates of Indian coals-an investigation. In: Proceedings of the 27th US Symposium Rock Mechanics, pp. 59–61. Balkema, Rotterdam (1986)

Ghosh, D.K., Srivastava, M.: Point load strength: an index for classification of rock material. Bull. Int. Assoc. Eng. Geol. **44**, 27–33 (1991)

Grasso, P., Xu, S., et al.: Problems and promises of index testing of rocks. In: Tillerson, Wawersik (eds) Proceedings of 33rd US Symposium on Rock Mechanics, Sante Fe, pp. 879–888 (1992)

Gunsallus, K.L., Kulhawy, F.H.: A comparative evaluation of rock strength measures. Int. J. Rock Mech. Min. Sci. **21**, 233–248 (1984)

Gupta, V.: Non-destructive testing for some higher Himalayan rocks in the Satluj valley. Bull. Eng. Geol. Environ. **68**, 409–416 (2009). doi:10.1007/s10064-009-0211-4

Haramy, K.Y., Marco, M.J.: Use of the schmidt hammer for rock and coal testing. In: 26th US Symposium on Rock Mechanics, Rapid City (1985)

Hassani, K.Y., Scoble, M.J.J., Whittaker, B.N.: Application of point-load index test to strength determination of rock and proposals for new size-correction chart. In: Summers, D.A. (ed.) Proceedings of the 21st US Symposium Rock Mechanics, Rolla, Missouri, pp. 543–553 (1980)

Hawkes, I., Mellor, M.: Uniaxial testing in rock mechanics laboratories. Eng. Geol. **4**, 177–285 (1970)

Inoue, M., Ohomi, M.: Study on the strength of rocks by the Schmidt hammer test. Rock Mech. Japan **1**, 177–179 (1970)

Brown, E.T. (ed.): ISRM. Suggested Methods-Rock characterization, testing and monitoring. Pergamon Press, Oxford (1981)

ISRM: Suggested method for determining point load strength. Rock Mech. Min. Sci. Geomech. Abstr. **22**, 53–60 (1985)

ISRM. Suggested method for determining hardness and abrasiveness of rocks. Rock Mech. Min. Sci. Geomech. Abstr. **15**, 89–97 (1987)

Kahraman, S.: Evaluation of simple methods for assessing the uniaxial compressive strength of rock. Rock Mech. Min. Sci. **38**, 981–994 (2001)

Kahraman, S., Gunaydin, et al.: The effect of porosity on the relation between uniaxial compressive strength and point load index. Rock Mech. Min. Sci. **42**, 584–589 (2005)

Kahraman, S., Bilgil, A.: A comparative evaluation of indirect methods to estimate the compressive strength of rocks. Rock Mech. Rock Eng. **38**(4), 329–343 (2005). doi:10.1007/s00603-005-0061-8

Kahraman, S., Gunaydin, O.: Empirical methods to predict the abrasion resistance. Bull. Eng. Geol. Environ. **66**, 449–455 (2007). doi:10.1007/s10064-007-0093-2

Kahraman, S., Gunaydin, O.: The effect of rock classes on the relationship between uniaxial compressive strength and point load index. Bull. Eng. Geol. Environ. **68**, 345–353 (2009). doi:10.1007/s10064-009-0195-0

Karakus, M., Kumral, M., et al.: Predicting elastic properties of intact rocks from index tests using multiple regression modeling. Rock Mechanics and Mining Sciences **42**, 323–330 (2005)

Katz, O., Reches, Z., Roegiers, J.C.: Evaluation of mechanical rock properties using a schmidt hammer. Int. J. Rock Mech. Min. Sci. **37**, 723–728 (2000)

Kidybinski, A.: Bursting liability indices of coal. Int. J. Rock Mech. Min. Sci. **17**, 157–161 (1980)

Kilic, A., Teymen, A.: Determination of mechanical properties of rocks using simple methods. Bull. Eng. Geol. Environ. **67**, 237–244 (2008). doi:10.1007/s10064-008-0128-3

Kurtulus, C., Irmak, S.T.: Physics and mechanical properties of Gokceada: Imbros (NE Aegean sea) Island andesites. Bull. Eng. Geol. Environ. **69**, 321–324 (2010)

Li, L., Aubertin, M.: A general relationship between porosity and uniaxial strength of engineering materials. Can J. Civil Eng. **30**, 644–658 (2003)

Lillie, R.J., Johnson, G.D., Yousuf, M., Zamin, A.S.H., Yeats, R.S.: Structural development within the Himalayan foreland fold-and-thrust belt of Pakistan. In: Beaumont, C., Tankard, A. (eds.) Memoirs of the Canadian Society of Petroleum Geologists, vol. 12 (1987)

Palchik, V., Hatzor, Y.H.: The influence of porosity on tensile and compressive strength of porous chalk. Rock Mech. Rock Eng. **37**, 331–341 (2004)

Pells, P.N.J.: The use of point load test in predicting the compressive strength of rock material. Aust. Geomech. **G5**(N1), 54–56 (1975)

Potro, R., Hurlimann, M.: A comparison of different indirect techniques to evaluate volcanic intact rock strength. Rock Mech. Rock Eng. **42**, 931–938 (2009). doi:10.1007/s00603-008-0001-5

Quane, S.L., Russel, J.K.: Rock strength as a metric of welding intensity in pyroclastic deposits. Eur. J. Mineral. **15**, 855–864 (2003)

Rajabzadeh, M.A., Moosavinasab, Z., et al.: Effects of rock classes and porosity on the relation between uniaxial compressive strength and some rock properties for carbonate rocks. Rock Mech. Rock Eng. (2011) doi: 10.1007/s00603-011-0169-y

Read, J. R. L., Thornten, P.N., Regan, W.M.: A rational approach to the point load test. In: Proceedings of the 3rd Australian-Newzealand Geomechanics Conference, vol. 2, pp. 35–39 (1980)

Sachpazis, C.: Correlating Schmidt hardness with compressive strength and Young's Modulus of carbonate rocks. Int. Assoc. Eng. Geol. Bull. **42**, 75–84 (1990)

Schmidt, E.: A non-desructive concrete tester. Concrete **59**(8), 34–35 (1951)

Sheorey, P.R., Barat, D., et al.: Schmidt hammer rebound data for estimation of large scale in situ coal strength. Rock Mech. Min. Sci. **21**, 39–42 (1984)

Singh, D.P.: Determination of some engineering properties of weak rocks. In: Proceedings of International Symposium Weak Rock, Tokyo, pp. 21–24 (1981)

Singh, R.N., Hassani, F.P., Elkington, P.A.S.: The application of strength and deformation index testing to the stability assessment of coal measure excavations. In: Proceedings of the 24th US Symposium Rock Mechanics, Texas, pp. 599–609 (1983)

Smith, H.J.: The point load test for weak rock in dredfinnf applications. Int. J. Rock Mech. Min. Sci., 702 (1997)

Szucs, E.: Similitude and Modelling. Elsevier, Budapest (1980)

Tsiambaos, G., Sabatakakis, N.: Considerations on strength of intact sedimentary rocks. Eng. Geol. **72**, 261–273 (2004)

Tsidzi, K.E.N.: Point load-uniaxial compressive strength correlation. In: Proceedings of the 7th ISRM Congress, Aachen, Germany, vol. 1, 637–639 (1991)

Yilmaz, I., Sendir, H.: Correlation of Schmidt hardness with unconfined compressive strength and Young's modulus in gypsum from Sivas (Turkey). Eng. Geol. **66**, 211–219 (2002)

Vallejo, L.E., Welsh, R.A., Robinson, M.K.: Correlation between unconfind compressive and point load strength for appalachian rocks. In: Proceedings of the 30th US Symposium Rock Mech, Morgantown, pp. 461–468 (1989)

Xu, S., Grasso, P., Mahtab, A.: Use of schmidt hammer for estimation mechanical properties of weak rock. In: Proceedings of the 6th International Association of Engineering Geology Congress, pp. 511–519. Balkema, Rotterdam (1990)

Yasar, E., Erdogan, Y.: Estimation of rock physicomechanical properties using hardness methods. Eng. Geol. **71**, 281–288 (2004)

Isotope Stratigraphy of the Permian Rocks, the Volga River Region

N.G. Nurgalieva[1(✉)], B.I. Gareev[2], and D.K. Nurgaliev[1]

[1] Institute of Geology and Petroleum Technologies, Kazan Federal University, Kazan, Russia
nurgal07@mail.ru
[2] Kazan Federal University, Kazan, Russia

Abstract. In this investigation the $^{87}Sr/^{86}Sr$ values were considered for the Upper Kazanian regional section Pechishchi and accompanied sections of the Lower Kazanian substage and also the Lower Permian formation. The section Pechishchi is known as reference section formed within the Kazanian palaeosea. It is characterized by three modified Noinsky's cycles of Kazanian palaeosea evolution. The highest ratio value 0.70832 was received for the Asselian rocks. In the Artinskian stage, the $^{87}Sr/^{86}Sr$ ratios decrease to 0.70774. In the Kazanian stage, the strontium ratio is much lower: 0.70769 in the Lower Kazanian substage and 0.70740 in the Upper Kazanian substage. The discrepancies between local and global data observed at some points can be explained by regional features of the sedimentation in the eastern part of the Russian Plate during the Permian period because of arid climate trend and increasing of region isolation from the ocean.

1 Introduction

In the present paper the $^{87}Sr/^{86}Sr$ values were considered for the Permian regional reference section. Samples for studies were collected from the Pechishchi section: the reference succession of the Upper Kazanian substage of the Kazanian regional stage. The Permian trend was identified and described using also core samples from the sections of the Lower Kazanian substage, the Cisuralian (Lower Permian) series of the Permian system and the Gzhelian stage of the Upper Carboniferous series of the subsurface well continuation of the Pechishchi section.

The Pechishchi section area includes the most complete Upper Kazanian marine and evaporite members in Volga-Kama rivers region. The section clearly features three Noinsky's cycles. Each Noinsky's cycle consists of three facial components (marine carbonate, evaporite lagoon carbonate-sulphate and lake clayey facies) up the section (Noinsky 1924), modified after the XRF examination of the section (Gareev et al. 2016) (Fig. 1).

The Rb-Sr classification of carbonates was obtained using the bulk carbonate component after solving a weighed portion of the crushed sample in 10% acetic acid. Rb and Sr were conventionally separated by the ion exchange technique using Dowex AG50Wx8 cation exchanger (200 to 400 bags) and 2.5 N HCl as an eluent. Rb and Sr contents were determined by the mass-spectrometric method of isotope dilution using a

L.R. Hoyos and J. McCartney (eds.), *Advances in Characterization and Analysis of Expansive Soils and Rocks*, Sustainable Civil Infrastructures,
DOI 10.1007/978-3-319-61931-6_16

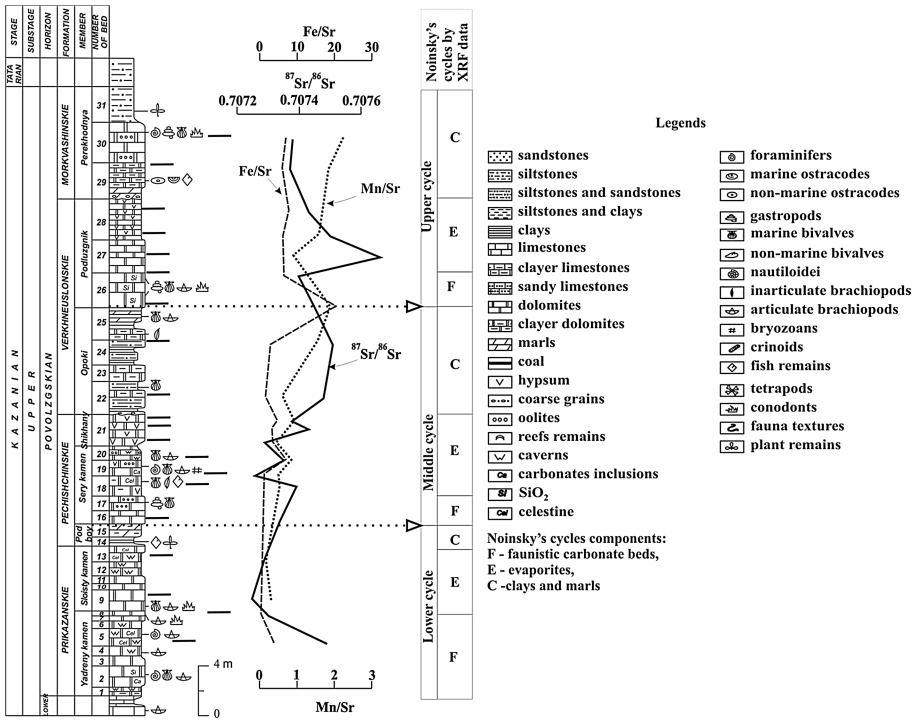

Fig. 1. Isotopic-geochemical ratios variations, Pechishchi section diagram after (Nurgalieva et al. 2007) with modified scheme of Noinsky's cycles using XRF data (Gareev et al. 2016)

mixed ^{87}Rb-^{84}Sr indicator. The Sr isotopic composition was determined by the Finnigan MAT-261 multiple collector mass-spectrometer simultaneously recording ion currents of all isotopes. The $^{87}Sr/^{86}Sr$ average ratio normalized to $^{86}Sr/^{88}Sr = 0.1194$ in the standard SRM 987 sample was estimated at 0.71025 ± 0.00001. The degree of preservation/alteration of carbonates was estimated using published criteria. The separation of samples with disturbed and undisturbed isotopic systems was performed using the following Mn/Sr and Fe/Sr values: <5 and <20 for limestones and <10 and <60 for dolomites, correspondingly (Table 1) (Nurgalieva et al. 2007).

The $^{87}Sr/^{86}Sr$ values are the highest in the Asselian stage, and average at 0.70832. In the Artinskian stage, the $^{87}Sr/^{86}Sr$ ratios decrease to 0.70774. In the Kazanian regional stage, the strontium ratio is much lower: 0.70769 in the Lower Kazanian substage and 0.70740 in the Upper Kazanian substage (Table 1, Fig. 1).

A decrease in the $^{87}Sr/^{86}Sr$ ratio, recorded for the Early Kazanian and early Late Kazanian, generally corresponds to the $^{87}Sr/^{86}Sr$ Phanerozoic evolution curve and indicates the ocean influence, but absolute values of $^{87}Sr/^{86}Sr$ ratios are relatively high reflecting the continent influence and climate change at later times (Nurgalieva et al. 2007).

The discrepancies between local and global data observed at data points can be explained by the local features of the sedimentation during the Permian period in the

Table 1. Average isotopic and geochemical characteristics of the composite stratigraphic succession (the fragment of data from (Nurgalieva et al. 2007))

Stratigraphy		Mn/Sr	Fe/Sr	$^{87}Sr/^{86}Sr$
Series, substage	Member			
Upper Kazanian substage (Pechishchi outcrop section)	Perekhodnaya	2.05	6.44	0.70738
	Podluzgnik	1.44	9.39	0.70749
	Opoki	1.08	2.06	0.70750
	Shikhany	0.69	3.86	0.70737
	Sery Kamen	0.54	2.47	0.70734
	Sloisty Kamen	0.23	0.46	0.70727
	Yadreny Kamen	0.04	2.06	0.70740
Lower Kazanian substage (subsurface section)	Middle Spirifer Limestone	4.95	2.31	0.70769
Cisuralian (Lower Permian) series (subsurface section)	Artinskian stage	–	–	0.70774
	Sakmarian stage	0.08	0.17	0.70775
	Asselian stage	1.06	3.23	0.70832
Upper Carboniferous series (subsurface section)	Gzhelian stage	0.14	1.64	0.70815

eastern part of the Russian platform (the arid climate trend and considerable isolation from the ocean); and problems with the chronostratigraphic positioning of the $^{87}Sr/^{86}Sr$ Phanerozoic evolution curve and local $^{87}Sr/^{86}Sr$ curves within the Permian (Nurgalieva et al. 2007).

2 Conclusions

Multiple determinations of strontium isotope ratios in the Permian carbonates and the absolute dating of key samples would allow the revision of the Permian stratigraphic record in regional and global scale.

References

Gareev, B., Georgii, B., Nurgaliev, D., Nurgalieva, N.: Studying the Permian cross-section (Volga region) using chemical and isotopic investigations. Geophysical Research Abstracts. 18, EGU2016-13097 (2016). http://meetingorganizer.copernicus.org/EGU2016/EGU2016-13097.pdf

Noinsky, M.E.: Some data on structure and facies of the Kazanian in the Prikazansky (Kazan) region. Bull. Geol. Comm. **13**(6), 565 (1924)

Nurgalieva, N.G., Ponomarchuk, V.A., Nurgaliev, D.K.: Strontium isotope stratigraphy: possible applications for age estimation and global correlation of late permian carbonates of the pechischi type section (Volga River). Russ. J. Earth Sci (2007). doi:10.2205/2007ES000221

Evaluating the Effect of Fines on Hydraulic Properties of Rammed Earth Using a Bench Scale Centrifuge

Abdullah Galaa[1(✉)], Gemmina Di Emidio[2], Benny Malengier[3], Herman Peiffer[2], R. Verastegui Flores[4], and Wim Cornelis[5]

[1] Geotechnical Institute, Housing and Building National Research Center, Giza, Egypt
[2] Laboratory of Geotechnics, Ghent University, Ghent, Belgium
[3] Department of Textiles, Ghent University, Ghent, Belgium
[4] iMMC, Université Catholique de Louvain, Louvain-la-Neuve, Belgium
[5] Department of Soil Management, Ghent University, Ghent, Belgium

Abstract. Unstabilized Rammed Earth (RE) has been historically used to form earth walls or blocks. Recently RE has resurfaced as a sustainable building material with little attention given to it in building codes and manuals. The percentage of the fine-grained fraction in RE is one of the most important factors affecting its behavior. Such percentage has been selected in practice based on experience and rules of thumb, not on a scientific rationale. This research examines the influence of the amount and type of fine particles on the hydraulic conductivity and water retention characteristics of compacted soils using a bench scale centrifuge. A Durner curve (1994) was applied to describe the water retention curve as it allows portraying a bimodal pore structure. In an attempt to understand the basis on which fines contribute to the strength of RE, two different types of fine grained soils were used in the mixtures, plastic fines (PF) and non-plastic fines (NPF). Each type was divided further into different mixtures, each with different percentages of fines. The influence of the fines' percentage was tested using different methods and by using saturated and unsaturated samples of the soil mixtures. Larger suction developed in samples with PF in comparison to those with NPF. Suction increased as the percentage of fines in the mixture increased. Such effect is more pronounced in samples with PF.

Keywords: Rammed earth · SWRC · Suction · Centrifuge · Hydraulic conductivity

1 Introduction

Building with rammed earth (RE) is a practice inherited over millennia in many regions in the world, especially arid regions. RE has surfaced to the attention of many builders and researchers during the past few decades due to the low embodied energy associated with building with such materials, the reduced energy bill for RE houses, and the reduced use of cement. Over millennia, bearing earth wall buildings developed with no reference to building codes or design manuals. Dimensioning the walls was merely

L.R. Hoyos and J. McCartney (eds.), *Advances in Characterization and Analysis of Expansive Soils and Rocks*, Sustainable Civil Infrastructures,
DOI 10.1007/978-3-319-61931-6_17

based on rules of thumb and experience (Maniatidis and Walker 2003). During the second half of the twentieth century, codes for earth construction were developed in a few countries such as New Zealand, Australia and Germany. However, some of the guidelines specified in such codes or other studies are still based on rules of thumb and not on a scientific rationale. Such practices resulted in having broad ranges and lack of consensus over the specified quantities, limits or capacities. An example to the lack of consensus is the proportion of fines (silt and clay) recommended to the earthen material. For instance, some studies and codes recommend limiting the maximum silt and clay percentage in the material to 30% while others to 80% (Alley 1948). Such discrepancy results from generalizing case-specific observations and lack of evaluation parameters.

1.1 Role of Fines

The fine-grained fraction in soils used in RE construction plays an important role in the strength gained by the material. Fines add to the strength through three major mechanisms:

- cohesion, which is mainly provided by clay particles in the fine grained soil,
- suction, which develops as the material dries due to the small pore size that leads to high capillary pressures, and
- compaction, which is influenced by the fines content in the soil.

It has already been well established to limit the plasticity and/or percentage of clay in the soil to avoid excessive volumetric changes caused by shrinkage and expansion upon drying or wetting, respectively (Easton 2007). Plastic fines (PF) and non-plastic fines (NPF) were used in this paper to highlight the effect of plasticity. Using NPF also enabled to decouple the effect of suction and initial compaction from plasticity.

Suction is one source for strength development in unstabilised RE materials (Jaquin et al. 2009) which is known to increase with the decrease of particles and pore sizes. While increasing fines content in RE materials will be associated with an increase in the magnitudes of the developing suctions, the density of the soil will increase with fines content only to a certain extent after which the compaction of the soil deteriorates. Figure 1 shows the relation between the void ratio (e) and fines content (FC) at maximum and minimum compaction. The void ratio indicates the compaction/density of the soil. The fines content after which compaction decreases (i.e. void ratio increases) is known as the critical FC.

Which effect will have superior influence on the strength of RE materials, initial compaction or desiccation suction? Compaction decreases once the critical fines content has been exceeded, whereas suction will continue to increase, but the combined or resultant effect on the strength and stiffness of the material has not yet been evaluated.

This paper focuses on investigating the effect of fines on the hydraulic characteristics (soil water retention curves (SWRC) and hydraulic conductivities) of the different mixtures while strength/stiffness measurements are still in progress. Hydraulic characteristics have direct impact on the development of stiffness as well as on the deterioration of stiffness in response to changing weather conditions.

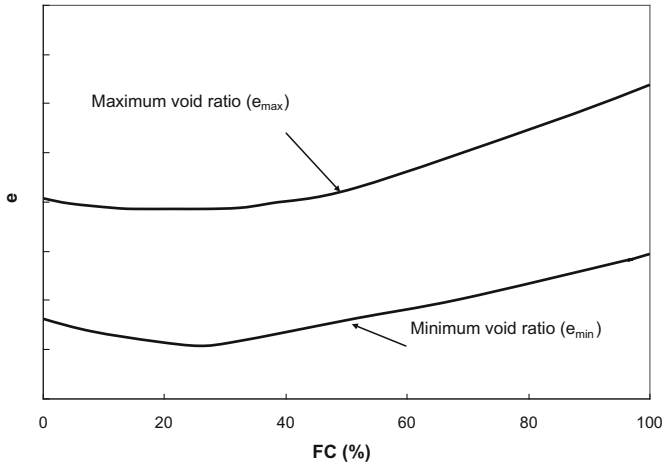

Fig. 1. Typical relationships between void ratio (e) and fines content (FC) at maximum and minimum compaction (after Galaa Abdelaal 2011).

1.2 Effect of Fines on Hydraulic and Water Retention Properties of Soils

The effect of fines on the hydraulic conductivity of soils has been already established in numerous studies. Fine particles decrease the hydraulic conductivity of soils at different rates and patterns depending on the fraction, size distribution, shape, compaction, specific surface area and plasticity of the fine particles. Various attempts were made to model the effect of fines on hydraulic conductivity such as Kozeny (1927) and Carman (1938; 1956). Estimating the specific surface area was the main focus of such attempts. Locat et al. (1984) and Chapuis and Aubertin (2003) highlighted the fact that for fines with plasticity index greater than 15 the estimates of specific surface area are not accurate. As the plasticity of fines increases, the available models fail to accurately predict the hydraulic conductivity of the soil matrix as the electrochemical forces between particles, and particles and water are not accounted for. A consensus is reached on the decrease of hydraulic conductivity for soils with higher plasticity as reported in various studies and reviewed by Benson and Trast (1995).

The effect of fines on the SWRC has been taken into account in various studies such as van Genuchten (1980) and Fredlund and Xing (1994), and models to predict SWRC were developed. The same factors influencing the hydraulic conductivity are incorporated in those models such as the pore size, percentage, packing, and shape of the fines particles. Fredlund et al. (2002) indicated that plastic fines (clay) are one of the soil materials that are difficult to model or estimate an SWRC for. Mariamma (2010) demonstrated that soils with higher fractions of fines develop greater suction forces at the same moisture content and exhibited higher water retention potential (greater field capacity and permanent welting point).

1.3 Centrifuge for SWRC

SWRC and suction measurements are done using several direct and indirect methods (Galaa 2012). Most of these methods are time consuming and require different samples of the same soil for each measurement point. Moreover, a single point could be the result of testing several samples of the soil to enhance the accuracy of the results. Examples of such methods are the filter paper method (ASTM D5298 – 10) and the pressure plate method (ASTM D6836-02(2008)e2). Two to three months is the expected duration usually taken to determine the SWRC.

During the past decade, a number of attempts were done to use bench-scale centrifuges to determine SWRC and hydraulic conductivity replacing custom centrifuges such as Martins Reis et al. (2011), Kison et al. (2015) and Malengier et al. (2015). Centrifugation based methods have been used as a faster and more accurate alternative for measurements of saturated and unsaturated hydraulic conductivity as well as determining SWRC (Malengier et al. 2015).

2 Materials Tested

Native soil material was obtained from an open pit in Badr City, Egypt, at depths ranging from 1 to 2 m. Normally, foundation levels of low-rise buildings fall in such range of depths. Therefore, the use of excavated material in the construction of walls of houses/buildings is encouraged. The obtained soils were separated into course and fine grains using sieve number 200. Soil batches were screened and only native fines with plasticity index less than 30 were used. Figure 2 shows the plasticity chart of the fines allowed in the mixtures of soil with plastic fines (PF). Soil mixtures (coarse and fines) with PF of 10, 15, 20 and 30% were prepared for the planned testing. For soil mixtures with NPF, silica powder (millisil M10, produced by Sibelco) was used and soil mixtures with NPF of 10, 20 and 30% were prepared for the planned testing.

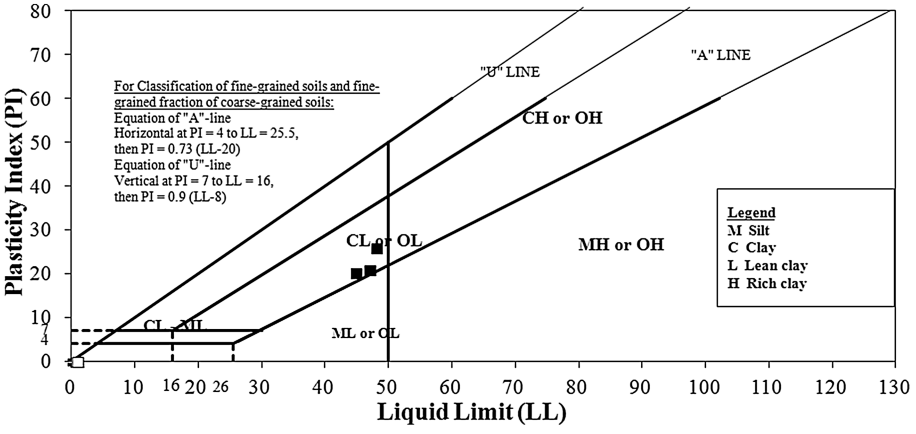

Fig. 2. Plasticity chart for the plastic fines used in soil mixtures

Grain size distributions for the mixtures with PF and NPF (using sieve analysis and hydrometer) show acceptable similarities to assume that variations in grain size distributions were insignificant (see Fig. 3).

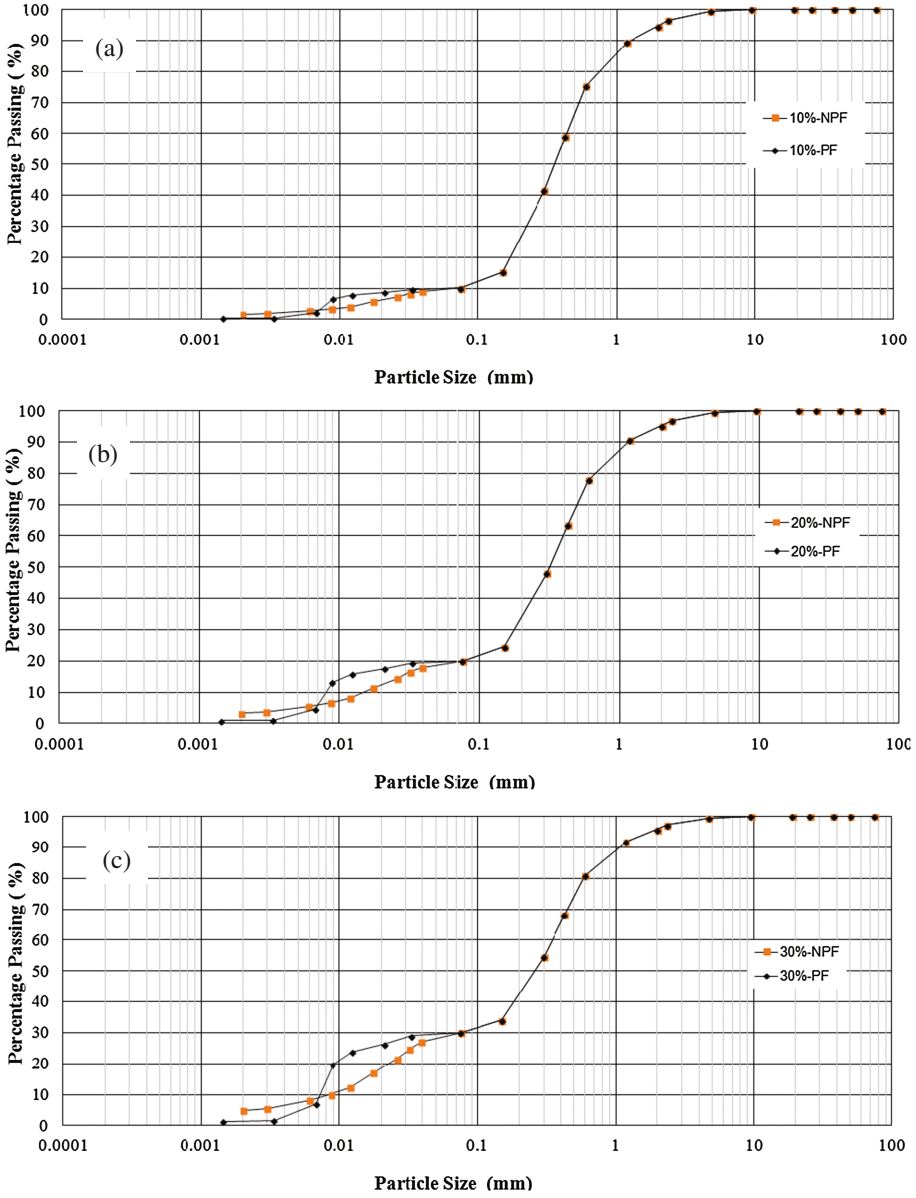

Fig. 3. Comparison of grain size distributions for mixtures with PF to mixtures with NPF at (a) 10% PF and 10% NPF, (b) 20% PF and 20% NPF, and (c) 30% PF and 30% NPF

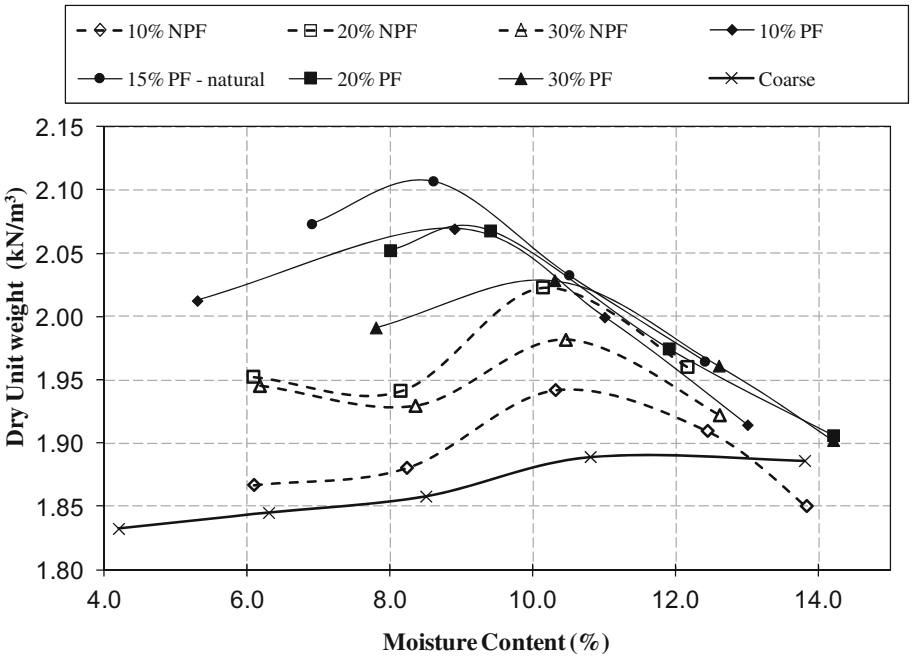

Fig. 4. Compaction curves for soil mixtures with PF and NPF

Maximum dry densities were obtained using a modified proctor compaction test for the various soil mixtures (including one without fines) as shown in Fig. 4. Soil with no fines had the smallest density of all mixtures. Figure 5 shows the relation between the void ratio and percentage of fines added for all mixtures. The critical FC was found to

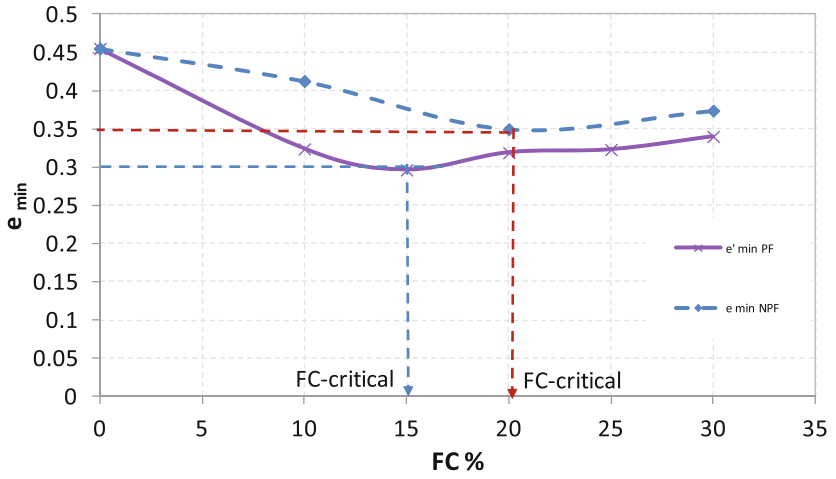

Fig. 5. Minimum void ratio variation with fines content for mixtures with PF and NPF

be ~15% for mixtures with PF and ~20% for mixtures with NPF where the minimum voids ratio was obtained as shown in Fig. 5. Since the critical FC for mixtures with NPF was ~20%, there was no need to test mixtures with 15% of NPF contrary to the case of PF.

3 Centrifuge Setup and Testing Methodology

The bench scale centrifuge described by Kison et al. (2015) was used to determine the hydraulic properties of the test materials, following the procedure outlined by Kison et al. (2015). A schematic of the centrifuge parts is shown in Fig. 6 and more illustrative photos of the setup are shown in Fig. 7. Prior to the centrifuge runs, the samples (~2.2 cm height and 2.2 cm diameter at the maximum dry density) were saturated through centrifugation under a water head (for PF samples) or subjected to a falling head test (for NPF samples) to determine saturated hydraulic conductivity (k_{sat}) (see below). Saturated PF and NPF samples were then rotated in the centrifuge at different speeds and at different preset rotation durations. Once the centrifuge was stopped, the height of the sample was measured as well as the weight of the outflow water. During the rotations, water is expelled from the sample and collected in the overflow chamber and suction is developing. In case equilibrium (i.e., equilibrium of a specific speed of rotation with the suction forces retaining water within the sample) was not reached at a specific rotation speed and after the preset duration, a mathematical model is used to determine how near to equilibrium the test came rather than increasing the duration till equilibrium before applying a higher rotation speed in order to accelerate the test thus saving considerable time.

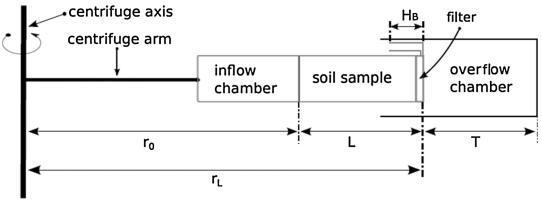

Fig. 6. Schematic of the centrifuge parts in horizontal position (rotation position) (after Kison et al. 2015).

Saturation was calculated by measuring the amount of water expelled from the sample (i.e. collected in the overflow chamber) and correcting it for equilibrium with the mathematical model. By measuring the center of gravity (COG) of the water in the soil sample (using the setup shown in Fig. 8), the SWRC or the relation between suction and saturation (or volumetric water content) was established. The detailed calculation procedures are presented in Kison et al. (2015).

The centrifuge used for the experiments is a laboratory bench-scale centrifuge type Sigma 3–18, which costs less than 10.000 Euro. This set-up is equipped with two microprocessors for the independent control of the rotor recognition and the

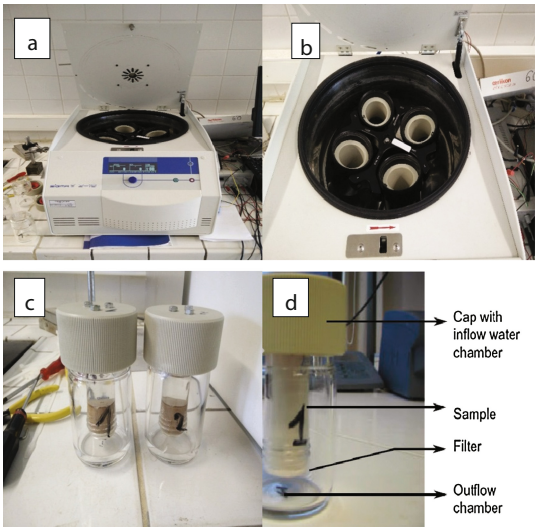

Fig. 7. (a) The used centrifuge, (b) chamber housing inside the centrifuge, (c) inflow and overflow chambers, and (d) details of the chambers.

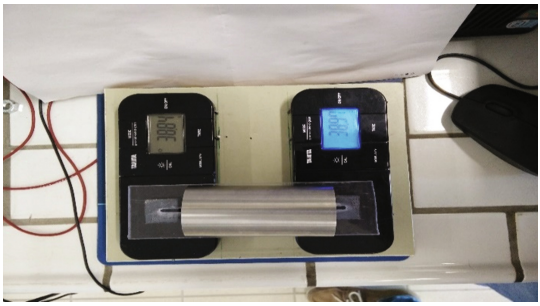

Fig. 8. Setup of weighing scales used to locate the center of gravity of soil and water

overspeed signal. The speed is continuously controlled by these microprocessors with an accuracy of 1 rpm to a maximum of 4200 rpm. Soil sample containers/chambers can, however, only withstand 2500 rpm. The duration of centrifugation, acceleration and deceleration curves can be set. The centrifuge is equipped with four buckets. Uneven loading of oppositely located buckets may lead to imbalance; in such case the drive automatically switches off and an imbalance warning message is displayed. The maximum radius from the central rotor to the base of the buckets is 171 mm.

The soil sample is housed in a custom designed fully closed system where a constant pressure prevails (see Fig. 7b). This closed system (Fig. 7b) consists of a Duran glass tube (LSB inner tube, inner diameter 21.55 mm × height 85 mm) containing the soil sample. This tube is screwed to a screw cap which is fixed in the screw cap of an outlet reservoir (LSB centrifuge, glass thread GL 60, out diam. 62.3 mm

height 110 mm). The soil container tube is provided with a Borosilicate glass 3.3 Vitra POR filter, welded to the tube, with a thickness of 2.55 mm to 3 mm, a diameter of about 21.55 mm, and a nominal pore size 1 μm–1.6 μm (class 5, ISO/4793 = P1,6). The glass containers have sufficiently thick walls (3 mm) resistant to centrifugal forces. Prior to the centrifuge tests on soil samples, k_{sat} of the Borosilicate glass POR filters was measured using a similar setup as for the soil samples.

4 Results

4.1 Saturated Hydraulic Conductivity, K_{sat}

Results of k_{sat} obtained from the bench scale centrifuge for the various PF mixtures are summarized in Table 1. Samples with 20% NPF exhibited too fast water outflow to be monitored or measured in the centrifuge, which may be attributed to large hydraulic conductivity. Therefore, permeability was instead measured for all NPF samples (contained in the same tubes as used in the centrifuge) by a falling head permeability test. However, this test resulted in very low hydraulic conductivities. Results of K_{sat} of samples with NPF obtained from the falling head permeability tests are summarized in Table 1. Results from both methods cannot simply be compared since different methods, different gradients and test conditions will result in different K_{sat} values (Verbist et al. 2009, 2013; Rezai et al. 2016).

Table 1. Saturated hydraulic conductivity, k_{sat}, for samples with PF and NPF. Values given are arithmetic means.

Fines content (%)	Average hydraulic conductivity (m/s)	
	PF[a]	NPF[b]
10	4.8E−07	3.0E−8
15	1.3E−07	–
20	1.2E−07	7.9E−9
30	9.9E−8	7.2E−9

[a] Using centrifuge
[b] Using falling head test

4.2 Determination of SWRC

During the test, samples with 20% and 30% PF did not reach or become close to equilibrium at any of the lower speeds (<2400 RPM) as a result of the low permeability and the high suction. As mentioned earlier, a mathematical model was used in those cases to correct for equilibrium as in Kison et al. (2015), as will be shown in the discussion section. However, this model is applicable when samples are near equilibrium in contrary to the case of samples with 20% and 30% PF. The glass chambers

Fig. 9. Pictures showing broken chambers and sample tubes at higher speeds (>2400 RPM)

and plastic lids did not withstand the centrifugal force when the speed exceeded 2400 RPM. Figure 9 shows the different broken parts at the higher speeds. Prior to the application of the mathematical model to correct for equilibrium, SWRC obtained from raw centrifuge results for all soil-PF and soil-NPF mixtures, except samples with 20%

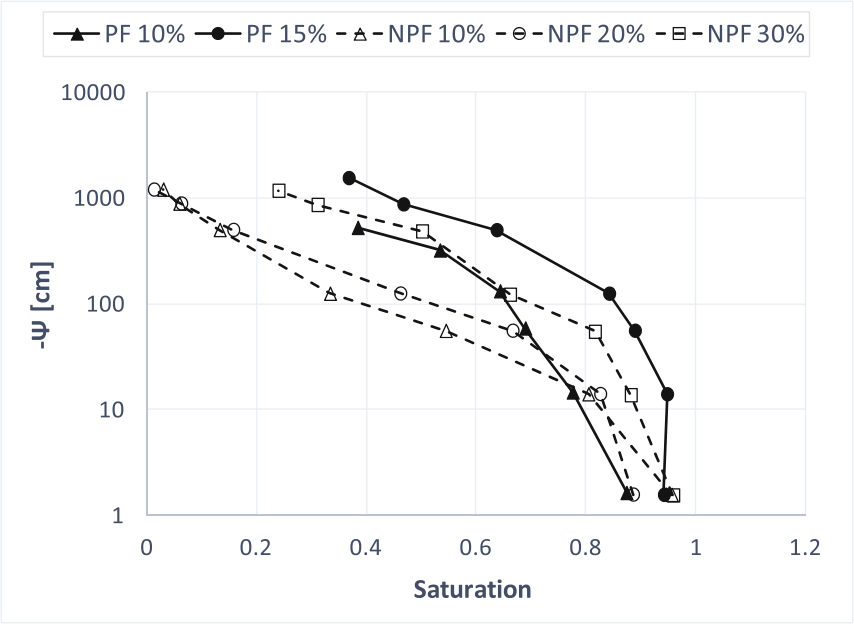

Fig. 10. SWRC from centrifuge for samples with PF and NPF based on an equilibrium analysis of the results.

and 30% PF, are presented in Fig. 10. The saturation value of the sample at the end of a centrifugation run (based on the measured outflow) is given with the generated suction value (ψ) at the middle of the sample.

5 Discussion

5.1 Saturated and Unsaturated Flow in the Centrifuge

On one hand, samples with NPF exhibited large hydraulic conductivity in the centrifuge even at low RPMs and durations of rotation. On the other hand, k_{sat} values of mixtures with NPF using the falling head permeability test were lower than those obtained for soils with PF in the centrifuge (see Table 1). Mixtures with PF were significantly denser (see Fig. 6) typically resulting in lower k_{sat}. Due to the low k_{sat} and the upper limit on the RPMs that could be reached by the centrifuge (due to the low strength of the glass), two concerns are raised in this paper:

- Values of k_{sat} measured for RE samples with PF and NPF may not be accurate. The reasons are not yet known. However, hydraulic conductivities are considered inaccurate as PF is expected to have lower k_{sat} than NPF. The counter-intuitive results are not supported by other observations made such as the time required for saturation, the drainage rates obtained in the centrifuge, and the higher suctions developing within RE samples with PF compared to those with NPF at the same fines content. In addition, the difference in k_{sat} between PF mixtures is less than the expected change to reflect the variation in the fines content. In addition, the effect of fines content and plasticity on the K_{sat} established in the literature (e.g. Kozeny (1927), Carman (1938; 1956), and Benson and Trast (1995)) has not been observed in the current study. The proposed action to address this issue is to measure k_{sat} for all mixtures with another method (flexible wall permeameter) and compare the results of all the different mixtures based on this one method.
- Low saturations could not be reached for RE with 20% and 30% PF while desaturating the sample prohibiting to obtain the dry side of the SWRC as it requires rotation speeds larger than 2400 RPM which could not be achieved with the available glassware. The proposed action to address this issue is to obtain SWRCs using the sand box/pressure plate method for all samples to compare the resulting curves (up to 15 bars) with the ones modeled by the centrifuge.

Both actions are currently in progress. To further gain insight into the hydraulic behavior of the samples and to further test and improve the methodology presented here, test enabling to simultaneously derive SWRC and hydraulic conductivity curves would be warranted. We envisage tests with the modified evaporation method (Schindler et al. 2010) in the very near future.

5.2 SWRC Modeling

As a rough approximation, the weighed outflow values at the end of each run are considered for calculating an average saturation $\bar{S}_\omega$ over the entire sample, while the average head value $\bar{h}$ is set using the following formula:

$$\bar{h}_\omega = \frac{\omega^2}{2g} L\left(\frac{L}{3} - r_E\right), \tag{1}$$

where, L is the height of the sample, r_E is the radius to the base of the sample, and ω is the rotational speed. The set of computed $\left(\bar{S}_\omega, \bar{h}_\omega\right)$ values was then used to determine the best SWRC using Durner's bimodal function (Durner, 1994) that fits the given points (Seki 2007). The Durner SWRC is determined by following formula:

$$S_e = w\left[\frac{1}{1+(\gamma_1 h)^{n_1}}\right]^{m_1} + (1-w)\left[\frac{1}{1+(\gamma_2 h)^{n_2}}\right]^{m_2} \tag{2}$$

where S_e is the effective water content, w is a weight term for two van Genuchten SWRC curves, and $m_1 = 1 - 1/n_1, m_2 = 1 - 1/n_2$.

For the different samples the best Durner curve fitting parameters are given in Table 2.

Table 2. Optimized parameters of Durner's SWRC function

Sample type	n_1	γ_1	n_2	γ_2	w
10% PF	29.497	−0.631	1.187	−0.024	0.165
15% PF	1.111	−27.403	1.627	−0.003	0.156
20% PF	–	–	1.171	−0.039	0
10% NPF	1.173	−0.535	1.839	−0.022	0.208
20% NPF	47.077	−0.646	2.011	−0.012	0.171
30% NPF	5.926	−0.0015	1.321	−0.035	0.229

This fitted Durner SWRC is then used as initial estimate in an inverse optimization to fit the measured outflow values in terms of parameters describing the SWRC and the relative permeability (unsaturated hydraulic conductivity). In this inverse optimization the deceleration time of the centrifuge, and the time the sample spends outside of the centrifuge for measurement of the outflow was not considered for simplicity. Given the low k_{sat} values, this will result in a small error only, once the sample becomes unsaturated. Also the change in sample height was neglected, which also might lead to a deviation from the true SWRC. However, this is acceptable given that only small height changes were detected. The parameters we consider are the saturated conductivity K_{sat}, the Durner SWRC parameters (w, n1, γ1, n2, γ2,), and for the relative

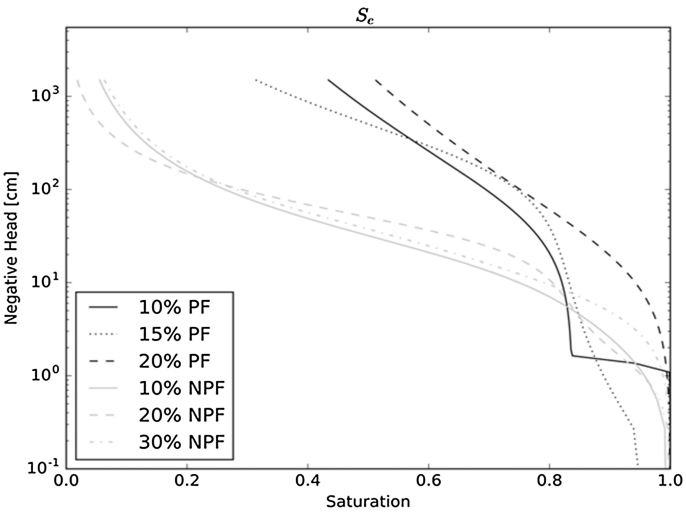

Fig. 11. Durner SWRCs resulting from modeling centrifuge data

permeability a freeform monotonic cubic interpolation with variable control points, as in Bitterlich and Knabner (2004). For the freeform interpolation, the optimal number of control points is determined based on AIC (Akaike's Information Criterion; Akaike 1974). The resulting SWRCs are given in Fig. 11 with the new optimized parameters in Table 3.

Table 3 shows that for the PF samples, the optimized k_{sat} values are consistent with those of the centrifuge test. For the NPF samples, the optimized k_{sat} values deviated from those of the falling head test, but also here, they are overall lower than the PF values. A drainage test appears not to be a good method to determine the k_{sat}, and this thus hint at the fact that k_{sat} value of the NPF samples needs further investigation and experiments need to be repeated. The full hydraulic conductivity curves obtained via freeform fitting are given in Fig. 12.

Table 3. Inverse optimization results.

Sample type	Ksat [m/s]	n1	γ1	n2	γ2	w
10% PF	5.82E−7	29.497	−0.631	1.187	−0.024	0.165
15% PF	5.07E−7	1.380	−7.303	1.490	−0.004	0.205
20% PF	5.27E−7	1.191	−0.057	1.172	−0.042	0.015
10% NPF	8.81E−8	1.293	−0.586	1.856	−0.039	0.226
20% NPF	3.76E−6	47.034	−0.640	2.011	−0.015	0.175
30% NPF	1.80E−8	2.302	−0.037	1.567	−0.065	0.039

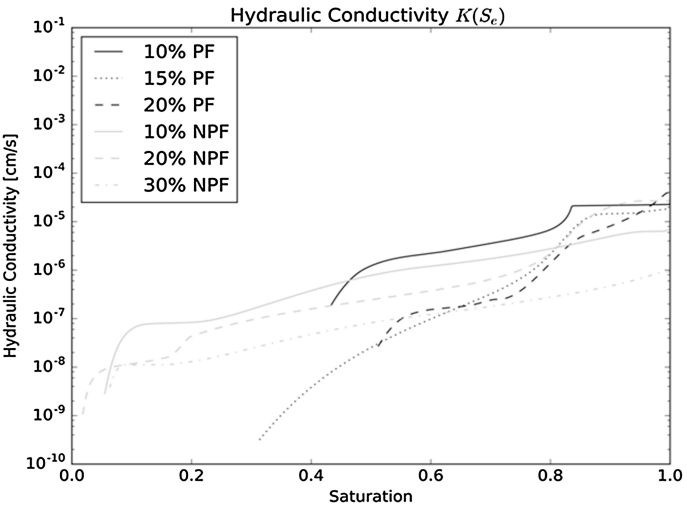

Fig. 12. Freeform Hydraulic Conductivity resulting from modeling centrifuge data

6 Conclusions

An experimental program was implemented to determine the effect of fines content on the development of suction in RE with PF and NPF and to investigate the coupled effect of suction and compaction. A bench-scale centrifuge has been used to determine the SWRC and hydraulic conductivity of RE samples. Durner SWRC was found to give the best fit for the obtained SWRC, as evident by the significant value of the w parameter. Form the centrifuge results and Durner fit it was found that:

- RE samples with PF exhibited larger suctions than those with NPF for the same fines content. Larger densities and lower void ratios were obtained for RE with PF in comparison to those with NPF which might have caused the development of larger suctions.
- For the same type of fines, suction was found to increase with the increase in fines content at the same degree of saturation. This effect was more pronounced for samples with PF.
- Lower degrees of saturation were not reached for RE samples with 20% and 30% PF as it required rotation speeds greater than 2400 RPM. The strength of the glass tubes and the holding lids did not sustain the stress developed at higher speeds.
- A clear bimodal SWRC was found for 10%PF, 15%PF, and 20% NPF.

From the obtained freeform relative permeability it was found that:

- The permeability decreases much faster with decreasing saturation for plastic fines than for non-plastic fines.
- Increasing the NPF content (from 10 to 30%) decreases the relative permeability of the samples. On the other hand, increasing the PF content (from 10 to 20%) does not influence the relative permeability much.

– For NPF content, the hydraulic conductivity is only slowly decreasing over a large range of the saturation (0.2 to 0.95).

The measured hydraulic conductivities using the centrifuge and the falling head method show that the hydraulic conductivity of RE samples with PF is larger than that of those with NPF. These counter-intuitive results are not supported by literature or other observations made such as the time required for saturation, the drainage rates obtained in the centrifuge, and the higher suctions developing within RE samples with PF compared to those with NPF at the same fines content. K_{sat} values of the NPF samples needs further investigation and repeat experiments. In addition, comparing hydraulic conductivities obtained from two different methods of measurement under different conditions is not correct in principle. Therefore, hydraulic conductivity measurements using flexible wall permeameters are currently in progress to achieve more reliable hydraulic conductivity values.

In addition, the sand box/pressure plate tests are still in progress to obtain SWRC for all RE mixtures and to compare the resulting curves (up to 15 bars) with the ones obtained by the centrifuge.

Acknowledgments. The work is part of the project entitled "Evaluating the Role of Fines in Unstabilized Rammed Earth" which is funded by the Science and Technology Development Fund (STDF) of Egypt. The experimental work was also supported by the Laboratory of Geotechnics at Ghent University, Belgium. Our gratitude is extended to Bertram Koolen for his dedicated efforts to accomplish the experimental work included in this paper.

References

Abdelaal, A., Grabinsky, M.: Early age mechanical behavior and stiffness development of cemented paste backfill with sand. Ph.D. dissertation, Department of Civil Engineering, Univeristy of Toronto (2011)

Akaike, H.: A new look at the statistical model identification. IEEE Trans. Autom. Control **19**(6), 716–723 (1974). doi:10.1109/TAC.1974.1100705

Alley, P.J.: Rammed earth construction, New Zealand Engineering, 10 June, p. 582 (1948)

Benson, C.H., Trast, J.M.: Hydraulic conductivity of thirteen compacted clays. Clays Clay Miner. **43**(6), 669–681 (1995)

Bitterlich, S., Knabner, P.: Numerical methods for the determination of material properties in soil science. Inverse Prob. Sci. Eng. **12**(4), 361–378 (2004). doi:10.1080/10682760310001597482

Carman, P.C.: The determination of the specific surface of powders. J. Soc. Chem. Ind. Trans. **57**, 225 (1938)

Carman, P.C.: Flow of Gases Through Porous Media. Butterworths Scientific Publications, London (1956)

Chapuis, R.P., Aubertin, M.: On the use of the Kozeny-Carman equation to predict the hydraulic conductivity of a soil. Can. Geotech. J. **40**(3), 616–628 (2003)

Durner, W.: Hydraulic conductivity estimation for soils with heterogeneous pore structure. Water Resour. Res. **30**(2), 211–223 (1994). doi:10.1029/93WR02676

Easton, D.: The Rammed Earth House, rev. edn. Chelsea Green Publishing, Vermont (2007)

Fredlund, D.G., Xing, A.: Equations for the soil-water characteristic curve. Can. Geotech. J. **31**, 533–546 (1994)

Fredlund, M.D., Wilson, G.W., Fredlund, D.G.: Use of the grain-size distribution for estimation of the soil-water characteristic curve. Can. Geotech. J. **39**(5), 1103–1117 (2002)

Galaa, A., Grabinsky, A., Bawden, W.: Characterizing stiffness development in early age cemented paste backfills with sand in a non-destructive triaxial test. In: Canadian Geotechnical Conference, GeoManitoba (2012)

Jaquin, P.A., Augarde, C.E., Gallipoli, D., Toll, D.G.: The strength of unstabilised rammed earth materials. Geotechnique **59**(5), 487–490 (2009)

Joseph, M.: A study on the water retention characteristics of soils and their improvements. Doctor of Philosophy Dissertation, Cochin University of Science and Technology, India (2010)

Kišon, P., Malengier, B., et al.: Inverse determination of saturated and relative permeability with a bench-scale centrifuge. Inverse Prob. Sci. Eng. **23**(1), 16–37 (2015)

Kozeny, J.: Ueber kapillare Leitung des Wassers im Boden. Wien Akad. Wiss. **136**(2a), 271 (1927)

Locat, J., Lefebvre, G., Ballivy, G.: Mineralogy, chemistry, and physical properties interrelationships of some sensitive clays from Eastern Canada. Can. Geotech. J. **21**(3), 530–540 (1984)

Malengier, B., Di Emidio, G., Peiffer, H., Ciocci, M., Kišon, P.: Unsaturated permeability and retention curve determination from in-flight weight measurements in a bench-scale centrifuge. Geotech. Test. J. (2015). 10.1520/GTJ20140121

Maniatidis, V., Walker, P.: A review of rammed earth construction. In: DTI Project Report, Bath, UK (2003)

Martins Reis, R., Nogueira Sterck, W., Bastos Ribeiro, A., Dell'Avanzi, E., Saboya, F., Tibana, S., Roberto Marciano, C., Ramires Sobrinho, R.: Determination of the soil-water retention curve and the hydraulic conductivity function using a small centrifuge. Geotech. Test. J. **34** (5), 457–466 (2011)

Rezaei, M., Seuntjens, P., Shahidi, R., Joris, I., Boënne, W., Al-Barri, B., Cornelis, W.: The relevance of in-situ and laboratory characterization of sandy soil hydraulic properties for soil water simulations. J. Hydrol. **534**, 251–265 (2016)

Seki, K.: SWRC fit - a nonlinear fitting program with a water retention curve for soils having unimodal and bimodal pore structure. Hydrol. Earth Syst. Sci. Discuss. **4**, 407–437 (2007). doi:10.5194/hessd-4-407-2007

Schindler, U., Durner, W., von Unold, G., Mueller, L., Wieland, R.: The evaporation method: extending the measurement range of soil hydraulic properties using the air-entry pressure of the ceramic cup. J. Plant Nutr. Soil Sci. **173**, 563–572 (2010)

van Genuchten, M.T.: A closed form equation for predicting the hydraulic conductivity of unsaturated soils. Soil Sci. Soc. Am. J. **44**, 892–890 (1980)

Verbist, K., Baetens, J., Cornelis, W.M., Gabriels, D., Torres, C., Soto, G.: Hydraulic conductivity as influenced by stoniness in degraded drylands of Chile. Soil Sci. Soc. Am. J. **73**(2), 471–484 (2009)

Verbist, K.M.J., Cornelis, W.M., Torfs, S., Gabriels, D.: Comparing methods to determine hydraulic conductivities on stony soils. Soil Sci. Soc. Am. J. **77**(1), 25–42 (2013)

Author Index

L.R. Hoyos and J. McCartney (eds.), *Advances in Characterization and Analysis of Expansive Soils and Rocks*, Sustainable Civil Infrastructures,
DOI 10.1007/978-3-319-61931-6